UNIVERSITÀ DEGLI STUDI DI PADOVA, INAF – Osservatorio Astronomico di Padova
Dipartimento di Fisica e Astronomia "Galileo Galilei"
Scuola di Dottorato di ricerca in Astronomia
Ciclo XXVIII

Multi Conjugate Adaptive Optics correction on an 8 meters telescope: a NIRVANA from the lab to the sky

Direttore della scuola: Ch.mo Prof. Giampaolo Piotto
Supervisore: Ch.mo Prof. Roberto Ragazzoni

Dottorando: Luca Marafatto

ABSTRACT

In the last 50 years the apertures of the world largest ground-based telescopes doubled, passing from the 5 *m* of the Hale telescope (1948) to the over 10 *m* of the Gran Telescopio Canarias, serving the astronomers in their attempts to push further and further the boundaries of our knowledge of the sky. The astronomical community is now looking forward to the era of the 40 *m* telescope (Extremely Large Telescope, ELT), which will further improve the studies in many astronomical fields, enabling the observation of very faint and distant objects, beyond the limits of the currently known universe.

However, since these telescopes are located on the ground and they are naturally affected by atmospherical seeing, even the largest telescope would be equivalent, in term of resolution and image quality, to a telescope of few tens of centimetres in diameter, if the seeing is not compensated.

This is exactly the aim of Adaptive Optics, which plays a key role in the modern ground-based telescope, as it allows the telescope to recover, completely or partially, its theoretical resolution imposed by diffraction. Many different kinds and approaches to Adaptive Optics have been proposed in the last decades, each one with its level of correction, sky coverage, complexities etc.

LINC-NIRVANA, the Fizeau interferometer for the LBT, is equipped with a complex Multi-Conjugate Adapive Optics system (MCAO), which allows to uniformily correct a 2 *arcmin* Field of View, enabling interferometric imaging on a 10 x 10 *arcsec* Field of View with a 23 *m* telescope equivalent resolution. When operated in this configuration, the LBT can be considered a precursor of the ELTs.

In this Thesis I give a detailed description of the MCAO system serving LINC-NIRVANA, and in particular of its main subsystems, the Ground layer Wavefront Sensor (GWS) and the High layer Wavefront Sensor (HWS). I give an overview of the optical concepts and layout of the MCAO module, going through the definition of the alignment procedures defined to match the tight tolerances required to correctly operate the instrument, and concluding with the results and verifications of the alignment.

I also widely describe the operations and the results of a Pathfinder Experiment, in which one of the two GWSs has been tested at the LBT as a stand alone system in order to verify its ability to drive the Adaptive Secondary Mirror of the LBT and also our ability to make it possible. In this way we acquired experience in view of the LINC-NIRVANA commissioning, planned at the end of 2016.

Since LINC-NIRVANA is an Italian/German collaboration, the work described in this Thesis was carried out in three countries: Italy, Germany and U.S.

RIASSUNTO

Negli ultimi 50 anni il diametro dei principali telescopi a terra del mondo è più che raddoppiato, passando dai circa 5 *m* del telescopio Hale ai più di 10 *m* del telescopio Gran Telescopio Canarias, in risposta alle necessità del mondo astronomico nel suo tentativo di spingere sempre più lontano i confini della nostra conoscenza della volta celeste. La comunità astronomica è ora proiettata ed in attesa dell'era dei telescopi da 40 *m*, che permetteranno di migliorare le nostre conoscenze e la nostra comprensione in moltissimi campi astronomici, permettendo di osservare sorgenti sempre più deboli e lontane, spingendo il nostro sguardo oltre i limiti attuali, fino ai sfiorare i confini dell'Universo appena nato. Tuttavia, dal momento che i telescopi a terra sono affetti dal fenomeno naturale del seeing, dovuto alla presenza di un mezzo turbolento tra il telescopio e la volta celeste (l'atmosfera), anche il telescopio più grande diverrebbe equivalente, quantomeno in termini di risoluzione e qualità dell'immagine, a un telescopio di poche decine di centimetri se non si risolve il problema del seeing.

Questo è esattamente il proposito dell'Ottica Adattiva, che gioca un ruolo chiave nelle osservazioni astronomiche da terra, dal momento che permette ai telescopi di riacquisire, totalmente o in parte a seconda della tecnica di Ottica Adattiva utilizzata, il loro limite di risoluzione teorico imposto dalla diffrazione. Data la sua importanza, negli ultimi decenni sono stati sviluppati molti sistemi e concetti di Ottica Adattiva, ognuno con le sue peculiarità e caratteristiche.

LINC-NIRVANA, l'interferometro di Fizeau per il Large Binocular Telescope, è equipaggiato con un complesso modulo di Ottica Adattiva Multiconiugata (MCAO), che consente di correggere uniformemente un campo di vista di 2 *arcmin*, permettendo di ottenere immagini interferometriche su un campo di 10 x 10 *arcsec*, molto esteso se comparato ad altri interferometri, con una risoluzione equivalente a quella di un telescopio di 23 *m*. In sostanza, in questa configurazione, LBT può essere considerato un precursore degli ELTs.

In questo Tesi darò una descrizione dettagliata del modulo MCAO equipaggiato a LINC-NIRVANA, concentrandomi in particolare sui due principali sottosistemi che lo costituiscono: il Ground layer Wavefront Sensor (GWS) e l'High layer Wavefront Sensor (HWS). Darò una panoramica dei concetti di ottica su cui si basano questi sensori, definirò le procedure di allineamento utilizzate per soddisfare le rigide tolleranze imposte per poter operare lo strumento con buone prestazioni e infine descriverò i risultati dell'allineamento e di verifica.

Inoltre, descriverò le attività e i risultati ottenuti durante un Pathfinder Experiment, il cui scopo principale è stato sia verificare le prestazioni di uno dei due GWSs come un sistema a sé stante, comandando lo specchio secondario adattivo di LBT, sia le nostre capacità di renderlo possibile, acquisendo esperienza per il futuro commissioning di LINC-NIRVANA, previsto per la fine del 2016.

Essendo LINC-NIRVANA una collaborazione Italia/Germania, le attività effettuate dallo scrivente e descritte in questa Tesi sono state svolte in Italia, Germania e USA (per il Pathfinder).

ACKNOWLEDGEMENTS

Thank you to Kayla Friedman and Malcolm Morgan of the Centre for Sustainable Development, University of Cambridge, UK for producing the Microsoft Word thesis template used to produce this document.

CONTENTS

LIST OF TABLES

LIST OF FIGURES

LIST OF ABBREVIATIONS AND ACRONYMS

AIV	Assembly, Integration & Verification
AL	Agnostic Lantern
AM	Annular Mirror
AO	Adaptive Optics
ARGOS	Advanced Rayleigh guided Ground layer adaptive Optics System
ASM	Adaptive Secondary Mirror
BCU	Basic Computational Unit
BS	BeamSplitter
CCD	Charge Coupled Device
DM	Deformable Mirror
DSLR	Digital Single Lens Reflex
FDR	Final Design Review
FEA	Finite Elements Analysis
FLAO	First Light Adaptive Optics
FoV	Field of View
GLAO	Ground-Layer Adaptive Optics
GWS	Ground-layer Wavefront Sensor
HWS	High Wavefront Sensor
IR	InfraRed
IRTC	InfraRed Test Camera
LBC	Large Binocular Camera
LBT	Large Binocular Telescope
LGS	Laser Guide Star
LINC-NIRVANA: The LBT INterferometric Camera and Near-InfraRed/Visible Adaptive iNterferometer for Astronomy	
LN	Linc-Nirvana
LO	Layer-Oriented
MAD	Multi-conjugated Adaptive optics Demonstrator
MCAO	Multi-Conjugated Adaptive Optics
MFoV	Multiple Field of View

ML	Magic Lantern
MOAO	Multi-Object Adaptive Optics
MPIA	Max Planck Institute für Astronomie
MTF	Modulation Transfer Function
NGS	Natural Guide Star
OAP	Off-Axis Parabola
OPD:	Optical Path Difference
PR-I	Pupil Re-Imager
PS	Plastic Screen
PSF	Point Spread Function
RMS	Root Mean Square
RON	Read-Out Noise
RR	Retro-Reflector
SE	Star Enlarger
SNR	Signal-to-Noise Ratio
SO	Star-Oriented
SR	Strehl Ratio
VLT	Very Large Telescope
WFE	WaveFront Error
WFS	WaveFront Sensor

1 Introduction

Astronomy is one of the oldest sciences in humankind history, directly deriving from the human instinct, which leads him to research and discovery of new knowledges: the curiosity. Astronomy began with the observation of the motion of planets and stars, using just the naked eye, and subsequently evolved over the centuries, building large and powerful tools that helped humankind to look deeper into the sky, increasing the heavenly borders. The size of optical telescopes has exponentially grown from Galileo's era, allowing observing fainter and more distant objects.
Since a telescope collects only a portion of the wavefront coming from a celestial object, such a spatial selection translates into an uncertainty, directly resulting from Heisenberg's principle, on the propagation direction of the collected photons, resulting in an enlargement of the image of the source on the focal plane, according to:

$$\theta = \frac{\lambda}{D} \qquad [1\text{-}1]$$

Where θ is the angular size of the spot on the focal plane obtained with a telescope of diameter D at wavelength λ. When a telescope reaches this angular resolution it is said to be diffraction limited, it has reached its physical resolution limit imposed by diffraction.
However, the angular resolution of ground based telescopes larger than few tens of centimetres is limited by seeing, an atmospheric phenomenon caused by spatial and temporal variations in the refractive index of the air, which introduces distortions to the wavefront passing through it. Therefore, to fully exploit the potential of modern telescopes, whose apertures D reach 10 m, it is necessary to overcome this problem. The construction and maintenance of a telescope out of the atmosphere, although it has the advantage not to suffer from atmosphere limitations, has a huge cost, as demonstrated by the Hubble Space Telescope. Moreover, due to the complexity of carrying large objects into orbit, the aperture of a space telescope is much less than the one of a ground based telescope, resulting in a lower angular resolution.
The goal of Adaptive Optics is to reduce, if not cancel, the distortions introduced from the atmosphere on the wavefront of a scientific object, using a tool to sense these distortions, the Wavefront Sensor, and deformable mirrors to apply the correction.
Its application allow thus the telescope to regain almost completely its theoretical resolution, the level of correction depending on the adaptive optics technique used. Each technique, in fact, has different characteristics from the others, in terms of correction and sky coverage, i.e. the portion of the sky where adaptive optics can be successfully exploited.
The Large Binocular Telescope (LBT) consists of two mirrors, 8.4 m in diameter, on a single mechanical mount, and it will take advantage of a Multi-Conjugate Adaptive Optics (MCAO) correction thanks to LINC-NIRVANA. This instrument is designed to perform Fizeau interferometry, allowing the telescope to reach an angular resolution equivalent to that of a 22.8 m telescope. To obtain good interferometric images it is necessary that the light coming from the two apertures of LBT be co-phased on the common focal plane, so to interfere correctly. For this reason, LINC-NIRVANA is

equipped with a MCAO system to compensate in real time the actions of the atmosphere, which would otherwise destroy any possibility to perform interferometry. In this context, the deformations introduced in the wavefront from the ground layer are sensed by a couple (one for each arm of LBT) of Ground layer Wavefront Sensors (GWS), while the turbulence introduced by a high layer (7.1 *km*) above the telescope pupil is sensed by a couple of High layer Wavefront Sensors (HWS).

In my PhD project, I have been involved in the assembly, integration and verification of the GWSs and, during a period of 9 months in Heidelberg, where LINC-NIRVANA was assembled and tested, in the alignment and verifications of the MCAO system (GWSs + HWSs) and its calibration unit. The whole instrument was ultimately aligned at the end of last year and after having successfully closed the loop in the lab was finally shipped to the LBT, where it is currently being aligned to the telescope.

Due to the complexity of the project, to reduce the risks for the project as a whole, a Pathfinder experiment was conceived. One of the two GWSs was mounted at the LBT as a stand-alone system, to prove its capability of drive the adaptive secondary mirror of the LBT and to identify critical interface problems early (mechanical or optical), thereby keeping the task of solving those eventual interface problems out of the critical path.

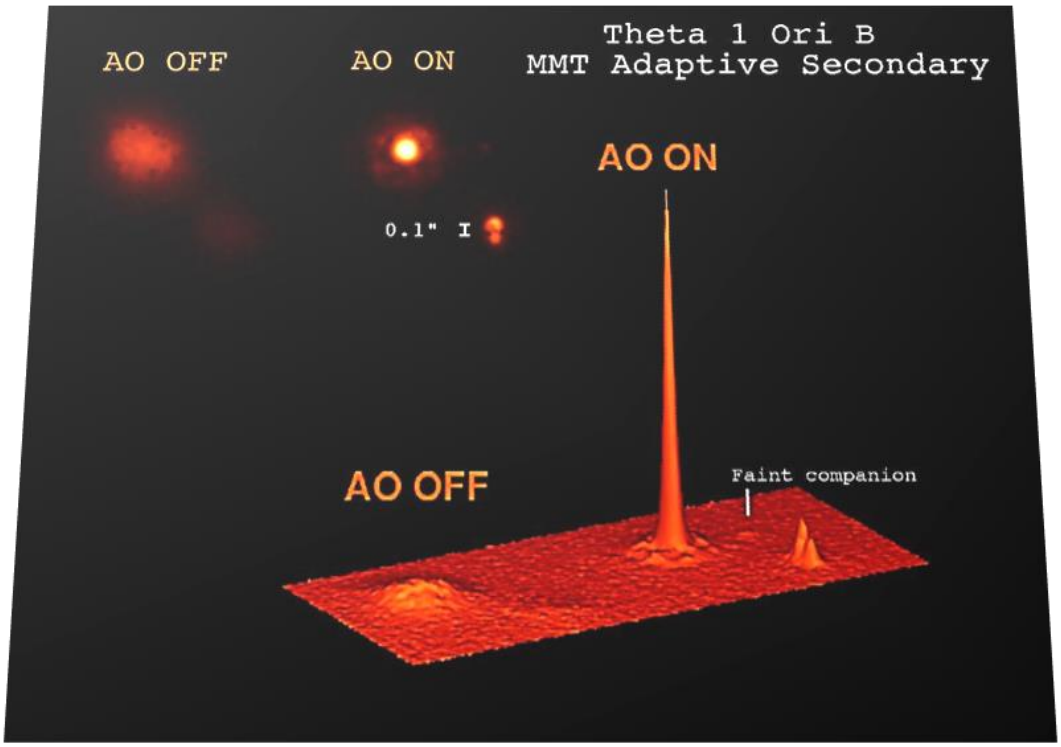

Figure 1-1: Example of the adaptive optics correction. When the correction is off only two very blurred objects appear in the picture. "Turning on" adaptive optics, four objects are visible: a binary system, a bright star and a very faint star. It is clear the improvement in both angular resolution and sharpness.

2 The Atmosphere

2.1 Atmospheric limitations

The Earth's atmosphere poses severe limitations to ground-based astronomy, manly for three reasons:

- It absorbs part of the incoming radiation
- Background radiation
- Atmospheric turbulence

The absorption of the light is due to the interaction between the radiation and the atoms and molecules present in the atmosphere, which usually occurs at discrete wavelengths. However, since the molecules have a very high degrees of freedom, mainly vibrational and rotational, the energy levels are so close one to each other to simulate a continuum and the light is absorbed in a quite wide band.

The regions of the electromagnetic spectrum to whose the Earth's atmosphere is mostly transparent are called "windows". These windows are mainly located in the visible, infrared and radio domains. At short wavelength, between 100 and 300 *nm* the atmosphere is opaque, because of the absorption from O_2 and N_2 molecules in the 100 – 200*nm* band and of the O_3 absorption in the 200 – 300*nm*. In the Infrared domain the absorption is characterized by a series of narrow windows, at 1.25μm (J band), 1.6μm (H band), 2.2μm (K band) and 3.4μm (L band), interrupted by a series of wide bands of absorption due to oxygen and water vapour. The last window is in the radio domain and it extends from about 8*mm* to about 15*m*, where it is limited by the reflection caused from the high percentage of free electrons and ions in the ionosphere.

The brightness of the sky background affects the observation from the ground of faint sources, since the objects fainter than the background cannot obviously be detected (in the visible domain the threshold is about 22mag, in a night without Moon), while objects close to this limit necessitate of very long exposure time to obtain an acceptable Signal to Noise Ratio (SNR). The major component of the background radiation during the nights with the Moon is the reflected light from the Sun. During Moonless nights most of the atmospheric radiation in the range 0.5 – 2.5 *mm* is due to the emission from hydroxyl molecules (OH).

Finally, the atmospheric turbulence is due to the injection of energy in the atmosphere from solar heating. This causes different air masses moving in different directions and with different velocities. Usually the most turbulent layer is close to the ground, where a very efficient heating exchange between the air and the ground takes place.

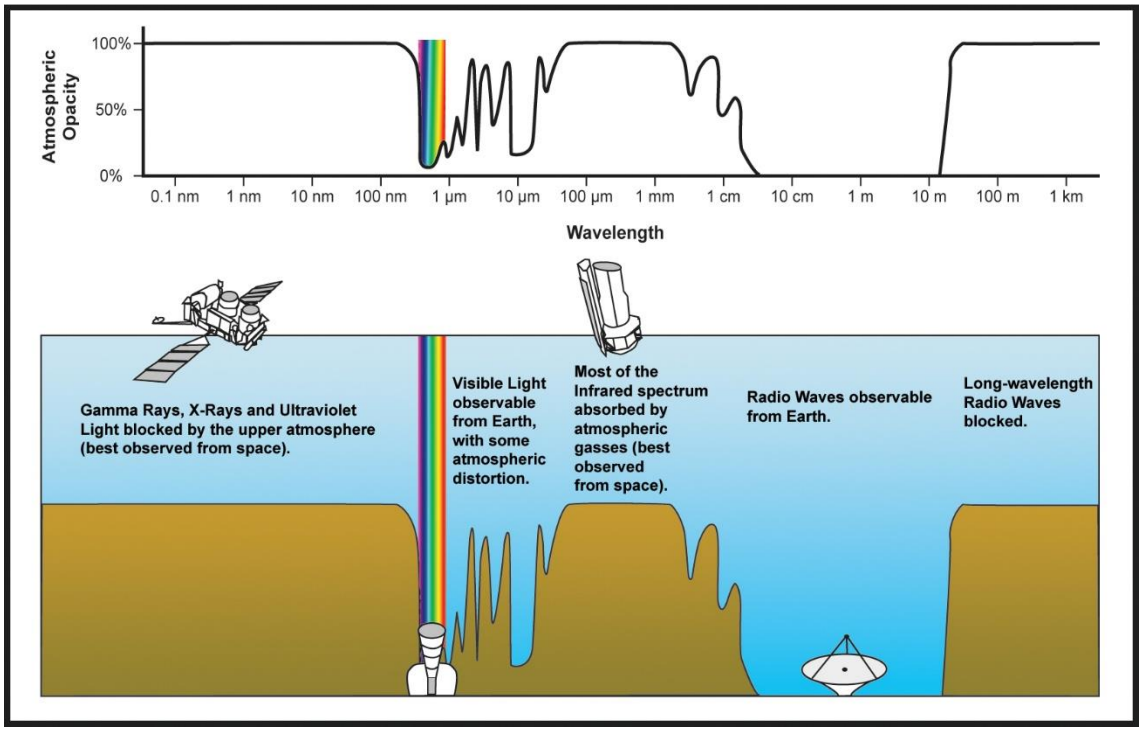

Figure 2-1: Earth's atmosphere opacity. The high frequency radiation (γ rays, UV) is blocked by the upper atmosphere layers, composed mainly of molecular oxygen (O_2) and ozone O_3. The atmosphere is transparent in the Visible and Near-Infrared bands. Radiation with λ > 1 µm is absorbed by several gas molecules as CH_4, N_2O, CO_2 and especially H_2O and just few narrow windows are present until the Radio band, where the atmosphere becomes transparent again.

2.2 Atmospheric turbulence

The atmosphere in an inhomogeneous medium constituted of regions with different and time-varying optical properties. From the geometrical optics we know that when a light beam passes between two mediums with different refraction indices *n*, its direction of propagation changes, accordingly to the Snell's law:

$$\frac{sin\theta_1}{sin\theta_2} = \frac{n_2}{n_1} \qquad [2\text{-}1]$$

Where n_1 and n_2 are the refractive indices of the two media and θ_1 and θ_2 are the angles between the direction of propagation of the beams and the normal to the discontinuity surface between the two media. By definition, the refractive index of vacuum is $n = 1$ and it increases as the light travels to the ground, through the atmosphere. If we assume for simplicity the Earth's atmosphere as a combination of shells with a continuously increasing refraction index as getting closer to the ground, the light will always bend towards the Earth's surface normal, accordingly to the Snell law. Unfortunately, the refractive index has gradient not only in vertical direction but also in horizontal direction. In addition, gradient is not a monotone function. There are continuous spatial and temporal vertical and horizontal variations of refractive index on small scales. This phenomenon, called *seeing*, continuously bends the wave trajectories. The net result of this effect is wavefront perturbation.

The refraction index varies as a function of the wavelength λ, of the pressure *P*, of the temperature *T* and of the water vapour pressure *e*, as described from the Cauchy's equation:

$$n \approx 1 - \frac{77 \times 10^{-6}}{T[K]} \cdot (1 + 7.52 \times 10^{-3}\lambda^{-2}) \cdot \left(P[mbar] + 4810 \frac{e[mbar]}{T[K]} \right) \qquad [2\text{-}2]$$

The *e* term is negligible for the Visible and Infrared bands, and the [2-2] can be approximated by the Gladstone's law:

$$n \approx 1 - 77 \times 10^{-6} \cdot \frac{P[mbar]}{T[K]} \qquad [2\text{-}3]$$

From which is clear that temperature variations lead to refraction index fluctuations. These fluctuations start at large spatial and temporal scales, and volumes of atmosphere with constant *n* are called *turbulent vortices.* The parameter, which describes the behaviour of a fluid, is the ***Reynold's number*** *Re*, described as the ratio between the kinetic energy of the fluid and the viscous frictional energy:

$$Re = \frac{L[m] \cdot v[m/s]}{\zeta[m^2/s]} \qquad [2\text{-}4]$$

Where L is the characteristic dimension of the air mass, ν is the wind velocity and ζ is the kinematic viscosity coefficient of the gas. When *Re* is higher than 10000 (critical threshold) the fluid is in a turbulent flow regime, while for *Re* values lower than 2000 a laminar flow regime is established. For the air, $\nu \approx 15 \times 10^6$ m^2/s and for the atmosphere $L = L_0 > 15\ m$ e $v_{L0} > 1 - 10\ m/s$, meaning that $Re(L_0) \approx 10^6 \gg Re_{cr}$, so we can state that all ground-based observations belong to a highly turbulent regime.

2.3 Kolmogorov's Theory

Kolmogorov suggested that for values of *Re* so high, the energy dissipation due to viscous friction is negligible compared to the energy injected at scale L_0. This energy is consequently totally transferred at the smaller scales. The energy transition between different scales is due to non-linear processes that regulate a fluid flow. For each scale L, for which *Re*(L) is higher than Re_{cr}, a similar process takes place, establishing a regime in which the energy for a unit of time and mass ε introduced into the turbulent flow at the scale L_0 is transferred, basically without losses, from scale to scale, increasing the turbulence at smaller scales. Once the l_0, called *inner scale*, is reached, so that $Re(l_0) \approx Re_{cr}$ ($l_0 \approx 1 - 10\ mm$), the kinetic energy is converted into thermal energy for viscous friction and the cascade transfer process arrests and we enter in the so-called dissipation range.

In the range $l_0 << L << L_0$, called *inertial regime*, the viscosity effect is negligible ($L >> l_0$) and the turbulence can be considered as isotropic and homogeneous ($L << L_0$), so that

turbulence structure is regulated only by ε, which is transferred from scale to scale. In this stationary regime, ε has to coincide with the kinetic energy loss from the fluid, corresponding to the dissipated energy due to viscous friction ε_0 at inner scale l_0. Since the kinetic energy depends only on the velocity of the fluid, from a dimensional analysis we can write:

$$v = \varepsilon_0^{1/3} l^{1/3} \qquad [2\text{-}5]$$

Meaning that the velocity fluctuations at which turbulence vortexes vary depend only on the scale size and on the energy transmissivity range. The kinetic energy depends on the squared velocity, then the energy fluctuations E_l in l scale perturbation is:

$$E_l dl \propto \varepsilon_0^{2/3} l^{2/3} \qquad [2\text{-}6]$$

The turbulence power spectrum can be deduced by the equation [2-6], integrating between l and $l + dl$, obtaining $E_l \propto l^{5/3}$. Defining the wave number as $k = 2\pi/l$, the vortex-associated energy E_k is:

$$E_k \propto k^{-5/3} \qquad [2\text{-}7]$$

This relationship describes the one dimensional energy distribution at different spatial frequencies inside the inertial range, and it is called *Kolmogorov Power Spectrum.* Integrating over the 3 spatial coordinates the relationship becomes:

$$E_k \propto k^{-11/3} \qquad [2\text{-}8]$$

The environmental conditions may affect the fluids regime. In the case of the atmosphere, the gravity, through the hydrostatic forces, affects the development of turbulence, when the scale is sufficiently large. This condition is described by the Richardson parameter R_i, defined as the ratio between the vertical thermal gradient (which conditions the hydrostatic equilibrium) and the wind speed gradient:

$$R_i \propto \frac{\frac{dT}{dZ} - \gamma}{\left(\frac{\Delta v}{\Delta z}\right)^2} \qquad [2\text{-}9]$$

With γ the adiabatic vertical thermal gradient (-1°C/100 *m*). When $R_i > 0{,}25$ the turbulent regime is sustained by the atmospherical conditions, otherwise it will weaken.

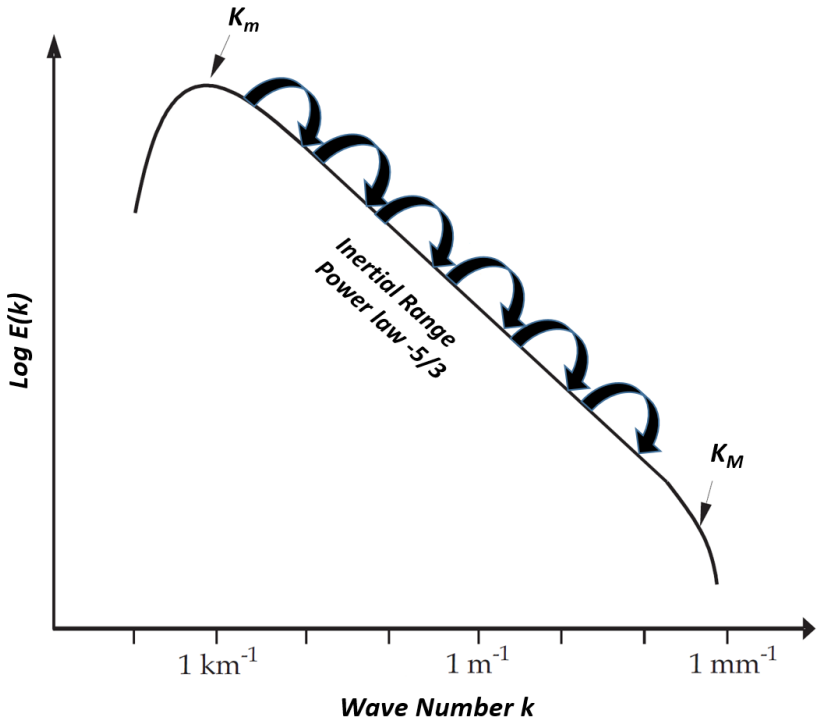

Figure 2-2: One dimensional power spectrum of the energy connected to vortexes in turbulent regime. The inertial range obeys to the Kolmogorov law. In the graph $K_m = 2\pi/L_0$ and $K_M = 2\pi/l_0$

Let us now examine how the atmospherical turbulence affects the light propagation across the atmosphere. We consider here, for simplicity, monochromatic waves, described by the wave function:

$$\varphi = Ae^{i\theta} \qquad [2\text{-}10]$$

Where A is the wave amplitude and θ its phase. The set of points with the same phase represents the wavefront. When a wavefront incoming from an object at the infinity, like a star, reaches the outer layers of our atmosphere it is plane. The turbulence in the atmosphere and temperature variations in different layers translate into local fluctuations of the refraction index. Different portions of the original wavefront propagate with different velocities, depending on the local value of the refraction index. From [2-3] we can derive how the refraction index n changes with temperature and pressure:

$$d\tilde{N} \approx \frac{0.77(TdP - PdT)}{T^2} = \frac{0.77dP}{T} - \frac{0.77P}{T^2}dT \qquad [2\text{-}11]$$

With $\tilde{N} = (n-1) \times 10^6$. Multiplying this equation by $1/dh$ we obtain the refraction index as a function of the height above the sea level:

$$\frac{d\tilde{N}}{dh} \approx \frac{0.77}{T}\frac{dP}{dh} - \frac{0.77P}{T^2}\frac{dT}{dh} \qquad [2\text{-}12]$$

Showing a strong dependency of the refractive index variations from the temperature.

The speed propagation of a wave in a medium *v* is linearly depending on the value of the refractive index, according to:

$$v = \frac{c}{n} \qquad [2\text{-}13]$$

As a consequence, portion of the wavefront crossing portion of the atmosphere with different *n* will propagate with different velocities, resulting in differential phases inside the wavefront, which is no more plane, but distorted.
The fluctuations of the phase in the wavefront as a function of the refractive index variations are described by the *Roddier equation*:

$$\varphi = k \int_0^z n(z)dz \qquad [2\text{-}14]$$

With *k* the wave number and *n*(*z*) the refraction index along the line of sight. It is important to notice that the phase fluctuations inside the wavefront are not achromatic, but at larger wavelengths the effects on the phase are smaller and smaller.
A more interesting measure is the variance of the phase fluctuations. It can be represented by a structure function (function of the distance ξ between two positions) as:

$$D_\varphi(\xi) = \langle|\varphi(x) + \varphi(x+\xi)|^2\rangle \qquad [2\text{-}15]$$

Where the brackets < > represent an ensemble average. The structure function of the refracting index is espressed by:

$$D_{\tilde{\mathrm{N}}}(\rho) = \langle|\varphi(r) + \varphi(r+\rho)|^2\rangle \qquad [2\text{-}16]$$

Representing the fluctuations of *n* between two points at distance ρ. Assuming a constant pressure and using [2-12]:

$$\frac{dN}{dh} \approx -\frac{0.77P}{T^2}\frac{dT}{dh} \qquad [2\text{-}17]$$

We derive:

$$C_{\tilde{\mathrm{N}}}^2 \approx \left(\frac{77 \cdot 10^{-6}P}{T^2}\right)^2 \cdot C_T^2 \qquad [2\text{-}18]$$

$$D_{\tilde{\mathrm{N}}}(\rho) \approx \langle\Delta n^2\rangle \approx \langle\Delta N^2\rangle \approx C_N^2 \rho^{2/3} \qquad [2\text{-}19]$$

With C_T^2 indicating the temperature structure constant and $C_{\tilde{\mathrm{N}}}^2$ is the refractive index structure function constant. This is the squared value of the fluctuations of $\tilde{N}$ around its mean value, giving an estimate of the local inhomogeneities of the refraction index and, consequently, of the strength of the turbulence. The vertical distribution of such a parameter describes the perturbation acting on the wavefront in a certain astronomical site. On average, $C_{\tilde{\mathrm{N}}}^2$ decreases with height, but it presents some peaks under particular conditions: when two air masses in relative motion cross each other, in mechanical turbulence conditions and in regions characterized by high temperature gradient.

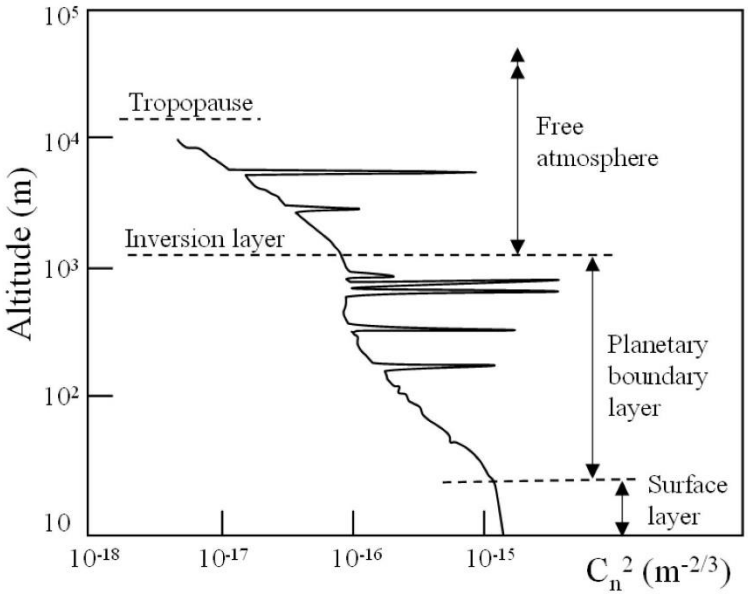

Figure 2-3: Example of the atmospherical structure parameter behaviour as a function of the altitude.

Examples of such conditions are usually found at less than 1000 *m* from the ground, because of meteorological events, in the troposphere at 5000 *m* and in correspondence of the so-called tropopause at 10000 *m* height, where a thermal inversion occurs. The atmospherical turbulence's profile so depends on C_N^2, but typically the atmosphere can be divided in 3 turbulent regions:

- The wavefront perturbations on a small scale occur usually at the lowest layers of the atmosphere, typically from the ground up to 1 *km* during the day and around 100 *m* during the night. In this region small turbulent eddies (0.05 – 0.3 *m*) are present, produced by the heat exchange between the ground and the atmosphere.
- Perturbations on a medium scale are mainly originated in the layers between 1 *km* up to 10 *km*. In this region the dimension of the eddies varies between few tens of meter up to few km and they are generated by updrafts, convection and wind. The wind moves these eddies and plays a key role in the refraction index variations on timescales of few seconds.

On large scales, the perturbations occur in the tropopause, at 10 – 15 *km* above the ground, where strong wind shear might produce strong turbulence and pressure gradients. The effect on the wavefront here is very small, due to the very low gas density, but strong horizontal pressure gradient might lead to errors in determining the position of the light source.

2.4 Seeing

In astronomy, the term seeing refers to the effect of distortion in the wavefront through the atmospheric layers until it arrives at the telescope. Therefore, it is a parameter that

defines the quality of the sky. Under ideal conditions (in the absence of seeing), the image of a point source on the detector will be a disc whose size is limited only by the size of the opening of the telescope and by the wavelength of observation. Technically it is defined as the width at half maximum (Full Width Half Maximum, FWHM) of the PSF (Point Spread Function) of the star. It is the theoretical resolution of a telescope, which corresponds to the angular size of the Airy disk diffraction. However, the actual resolution will be reduced by the atmospheric seeing and it is therefore important to know when the seeing begins to dominate. The wavefront aberrations results in the image translation, deformation and scintillation at the focal plane of the telescope. All these effects integrated in time causes the enlargement in the image of a point-like source and therefore the decrement in the resolving power of the telescope.

2.4.1 Seeing parameters

The main parameters that characterize the seeing are mentioned below:

- ***Fried radius r_0*** is a mathematical parameter introduced by Fried (1966) which can be expressed in 2 different ways:

  1. It is the average dimension of the unperturbed wavefront
  2. It is the average dimension of a turbulent bubble

  It is defined as:

$$r_0 \approx \left[0.423k^2(cos\varphi)^{-1}\int_0^{\infty} C_{\tilde{N}}^2(h)dh\right]^{-3/5} \qquad [2\text{-}20]$$

  And represents the length scale, in the wavefront plane, after which the wavefront itself varies statistically more than one radian. Where φ is the zenith distance (between Earth surface's normal and observing direction angle) and h is the height over the ground.
  As it is possible to see, Fried's radius decreases with the turbulence (expressed by the integral of C_n^2), but grows almost linearly with the wavelength $\lambda^{6/5}$. A telescope with an aperture $D > r_0$ not provided of any adaptive optics system, to sense and correct the deformations injected in the wavefront by the atmospheric turbulence, will never reach its maximum resolution, but it will be limited to

$$\varepsilon \approx \frac{\lambda}{r_0} \cdot 206265'' \qquad [2\text{-}21]$$

  Which, expressed in arcsec, is the value given to the seeing. The r_0 average values are about 10 – 20 *cm* in V band and about 30 – 60 *cm* in K band, so the seeing measured at larger wavelengths is slightly lower($\varepsilon \propto \lambda^{-1/5}$). Local effects as

instrumental seeing or dome seeing can significantly contribute to the seeing observed over images, meaning that the measured values need to be deconvolved for the local turbulence effects. Moreover, as seen from formula [2-20], since $r_0(cos\varphi)^{3/5}$, the seeing worsen when increasing the zenith distance. This is obvious as increasing the zenith distance the wavefront passes through a thicker portion of the atmosphere.

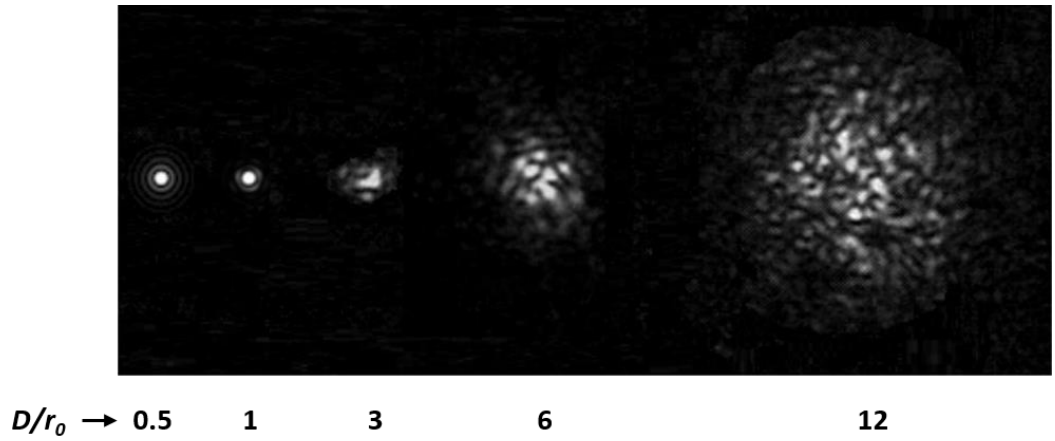

Figure 2-4: At fixed aperture size, continuous increasing is seeing (r_0 becomes smaller), causes the diffraction pattern to break into speckles structure, and greatly expands.

- ***Isoplanatic patch θ_0*** is the angle subtended within the FoV inside which the wavefront phase varies less than one radian. That is, the maximum angle of separation between two sources beyond which there is no longer a significant correlation between the distortions suffered by the wavefronts, expressed as:

$$\theta_0 \approx \left[2.914k^2(cos\varphi)^{-8/3}\int_0^\infty C_{\tilde{N}}^2(h)h^{5/3}dh\right]^{-3/5} \qquad [2\text{-}22]$$

Comparing it with [2-20] we derive:

$$\theta_0 \approx 0.314(cos\varphi)\frac{r_0}{H} \propto \lambda^{6/5} \qquad [2\text{-}23]$$

Where:

$$H = \left(\frac{\int_0^\infty C_{\tilde{N}}^2(h)h^{5/3}dh}{\int_0^\infty C_{\tilde{N}}^2(h)dh}\right)^{3/5} \qquad [2\text{-}24]$$

With *H* the turbulence average height. From [2-23] it is clear that the isoplanatic patch is much more affected form the high layers than from the one closer to the ground, for a simple effect of optical lever. It depends on the observation wavelength in the same way as r_0 and therefore the isoplanatic patch will be slightly wider at longer wavelengths, but has a dependence on the zenith distance

greater than r_0. For r_0 = 20 *cm* and turbulence at a height H = 7 *km* we obtain θ_0 = 1.8 *arcsec*. Typically in V band θ_0 is few arcsec, while at 2.2 μm it is 20-30 *arcsec*. Thus, two sources separated in the sky more than θ_0 have different PSFs, for images taken with short exposure time. For long exposure times their PSFs represent the average of atmospheric fluctuations, so that we can assume the wavefronts, although they crossed different portions of the atmosphere, have suffered the same distortions on average, generating PSFs virtually identical.

- ***Coherence time τ_0*** represents the time scale in which the wavefront phase varies by one radian inside the isoplanatic patch. It is the measure of the time scale variability of atmospheric turbulence or distortion. Since the life-time of the turbulent cells is much longer than the time that they take to cross the line of sight, dragged by the wind, the turbulence is assumed to be "frozen" (Taylor's hypothesis). In this case the coherence time is the time the turbulent cell spends to cross the entire aperture of the telescope, dragged by the wind, and therefore:

$$\tau = \frac{r_0}{v} \qquad [2\text{-}25]$$

  Where v is the wind velocity. Assuming r_0 = 20 *cm* and v = 20 *m/s*, $\tau_0 \approx$ 10 *ms*. Obviously also the coherence time scale as $\lambda^{6/5}$. The inverse of τ_0 is the Greenwood frequency, another very important parameter in Adaptive Optics, since it represents the minimum frequency at which the control electronics must work to be able to correct in real time the wavefront aberrations.

The images with long exposure time are those images for which the exposure time is much longer than the coherence time, and vice versa for the short pose images. The short pose images show a speckle structure, which means that the images are characterized by a large number of bright speckles (see Figure 2-6), generated by interference phenomena between the coherent light coming from different areas of the pupil of the telescope. The angular dimension of each speckle is the resolving power of the telescope, λ/D. When the exposure time is much longer than the coherence time, the speckles move, because the turbulence along the line of sight of the telescope has changed the structure, forming the disc of seeing whose angular size is λ/r_0. Being the most modern telescopes in the 10 *m* class and typical values of r_0 ~ 10-20 *cm* in the visible range, it is clear the importance of overcoming this problem.

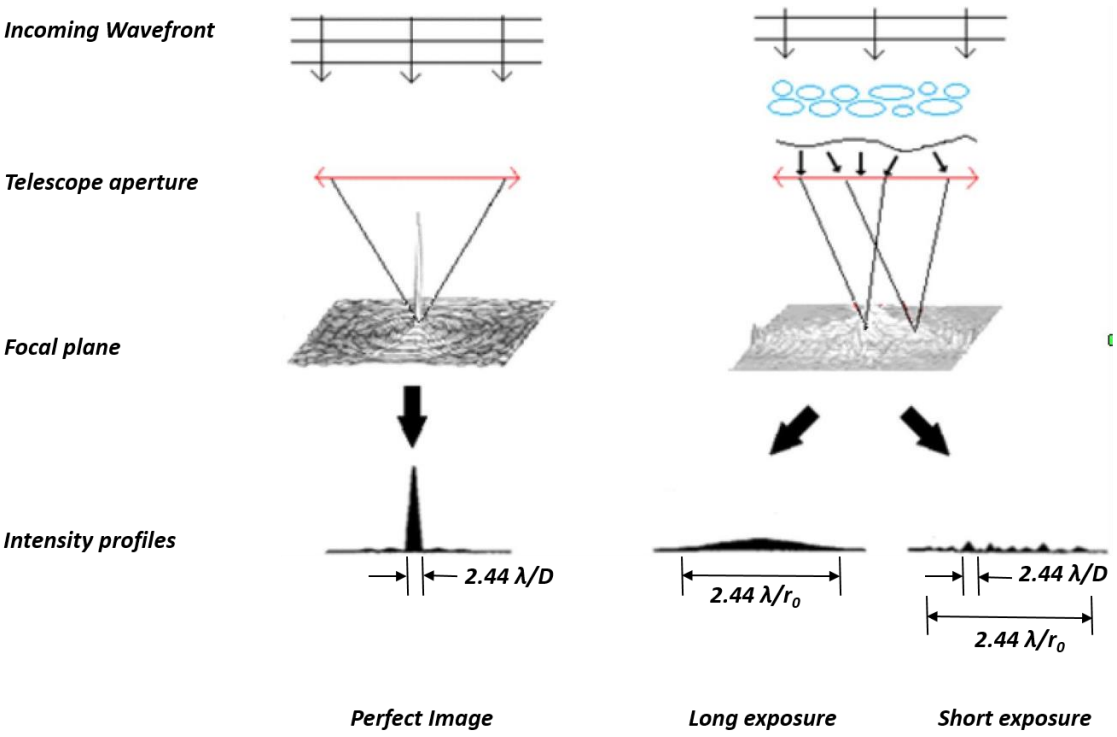

Figure 2-5: Effects of the turbulence on the image of a point-like source. In the ideal case (left panel) the wavefront arrives at the telescope unperturbed, and the star image is diffraction limited. In the case of atmospheric turbulence (right panel), the wavefront is aberrated when reaches the telescope, forming an image much less defined, with an angular diameter λ/r_0. If the image is taken in a very short integration time it shows several speckles, whose dimension is λ/D, distributed in the seeing disk λ/r_0 in diameter.

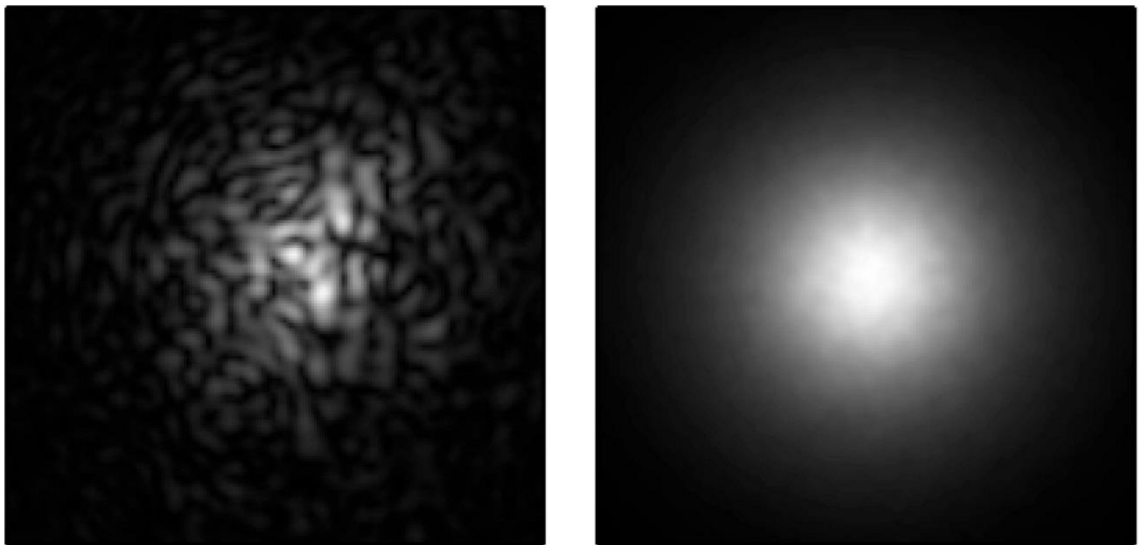

Figure 2-6: On the left the image of a star with an exposure time of few ms, it is clear the speckle structure. On the right, the same star with an exposure time of few seconds.

3 Adaptive Optics

We have seen, in the last chapter, the impossibility to obtain high-resolution images from ground based observations, because of the distortions introduced in the wavefront by the atmosphere. In order to improve the performances of the ground-based telescopes it is therefore essential to compensate the atmospheric turbulence in real time, which is the purpose of Adaptive Optics.

The concept of AO was first introduced by Horace W. Babcock in 1953. However, implementing his idea for the astronomical purposes was very slow due to lack of funds and technology. The first attempt was done by Buffington and collaborators in mid-1970s and later by Hardy in 1980s. The results of the experiments were encouraging, in demonstrating the concept, as well as discouraging, in making the complexity of the adaptive optics systems and its very high costs.
There are three main effects on the wavefronts when they pass through the turbulence:

- ***Piston***: mean value of the wavefront profile value across the telescope pupil (not relevant for a single telescope).
- ***Tip-Tilt***: mean inclination of the wavefront, that is to say the first derivative of the wavefront. Tip-Tilt causes a motion of the image on the focal plane, and for long exposure-time, it translates in a target image enlargement and a degradation of image resolution.
- ***High orders aberrations****:* These are the deformations on the wavefront at the higher order spatial frequencies. The portions of the wavefront separated more than r_0 will undergo different phase delays. This results in the division or compartmentalizing the wavefront into several parts in units of D/r_0. Each one will be locally planar and form different images. For long exposure hence, it ends in broadening of the image.

The combined effect translates in the net degradation in the resolution of the telescope from λ/D to λ/r_0. The telescopes with $D < r_0$ obviously do not suffer the high orders since the portion of the wavefront intercepted is smaller than the average size of the wavefront unperturbed, and therefore will be dominated by the tip tilt.
With big telescopes ($D >> r_0$), instead, high order perturbations are dominating. The telescope aperture, indeed, is wide enough to contain the scale r_0 several times. Because of this, the selected wavefront will be perturbed on small scales. The mean tilt on such a large scale, instead, is statistically lower than on smaller scales.

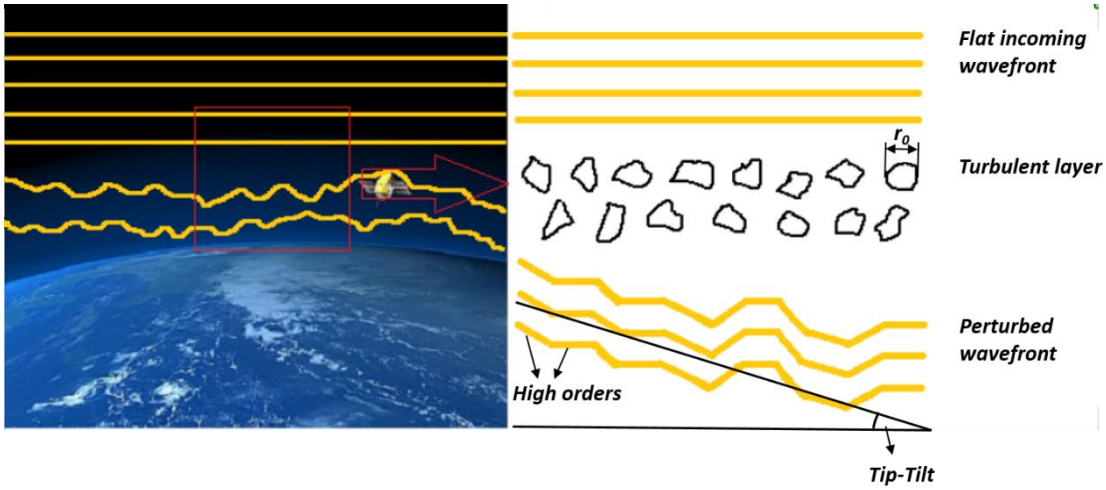

Figure 3-1: schematic representation of the wavefront deformations caused by the atmospheric turbulence, characterized by bubbles of mean size r_0.

Small telescopes are also suffering from the problem of scintillation. In this phenomenon, the light of a point source, like a star, seems to pulsate while that of an extended object, like a planet, does not. The light of a point source must follow a precise path in the atmosphere before entering in the pupil of a telescope. As this light passes through the atmosphere, it crosses turbulent cells with different refractive index which, acting like lenses, deflect the light. In this way, the light rays can reach the telescope focal plane (or our retina) convergent or divergent, causing the sudden changes in light intensity. In the case of a large telescope, this effect is much reduced because the light collected by the telescope aperture span a wider region of the atmosphere before reaching the focal plane. The light then passes through a large number of turbulent cells, reaching the pupil divergent in some areas and convergent in others, so that the sum of these contributions gives an almost steady light.

3.1 Wavefront correction by AO

The goal of Adaptive Optics is to correct the distortions described above, in order to obtain images whose resolution is as close as possible to the limit imposed by diffraction. To correct the tip-tilt, a flat mirror, to be properly tilted accordingly to the wavefront sensor signal, is usually introduced inside the optical path, to reproduce the opposite of the incoming wavefront mean inclination. The high order perturbation correction is performed with a Deformable Mirror (DM), which can reproduce the opposite of the retrieved small-scale distortions of the wavefront, pushing and pulling actuators below the mirror surface. This correction should be performed in a time shorter than the coherence time of the turbulence, and therefore with a frequency at least equal to the Greenwood frequency. The deformations to be applied to the DM are determined by the Wavefront Sensor (WFS). WFS analyses the wavefront of a reference source, could be a star or an artificial source, contained within the isoplanatic patch of the FoV and determines the distortions has been subjected by the wavefront. This information is then

passed to the control electronics, which elaborates them and accordingly sends signals to the DM.

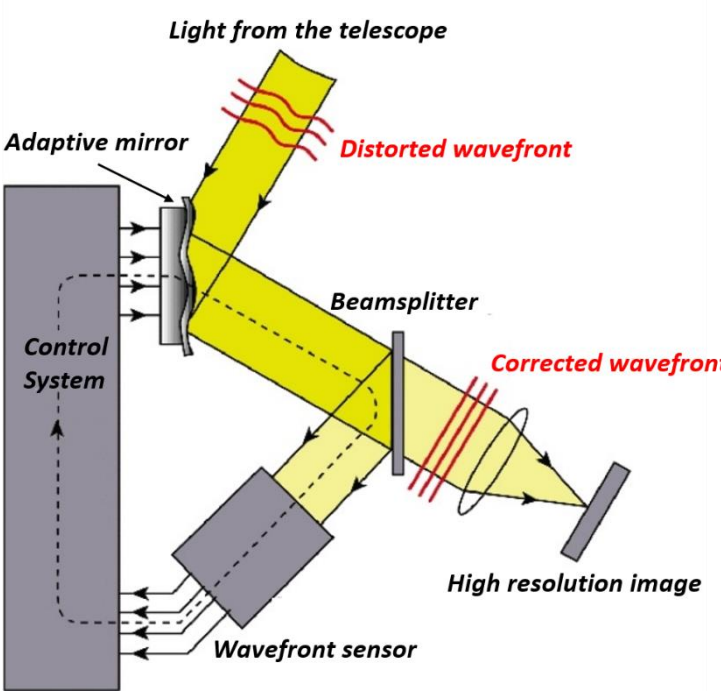

Figure 3-2: sketch of a classical adaptive optics system working in closed loop. A WFS retrieves the wavefront shape and sends the informations to the electronic controlling the deformable mirror, which translates them into a signal correction to apply to the DM. The scientific camera will receive then a corrected wavefront.

There are two different ways in which AO correction can be performed: ***open loop*** and ***closed loop***. In an open loop, the perturbed wavefront reaches the WFS before the DM, making extremely important the exact measurement of the wavefront and the knowledge on how the DM actually corrects it. In a closed loop system, the light reaches first the DM and the WFS measures the residual aberration after the correction. In this way, the sensor will receive a wavefront whose deformations are given only by the residuals of the previous correction, increasing the adaptive optics system efficiency, reducing at each iteration the correction residuals.
An AO system has three main components: a corrector (typically a DM), a WFS and a reconstructor.

3.1.1 The corrector

When the wavefront reaches the telescope, it is affected by differential phase delays. These phase fluctuations can be corrected by introducing in the light path an Optical Phase Difference (OPD), in order to shorten the path of the delayed wave components and to lengthen that of the components in advance. These OPDs are introduced by a DM. The main technical characteristics of a DM are driven by the typical spatial and temporal phase variations of the wavefront, as well as by the observational wavelength. In fact, the

worse is the seeing (and therefore the smaller is r_0) at higher spatial and temporal frequencies the mirror must change its shape.
Many types of DMs are existing today, but in the most common, the deformation is induced by small pistons placed behind the mirror surface, called actuators. Obviously, the greater the number of actuators and the greater will be the spatial correction that could be obtained. The ideal number of actuators is proportional to $(D/r_0)^2$. Recalling 1.20 we obtain that $N_A \propto \lambda^{-12/5}$, and therefore the number of actuators required grows very rapidly decreasing the wavelength. The speed response of the actuators is typically of a few milliseconds and must be in any case shorter than the turbulence coherence time.
An example of DM is the segmented mirror: it is constituted by a series of small-segmented mirrors positioned one next to the other, forming almost a single surface. Three actuators are placed behind each of these segments, allowing piston and tip-tilt movement. The advantage of this technique is that the segments can be combined together to form very large mirrors, they can be indipendently controlled and allow large corrections. However, the space between a segment and the neighbours, even if very small, can be source of radiation in infrared band, causing a deterioration of image quality. These mirrors are thus mainly used as primary mirrors in large telescopes (such as Keck, GLT, E-ELT), allowing to perform the slower corrections required by active optics, necessary to compensate for the mirror deformations due to the weight of the mirror itself. In adaptive optics, however, a DM with continuous surface, thin and very flexible, is favourable. Such a mirror, equipped with piston actuators, allows a very smooth correction, thanks to the high number of actuators that can be inserted behind the surface. Their cost, however, is very high and increases with the number of actuators required.

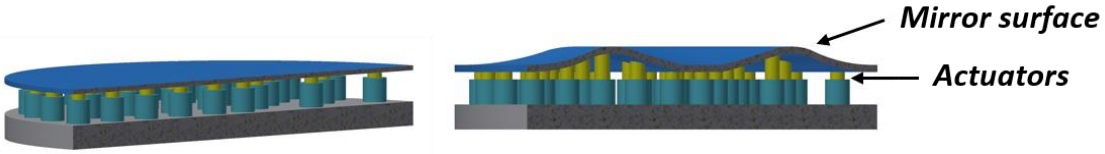

Figure 3-3: section of a deformable mirror with continuous surface. A finite number of actuators allows changing the mirror shape.

Another example of DM with continuous surface is the bimorph mirror, consisting of two piezoelectric layers, located below the reflective surface, glued together and oppositely polarized. The actuators are constituted by electrodes placed between the two layers. When a different potential is applied to an electrode, a layer shrinks while the other expands. This produces a local deformation of the mirror surface, whose curvature is proportional to the applied voltage.
A very quick response to mechanical stresses requires deformable mirrors of small size.
Another type of actuator, used for the secondary mirrors of the LBT, relies on the presence of a magnetic field generated by current in a solenoid (electromagnetic actuator). Behind the mirror, magnets are placed, in correspondence of the solenoid.

3.1.2 The wavefront sensor

A WFS uses the radiation of a reference source in order to quantify wavefront distortion. Let consider a wavefront W(x,y) which has already crossed a turbulent atmospheric layer and let measure the intensity I in two subsequent layers z_1 and z_2. The variation intensity in a function of z is:

$$\frac{\partial I}{\partial z} = -(\nabla I \cdot \nabla W + I\nabla^2 W) \qquad [3\text{-}1]$$

∇W is the slope and $\nabla^2 W$ the wavefront curvature. Some WFSs reconstruct a signal which is proportional to the first derivative of the wavefront from light intenisity variations (as Shack-Hartmann WFS and Pyramid WFS), others through second derivative (like curvature WFS), others through interferometric technique reconstruct directly the wavefront (Smartt interferometer). Generally, to identify high order aberrations, it is necessary to divide the wavefront in smaller parts. The main wavefront is divided in several parts in order to analyse the tilt of each portion. The wavefront shape is reconstructed integrating gradients in every sub-area over the entire aperture. The reconstruction of the wavefront improve as the number of sub-areas increase. However, there are some constraints and limitations in the maximum number of sub-aperture to consider:

- The SNR of each single sub-aperture, since it is obvious that increasing the number of sub-aperture the number of incident photons for each one becomes lower.
- DM actuators density; it is useless to sample the wavefront at spatial frequencies higher than the one of the actuators of the DM.
- The seeing; it makes no sense to divide the wavefront in portions smaller than r_0, since below this value the wavefront can be considered unperturbed.

3.1.2.1 Quad cell wavefront sensor

To evaluate the tip-tilt of the wavefront, the so-called Quad-Cell WFS can be used, splitting the light coming from a reference target into four beams. The sensor is positioned on the focal plane of the system and its centre is in the position where the centre of mass of the image should lay in absence of tilt. The sensor evaluates the light percentage that illuminates each of the quadrants and measures the shift of the spot, which is proportional to the first derivative of the incoming wavefront. Shift along *x* and *y*-axis can be quantified through the signal *S*:

$$S_x = \frac{B + D - (A + C)}{A + B + C + D} \qquad S_y = \frac{A + B - (C + D)}{A + B + C + D} \qquad [3\text{-}2]$$

Where A, B, C and D are the integrated fluxes reaching the respective quadrants of the sensor and S_x and S_y are proportional to the first derivative of the wavefront, computed along two orthogonal directions. The useful range to determine tip-tilt is the one in which S_x and S_y increase linearly, which happens when the light of the spot hits all the four quadrants of the WFS.

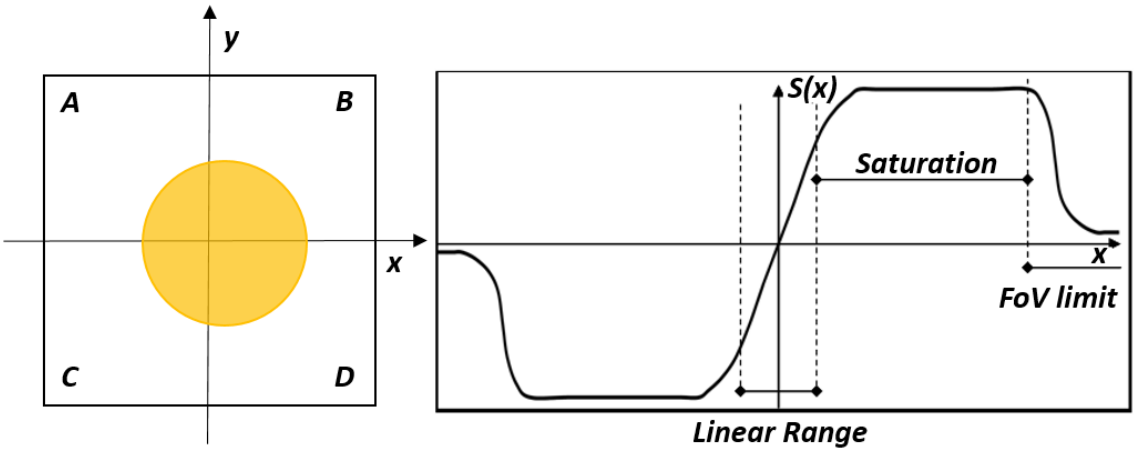

Figure 3-4: in the left panel the Quad-Cell WFS concept, in the right panel the signal S(x) as a function of the spot shift along the x axis.

Let us consider for example the case of a spot illuminating only quadrants *A* and *B*, so *C*, *D* = 0. Then, the signal $S_x = (B - A)/(A + B)$ would be still in the linear regime, giving the true inclination of the wavefront in the *x* direction while the signal $S_y = 1$ has reached the saturation.
Obviously, the linear range width is related to the spot dimension: the smaller the spot, the more sensitive the sensor, because the S_x and S_y slopes in the linear regime are steeper and a smaller shift of the spot barycentre is enough to retrieve a high tilt signal. Increasing the dimension of the spot, the sensor gains in linearity range but decrease its sensitivity. The slope of the signal function in linearity regime is in fact $m = 2/d$, with *d* spot diameter. The same basic idea of the Quad-Cell WFS is used in two of the most commonly used WFS nowadays, the Shack-Hartmann WFS and the Pyramid WFS.

3.1.2.2 Shack-Hartmann Wavefront Sensor

In 1904, Hartmann developed a test to verify the optical quality of the telescopes mirrors, the so-called Hartmann test, consisting in positioning a perforated mask just in front of the telescope aperture. In this way, each small hole samples a small area of the whole aperture. In presence of errors in the mirror manufacturing the images produced by the light passing through each hole in the mask are shifted with respect to the nominal position in the case of a perfect mirror.

This method shows some severe limitations: first of all the insertion of the mask makes the system lose a lot of light coming from the reference source and, consequently, only very bright stars could be selected as references, reducing considerably the sky coverage. Secondly, the selected areas corresponding to the holes on the mask are often not representative of the local mean tilt of the wavefront.
These problems have been solved in 1977 with the Shack-Hartmann WFS, substituting the perforated mask with a lenslet array, positioned on a pupil plane inside the optical path.

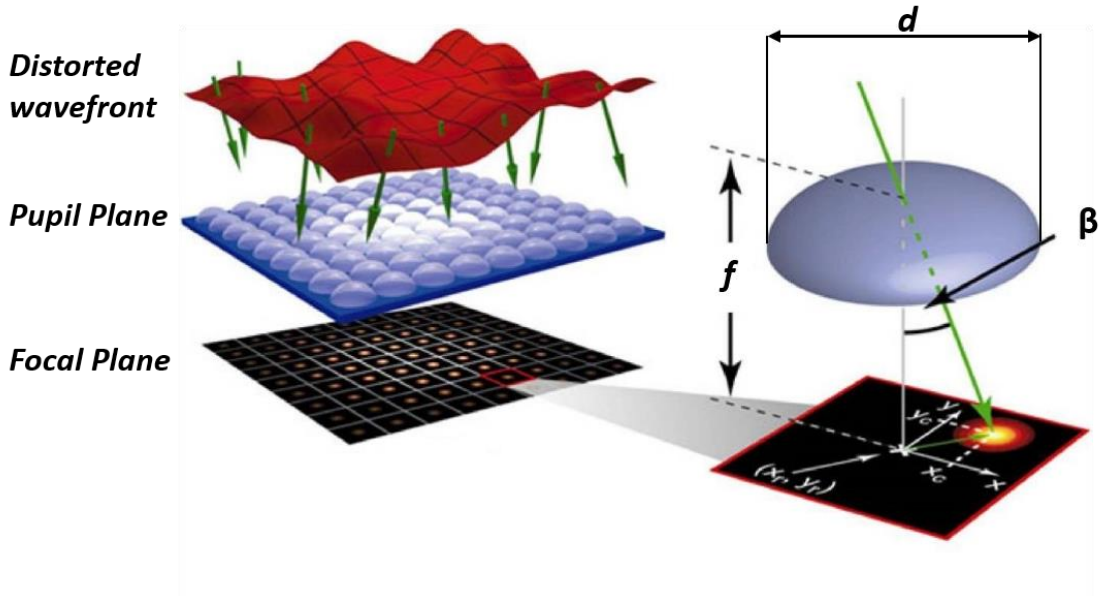

Figure 3-5: scheme of a Schack-Hartmann WFS. If the incoming wavefront were flat, each lens of the array would produce an image of the telescope pupil perfectly centred wrt a quad-cell. If the wavefront is aberrated, each lens produces images translated wrt the unperturbed case of a quantity dependent on the local tilt of the wavefront.

In this configuration, the WFS receives all the flux collected by the telescope aperture, since the pupil is not masked. Moreover, the measured tip-tilt actually corresponds to the mean inclination of the wavefront in the selected sub-aperture. Lenses have the scope of dividing the wavefront and, to obtain the maximum efficiency, they need to be adjacent and cover the entire optical aperture. The number of lenses must be chosen in order to avoid oversampling of the wavefront to prevent light losses. For example, with a telescope of 10 *m* and r_0 = 10 *cm* a lenslet array of 100 x 100 lenses is optimal. To change the spatial sampling of the wavefront, in case of variations of the seeing, it is necessary to change the lenslet array on the pupil plane. Without turbulence, the barycentre of each spot produced by each lens should fall in the centre of a quad-cell.
When turbulence is active the images of the spots start moving independently, and the displacement of the barycentre of each spot wrt the unperturbed case is defined by:

$$\Delta x = \frac{1}{2}\left(\frac{\lambda f_l}{d}\right)\frac{(A+C)-(B+D)}{A+B+C+D} \qquad [3\text{-}3]$$

$$\Delta y = \frac{1}{2}\left(\frac{\lambda f_l}{d}\right)\frac{(A+B)-(C+D)}{A+B+C+D} \qquad [3\text{-}4]$$

Where $\lambda f_l/d$ is the physical size of each spot on the detector, with f_l and d respectively the focal length and the diameter of the lens. Geometrically, these movements can be written as:

$$\Delta x \propto f_l \frac{\partial W}{\partial x} \quad [3\text{-}5]$$

$$\Delta y \propto f_l \frac{\partial W}{\partial y} \quad [3\text{-}6]$$

Where $\partial W/\partial x$ and $\partial W/\partial y$ are the partial first derivatives of the wavefront W, and provide the inclination of the wavefront wrt the plane of the lenslet array. Substituting [3-5] and [3-6] in [3-3] and [3-4] we derive a direct relationship between the local slope of the wavefront and the displacement of the spot measured by the quad-cell WFS:

$$\frac{\partial W}{\partial x} = \frac{1}{2}\left(\frac{\lambda}{d}\right)\frac{(A+C)-(B+D)}{A+B+C+D} \quad [3\text{-}7]$$

$$\frac{\partial W}{\partial y} = \frac{1}{2}\left(\frac{\lambda}{d}\right)\frac{(A+B)-(C+D)}{A+B+C+D} \quad [3\text{-}8]$$

Therefore, the Shack-Hartmann sensor determines the value of the wavefront first derivative. As for the quad-cell WFS the sensitivity of the SH is defined by the size of the spot, which is ultimately determined by the number of lenses used in the lenslet array. The error associated to the position of each spot is, in the approximation of frozen atmosphere and perfect optical system, dominated by the Poissonian error. Because of this uncertainty, which is intrinsic in the photon nature, if at the telescope arrive I photons, the photons collected by the optical system is inside the range $I + \sqrt{I}$. Propagating this error in the quad-cell signal expression, results:

$$\Delta\left(\frac{\partial W}{\partial x}\right) = \frac{1}{2}\left(\frac{\lambda}{d}\right)\frac{\left(\frac{I}{2}\pm\frac{\sqrt{I}}{2}\right)-\left(\frac{I}{2}\pm\frac{\sqrt{I}}{2}\right)}{I\pm\sqrt{I}} = \pm\frac{1}{2}\left(\frac{\lambda}{d}\right)\frac{\sqrt{I}}{I\pm\sqrt{I}} \approx \pm\frac{1}{2}\left(\frac{\lambda}{d}\right) \quad [3\text{-}9]$$

Similarly, for the error associated to the slope in the y-axis. Therefore, the higher is the number of photons collected, the smaller will be the error associated. Assuming an array of $N \times N$ lenses, each of them will collect, on average, $n = I/N^2$ photons. Let us assume also $N = D/r_0$, so $d = r_0$. In this case the error on the tilt determination for each sub-aperture is:

$$\sigma_{tilt} = \frac{\lambda}{D/_N}\cdot\frac{1}{2\sqrt{n}} = \frac{\lambda}{r_0}\cdot\frac{1}{2\sqrt{n}} \quad [3\text{-}10]$$

While the tilt error averaging on all the sub-apertures is:

$$\sigma_{SH-tilt} = \frac{\lambda}{N\cdot r_0}\cdot\frac{1}{2\sqrt{n}} = \frac{\lambda}{D}\cdot\frac{1}{2\sqrt{n}} \quad [3\text{-}11]$$

Summarizing, the SH WFS can retrieve the wavefront aberration concerning both low and high orders, but it presents also some technical difficulties. The lenslet array is constituted by many optical surfaces, which need to be produced within quite tight

specifications, concerning both the surface accuracy and the optical power. However, the main difficulty is represented by the conjunctions between the lenses, since the wider is the gap, the higher the amount of light that is lost and diffused because of diffraction, also introducing noise on the CCD. Everything is made even more complicated by the fact that the alignment of such an array with respect to the detector is not simple.
Finally, the sensitivity of the SH WFS does not improve in closed loop, as for the Pyramid WFS.

3.1.2.3 Pyramid Wavefront Sensor

The Pyramid WFS, initially used in optical microscopes, has been developed and applied in astronomical field by Ragazzoni (1996). The key element of this kind of WFS is a four faces glass pyramid, whose vertex lies on the focal plane of the telescope, in correspondence of a reference star. The light from this star focuses on the vertex of the pyramid and is divided into four distinct beams that, once collimated, will produce four images of the pupil, each with an intensity proportional to the number of photons that hit the face of the pyramid that produced it. The separation and the enlargement of the four images are determined respectively by the pyramid angle and by the focal length of the collimator lens:

$$d_{centers} = \alpha(n-1)f_{coll} \qquad [3\text{-}12]$$

Where α is the pyramid vertex angle and n the refraction index of the pyramid. The wavefront tip-tilt estimation is performed in the same way as for the quad-cell, with the four faces of the pyramid acting as four quadrants, comparing the light intensities in the four images of the pupil.
To determine the aberrations at higher orders it is necessary, as for the SH, divide the wavefront in sub-sections, but, differently from the SH, this operation does not require any additional optical element. In the pyramid WFS, in fact, the sub-apertures are defined directly on the CCD, and it is possible to change the spatial sampling of the wavefront just changing the binning of the CCD. In particular, if we identify the same pupil portion in the four pupil images, it is possible to retrieve the local tip-tilt in that sub aperture using [3-2]. Repeating the same operation for all sub aperture, it is possible to reconstruct the high order aberrations. The maximum sampling is obviously the one in which a sub-aperture corresponds to one pixel, remembering that the optimal number of sub-apertures to consider is $N = D/r_0$.

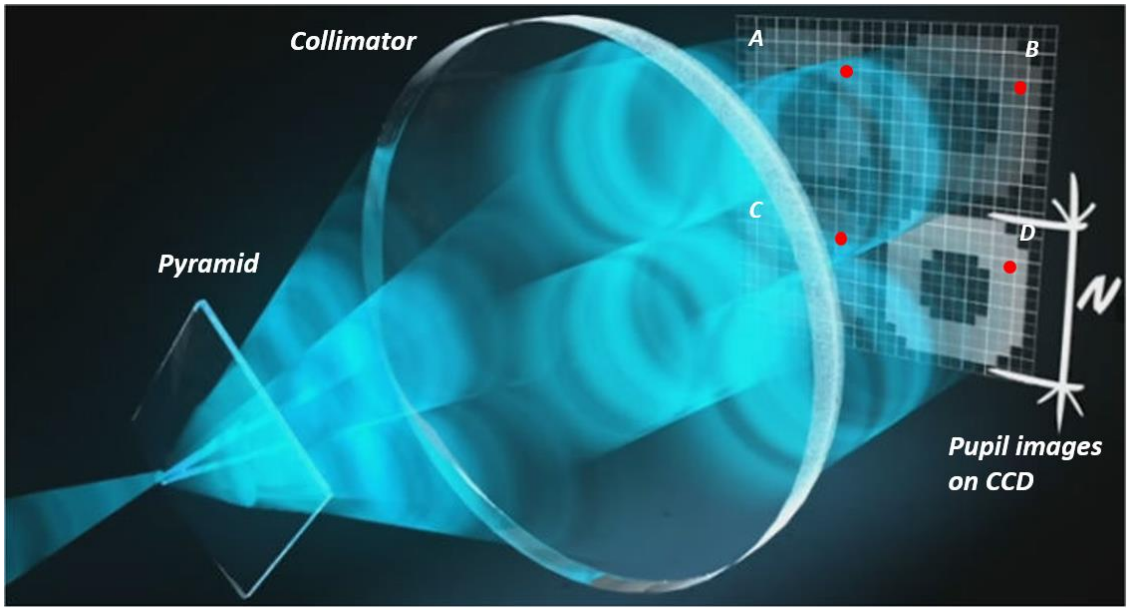

Figure 3-6: Scheme of a Pyramid WFS. The pyramid vertex is located in the focal plane, in correspondence of the image of a star, and split the light into 4 beams, which, after collimation, produce 4 images on the telescope pupil on a CCD. The mean tip-tilt of the wavefront is determined integrating separately the light of the 4 images of the pupil. Similarly, the tip-tilt in a sub-aperture is evaluated integrating the light in the same pupil portion (red dots in the figure) in the four images. Image credits: Marco Dima

Another great advantage of the pyramid WFS wrt SH is that, working in closed loop, it improves its sensitivity. In fact, during the first few cycles, the wavefront is highly aberrated, and the size of the spot on the tip of the pyramid is dominated by the seeing, so λ/r_0. As the correction becomes more accurate, the spot size decreases, until arriving, potentially, to the diffraction limit λ/D. Since the light from the reference star is now focused in a smaller area, the SNR and the sensitivity increase. The sensitivity improvement translates into a gain in the theoretical limiting magnitude of the WFS when compared to the SH in the order of 1-2 magnitudes for a 10 *m* class telescope. However it is important to prevent the spot on the top of the pyramid becomes too small, since in this case sudden changes in the atmospheric turbulence could move the spot enough to leave dark two sides of the pyramid, reaching the saturation regime along *x* or *y* axis. When a linear signal is no more available, the correction degrades, resulting in an increasing size of the spot on the tip of the pyramid and loss of sensitivity of the sensor.
To avoid these conditions occurring too frequently it is possible to reduce the pyramid sensitivity by applying a diffuser at the vertex, or introducing a modulation (i.e. an oscillatory movement of the spot around the tip of the pyramid, or a movement of the pyramid itself), with a frequency higher than the one of CCD readout. In this way, all four faces have been illuminated before CCD reading. In this last case, the pyramid sensitivity is given by the modulation amplitude.
Obviously, when the sensitivity is low, the linear range is wider, allowing correcting large aberration, preventing the risk of saturating the signal, whereas at high sensitivity, the linear range is narrower, but the signal will be very high even for small aberrations. It is then clear the convenience of using larger modulations during the first few correction cycles, when the wavefront is strongly aberrated, and reduce it gradually, when the residual aberrations are on small spatial scales.

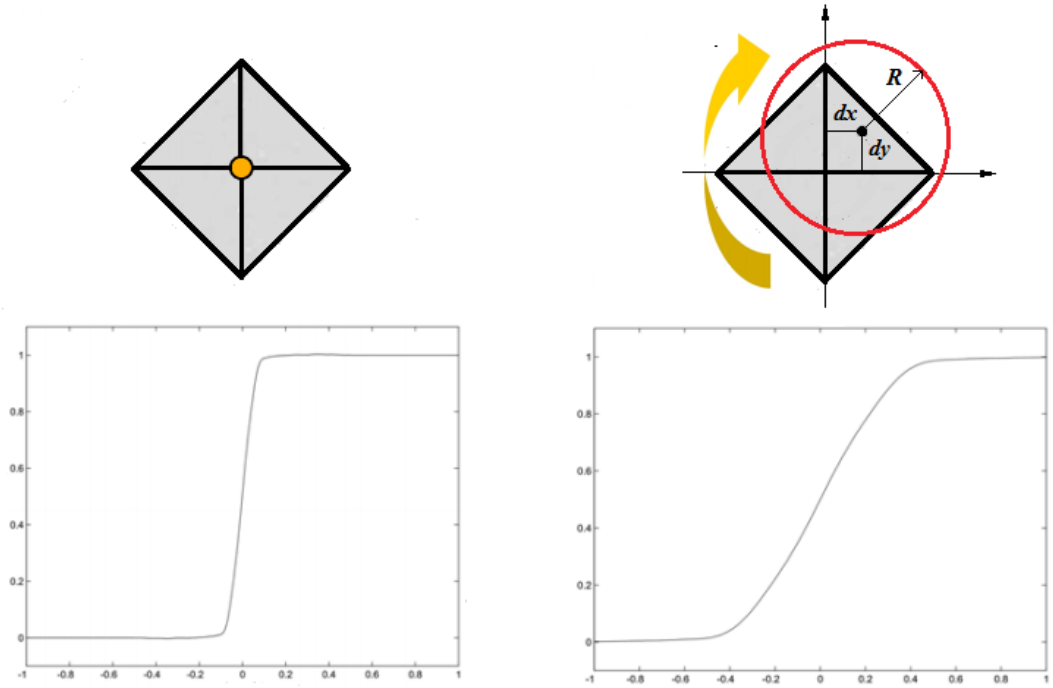

Figure 3-7: In the left panel the dynamic range of a Pyramid WFS without modulation. The signal is linear within the width of the spot, which is very small, especially after some correction cycles. The linear range is very narrow but the sensitivity is high. In the right panel, a modulation of amplitude R has been introduced. Now the pyramid is linear within the modulation amplitude R but it is not very sensitive. Thanks to this modulation, an aberrated ray hitting the pyramid displaced of dx and dy wrt the pyramid vertex will distributes anyway its light to the four images of the pupil.

Afterwards, it has been devised that modulation is not necessary to have a pyramid WFS properly working (Costa et al., 2003). In fact, the atmospheric turbulence gives a natural modulation of PSF light on the pyramid pin. During first few open loop cycles the atmospheric PSF size is of the order of λ/r_0, with a result equivalent to those of a large modulation. When the open loop is closing, lower orders, which contains most of the turbulence, are corrected and the PSF size decreases. Improving the wavefront correction, r_0 increases, in theory, until reaching the telescope dimension in closed loop. At this point, it is possible to see speckles with dimension of the order of λ/D, randomly moving on the pyramid, producing a natural modulation.
Another advantage of the pyramid WFS is given by the Poisson error reduction wrt a SH WFS. The spot dimension on the pin of the pyramid, in closed loop, is λ/D, so the associated error will be:

$$\sigma_{PS-tilt} = \frac{\lambda}{D}\frac{1}{2\sqrt{I}} = \sigma_{SH-tilt} \cdot \frac{r_0}{D} \qquad [3\text{-}13]$$

It is clear how the gain is huge, especially for the large telescopes. The pyramid WFS is the one used for LINC-NIRVANA at the LBT, as described in the next chapters.

3.1.2.4 Curvature Wavefront Sensor

The curvature sensor was conceived and developed by Roddier (1981) to measure the curvature of the wavefront rather than its inclination. In fact, this sensor measures the second derivative of the wavefront, differently from pyramid and Shack-Hartmann, which measure first derivative.
It consists of two detectors, symmetrically positioned before and after the telescope focal plane. In this ways, it measures the light distribution in an intrafocal plane and in an extrafocal plane. A local curvature of the wavefront generates an excess of illumination on one of the two planes and a defect of illumination on the other.

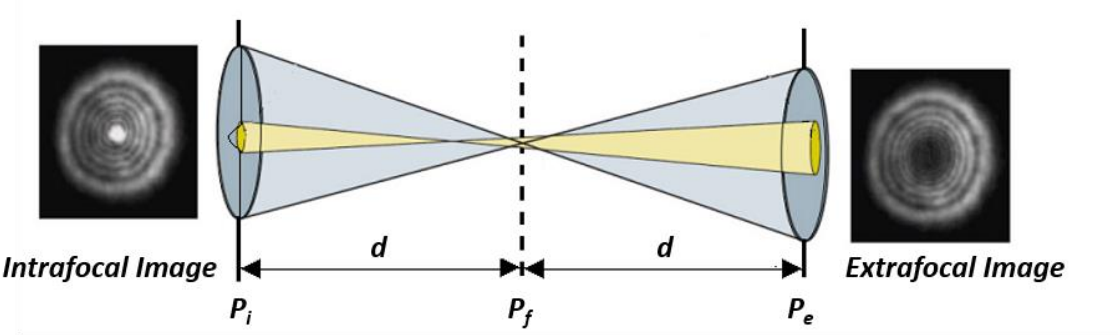

Figure 3-8: curvature WFS scheme. The rays coming from wavefront portions with positive curvature will focus before the telescope focal plane, and the intrafocal image is brighter than the extrafocal one. The opposite occur for the rays from negative curvatures.

The signal is given by the difference between the intrafocal and extrafocal image intensities, according to:

$$S(r) = \frac{I_e(r) - I_i(r)}{I_e(r) + I_i(r)} = \frac{\lambda f(f-l)}{2\pi l}\left[\nabla^2 W\left(\frac{fr}{l}\right) - \frac{\partial W}{\partial n}\left(\frac{fr}{l}\right)\delta_c\right] \propto \nabla^2 W \quad [3\text{-}14]$$

Where I_i and I_e are the intensities of the intrafocal and extrafocal images respectively, at a distance l from the focal plane; f is the focal length of the telescope and r is the radius of curvature of the wavefront.
In principle it would be sufficient only an image out of focus to determine the wavefront curvature, but using two images makes the system more efficient. In this way, the systematic errors, such as the CCD quantum efficiency and the electronic gain, are automatically compensated. Moreover, the atmospheric scintillation is also compensated; the control algorithm is much simpler.
Measuring the second derivative of the wavefront, this sensor is not sensitive to the mean tilt (associated with the first derivative), except at the edge of the pupil, where the intensity of the wavefront varies very quickly. In presence of tilt the intrafocal and extrafocal images will be mutually translated from the position they would have in absence of tilt, and this results in an excess of signal at the edges of the pupil, as visible in Figure 3-9, that can be used to estimate the mean tip-tilt of the wavefront.

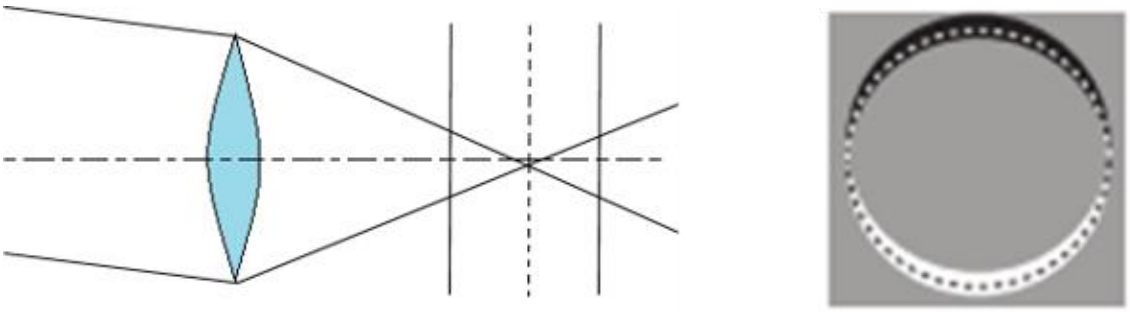

Figure 3-9: on the left the propagation of a plane, but tilted, wavefront. On the right the signal given by the curvature WFS. In grey in the curvature signal equal to 0, the black and white are the positive and negative curvature signals, used to retrieve the tip-tilt of the wavefront. The dashed line is the contour of the pupil.

The maximum number of sub-apertures that can be considered on the wavefront is limited by technical issues. This sensor, in fact, uses as a detector an array of avalanche photodiodes (since they have zero readout noise), whose physical size imposes a minimum distance between adjacent photodiodes. Consequently, the curvature WFS cannot retrieve very high order aberrations.
Operatively, this sensor can be used with a single detector, just inserting a membrane mirror on the telescope focal plane, alternatively changing its curvature to increase and reduce the light optical path.
The vibration of this mirror must occur at a frequency at least twice the Greenwood frequency. When the membrane mirror is concave, it acts as a converging lens, producing intrafocal images on the detector and vice versa, when the mirror is convex, it acts as a diverging lens, producing extrafocal images. Varying the oscillation amplitude of the membrane mirror, it is possible to change the gain of the system.

3.1.3 The reconstructor

The WFS measures the tilt or the local curvature of a wavefront. Since the wavefront is continuous, stitching together these measures provides the wavefront profile. This operation is called reconstruction of the wavefront. It generates a function of Optical Path Difference (OPD) that describes the shape of the wavefront. The reconstructor converts the signals in terms of phase and measures the deviations of the wavefront from the ideal case, then sending the corresponding commands to the deformable mirror.
There are two main types of approach to reconstruction: zonal and modal. The first describes the wavefront in terms of OPD in different regions of the pupil of the telescope, usually chosen to correspond to sub-aperture in which the gradient of the wavefront is determined. The second one describes the wavefront as a polynomial expansion over the entire aperture. Describing the surface of the wavefront as a linear combination of analytical terms:

$$W(x,y) = \sum_n C_n P_n(x,y) \qquad [3\text{-}15]$$

Where *x, y* are the spatial coordinates, the P_n are the analytical terms (modes) and C_n are the linear combination coefficients. Since the P_n terms are continuous and analytical, the gradient of the wavefront can be expressed as:

$$\begin{bmatrix} \frac{\partial W(x,y)}{\partial x} \\ \frac{\partial W(x,y)}{\partial y} \end{bmatrix} = \begin{bmatrix} \sum_n C_n \frac{\partial P_n(x,y)}{\partial x} \\ \sum_n C_n \frac{\partial P_n(x,y)}{\partial y} \end{bmatrix} \qquad [3\text{-}16]$$

We thus have an analytical description of the slope of the wavefront at each point (*x*,*y*) which can be compared to the measured values of the gradient in order to obtain an appropriate set of coefficients C_n. Once C_n are known, the surface of the wavefront is obtained by using the formula [3-15]. Detailed information on the shape of the wavefront is contained in the P_n. It has been shown by Noll in 1976 that a good approximation to describe the aberrations introduced by a turbulence that follows the Kolmogorov spectrum is one in which the terms P_n are the Zernike polynomials.
They form an orthogonal basis for the functions defined on a circle with unitary radius and are defined in polar coordinates (ρ; θ):

$$Z_n^m(\rho,\theta) = \rho^n cos(m\theta) \qquad [3\text{-}17]$$

Where *n* is the radial order and *m* is the angular frequency. Each Zernike polynomial is the product of two terms: the first contains the radial part and the second contains the angle. The advantage of using these polynomials is the fact that each of them describes an optical aberration independent from the other, and being mutually orthogonal the presence (or absence) of one does not affect the others. In addition, all Zernike polynomials, except the first one, have zero mean and are calibrated in order to have uniform variations. This puts all polynomials on a common basis, so that their relative magnitudes can be easily compared.
In Figure 3-10 the main terms of the decomposition are shown and the most known aberrations are identified. The term of order $n = 0$ represents the piston, a rigid translation which changes the wavefront phase and which is extremely important for interferometry; with $n = 1$, i.e. the first derivative of the wavefront, are defined tip and tilt, with $n = 2$, the second derivative of the wavefront, there is the defocus term ($m = 0$) and astigmatism ($m = \pm 1$).
In Figure 3-11 the effects of different aberrations on focal plane are shown. Zernike polynomials are used in all codes throughout the thesis to analyze or simulate wavefront aberrations on pyramid pupils.

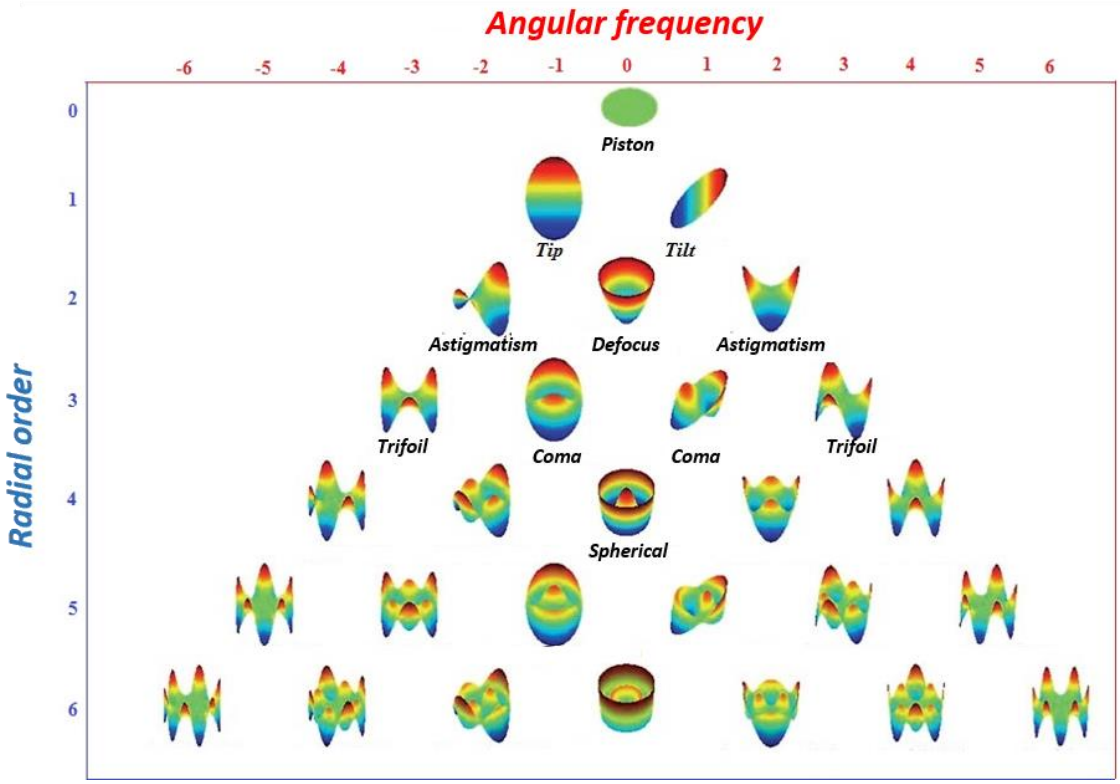

Figure 3-10: Principal optical aberrations and associated Zernike polynomials.

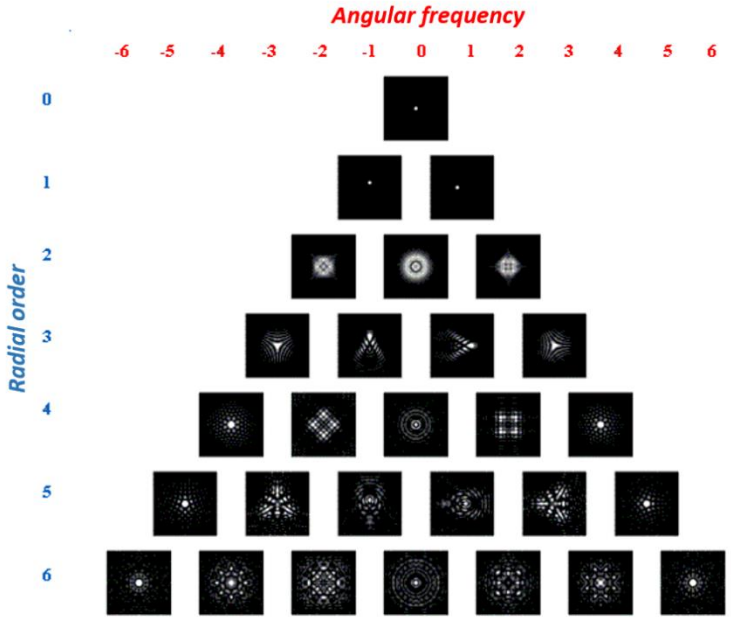

Figure 3-11: Effect of the main aberrations on the focal plane.

3.2 Accuracy of Wavefront Correction

The quality of the image and the performance of the telescope are determined by the accuracy of the wavefront correction by the adaptive optics system. It is measured in terms of the Strehl Ratio (SR), which is the ratio between the peak intensities of the observed PSF and the diffraction-limited image, ideally obtained with the same instrument. The correction is perfect when SR = 1, which is just an ideal case. In all real cases SR < 1 and the smaller its value, the worse the image quality. The main errors that adversely affect the correction are the sampling error, the timing error and the error due to anisoplanatism.

The sampling error is because, while the wavefront may be aberrated up to spatial scales of the order of millimeter, the number of actuators of the deformable mirror usually limits the sampling that is performed. The number of actuators is dictated by cost-performance optimization done on a statistical basis, which leaves a residual error. In this way, some aberrations (those at the higher orders) cannot be corrected; thereby this implies a residual in the correction, whose variance is:

$$\sigma_F^2 = k\left(\frac{d_a}{r_0}\right)^{5/3} \qquad [3\text{-}18]$$

Where k is a constant that depends on the geometry of the actuators and d_a is the distance between the actuators.

The temporal error is due to the time delay between the measurement of turbulence and its effective correction. The fluctuations of the disturbances are mainly due to the speed with which the wind moves the cells through the field of view of the telescope. The error associated with this delay τ is given by:

$$\sigma_\tau^2 = \left(\frac{v\tau}{r_0}\right)^{5/3} = \left(\frac{\tau}{\tau_0}\right)^{5/3} \qquad [3\text{-}19]$$

The error due to anisoplanatism is associated with the angular distance in the sky between the scientific object and the reference object used to make the correction. It is defined as:

$$\sigma_\theta^2 = \left(\frac{\theta H}{r_0 cos\varphi}\right)^{5/3} = \left(\frac{\theta}{\theta_0}\right)^{5/3} \qquad [3\text{-}20]$$

The isoplanatic angle is typically very small, of the order of few arcsec. In order not to excessively degrade the SR, the scientific object and the reference source should be within the same region defined by the isoplanatic angle. In addition, since the time for the acquisition of images to perform the corrections must be very short, the reference object must be very bright (typically not more than 16th magnitude). Generally, the scientific object is very faint, so it typically cannot be used as reference for the adaptive optics system. This poses severe limitations to the sky coverage, i.e. the portion of the sky where the adaptive optics system can be successfully implemented.

Obviously, the SR decreases with increasing the residual errors, accordingly to:

$$SR = e^{-\sigma_i^2} \qquad [3\text{-}21]$$

It can be immediately noticed how the shorter the time in which the correction is applied and lower is the degradation of the SR, and the same applies to the other residuals.

3.3 Reference Objects

As mentioned in the last section, except a few rare cases, it is not possible to use the scientific object as the reference object as well. It is therefore necessary to find another source inside the isoplanatic angle. The number of natural stars with the required characteristics is not enough to cover the entire sky and the probability of finding a suitable star varies depending on the galactic latitude. In the direction of the galactic poles the coverage will be minimal due to the scarcity of stars in this direction (only 0.1% of the sky is covered in band V and 0.5% in K band), while in the direction of the galactic equator coverage is maximum (1% in V band and 4% in K band).
The main solutions proposed are:

- Creating an artificial source in the desired position; Laser Guide Star (LGS).

- Using multiple reference objects and more deformable mirrors to correct the turbulence in several directions, thus expanding the isoplanatic patch.

The creation of laser guide stars was proposed by Foy & Labeyrie in 1985. Now two typologies are mostly used: sodium and Rayleigh LGSs. In the first case the laser ray, tuned on the sodium doublet wavelength at $\lambda = 589$ *nm*, covers the same atmospheric path covered by the object light, and then reaches the mesospheric sodium layer at about 90 *km* height and stimulates its fluorescence: in this way a monochromatic artificial source at a finite distance is created in the desired direction. In the second case, the scattering of dust present at low atmospheric layers (around 20 *km*) is exploited. In both cases, the sources re-emit light for fluorescence or for diffusion in all directions. Part of this light goes back to the telescope following the same path and is used as the reference source for the AO system. The LGS magnitude depends on the laser power, which is of course proportional to its cost. Moreover, the finite distance of the laser star from the telescopes has several drawbacks such as:

- It is insensitive to tip-tilt, as the beam travelling back and forth from the laser source to the detector passes through the same atmosphere portion, in a time range in which no significant variations of the mean tilt of the wavefront takes place, having as a net effect the nulling after the two paths. This problem can be solved using a Natural Guide Star (NGS) to sense the tip-tilt. This brings back to the original problem of NGSs, the anisoplanatism.

- The correction for atmospheric layer higher than the one where the LGS is generated cannot be performed, although above 90 *km* the wavefront is practically unperturbed.

- Due to its finite distance, the rays coming from the LGS are not parallel but are arranged on a spherical wavefront. The section of atmosphere crossed before reaching the telescope is then conical, while for a NGS the wavefront arrives plane and the rays cross a cylindrical section of atmosphere. This means that a portion of atmosphere traversed by the light of the scientific object is not analysed. This phenomenon is known as "cone effect". The residual error due to the cone effect is:

$$\sigma_C^2 = \left(\frac{D}{d}\right)^{5/3} \qquad [3\text{-}22]$$

  With $d_0 \approx 2.91\theta_0 H$ the parameter characterizing the cone effect, depending from the height of the LGS.

- In the sodium case, another problem is due to the thickness of the atmospheric sodium layer that is crossed (≈ 10 *km*). Therefore the LGS is not point-like but rather a segment, problem known as "spot elongation"

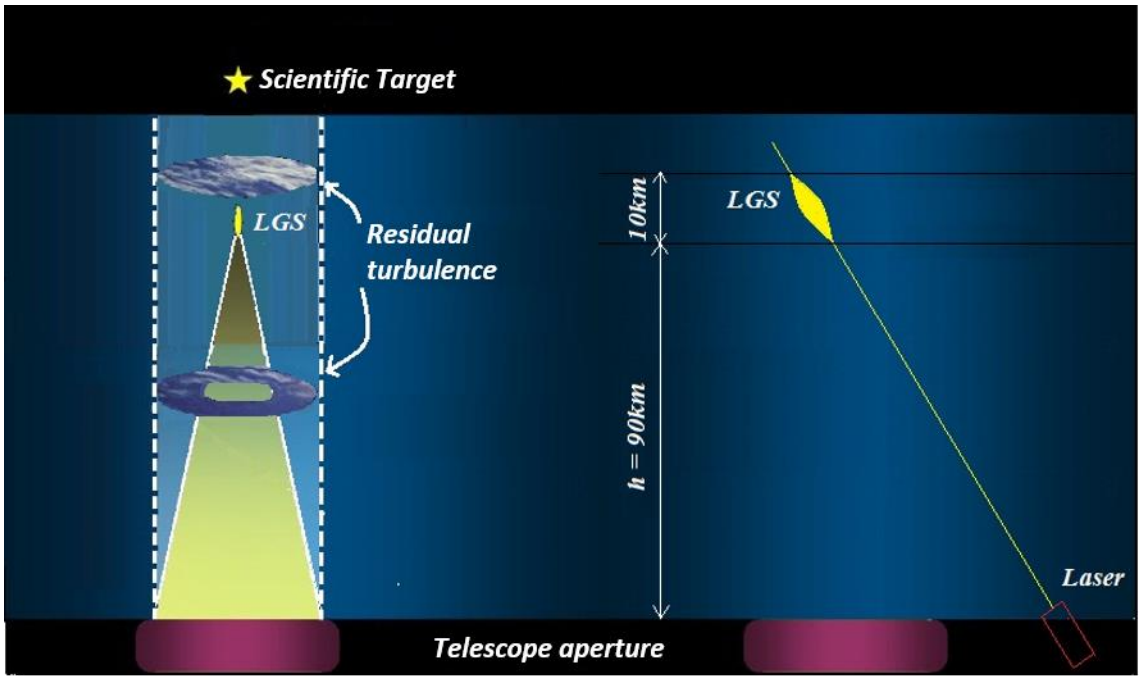

Figure 3-12: sketch of the cone effect (left) and of the elongation of the spot. The lower is the height of the LGS and the greater is the cone effect. Rayleigh LGS, therefore, suffer particularly from this effect.

The use of LGS leads to a larger sky coverage, but at the expense of the performance of adaptive optics system that can be reduced, depending on the conditions, up to 50%. Furthermore, the cost of a system for the creation of LSG is very high.

3.4 Multi-Conjugated Adaptive Optics

The Multi-Conjugated Adaptive Optics (MCAO) is a technique suggested by Beckers in 1988 to overcome the limitations imposed by anisoplanatism in classical adaptive optics. This problem arises from the fact that, using a single reference star, only the volume of the atmosphere traversed by the light of the guide star is sensed and perfectly corrected, while the light coming from the scientific object is only partially corrected, since it passes through a volume of atmosphere slightly different. This results in the degradation of the image. This effect is more pronounced when the distance from the guide star is larger.
MCAO can overcome this limitation by sensing and correcting the volume of atmosphere that affects the entire FoV. This process takes place in three stages. At first, the deformation of the wavefront along different directions within the FoV is measured. This is possible by using multiple wavefront sensors associated with several guide stars in the FoV. The greater the number of guide stars used and the better the measure of the distortions introduced on the wavefront from the atmosphere region in exam.

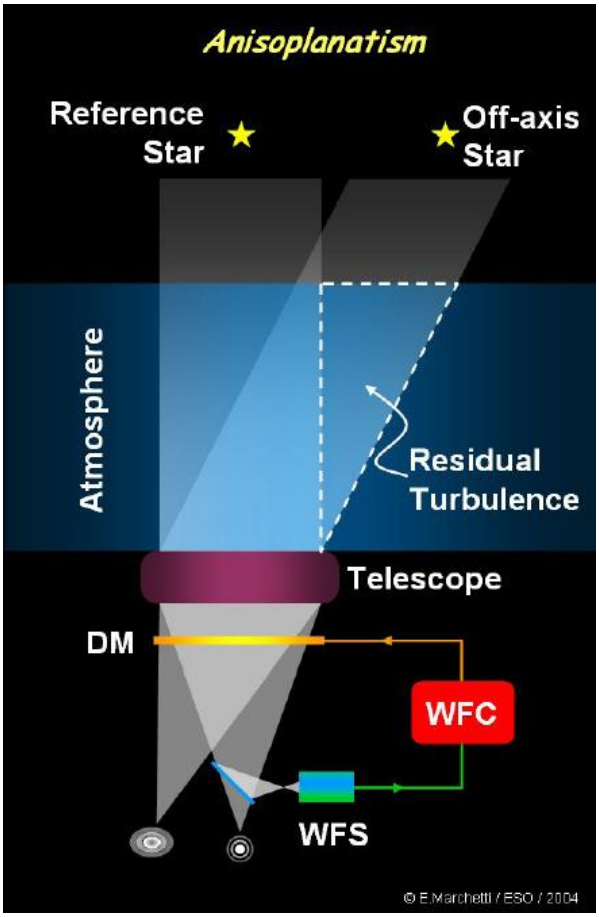

Figure 3-13: Anisoplanatism effect. When the reference star is angularly, too far from the scientific object the portion of shared turbulence is too low to allow a good correction in direction of the scientific target.

The second step is called atmospheric tomography and consists of reconstructing the vertical distribution of turbulence in different areas of the telescope field of view, observing it from different angles (Ragazzoni et al., 1999). This operation is quite

complex, since the number of measurable quantities (guide stars) will always be less than the number of unknowns (the turbulence at the different heights above the telescope). In fact, the vertical distribution of atmospheric turbulence is continuous, and therefore technically an infinite number of turbulent layers should be considered, while the guide stars available are typically very few, for obvious natural and technical reasons. This problem can be partially resolved by dividing the atmosphere in layers and considering just the layers where the turbulence is high.

Finally, the third stage consists in applying the correction to the wavefront on the entire FoV, and not only in a specific direction. This is possible by using more deformable mirrors, each of them optically conjugated at different heights. Each DM receives light from the entire FoV and, in this way, it is possible to tune the correction accordingly to the position in the field of view.

A DM conjugated to a certain height corrects the aberrations introduced at that height. For example, a mirror conjugated to the telescope entrance pupil removes only the turbulence introduced in its proximity, (the ground layer, which is typically the most turbulent layer).

Obviously, it is not possible to use an infinite number of DM conjugated to the infinite number of layers in which the atmospheric turbulence is distributed. However, the evidence shows that the turbulence is mainly distributed in 2-3 layers at different heights, and one of them is always the ground layer. Therefore, it is sufficient to use 2-3 DM conjugated to these layers to obtain a satisfactory correction.

The DM conjugation height depends on the position that allows minimizing the residual correction and does not necessarily coincide with the height of the most turbulent layer. In this way, not only the conjugated layers are corrected, but also the neighbour layers, even if the correction efficiency degrades as the distance from the conjugated DM increases.

The projection of the entrance pupil in the FoV at any given altitude is called meta-pupil. Its size varies with the conjugation height and with the FoV amplitude as:

$$D_{mp} = D + 2Htan(\theta) \qquad [3\text{-}23]$$

Where D is the diameter of the telescope entrance pupil, θ is the radius (expressed as angle) of the FoV and H the conjugation height. To obtain a good correction of the turbulent layer at the height H, it is necessary that the `footprints' (the projections of the entrance pupil in the direction of each guide star on the turbulent layer in examination) completely cover the meta-pupil, with the correction degradation increasing as the meta-pupil coverage decreases.

From [3-23] it is clear that the higher is the layer to correct, the bigger is the meta-pupil and the larger is the number of guide stars necessary to completely cover the meta-pupil. Let us see a practical example: in order to correct a turbulent layer at 8 *km* and one at 15 *km* height on a FoV of 2', using a telescope with an entrance pupil of 8.25 *m* (LBT), from expression [3-23] the diameter of the meta-pupils are 12.9 *m* and 17 *m* respectively. Correspondingly, it is necessary to use at least 5 and 7 guide stars, respectively, to cover them completely. Of course, it is difficult to find enough bright stars bright to cover the meta-pupil, and moreover the distribution of NGSs is not uniform and this translates in

some regions of the meta-pupil not covered. This, along with the fact that typically the NGSs have different magnitudes, translates into a correction quality and a SR variable across the FoV, and dependent from the observed direction.
MCAO refers essentially to the way in which DMs are introduced in the optical path, but a key role is represented by the way in which the WFSs operate and the DM are controlled. The main approaches proposed in the last years are: Star-Oriented (SO) and Layer-Oriented (LO), described in the following sections.

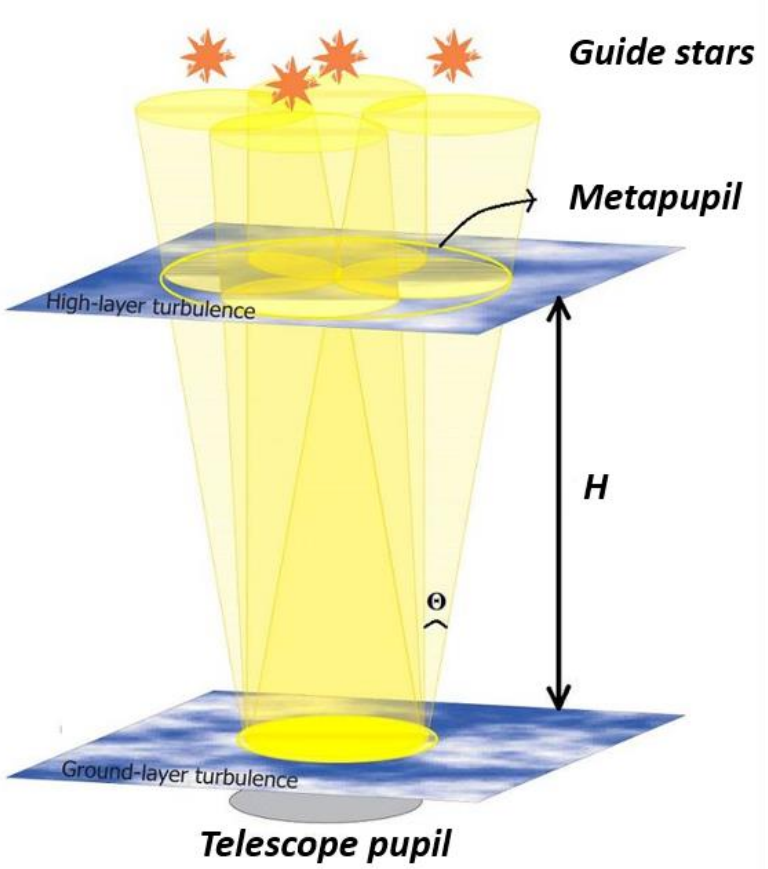

Figure 3-14: Representation of meta-pupil at any given height H for a FoV of radius θ. Four guide stars are sufficient to cover the entire meta-pupil at height H, while at higher altitudes this coverage decreases and the turbulence correction degrades. The superposition of the footprints at the ground layer is complete for any FoV.

3.4.1 Star Oriented MCAO

The Star Oriented (SO) technique uses a WFS and a single detector for each reference star. Each sensor retrieves the wavefront perturbation of each single object and analyses the atmosphere cylinder selected by the telescope entrance pupil projection in the guide star direction. In this way, a three-dimensional reconstruction of the distorted wavefront can be made and the correction applied to a certain number of DMs. The complexity of the system is proportional to the number of guide stars and DMs, since the signals coming from all sensors are combined together to calculate the atmospheric turbulence correction over the entire meta-pupil. This technique is called ***Global reconstruction*** and has one of

its bigger limitation in the complexity from a computational point of view. Moreover, the limiting magnitude for the guide stars is the same of the classical adaptive optics, and therefore the Star Oriented does not allow a significant increase in the sky coverage. The number of guide star that can be used is limited by the number of WFSs available. On the other hand, this technique allows optimizing the correction in a particular direction within the FoV.

3.4.2 Layer Oriented MCAO

In this technique (Ragazzoni et al., 2000) WFSs are optically conjugated to a specific height and guide a DM conjugated to the same altitude. Each WFS uses simultaneously the light from all the guide stars in the FoV. This can be done only using pupil plane WFSs (which means that the detector is positioned at the level of a pupil image), such as the pyramid WFS. Operatively, many pyramids are positioned in the focal plane, in correspondence of the image of each guide star. An objective placed after the pyramids collect the light from all the pyramids and optically superimposes the light coming from each of the four faces of the pyramids on four common pupil images in the pupil plane. The detector of each WFS is then moved along the optical axis in order to focus at the height to which the corresponding DM is conjugated, to retrieve only the perturbations introduced by the layer of interest. The overlap of the pupils on the detector is equal to that occurring in the atmosphere at the height of the conjugated layer.
The Layer-Oriented (LO) system reconstructs the phase delay introduced by the conjugated layer in an independent manner for each single layer, to which the DM is conjugated, and the correction applied to the DMs is calculated using entirely signals of the corresponding sensor. This technique is called ***Local reconstruction***.
This approach has several advantages, such as:

- The superimposition of the light is optical and not numerical, like in the star oriented approach, with the advantage of increasing the limiting magnitude on single guide stars. In fact, the limiting magnitude is given by the integral of the reference star magnitudes. In this way, even stars that are fainter than the ones used in classical adaptive optics can be used. This clearly translates in an increased sky coverage.

- Using pyramid WFS determines a gain in magnitude wrt other sensors, as already said.

- Uses less WFSs than the star oriented approach

- The correction cycles for the WFS-DM system conjugated to a certain layer are independent from those of the other layers. This results in a faster calculation, reducing the computation complexity and therefore an improved response in the control electronics.

- Since the correction cycles are executed in parallel, it is possible to optimize the parameters of the spatial and temporal sampling separately for each layer. In fact, depending from the height, r_0 and τ_0 change (for example at higher layers the wind velocity is higher than at lower layers) and the possibility to individually tune these parameters for each layer avoids the wavefront oversampling, increasing the SNR.

LO approach limitations are due to different aspects, some of which can be overcome. Since the FoV size in the focal plane and the metapupil images diameter on the detector are inversely proportional one to each other, increasing the FoV would require either wide re-imaging optics or very big detectors, characterized by high readout time, with the risk of not reaching the required time sampling. Finally, in MCAO systems it is necessary to separate the light to be sent to the various WFSs and this can be easily done introducing beam splitters, but decreasing the number of photons reaching each WFS, which translates into a SNR decreasing. A smarter way to split the light coming from the references is the Multiple Field of View approach.

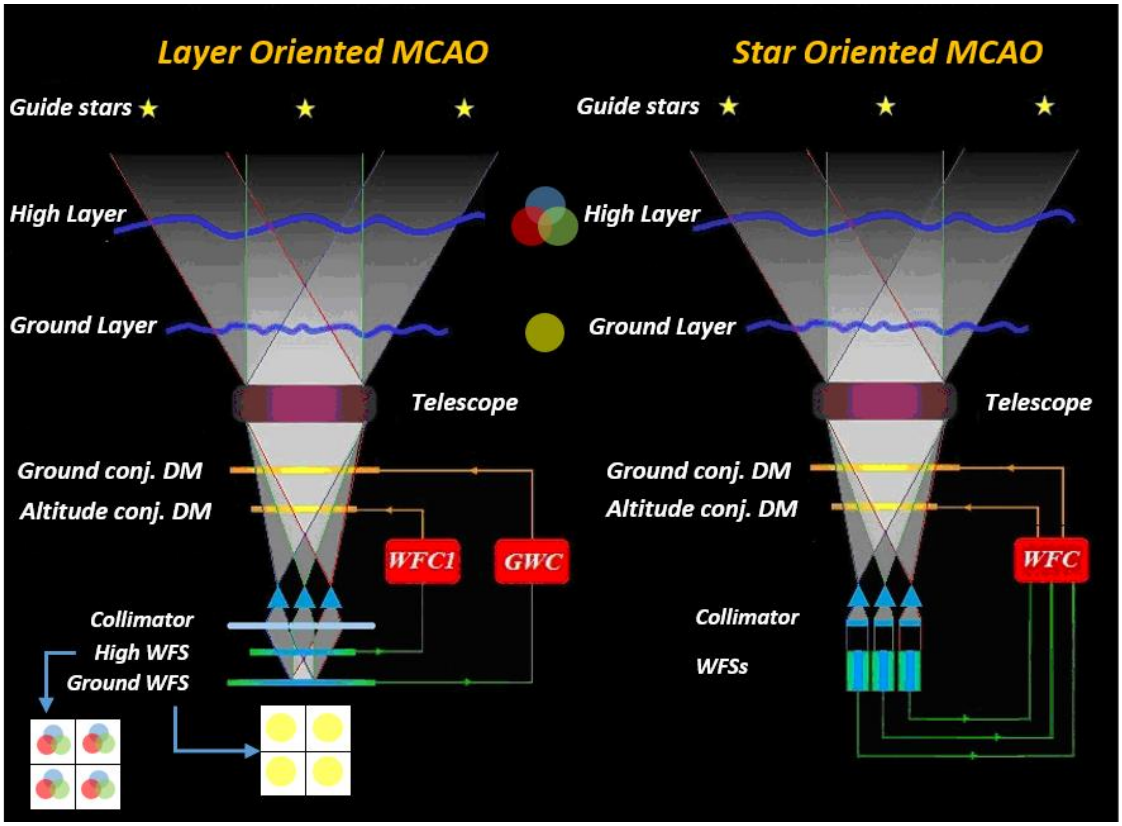

Figure 3-15: a schematic comparison between the layer oriented and the star oriented approaches. On the left the layer-oriented technique is shown, in which the light coming from all the guide stars is optically superimposed on two different WFSs, each sensing the turbulence introduced at the conjugation heights. The footprints superposition on the WFS is the same occurring in the atmosphere at the WFS conjugation height. On the right the star oriented approach, in which each WFS is associated with a guide star. A computer receive data from all the WFSs and computes the 3-dimensional structure of the whole atmospheric volume which is crossed by the light from the guide stars, with the temporal and spatial sampling required by the most turbulent layer.

3.4.3 Multiple Field of View

The Multiple Field of View Layer Oriented (MFoV-LO) (Ragazzoni et al., 2002) is an evolution of the Layer-Oriented technique. It proposes to associate to each WFS a different FoV where to look for guide stars, avoiding to divide the light between the WFs and decreasing the SNR. As can be seen from Figure 3-16, the guide star footprints overlap is total at the ground layer, so at this height their wavefronts will suffer the same perturbation. It is then possible, to estimate the turbulence introduced at the ground layer, using also guide stars angularly far away from the scientific object. The same is not valid for the layers at higher altitudes, since the overlap of the footprints decreases as the FoV and the altitude increase, leaving unilluminated some areas of the meta-pupil. It is then more appropriate, for the correction of the layers at high altitude, to choose guide stars in a FoV closer to the scientific target, ensuring in this way a good coverage of the meta-pupil.
The increase in the FoV, inside which a higher number of NGSs can be selected, in order to collect more photons and increase the SNR, translates into a gain in terms of photon density only up to a critical angle, given by:

$$\theta_\gamma = \frac{D}{h} \qquad [3\text{-}24]$$

Where D is the telescope aperture diameter and h the maximum height of the considered turbulent layers, above which the photon density tends to stabilize, because for a further FoV enlargement, the telescope pupil projections in the reference stars directions do not overlap anymore and the increasing collected photon number is divided for an increasing surface. Note however that considering only the ground layer the critical angle $\theta_\gamma \longrightarrow \infty$ because the height $h \sim 0$. That is to say, those NGSs can be selected in a very wide FoV, while as the altitude increases the critical angle decreases. The higher layers, therefore, determine the sky coverage.

A relevant issue is the depth of focus. If a zero FoV were observed, each point along the optical axis would be focused during the observation, which is to say that the depth of focus would be infinite.
While the FoV is enlarged, instead, the depth of focus decreases, causing a WFS being sensitive to each scale perturbations introduced at the conjugation height, but only to the large scale distortions introduced by upper and lower layers, since the WFS is not focused on them. LINC-NIRVANA is based on this concept.
For each of the 2 arms of LBT, a 2 *arcmin* FoV is used to correct the layer at high altitude, between at 7.1 km, using up to 8 NGS (Natural Guide Star), while for the correction of the ground layer is used a larger annular FoV (internal diameter 2 *arcmin* and an outer diameter of 6 *arcmin*) in which up to 12 NGS can be selected. In this way, it is not necessary to separate the light between the WFSs, leading to a gain in terms of photons by a factor of 2 for the WFS conjugated to the high layer and a factor of 10 for the WFS conjugated to the ground, compared to the classical approach.

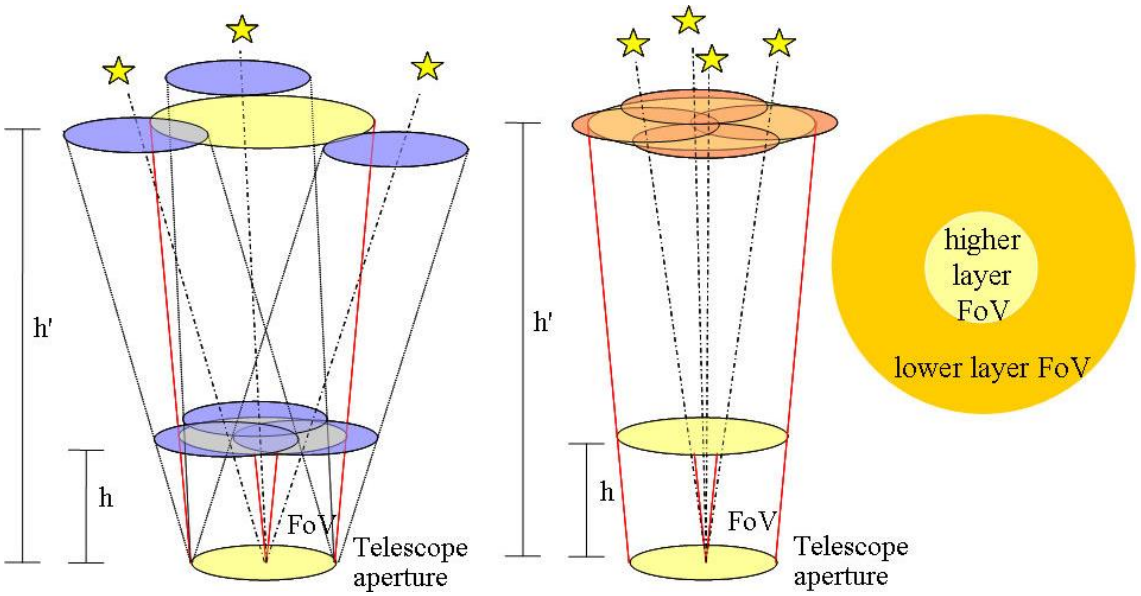

Figure 3-16: MFoV concept. On the left, the meta-pupil at height h is fully filled by the telescope pupil projections in the direction of 3 guide stars very far from the scientific FoV. The same projection at height h' is not covering the meta-pupil at all. The stars on this FoV can be used to correct the layer h but not the layer h'. In the center, the meta-pupil at a height h' is completely filled using 4 guide stars selected in a smaller FoV. Using different FoV, it is possible to correct different layers.

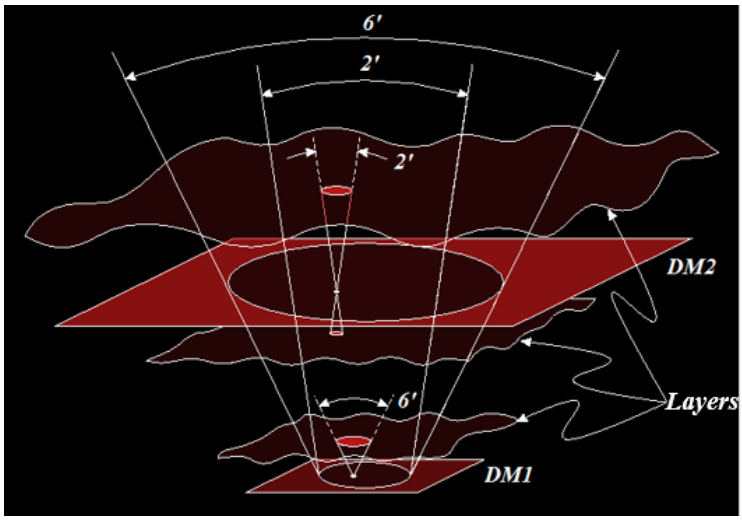

Figure 3-17: MCAO-LO MFoV applied to LINC-NIRVANA. There are two deformable mirrors, conjugated respectively to the Ground layer and at a layer at high altitude. For the correction of the high layer guide stars on a 2 arcmin FoV are used, while for the correction of the Ground layer the technical FoV is an annulus of 2 – 6 arcmin.

3.5 Ground Layer Adaptive Optics

Suggested by Rigaut (2002), this technique aims to compensate for the distortions introduced only by the ground layer on a large FoV, up to 10 – 20 *arcmin*. As already mentioned, the ground layer usually introduces the main part of the overall perturbations on the incoming wavefronts. It is clear then that a ground layer limited correction can considerably reduce the PSF diameter, even if the diffraction-limited performance will not be achieved. This is because, as said for the MFoV approach, a GLAO WFS FoV can be very wide, since the distortion introduced by the ground layer on the incoming wavefront is the same for sources which are very far one from the other. However, increasing the technical FoV where searching for reference stars leads to a reduction of the depth of focus, and the layers next to the ground layer will be only partially corrected. In fact, the spatial scales smaller than $\theta \Delta H$ are not compensated, with θ the angular diameter of the FoV and ΔH the distance between the conjugation height and the height of the layer. So increasing the FoV, the thickness of the corrected turbulent layers decreases. A good approximation of the thickness that can be corrected by a single deformable mirror is given by:

$$\Delta H \approx \frac{2r_0}{\theta} \qquad [3\text{-}25]$$

For a 5 *arcmin* FoV and good seeing conditions, in the V band (r_0 = 20 *cm*) the corrected thickness is about 275 *m*, while in the K band (r_0 = 90 *cm*) the corrected thickness is about 1200 *m*. The turbulence of the ground layer is typically distributed in a thickness ranging, depending on the sites and conditions, from a few tens to several hundreds of meters.
The WFS is conjugated at a height just above the telescope entrance pupil and it collects the light coming from the references, re-imaging perfectly super-imposed pupils. This allows a uniform correction over the whole FoV, translating into a uniform PSF.
The best performances with GLAO are obtained in bad seeing conditions, when the turbulence near the ground is strong. This means that the best seeing conditions, which spontaneously take place 20% of the time, with GLAO will happen 60-80% of the time.
The sky coverage with GLAO is much higher than the one of MCAO, especially at the galactic poles. Furthermore using LGSs with GLAO is less problematic, since the cone effect is negligible at the considered heights.

3.6 The Multi-Conjugated Adaptive Optics Demonstrator

To verify the feasibility and functionality on sky of these techniques ESO decided to develop a project, called MAD (multi-Conjugated Adaptive Optics Demonstrator). The project started in 2003 and saw the first light on the night of March 25th 2007, mounted to one of the Nasmyth foci of Melipal, one of the four 8.2 telescopes of VLT.
MAD was conceived to achieve MCAO correction on a 2 *arcmin* FoV using relatively bright guide stars M_V < 14. The correction is obtained by means of two DMs, one

conjugated to the ground layer, and the other conjugated to a layer 8.5 *km* above the telescope pupil. Two different WFSs were permanently mounted on MAD optical bench, to verify the performances of both star oriented and layer oriented approach.
Here I will briefly report the on sky results obtained in the two layouts during the MAD campaign at the telescope (Marchetti et al., 2007 – 2008, Arcidiacono et al., 2007 – 2008)
To test the performances in SO mode the telescope pointed Omega Centauri, a globular cluster with many bright stars evenly distributed, ideal condition to map a 2 *arcmin* FoV. Three bright stars, $M_V \sim 11.5$, separated by 1.8' were used as reference stars. Images were obtained using a narrow band Bracket-γ filter, 2.166 *μm*.
In Figure 3-18, are showed the corrections obtained with MCAO and GLAO respectively, with a seeing of 0.7 *arcsec*. As you can see the correction in MCAO, it is quite uniform over the entire FoV, thus ensuring a uniform FWHM across the field, with peaks in the direction of the guide stars. The correction with GLAO is lower and uniform on the whole FoV, as expected, without any particular peak in correspondence of the guide stars.

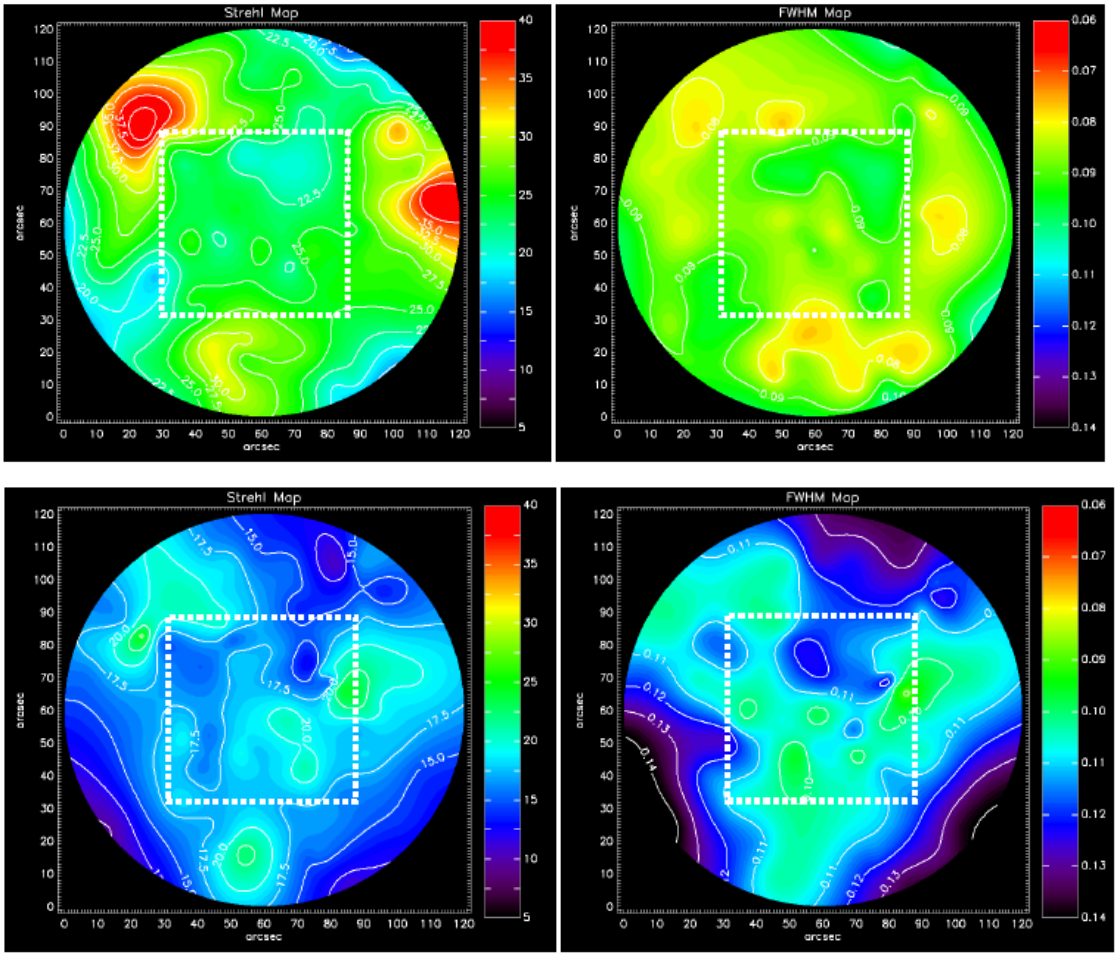

Figure 3-18: top panel the MCAO correction in closed loop on a 2 arcmin FoV, at 2.166 μm. Bottom panel the GLAO performance, on the same FoV. One the left is the Strehl map (%), on the right the FWHM map (arcsec). The dotted white square is the central arcmin FoV.

The performances obtained obviously depend on the seeing condition, and on the turbulence distribution above the telescope. As visible in Figure 3-19, the worse is the seeing and the worse is the correction. In good seeing conditions (< 0.8 *arcsec*) MCAO

has better performances than GLAO, while the trend is opposite when the seeing degrades. The average Strehl ratio for MCAO, when seeing is < 0.8 *arcsec*, is ~ 22 – 23% in the central arcmin, and ~ 25% in the 2 *arcmin* FoV, while for GLAO the average Strehl ratio is ~ 17 – 18% in the central arcmin and ~ 15% in the 2 *arcmin* FoV.
The performances of GLAO and MCAO, however, do not depend only from the seeing, but also from the turbulence distribution above the telescope. In fact, GLAO is very efficient when the main part of the turbulence in concentrated toward the ground, while its performance diminish when the turbulence is more concentrated at higher layers. MCAO is less affected by this problem, since it benefits from a DM conjugated to a high altitude layer.

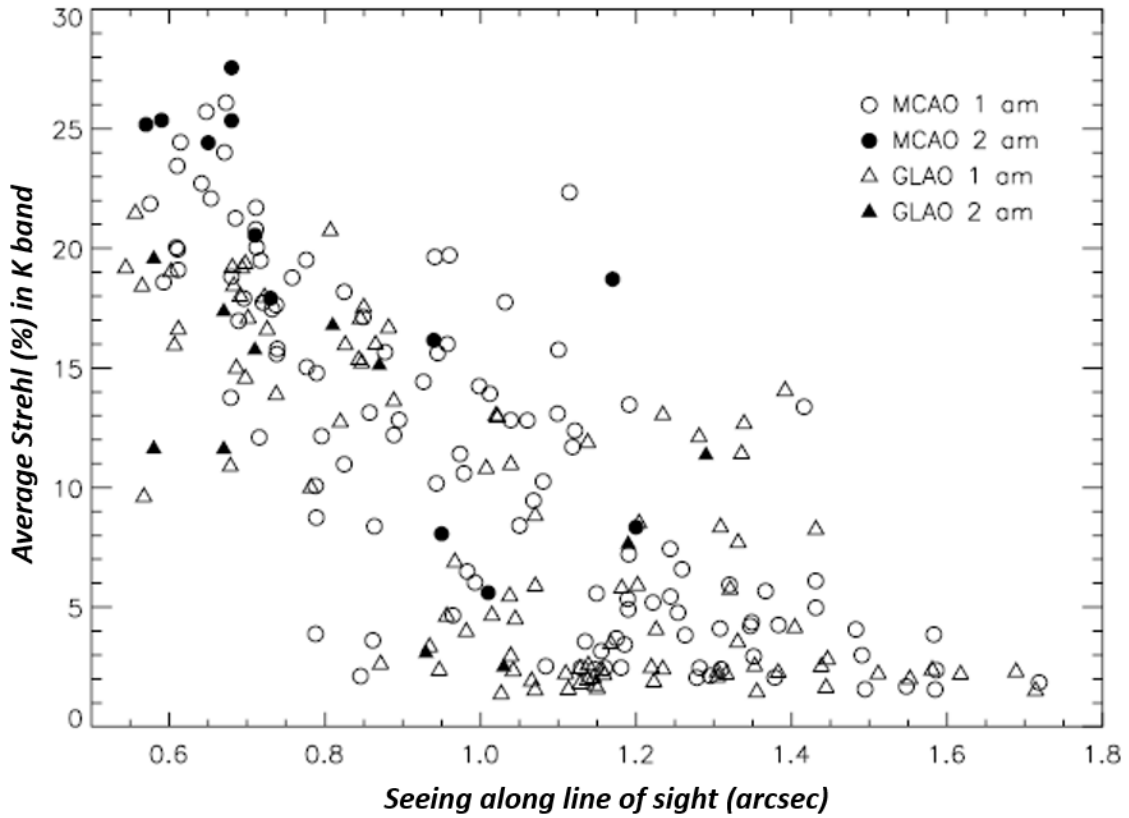

Figure 3-19: average Strehl in K band as a function of the seeing along the line of sight.

An example of this behaviour can be seen in Figure 3-20. The trend is similar for the FWHM as a function of the turbulence distribution. When most of the turbulence is located above 500 *m*, the FWHM obtained with GLAO may be worse than those obtained with MCAO even by a factor 2, while when the turbulence is strong at the ground layer the FWHM obtained with GLAO and MCAO are equivalent.
The correction uniformity is similar for MCAO and GLAO when the seeing is good, while when the seeing get worse, MCAO correction uniformity degrades faster than GLAO. This is clear, considering that, even in poor seeing conditions, MCAO still provide a good correction in the direction of the guide stars, thanks to the DM conjugated at high layer.

This translates in a large variability of the correction in the FoV, which does not happen with GLAO.

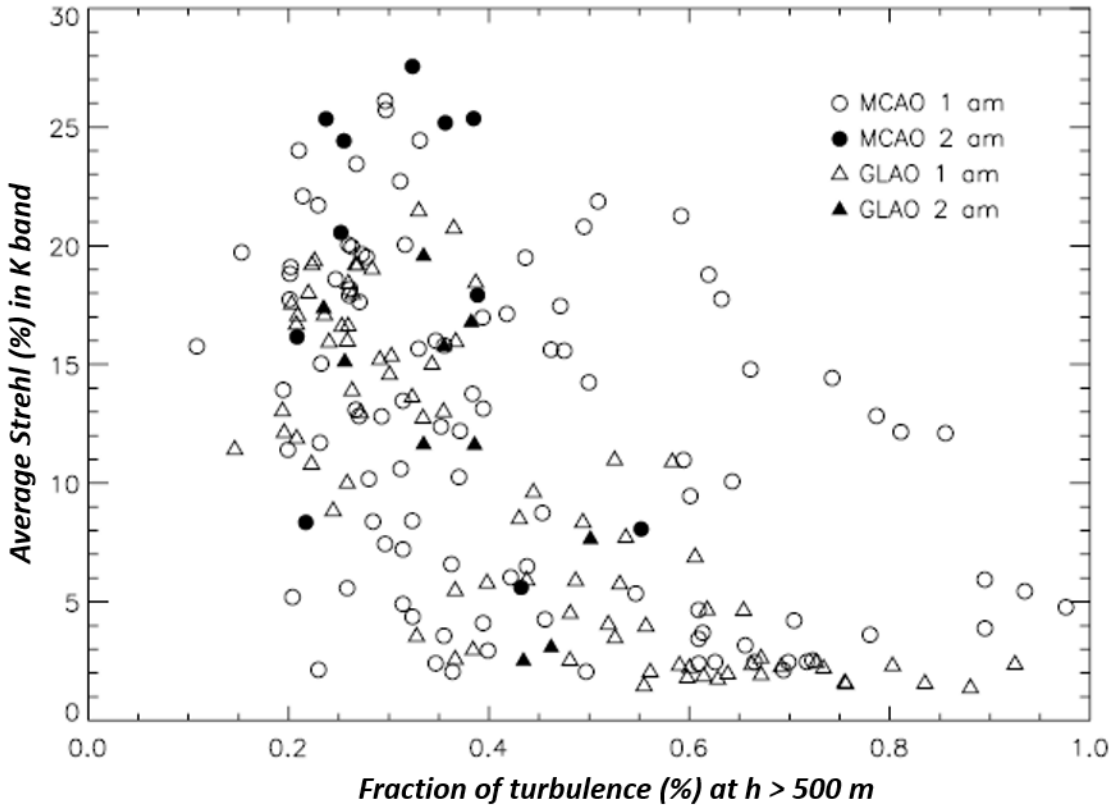

Figure 3-20: Average Strehl in K band as a function of the turbulence distribution above the telescope, in a 1 arcmin and 2 arcmin FoV.

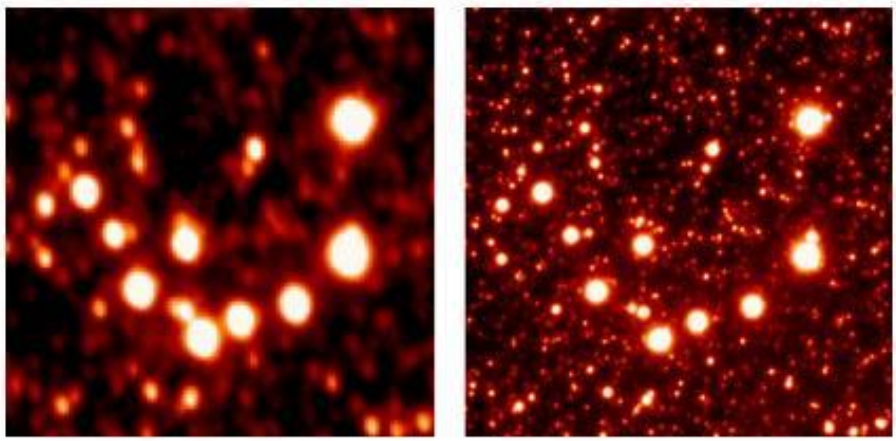

Figure 3-21: a 20" x 20" FoV near the centre of the Omega Centauri globular cluster. On the left, an image with natural seeing in K band. The mean FWHM is 0.6 arcsec. On the right, an image of the same region obtained with MCAO correction. The closest reference star is 1 arcmin away. The FWHM is below 0.1 arcsec. The angular resolution is hugely improved and allows detecting faint stars very close on to each other.

MAD performances in layer-oriented mode were tested in September 2007. As for the star oriented, a globular cluster rich of guide stars was selected for the first light, 47 Tucanae (NGC 104).

To estimate the GLAO correction were used four stars well distributed in the FoV, with M_V = 11.9, 11.9, 12.4 and 12.4, giving an integral magnitude of 10.63.
The results obtained on the entire 2 *arcmin* FoV and in the central 1 *arcmin* FoV are shown in Table 3-1.

	M_V	FWHM ['‘]	SR [%]	Seeing ['‘] in V
Open Loop	-	0.64 ± 0.06	1.7 ± 0.4	1.71
GLAO loop 2' x 2'	11.9, 11.9, 12.4, 12.5	0.38 ± 0.04	2.5 ± 1.0	1.54
GLAO loop 1' x 1'	11.9, 11.9, 12.4, 12.5	0.21 ± 0.04	6.1 ± 3.1	1.42

Table 3-1: GLAO results on globular cluster 47 Tucanae. FWHM and SR are median values, obtained with a Bracket-γ filter at 2.166 μm. Errors are the data standard deviations.

Later also the MCAO performances were tested, pointing the telescope toward the globular cluster NGC6388. The loop was closed using first three bright stars as reference, M_V ~ 11.1, 11.2 and 12.1, and subsequently using faint stars. The results are summarized in Table 3-2.

	M_V	FWHM ['‘]	SR [%]	Seeing ['‘] in V
Open Loop	-	0.45	1.8	1.48
GLAO loop	11.1, 11.2, 12.1	0.17 ± 0.02	9.2 ± 2.6	1.46
MCAO loop	11.1, 11.1, 12.1	0.12 ± 0.04	17.3 ± 9.1	1.39
Faint MCAO loop	15, 15, 15.6,15.7,16.2	0.15 ± 0.01	10.8 ± 2.1	0.55

Table 3-2: GLAO and MCAO results on globular cluster NGC6388. FWHM and SR are median values, obtained with a Bracket-γ filter at 2.166 μm. Errors are the data standard deviations.

The performances are not excellent, in particular because of the very bad seeing occurred during the observations. However, it was demonstrated the efficiency of the layer oriented approach, and the possibility to use even faint objects as reference stars, improving the sky coverage, especially at the galactic poles.
Moreover, it is worth to highlight that, even if MAD was just a demonstrator it allowed to obtain many science results. On 23 nights of observations, 19 papers were published on refereed journals, and on 6 nights the layer-oriented mode was used, 7 papers were published, showing the great impact on science of this technique.

3.7 Multi Object Adaptive Optics

The AO techniques seen until now allow obtaining excellent resolution on small FoV (few tens of arcsec), with classical adaptive optics, or uniform good correction on larger FoV (about 2 *arcmin*), or modest correction but on a very large FoV (10 *arcmin*). However often the astronomers need to look at many small objects (few arcsecs) simultaneously, with a high resolution, and to select them over a wide FoV.
Multi Object Adaptive Optics (MOAO) has been proposed for the first time by Hammer et al. (2002) and aims to correct locally only small areas of interest, called IFU (Integral Field Unit), distributed on a large FoV. The turbulent volume above the telescope is determined and individual lines of sight toward astronomical targets are projected through this volume by the control system, and the resulting corrections fed to an independent adaptive optics system, one for each scientific target.
The apparent complexity of such a system, especially if a large number of IFUs is considered, is compensated by the reduced size of the FoV to be corrected. As already demonstrated by GIRAFFE (Hammer et al., 1999) a FoV of 3 x 2 *arcsec* is sufficient to measure the velocity fields of large spiral galaxies at redshift 1. Since this area is within the isoplanatic patch in the IR, it is sufficient just one DM, conjugated at the entrance pupil of the telescope, to correct the entire galaxy. WFSs observe guide stars around the scientific target.

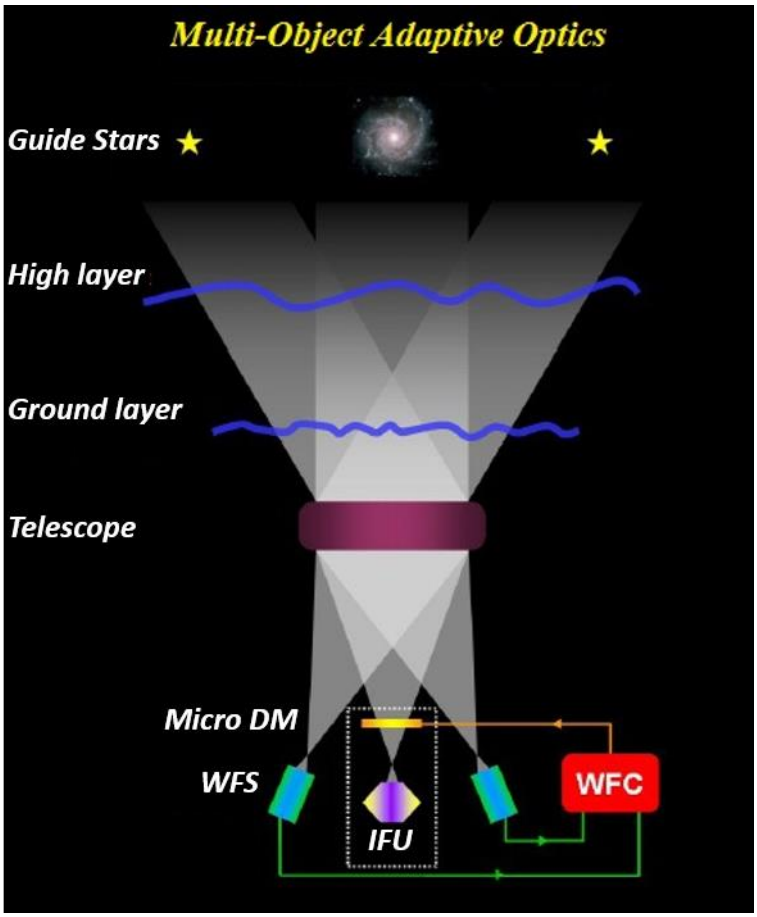

Figure 3-22: scheme of a MOAO open loop system.

A 3 x 2 *arcsec* FoV would occupy a physical area of 1.8 x 1.2 *mm* on the VLT focal plane, while a distance of 1 *arcmin* between the reference star and the scientific target results in a separation of ~ 35 *mm*. Optomechanical devices are needed on one hand to fold the light of the reference star toward the WFS, while on the other hand they position the adaptive IFU on the scientific target.

In this way, there is a complete separation between the light for the wavefront analysis and the scientific light, and the system works in open loop. The micro DM in fact, corrects only the light from the science target, while the WFS always sees a non-corrected wavefront, and must therefore have a high dynamic range and be extremely linear. Since with this layout the WFSs do not control the action of the micro DMs, their actuators must be calibrated very carefully.

Such a system, however, still suffer of the sky coverage problem. For this reason, MOAO uses modal tomography. Several guide stars, laser or natural, are selected to reconstruct the volume of atmosphere above the telescope. Once the turbulence profile is known, a computer determine the corrections to be applied in the direction of the scientific targets. Implementing a MOAO system is therefore technologically challenging, and since the system works in open loop, requires a very precise calibration and an accurate tomography of the turbulence above the telescope. Because of its novelty, several laboratory and on sky demonstrator projects have been implemented.

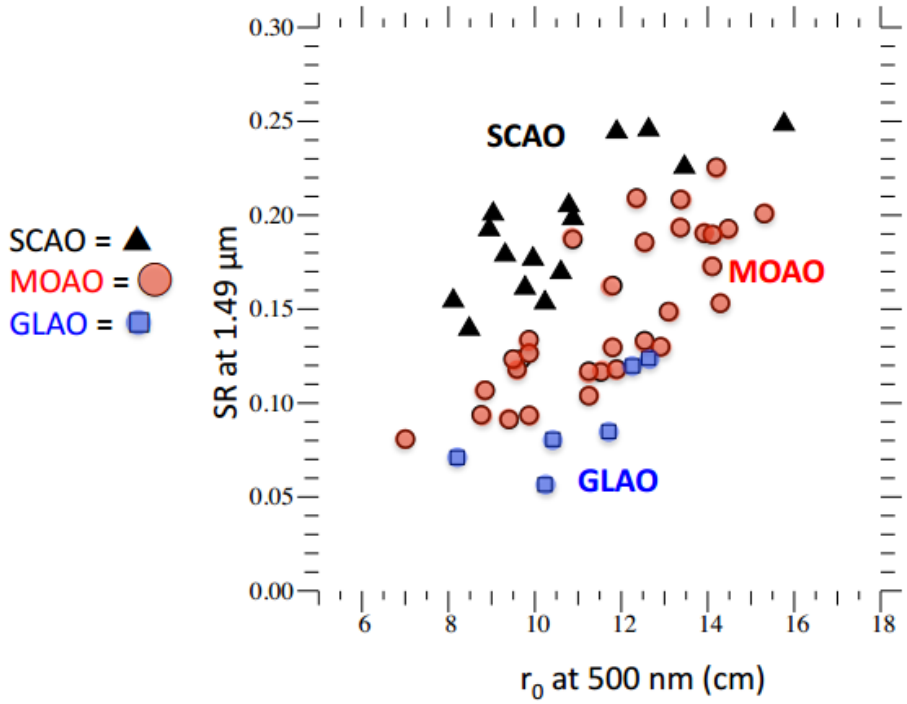

Figure 3-23: Strehl ratio in H band vs seeing (at 0.5 µm). Results obtained with CANARY using 3 NGSs on a 2.5' FoV around the scientific target. (Gendron et al., 2011)

CANARY in particular is a LGS MOAO pathfinder for the EAGLE MOAO for the E-ELT, installed at the William Herschel Telescope, which is going to investigate the LGS tomography and calibration problems (Gendron et al., 2011). The first, NGSs only, variant of CANARY has been successfully demonstrated on sky, using three WFSs in

open loop on three off-axis NGSs, arranged on a 2.5 *arcmin* FoV around the scientific target, showing results comparable to the classical adaptive optics.

4 LBT and LINC-NIRVANA

4.1 The Large Binocular Telescope

The Large Binocular Telescope (LBT) is one of the largest telescopes existing today (Hill & Salinari, 2003). It is located at Mount Graham, Arizona, USA, at 3191 *m* above sea level. Under the best conditions, the site ensures a seeing comparable to that of the best sites of observation - Hawaii and Chile. It is equipped with two primary mirrors of 8.4 *m* diameter each, equipped with 164 active optics actuators to compensate for the deformation due to their own weight. A central hole allows the light to proceed towards the scientific instruments placed under the mirrors. Each of the two LBT arms has a Gregorian configuration, allowing a real focus before the secondary mirror. The two arms are mounted on a single alt-azimuth mechanical structure. The focal ratio of the two primaries is F/1.14, ensuring compactness to the telescope. The total collecting surface of the LBT is equivalent to that of a single telescope with a primary mirror of 11.8 *m* in diameter. The baseline of LBT (the distance between the outer edges of the two mirrors) is 22.8 *m*, which makes the LBT, when used in interferometric configuration, the first of the ELTs. The secondary mirrors of LBT are adaptive and 0.91 *m* in diameter, optically conjugated to an altitude of 100 *m*, and under dimensioned in order to act as diaphragms of the system and minimize the thermal background (very high in the IR). This results in a reduction in the size of the entrance pupil of each of the two telescopes from 8.4 *m* to 8.25 *m*. The secondary mirrors have 672 electromagnetic actuators each. In this way, all the instruments located, in the optical path, after the secondary mirrors to benefit of the adaptive optics correction. Two flat tertiary mirrors tilted of 45° can be inserted in the optical path, if necessary, directing the light toward three different Gregorian focal stations in an area between the two primary mirrors. Here three instruments are allocated, enabling the telescope to operate in the interferometric mode. LBT in fact can operate in three different modes (Herbst and Hinz, 2004):

- The two arms working as independent telescopes of 8.4 *m* in diameter, each using their own instruments.
- As a single telescope of 11.8 *m* equivalent diameter. It is sufficient to combine incoherently the light from the two arms on a common focal plane. However, in this mode, the resolution remains the one of an 8.4 *m* telescope.
- As interferometer, coherently combining the light from the two arms. In this mode, the LBT reaches the diffraction limited angular resolution of a 22.8 *m* telescope.

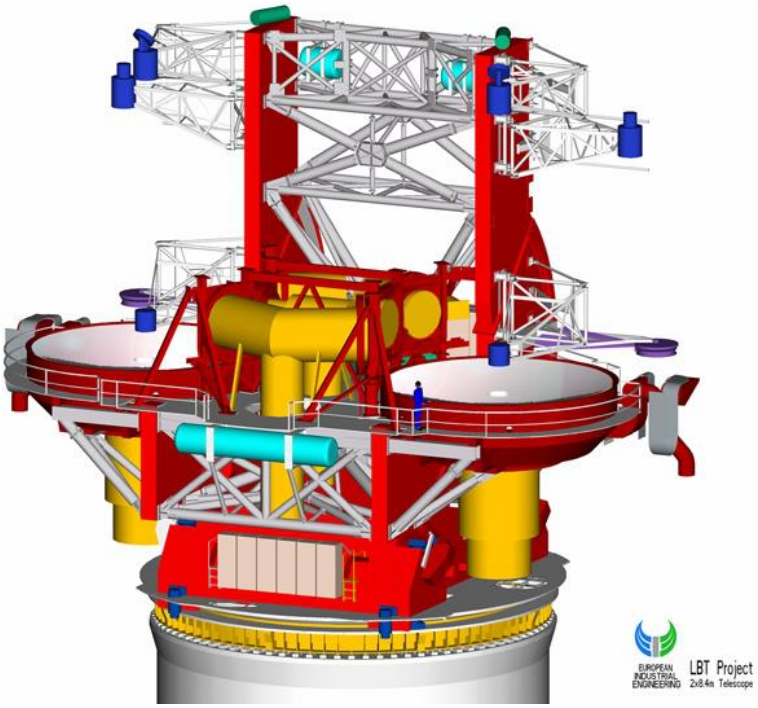

Figure 4-1: the Large Binocular Telescope

4.2 Interferometry with the LBT

The LBT structure is particularly indicated for interferometry, the coherent superposition of electromagnetic waves. In the case of the LBT, the electromagnetic waves are the light collected by the two primary mirrors, combined in one of the central focal stations. The main configurations for astronomical interferometry are Michelson and Fizeau. In the first configuration, also known as pupil plane interferometry, the beams are combined on the pupil plane. In this way, the image of a point source, like a star, on the pupil plane is an interference pattern in which the modulation of the signal intensity is due to the Optical Path Difference (OPD) of the rays coming from different apertures. This kind of interferometer has no theoretical limits to the baseline, allowing thus to achieve very high resolutions, of the order of λ/B, where B is the baseline. However, it is necessary to maintain the condition of coherence to have the interference. This implies that the optical paths of the light from different apertures must be equal and this happens only for the sources in axis with the telescope. Moving from the optical axis by an angle θ introduces an OPD equal to $B\theta$. This difference is negligible when it is below the coherence length $\lambda^2/\Delta\lambda$, where $\Delta\lambda$ is the spectral width of the source. Therefore, the FoV that can be observed with this technique is given by:

$$\theta = \frac{\lambda}{B}\frac{\lambda}{\Delta\lambda} \qquad [4\text{-}1]$$

Thus extremely limited, especially for observations in visible and IR bands.
In Fizeau configuration, the beams from different apertures are combined on a common focal plane. The overlap of the PSFs produces interference, and the image of the star will

show two different components. An Airy disk with size λ/D, due to diffraction, modulated by interference fringes, as shown in .In this image there are simultaneously two different resolutions: the resolution along the y axis is given by the size of the Airy disk, while along the x-axis the resolution is the width of the central interference fringe, λ/B.

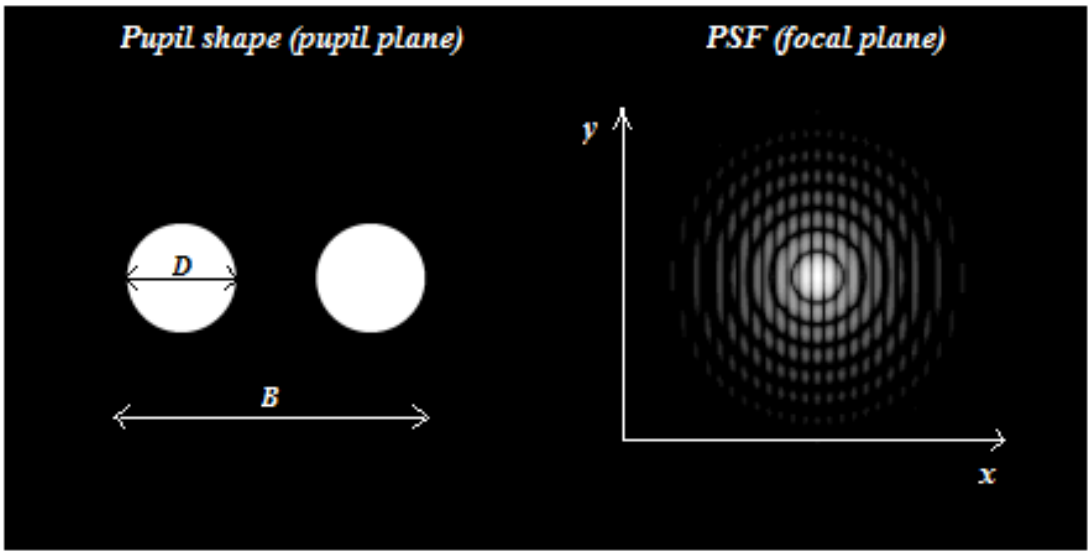

Figure 4-2: example of PSF obtained in Fizeau configuration, combining the beams from two apertures of diameter D, on a baseline B. The resolution of the Airy disk is λ/D, whereas the one of the interference fringes is λ/B.

Considering a generic field on the sky, the resulting image is a full field resolution-anisotropic image. To retrieve an image with a λ/B resolution in all directions, the data have to be deconvolved with the point like source PSF, obtained from the observation at different parallactic angles of some reference stars inside the FoV. This can be obtained exploiting the Earth's rotation, which causes a rotation of the baseline projection and, as a result, of the interferometric fringes.

The main limit of Fizeau interferometry is the baseline length. Such an optical system, indeed, has a blind range for spatial scales ranging from the single aperture resolution λ/D to the interferometric one λ/B. This imposes the choice of a baseline that is comparable with the single aperture diameter, to minimize such a blind zone, and this limits the maximum achievable resolution.

Moreover, the pupils' homoteticity must be maintained. This condition requires that the relationships between the dimensions, separations and mutual rotation of the entrance and exit pupils must be constant. In the case of LBT this problem does not exist, because both the telescopes are mounted on the same mechanical structure, ensuring that homoteticity, once obtained, is maintained.

The main advantage of Fizeau interferometry in the Visible and Infrared bands is the larger FoV that can be observed, limited only by the ability of the adaptive optics to deliver a corrected wavefront (atmospheric turbulence would destroys interferometry). In this configuration, the interferometric FoV is limited by the isoplanatic patch.

Because of these considerations, the LBT beams will be combined in a Fizeau interferometric configuration (Herbst et al., 2008).

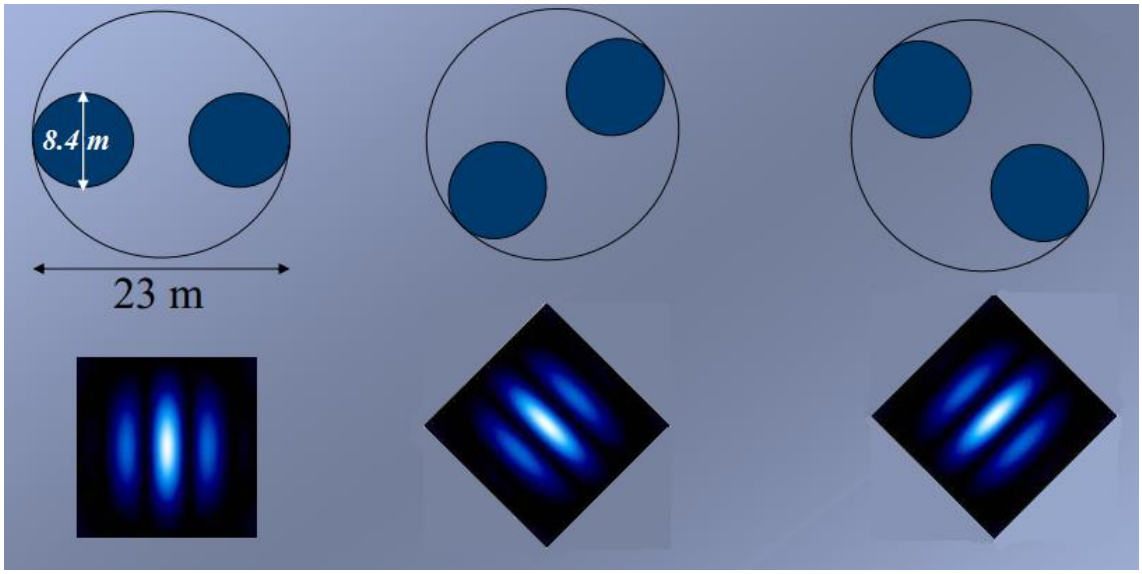

Figure 4-3: example of a PSF obtained in Fizeau configuration, with three different parallatic angles.

4.3 LBT Instrumentation

LBT can accommodate a large number of scientific instruments, some of them are designed to work in single arm configuration, while others are designed to use LBT in interferometric mode. The instruments for the single telescope are:

- The Large Binocular Cameras (LBC)
- The Multi-Object Double Spectrograph (MODS)
- The LBT-NIR Spectroscopic Utility with Camera and Integral Field Unit for Extragalactic Research (LUCIFER)
- The Potsdam Echelle Polarimetric and Spectroscopic Instrument (PEPSI)

The instruments for the interferometric configuration are:

- The LBT Interferometer (LBTI)
- The LBT Interferometric Camera and the Near-IR/Visible Adaptive Interferometer for Astronomy (LINC-NIRVANA)

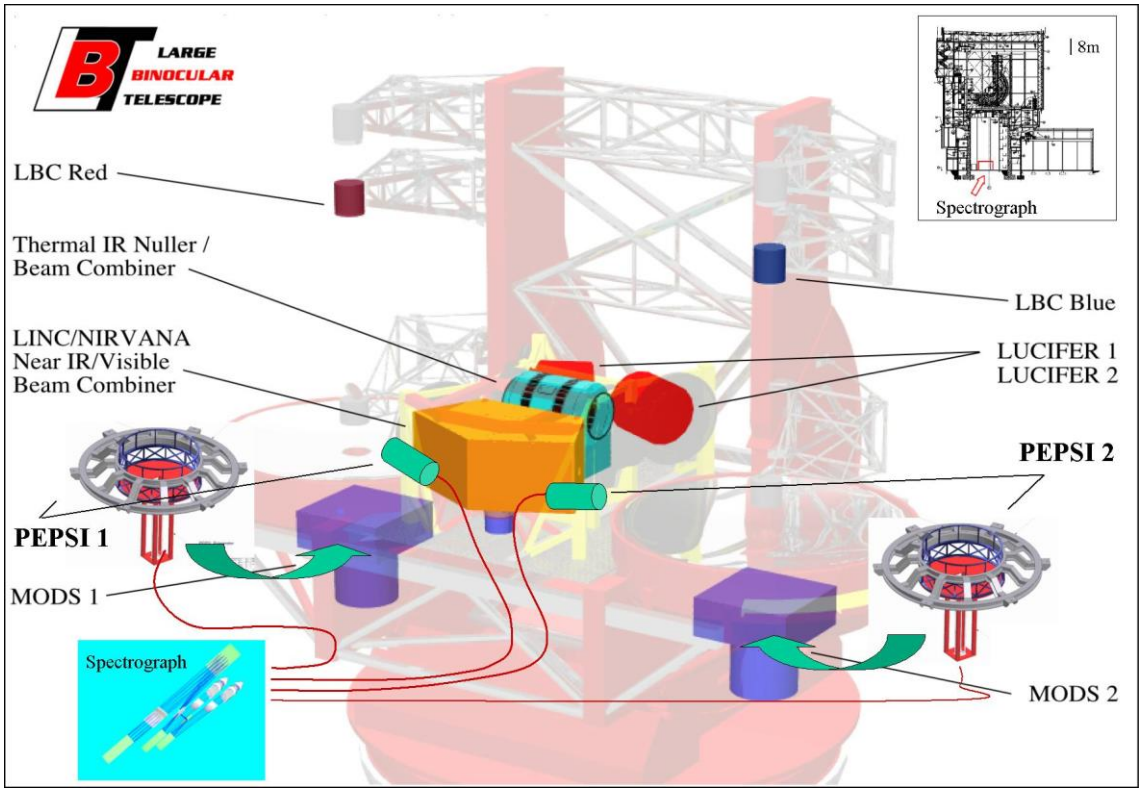

Figure 4-4: location of the instruments of the LBT.

4.4 LINC-NIRVANA

LINC-NIRVANA (LBT Interferometric Camera and Near-InfraRed/Visible Adaptive Interferometer for Astronomy) is a Fizeau interferometer working at the visible and near infrared wavelengths with and integrated MCAO LO system for the atmospheric turbulence correction (Herbst et al., 2003). The main aim of the instrument is to obtain near infrared images in the FoV of 10 x 10 *arcsec* with a resolution equivalent to the one of a telescope of 22.8 *m* in diameter.

LINC is a cryogenic chamber in which the infrared beams from the two arms of the LBT interfere (German responsibility), while NIRVANA analyse the incoming wavefront, to determine and correct the aberrations by means of 4 WFSs (Italian-German responsibility).

Recalling that the isoplanatic angle with MCAO is much wider than in SCAO mode and that the possibility of making Fizeau interferometry is limited by this parameter, the MCAO correction provided by LINC-NIRVANA allows using LBT as an interferometer on large fields, compared to the other interferometers existing today.

The instrument is located on a large carbon fiber optical bench on the central platform of the LBT, in one of the combined focal stations.

To perform MCAO correction, NIRVANA uses a pair of WFSs for each aperture of the telescope: the Ground layer Wavefront Sensor (GWS), detecting the turbulence introduced by the ground layer and the High layer Wavefront Sensor (HWS), detecting the turbulence introduced at a height of 7.1 *km*.

NIRVANA relies on the MFoV approach, in which the two sensors observe at different FoV.
The incoming F/15 beam is split in two parts by an annular mirror: the annular portion of the beam, corresponding to a 2 – 6 *arcmin* FoV is reflected toward the entrance of the GWS, which uses up to 12 natural guide star. The GWS is equipped with a bearing to compensate for the FoV rotation. The information on the wavefront distortions retrieved by the GWS are sent to the adaptive secondary mirror of the LBT, equipped with 672 actuators, at a maximum frequency of 1 KHz.
The central 2 *arcmin* are collimated, to avoid a separation of the PSFs in the common focal plane of the two arms of LBT. After the collimator, the beam is separated by a

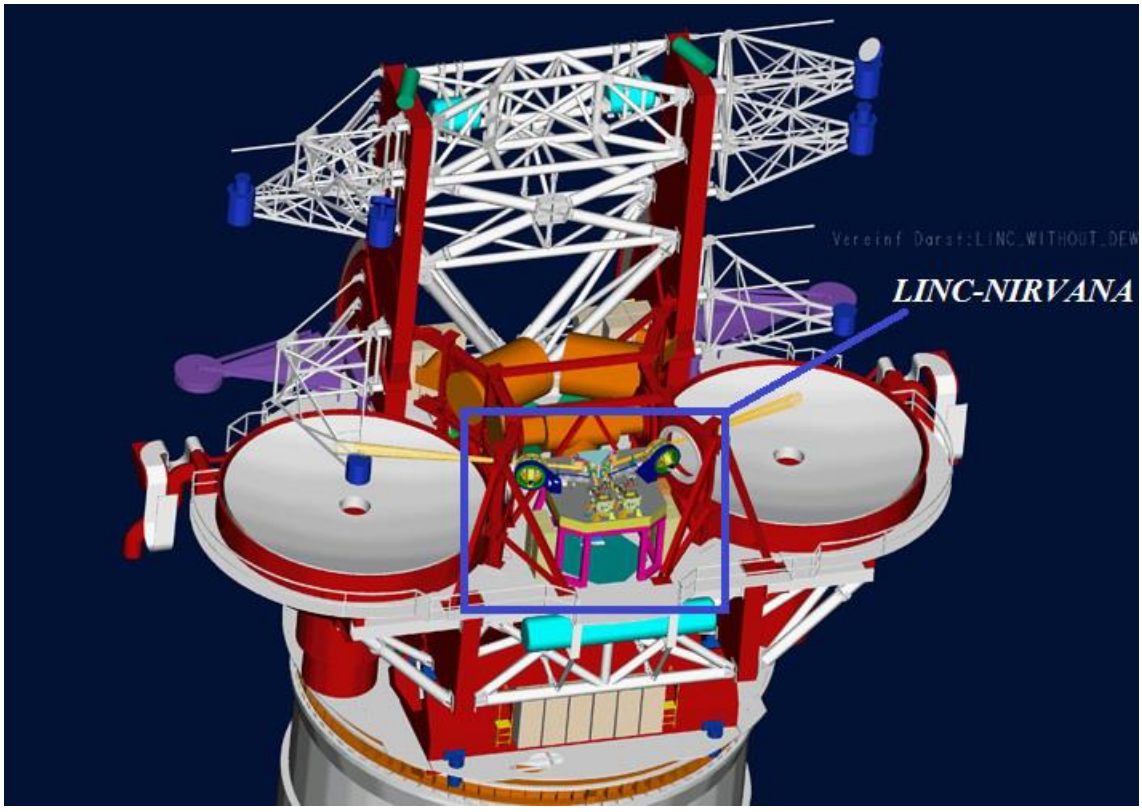

Figure 4-5: LINC-NIRVANA position in the LBT

dichroic into visible and IR light. The IR light is co-phased with the light coming from the other arm of the telescope by the so-called piston mirror, a flat monolithic mirror, acting as the actuator for the fringe-tracking loop. Such a recombination mirror compensates for the difference in path between the beams, producing in the interferometric focal plane a fringe pattern. The scientific image forms on a CCD "HAWAII-2", 2048 x 2048 pixels, 0.005 *arcsec*/*pixel* located in a cryostat below the optical bench to minimize the thermal background.
The visible beam, 0.6 – 0.9 μm, inside the 2' FoV is re-focused by an F/20 optics at the entrance of the HWS, conjugated at 7.1 km, which uses up to 8 NGSs. The corrector for the high layer perturbations is a XINETICS piezostack DM, conjugated at the same height as the HWS, and deformable by using 349 actuators. To derotate the FoV of the HWSs optical derotators, called K-mirrors, are inserted in the optical path toward the HWSs.

The astrometry of the HWS reference stars is done using a Patrol Camera, which collects part of the light sent to the HWS, when a beam splitter is inserted in the optical path.

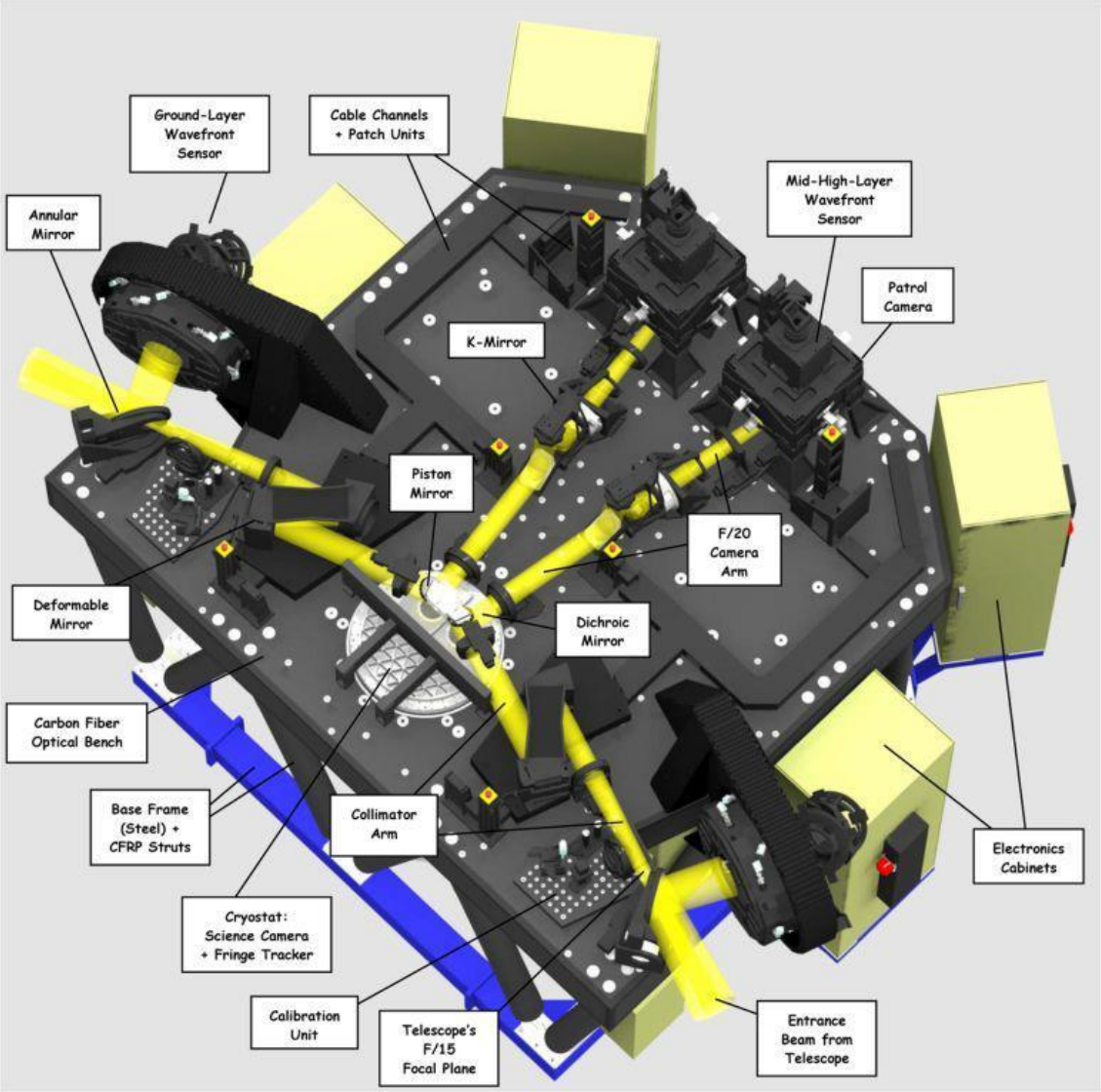

Figure 4-6: the optical bench of LINC-NIRVANA.

4.4.1 Science with LINC-NIRVANA

LN increases the resolution power of the LBT to the one of a 23 *m* telescope, and this results into benefits to a wide variety of astrophysical goals. The high-resolution power, however, is not the only peculiarity of such an instrument, as other interferometers can reach comparable or higher resolutions (like VLTI and Keck). The real uniqueness of LN resides in its true imaging capability, allowing disentangling structures that could not be easily understood with Michelson interferometry. The MCAO correction enables high-

resolution imagery on an interferometric field of 10 x 10 *arcsec*, very wide if compared with the typical FoV of other interferometers (few arcsecs).
With these peculiar characteristics, LN will influence many astronomical fields, from extragalactic to star formation studies. In general, LN will allow observation of faint objects, and will resolve regions not yet resolved in the IR wavelengths.

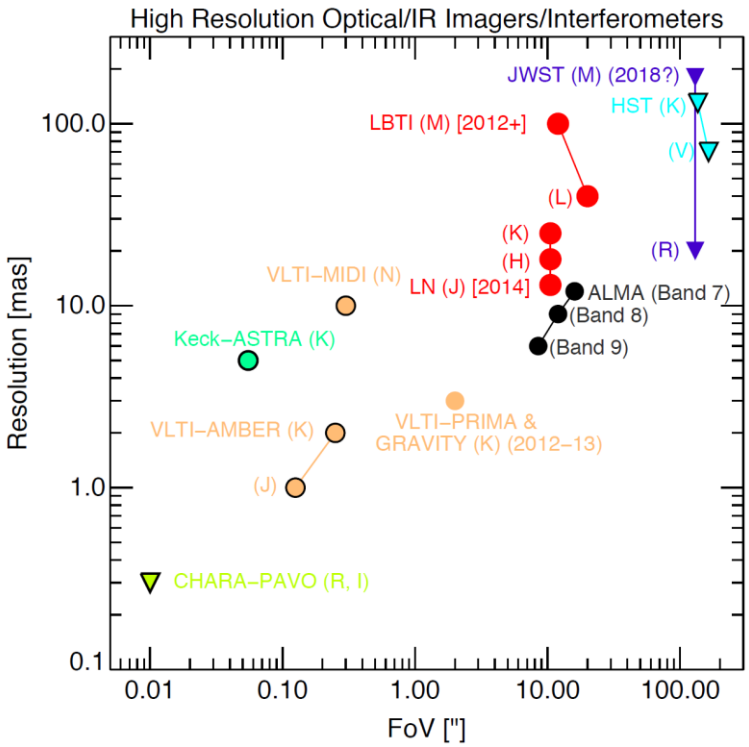

Figure 4-7: Resolution – FoV diagram for the main IR observing facilities. LN will deliver a resolution from 10 mas (J band) to 20 mas (K band) on a 10" FoV, much wider than other existing interferometers.

Protoplanetary Discs and search for Extrasolar Planetary Systems

Circumstellar discs are of fundamental importance for the formation of planets. They not only provide the necessary matter for the planets to be created, but they also act like a shield against the stellar wind, making it therefore possible to form little clumps out of the scattered gas and dust in the first step. The newly formed planet will later on generate a free gap by accretion and resonant scattering and thus changing the structure and dynamics of the disc substantially.
With detailed observations at highest angular resolution and sensitivity, it will be possible to search for indications of these changes in the scattered light of the disc. At a wavelength of 1.2 μm LN will reach an angular resolution of about 20 *mas*. At distances of the nearest molecular clouds (e.g. the Taurus region at 140 parsec), this corresponds to orbital parameters similar to the ones of our Earth. The observation of protoplanetary discs might therefore result in the first detection of a planet via its perturbation influence on the structure of the disc. The unique ability of LINC to do real imaging is a great advantage at this point, in contrast to other interferometric cameras.

Currently the search for extrasolar planets is mainly based on two different techniques, either on the observation of Doppler shifted spectral lines from the central object due to the bound motion of the invisible companion, or on photometric changes of the system during occultation. Both techniques are biased towards the detection of heavy Jupiter-like objects on tight orbits around the central star. The majority of present detections shows semi-major axis of less than 0.5 AU, which would require the re-evaluation of current planetary theories.
LN on the other hand will allow the search for planets using a more classical approach by detecting periodic astrometric changes of the central star because of the gravitational forces of the planet. The very high precision of astrometric studies with LN opens up for the first time the regime of real Jupiter-like planets - planets with a mass comparable to Jupiter's mass moving on orbits of 5 AU around a solar-like star. At normal conditions, the achievable relative astrometric precision of LN will be in the range of 0.1 *mas*. This would already be sufficient to detect the gravitational influence of Jupiter on the motion of our Sun from an observing distance of 100 parsec. At many studied objects, it will be possible to improve the astrometric precision even more because of LN's large field of view, which increases the probability of having multiple reference stars for calibration. In addition, the availability of more than one reference star removes any ambiguity, which will be present at measurements of other interferometric cameras: the star hosting the orbiting planet can clearly be identified by its periodic movement with respect of several neighbouring objects.
Astrometric precise measurements with LN can be also employed in the follow-up of extrasolar planets candidates, allowing for the determination of their orbit and the estimation of their masses.

The Black Hole at the center of the Milky Way

Due to its unique combination of high angular resolution and large FoV, LN will be ideally suited for detailed studies of our closest massive black hole, the black hole at the center of our Milky Way. Although the galactic centre is located on the southern hemisphere of the sky, the LBT will be usable with its full interferometric resolution in east-west direction and unobscured field of view. The galactic centre will be observable for several hours per night what allows at least for a limited aperture synthesis. The angular resolution of LINC will be about 20 *mas* at a wavelength of 2.2 μm. At a given distance to the galactic centre of approximately 8000 parsec, this corresponds to only 160 AU. A comparable angular resolution in combination with the expected sensitivity and field of view is not reachable by any other infrared detector system existing today. LN will therefore offer unprecedented, outstanding and unique possibilities for detailed astrophysical studies of the direct environment of a massive black hole.
Exact stellar orbits can be derived very efficiently for all detectable stars near the SgrA* super-massive black hole, allowing the determination of the central mass of the Milky Way at unprecedented small distances. A flux density, monitoring on the NIR counter part of SgrA* and its immediate surroundings, will improve our knowledge on the accretion processes as well as the mechanism that leads to its strong flare activity.

Double and Multi Stellar Systems

The majority of main sequence stars in our galaxy is located in double or multi stellar systems (Duquennoy & Mayor, 1991). The distribution of the orbital semi-major axis of double stars shows a maximum at about 50 AU, what corresponds to approximately 0.3 *arcsec* at our nearest star forming regions.
At infrared wavelengths, LN will be able to penetrate the obscuring dust clouds and resolve individual stars in young binary systems down to an angular separation of 20 *mas*. The large FoV of LN will furthermore allow to do astrometry at an extraordinary high level of precision and to determine the orbital parameters for a large number of binary systems. The derived dynamical masses can be used to calibrate the mass-luminosity relation and the pre-main sequence of the Hertzsprung-Russel-Diagram.

Imaging of Planetary Surfaces and Atmospheres

For solar system targets, the wide field of view, high spatial resolution, and increased sensitivity of the LN interferometer will allow ground-based monitoring and investigations that rival spacecraft observations. In fact, the spatial resolution may prove to be an occasional problem, since atmospheric features can evolve on timescales short compared to that needed for Earth's rotation to sample all parallactic angles. As the only other body in the solar system with surface oceans and rainfall, Titan is the subject of much ongoing study and interest.

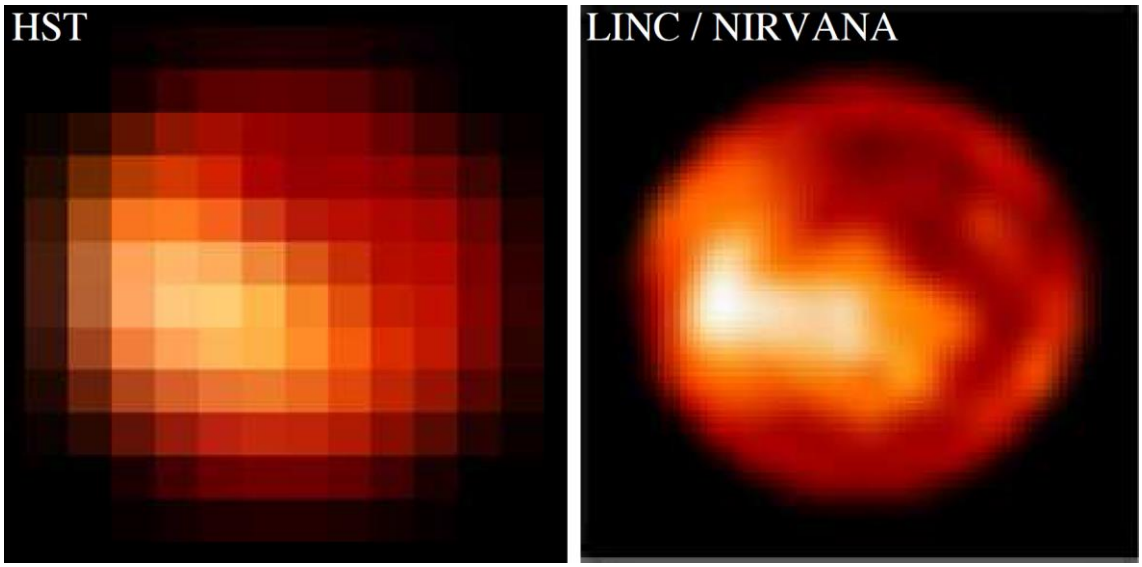

Figure 4-8: the surface of Titan imaged with LINC-NIRVANA and HST. LN will resolve surface structures 100 times smaller than that seen by HST. Note that the right image is a simulation.

Some planetary scientists believe that Titan's atmosphere resembles that of the Earth prior to the appearance of life and the oxygen it produced. Penetrating the thick cloud deck at near-infrared wavelengths will produce surface imagery of unparalleled clarity and resolution. The 20 *mas* K band resolution that LN can provide corresponds to 130 *km* at Saturn, and Titan's disk will be approximately 40 resolution elements or 80 pixels across.

For comparison, HST's resolution at K is ten times coarser, producing an "image" of Titan four resolution elements in diameter (see Figure 4-8).

Energy Balance in Stellar Nurseries

Stellar winds, through their interaction with circumstellar disks and the surrounding media, play a central role in catalyzing and regulating the star formation process. Unfortunately, the small angular scales and the presence of obscuring dust have severely limited our ability to probe the regions where these important interactions take place. LINC-NIRVANA will provide an unprecedented opportunity to study these fundamental processes. The angular scales sampled by the imaging beam combiner correspond to less than 1 AU at the nearest star forming regions. The ability to form true images will give LN an enormous advantage over other interferometers in disentangling these complex regions (see Figure 4-9). A monitoring program of circumstellar emission, coupled with high-resolution spectroscopy, can give the full, three-dimensional motions of the gas in the near stellar environment. Note that a shock front travelling at 25 *km*/*s* in Taurus will move noticeably during a single, weeklong observing run.

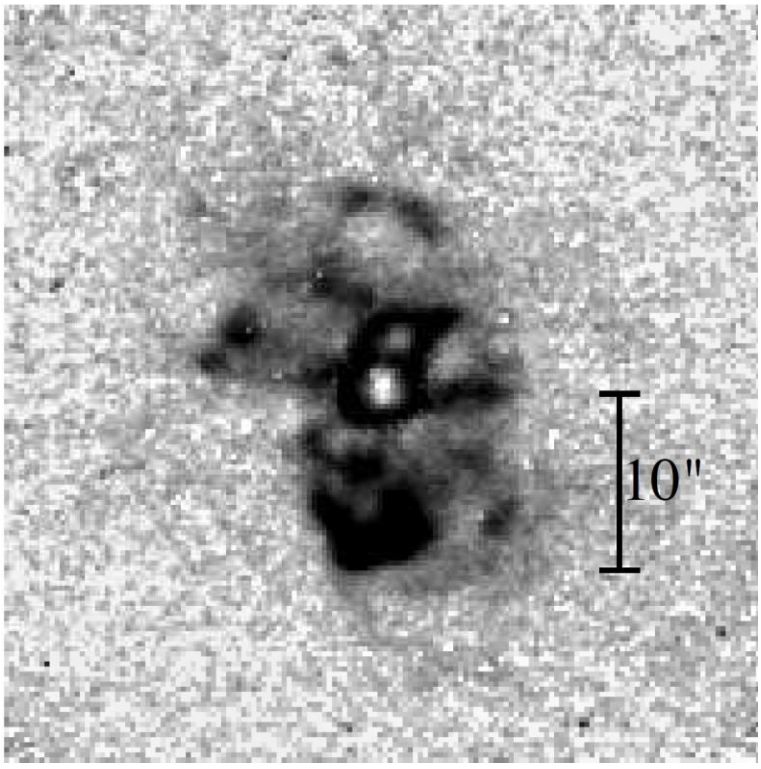

Figure 4-9: Arcs and loops of molecular hydrogen within 30" of T Tau. This image, taken with a Fabri-Perot interferometer in the 2.12 μm quadrupole line of H_2, demonstrates the complexity at all angular scales in star formation regions.

Galaxy Formation

The best way to understand galaxy formation is to use the enormous light gathering capability of large telescopes to look back in time at the era of galaxy assembly. The

current hierarchical paradigm predicts that the earliest galaxy fragments are small and faint. Unfortunately, the limited sensitivity of current instruments forces us to bias our investigations toward atypically luminous and massive galaxies, and toward galaxies that are undergoing a star-bursting episode. A deep multi-color, near-IR survey with LN could sample a volume of ~ 105 Mpc^3 in ~ 20 nights of observing time, detecting galaxy fragments in that volume with only 10^{-3} of the Milky Way's mass. Until the NGST mission, no other facility will reach this combination of sensitivity, areal coverage, and number of detected objects.

A detailed morphological study of external galaxies will be possible, since LN will allow retrieving the structural parameters down to very faint galaxies, to study, for example, the connection between GRBs occurrence and host galaxy properties, or detect, in brighter early type objects, possible relics of merging events to validate the hierarchical galaxy formation scenario.

Resolved Extragalactic Stellar Populations

Current technology limits our ability to resolve individual stars in galaxies further than ~ 5 *Mpc*, forcing us to assess their stellar content and formation history using integrated spectral energy distributions.

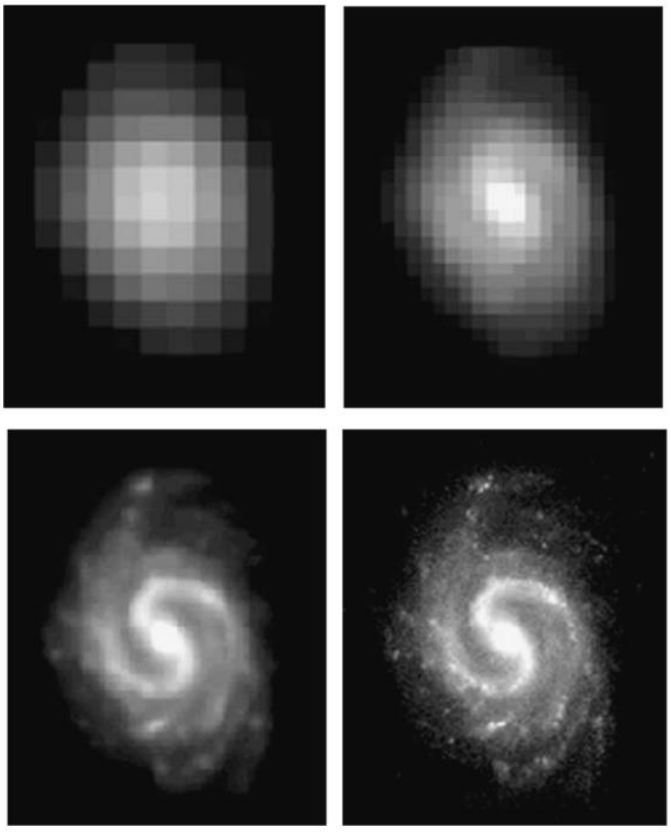

Figure 4-10: NGC 4535 at K artificially red shifted to z = 1 with seeing limited resolution of 0.4" in the upper left panel, HST resolution of 0.2" in the upper right panel, diffraction limited resolution of a 8.4 m telescope at about 0.06" in the lower left panel and diffraction limited fully reconstructed resolution with LN of 0.02" in the lower right.

In particular, there is not a single giant elliptical galaxy close enough to be fully resolved into individual stars, a situation which has generated a decade-long debate over their star formation history. LINC-NIRVANA will be able to resolve stellar populations in galaxies out to 20 *Mpc*, and can study the age and metallicity of the stars through a combination of narrow and broadband filters. With LBT, about 100 luminous galaxies will be accessible to this type of study. At larger distances, the sensitivity and resolution of the LBT can be used to study the surface brightness fluctuations of marginally resolved stellar populations, which provide a powerful distance indicator (Tonry and Schneider, 1988). Because the maximum measurable distance scales as the square root of the size of the PSF, LN will allow distance determinations within a volume 1000 times larger than that currently accessible.
As an example, in Figure 4-10 a simulation of nearby galaxy NGC 4535 in the K band, artificially red shifted to $z = 1$, is shown. LN still resolves star cluster at $z = 1$, while this is not possible using HST or a diffraction limited 8 *m* telescope.

Supernova Cosmology

Our view of the overall shape and content of the universe has been radically altered in recent years by the results of moderate-redshift supernova cosmology research. The technique takes advantage of the fact that type Ia supernovae have an intrinsic luminosity predictable from their light curves. Therefore, measurements of the light curve and a spectroscopic redshift give the luminosity distance to a given redshift, a mapping which depends on Ω_{mass} and Ω_{Λ}. Unfortunately, at the moderate redshifts accessible to the current generation of telescopes, the observations constrain a combination of Ω_{mass} and Ω_{Λ}, not their individual values. Observations of SN Ia at z = 2.5 can break the cosmological parameter degeneracy, however, and LN on LBT has the sensitivity to detect and measure these objects. A key program consuming ~ 25 nights and taking advantage of the improved sensitivity and wide field of view, would be able to constrain Ω_{mass} uniquely to 5% accuracy.

4.4.2 The Ground layer Wavefront Sensor

It consists of two identical units, each placed on the optical path of the beam coming from the tertiary mirrors of LBT. As suggested by its name, the GWS is optically conjugated to the ground layer, in a way to sense the deformations introduced on the incoming wavefront by the atmospheric lower layer, namely about the first 100 *m*. The information retrieved by each GWS about the shape of the wavefront are converted into a correction signal and sent to the corresponding Adaptive Secondary Mirror (ASM) of the LBT with a 1 KHz frequency. Both of them are equipped with 672 actuators, which change the mirror shape to reproduce the opposite of the perturbations introduced by the lower atmosphere, in order to correct them. The light from the 2 – 6 *arcmin* FoV is folded by an annular mirror into the GWS. Here 12 optical devices, the Star Enlargers (SEs), can

be positioned using as many linear stages in a way to be able to pick up the light of a maximum of 12 NGSs. Each star enlarger focus the light of its NGS on the pin of a pyramid WFS, so that the beam is splitted in 4 beams. The light coming from a certain face of each of the 12 pyramids is optically superimposed, according to the layer-oriented technique and, since the WFS is conjugated to the ground layer, the pupils completely overlap. The pupil re-imaging is performed by a classical Schmidt-camera, called the Pupil Re-Imager (PR-I). The beams coming from the SEs are firstly reflected by a flat annular folding mirror and then focused by a parabolic mirror toward a 4-lenses objective, re-imaging the 4 pupils on the CCD. The detector is a CCD50 128 × 128 pixels, 24 μm pixel size, mounted on the rear of the Pupil Re-Imager, on a remotely controllable XYZ linear stage.

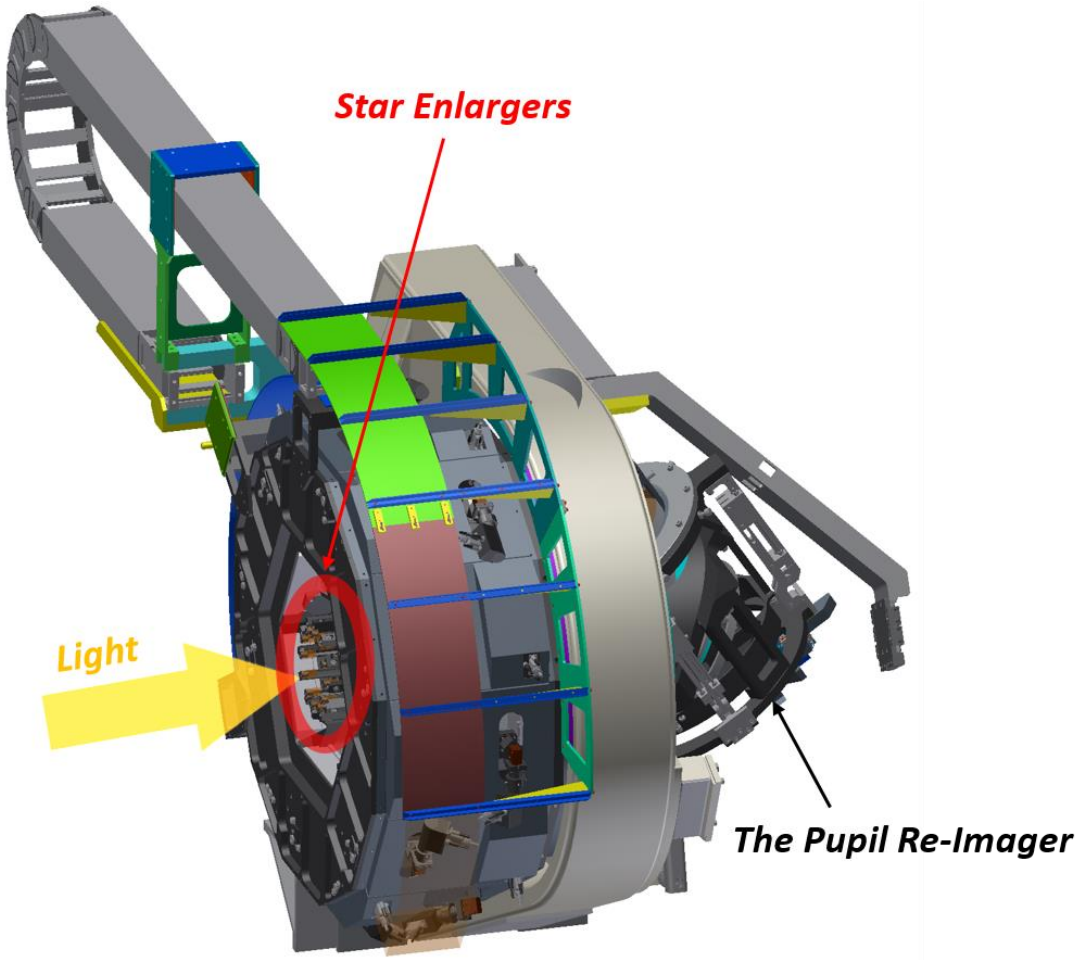

Figure 4-11: the GWS in a CAD drawing.

The whole unit is mounted on a rotation unit to follow the sky. Essentially, it is a big bearing with the purpose to mechanically rotate the whole GWS in order to compensate for the field rotation. This unit consists also of a mount, which fix the GWS to the bench. The GWS mount and rotation unit consists of a cylinder-like case, a bearing system and a support structure. The bearing is connected to the support structure that links the GWS to the bench on one side and to the cylinder on the other. A motor integrated with the

bearing, moving the whole cylinder-like case, allows following the circular path of the stars within the FoV.

As widely known, one of the main strengths of using the optical layer oriented approach is the optical co-addition of the light from the reference stars on the same detector, increasing the SNR of the system and permitting to use faint stars. This requires that the pupil super-imposition at the level of the detector must be kept as similar as possible to that occurring on sky at the detector conjugation quote. In our case, the conjugation quote is 100 *m*, where the pupils overlap is almost complete.

The achievement of a reasonably similar pupils super-imposition on the detector requires a great number of opto-mechanical constraints and tolerances, making the Alignment, Integration & Verification (AIV) of the system, described in the next Chapter, very challenging.

The Star Enlarges

Implementing the Layer Oriented technique poses some technical difficulties, due to the large size of the re-imaged pupils produced by the pyramids. This would require using very fast re-imaging optics and very large CCDs, not recommended in an AO system, where a very fast frame rate end low Read Out Noise (RON), generally characteristics of small CCD, are required.

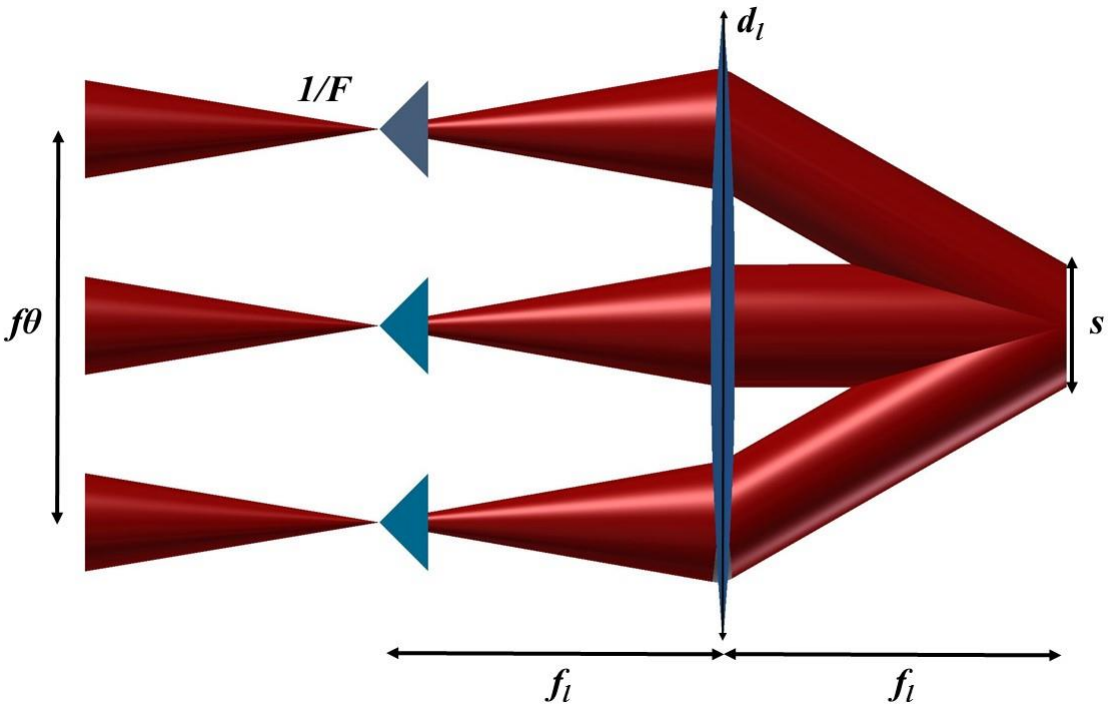

Figure 4-12: pupil dimension with the Layer-Oriented approach, without Star Enlargers. As a simplification, only one of the four beam refracted by the pyramid is shown.

Let's consider an optical system as shown in Figure 4-12, where the light coming from different NGSs hits the pin of different pyramids with a $F/\# = f/D$, where f and D are respectively the focal length of the telescope and its diameter (Ragazzoni et al., 2005). The minimum required diameter for the objective reconstructing the pupil image depends

upon the spot diameter in the pyramids focal plane, $f\theta$, where θ is the angular diameter of the FoV, and upon the beam divergence after the focal plane, according to the equation:

$$d_l = f\theta + \frac{f_l}{F}$$

Where f_l is the focal length of the objective. The re-imaged pupil diameter is given by:

$$s = \frac{f_l}{F} = \frac{d_l \times F_l}{F} \approx F_l \theta D$$

For the GWS, θ = 6 *arcmin*, D = 8.25 *m*, resulting in a pupil dimension of 14.4 *mm* x F_l, which would require a very big CCD, not suitable for AO applications, or unrealistically fast re-imaging optics. To reduce the re-imaged pupil size, the F/# on the pin of the pyramids has to be increased. This increasing of the F/#, however, will result also in an increasing of the FoV image diameter in the focal plane, resulting in the necessity to have very wide re-imaging optics, since $d_l \approx f\,\theta$ and $f = FD$. If $F_l = kF$, where F_l is the increased F/#, then $d_l^1 = kd_l$, where d_l ,d_l' is the required minimum re-imaging optics diameter. The solution implemented to solve this problem is the introduction of the so-called *Star Enlargers*. These are small optical systems that have to be placed in the FoV in correspondence of the NGSs used for the wavefront sensing. The Star Enlargers increase the F/# of the beams focusing on the pin of the pyramids, selecting only a small portion of the FoV. In this way the F/# of the whole FoV is linked to the telescope F/# but the NGSs focused images, which are linked to the new $F_l = kF$. The relative distances between the NGSs is unchanged, but their dimensions are increased, allowing to keep the re-imaging optics dimensions to a reasonable size.

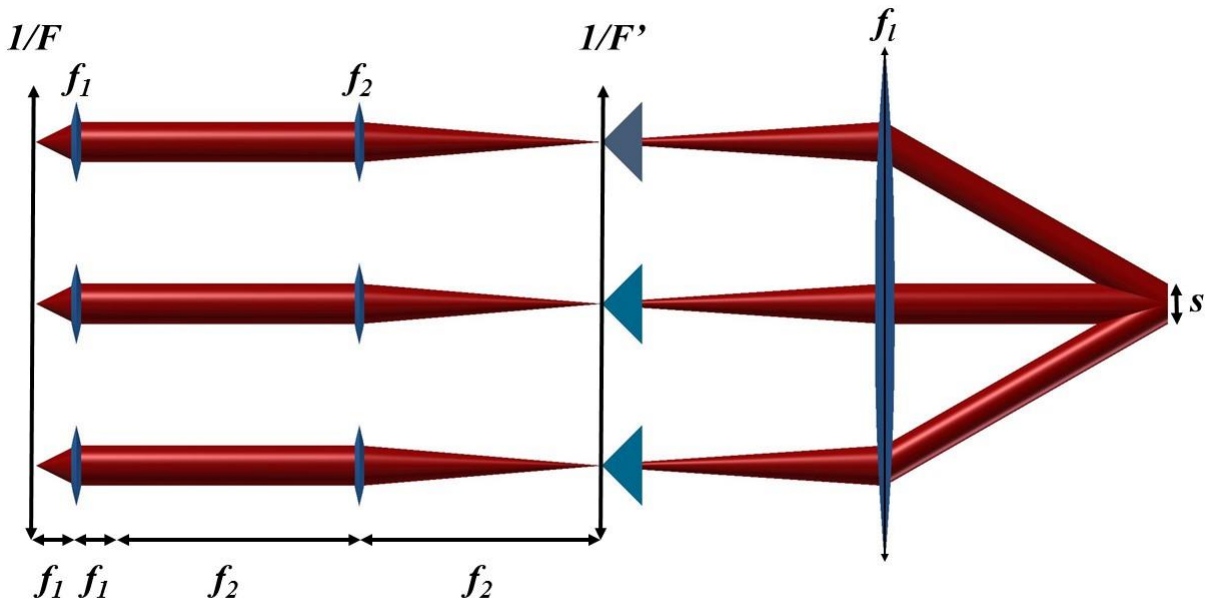

Figure 4-13: a schematic of the star enlarger. The incoming F beam gets enlarged to a F_l=kF beam on the tip of the pyramid by two achromatic doublets. An objective re-images and super-imposes the pupils from different star enlargers, with the size s= fl/F_l.

In the case of LN GWS Star Enlargers the F/15 beam coming from the LBT is collimated by an achromatic doublet with focal length $f_1 = 13\ mm$ and diameter $d_1 = 5\ mm$, producing a small pupil image. A second achromatic doublet, with focal length $f_2 = 162.5\ mm$ and diameter $d = 14.7\ mm$, is placed at distance $f_1 + f_2$ from the first lens. This system produces an output beam with a focal ratio $F = kF_1$ where the enlarging factor is $k=f_2 / f_1 = 12.5$, resulting in an F/187.5 beam focusing on the pin of the pyramid. Each pyramid is a 4 faces refracting prism, splitting the light in 4 beams to be analyzed according to the 4-quadrants concept, made in Schott BK7 glass with refraction index $n = 1.53$ and a vertex angle $\alpha = 1.1°$. The divergence angle of the 4 beams produced by each pyramid is given, for small angles, by:

$$\beta = \alpha \cdot (n - 1)$$

The resulting divergence angle for the GWSs pyramids is $\beta = 0.566°$. This value must be the same for all the pyramids with a strict tolerance (30 *arcsec*), to avoid that some pupils not perfectly super-impose to the ones produced by other SEs. This would lead to a degradation of the wavefront analysis and, consequently, to a degradation of the scientific images quality. This requirement has been satisfied as reported in Farinato et al. (2008).
Mechanically, a SE consists of an aluminum V-shaped support, which accommodates the small cylindrical lens mounts, realized in a way to minimize their obstruction in the field, to enable two SEs to be as close as the external diameters of the mounts of the bigger lens. The lenses of the star enlargers are mounted in small cylindrical aluminum mounts by using O-rings. A stopper with a rubber O-ring (to create friction with the mount) is inserted to block the lenses in place. These three mounts are inserted into three external mounts.

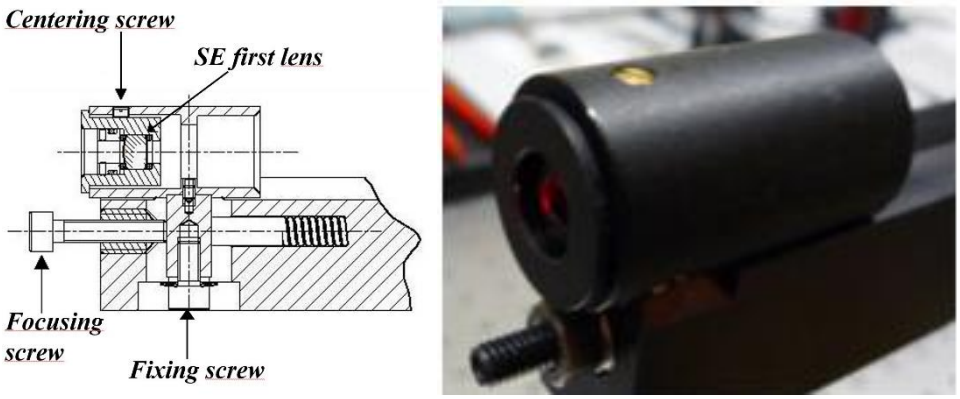

Figure 4-14: mount of the first SE lens. On the left the mechanical drawing of the mount. The lens can be focused using a preloaded screw, while three screws (only one is shown in this image) allows tip-tilt and centering tuning. On the right a picture of the mount.

Both the pyramid and the first and second doublets centering with respect to their external mount can be adjusted. In fact, the outer mounts of the first lens and of the pyramid are provided with three screws placed at 120° acting on the side of the elements to tune their centering. The pyramid is placed between two Teflon rings to reduce the friction, since,

in this case, the three centering screws act directly on the glass, while, in the first lens case, they act on the internal mount.

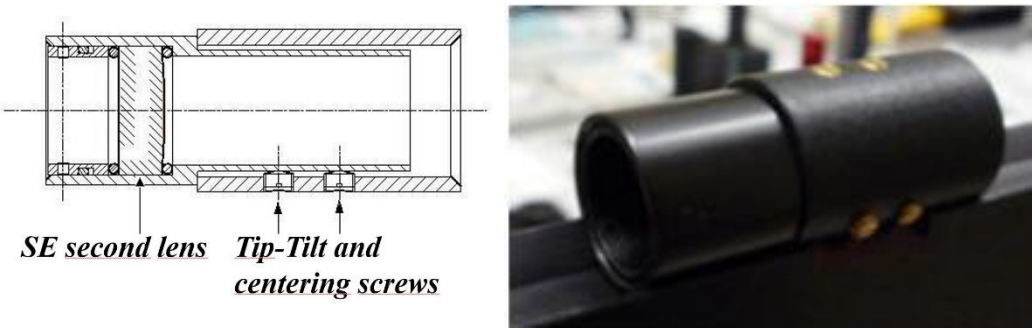

Figure 4-15: mount of the second SE lens. On the left the mechanical drawing of the mount. Tip-tilt and centering alignment is performed using three couples of screws (only one couple is shown here). On the right a picture of the mount.

The outer mount of the second lens is equipped with a double set of three screws (for a total of six) placed at 120° and acting on the side of the lens internal mount to tune its centering and tip-tilt. The second doublet external mount is fixed to the aluminum support with glue, while the first lens one and the pyramid one are connected to the Star Enlarger support and secured to it by a locking screw and they can be moved along the optical axis in order to focus the beam on the pin of the pyramid. The pyramids mount have the additional possibility to be rotated, in order to obtain the right orientation of the pyramids. In this case the internal mount is inserted with a small interference, just enough to keep it in position, in the external one. Since only this second part is connected to the aluminum support, it is possible to change the pyramid orientation even after fixing its position on the supports.

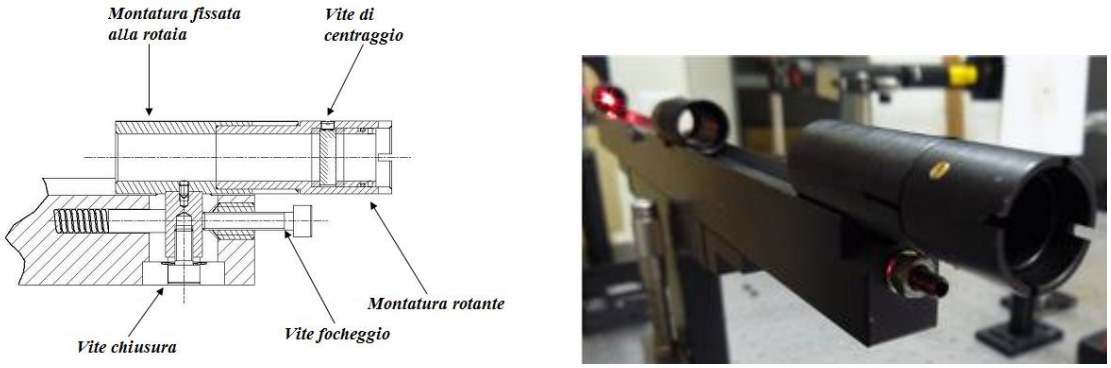

Figure 4-16: the pyramid mount. The pyramid can be focused using a preloaded screw and centered by means of three screws (only one screw shown here).

The aluminum bar holding the barrels is mounted on an aluminum T-shaped arm fixed by screws to a motorized stage (inside the GWS), that allows the movement in the field to search for a NGS. To avoid collisions that could happen during the movements of SEs, each of them has a mechanism to stop in case of emergency. This is based on a thin sheet of flexible copper that runs along the side of the T-arm of the SE. When the two SEs are on a collision course, the copper foils will touch before the physical contact between the

mechanical components, resulting in the immediate turn off the power to the motorized stages.

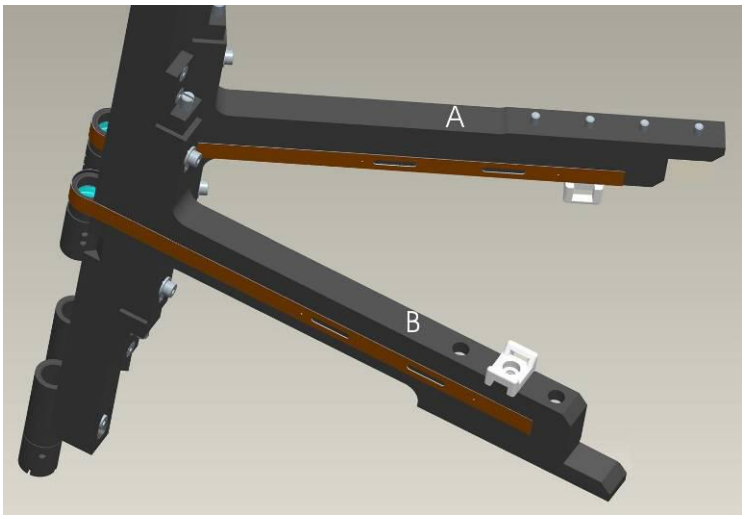

Figure 4-17: Anti-collision copper stripes.

The minimum separation between two stars in the sky is therefore limited by the diameter of the cylinder of the second lens, which is 16 *mm* plus 2 *mm* of air gap between the cylinder and the copper stripe. A diameter of 18 *mm* corresponds to an angular separation of 29.8 *arcsec* on sky, so two stars angularly closer than this value cannot be used simultaneously as references. The FoV of each SE is 0.96 *mm*, corresponding to 1.6 *arcsec* on sky.

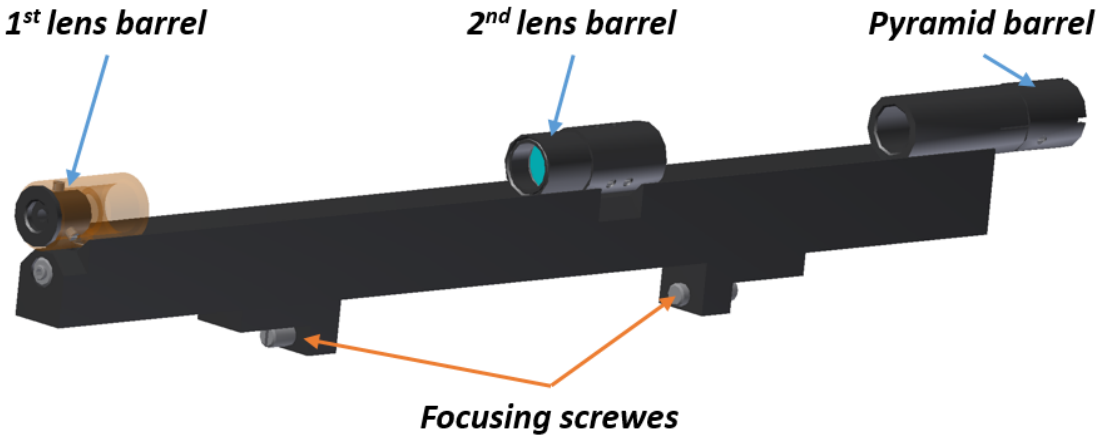

Figure 4-18: A Star Enlarger

The Pupil Re-Imager

The goal of the PR-I is to reimage and superimpose the 4 pupils generated by each star enlarger on the detector. It consists of a flat annular mirror, which reflects the beams towards a parabolic mirror with a focal ratio of F/1.25. This converges the beam towards a system of 4 achromatic doublets, custom made, located in the central hole of the mirror, resulting in a Schmidt-like camera. The beam is finally captured by the CCD on which

the images of the pupils will be formed. The Pupil Re-Imager has an aperture of 245 *mm* and a focal length of 220 *mm*, so its focal ratio is about F/0.9.
The mirrors are glued on the supports with different degrees of freedom for the alignment. The mechanical structure of the PR-I is designed to allow the optics in the right relative positions and that it can be fixed to the bearing.
The flat mirror is glued to 3 INVAR pads (the alloy INVAR is known for its low coefficient of thermal expansion) placed inside its frame, arranged in a fashion to avoid stress on the mirror resulting from temperature changes that might dilate the frame.
This mirror does not need any centering alignment, but only tip-tilt, and this is done using 3 screws separated by 120°, allowing to tilt the whole mount of the mirror with respect to the main PR-I structure.

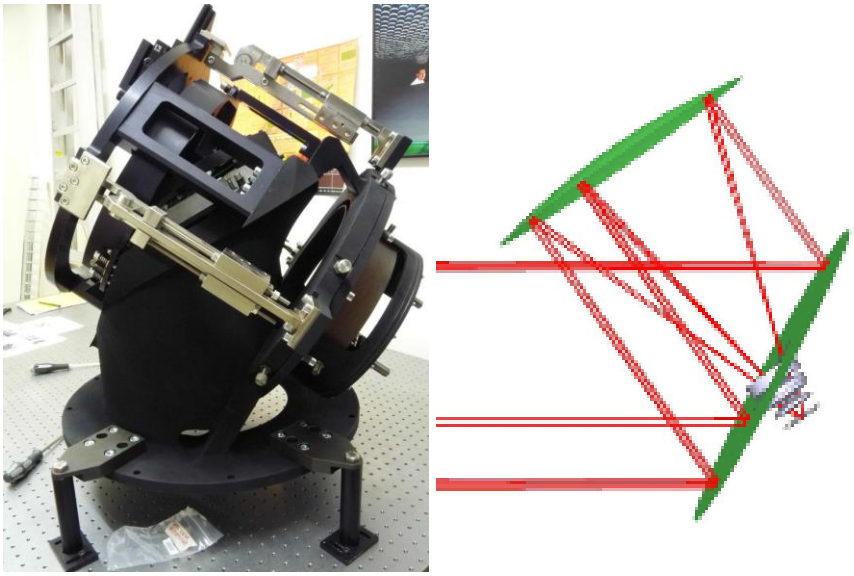

Figure 4-19: On the left the assembled PR-I, on the right its optical layout.

On the contrary, the parabolic mirror mount is equipped with centering capabilities, while the tolerance for the alignment in tilt is wide, ± 0.47°, and therefore there is no need for a dedicated tilt tuning system. The centering of the parabolic mirror is done using three screws, displaced of 120° on the mirror mount, acting on the mount itself and allowing the shift of the mirror on a plane perpendicular to the optical axis.
The optics of the corrector are enclosed in an aluminum cylinder located in the central hole of the flat mirror with a tolerance of ±1 *mm*. This cylinder is fixed to a support flange that has a mechanism to change the tip-tilt similar to that of the flat mirror.
Finally, the F/0.9 beam produced by the PR-I is collected on 128 x 128 pixels CCD50, 24 μm pixel size. The mechanical structure of the CCD consists of a flange, kept at the proper distance and orientation with respect to the optics of the PR-I using three spacers. The CCD is mounted on a system of motorized stages that allow remote controlled movements for centering and focusing operations. To reduce the action of push-ups on the structure of the CCD due to gravity action at different angles relative to the ground, 3 astatic levers are installed.

The mechanical structure

The optical components described above are integrated into a mechanical structure consisting of three main components:

- A cylindrical structure supporting the Star Enlargers
- A bearing which allows the system to rotate
- A support structure of carbon fiber which allows to fix the GWS to the optical bench

The mechanical structure has many purposes, they can be summarized as:

- Secure the GWS to the optical bench
- De-rotate the field of the telescope
- Provide a rigid support structure for the Star Enlargers and the Pupil Re-Imager, minimize the flexures

Given the physical size of the motorized stages, in order to obtain a compact structure for the support system of the SEs, it is constituted by two annular flanges interconnected one in front of the other. One each flange are mounted 6 linear stages to move the SEs. The entire structure is designed to minimize the bending due to the rotation and inclination of the instrument, and its dimension is driven by the physical dimension of the F/15 focal plane in front of the GWS entrance (217 *mm*). The entire structure is covered by casing to protect the optics from dust and scattered light.

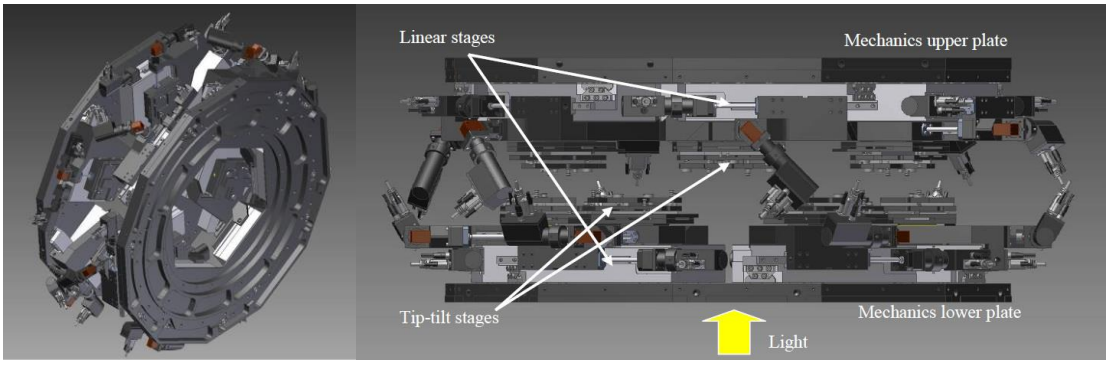

Figure 4-20: the Star Enlargers support structure.

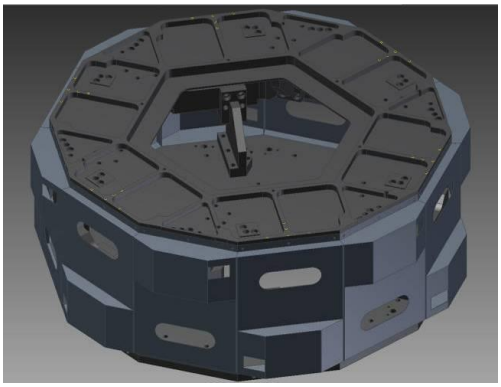

Figure 4-21: the Star Enlargers support structure covered by casing.

Between the linear stage and the star enlarger T-arm there is a mechanical interface that allows the fine-tuning of the SE tip-tilt. This tip-tilt stage, produced and tested in Heidelberg, consists of three aluminum plates bond by copper-beryllium foils. Two adjusting screws, counter-balanced by two preloaded screws, allow a completely de-coupled fine-tuning of the tip-tilt of the SE.

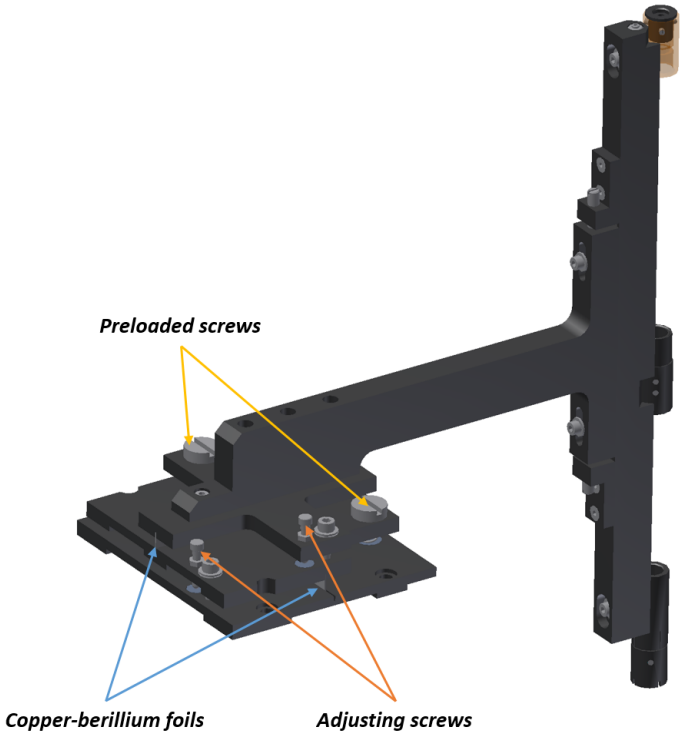

Figure 4-22: The SE tip-tilt interface stage.

To prevent the images of the pupils produced on the detector getting contaminated by scattered light, highly elastic cloth are fixed to the SEs T-arms, to mask as much as possible the background light not passing through any of the SEs.

Figure 4-23: the elastic cloth that will mask the background light not passing through the SEs, preventing pupils' contamination.

The support structure of the SEs is fixed to a side of the bearing, interfaced by an adapter ring, thereby enabling it to rotate 60°, while through the opposite side the PR-I is inserted and fixed after internal alignment. Finally the bearing is placed inside the support structure which allows to fix the entire system to the optical bench, in an orthogonal position with respect to the F/15 beam coming from the telescope and very close to the focal plane. The structure has been designed and implemented to minimize the flexures during rotation and tilt of the instrument.

Figure 4-24: The bearing allowing the rotation of the GWS.

A cable chain allows to fix large the number of cables (a power cable and signal cable for each of the 24 motors and other 2 cables from the collision control stripes from each SE, for a total of 72 cables) necessary for correct system operations.

4.4.3 The High layer Wavefront Sensor

Since the HWSs will sense the turbulence introduced by a layer at high altitude, recalling Section 3.4.3, the reference stars used by these sensors are in a smaller FoV around the scientific target than the one of the GWS, namely in the central 2' FoV.
Like the GWS, also the HWS is a multi-pyramids WFS that uses up to 8 reference stars, acquired by 8 Star-Enlargers, and working in layer oriented mode.
Obviously for the HWS the overlap of the pupils produced by the SEs on the CCD is not complete, as for the GWS, but only partial and equal to the one occurring in the atmosphere at the HWS conjugation height.
Each HWS drives a deformable mirror equipped with 349 actuators, internal to the LINC-NIRVANA bench, conjugated to the same height.

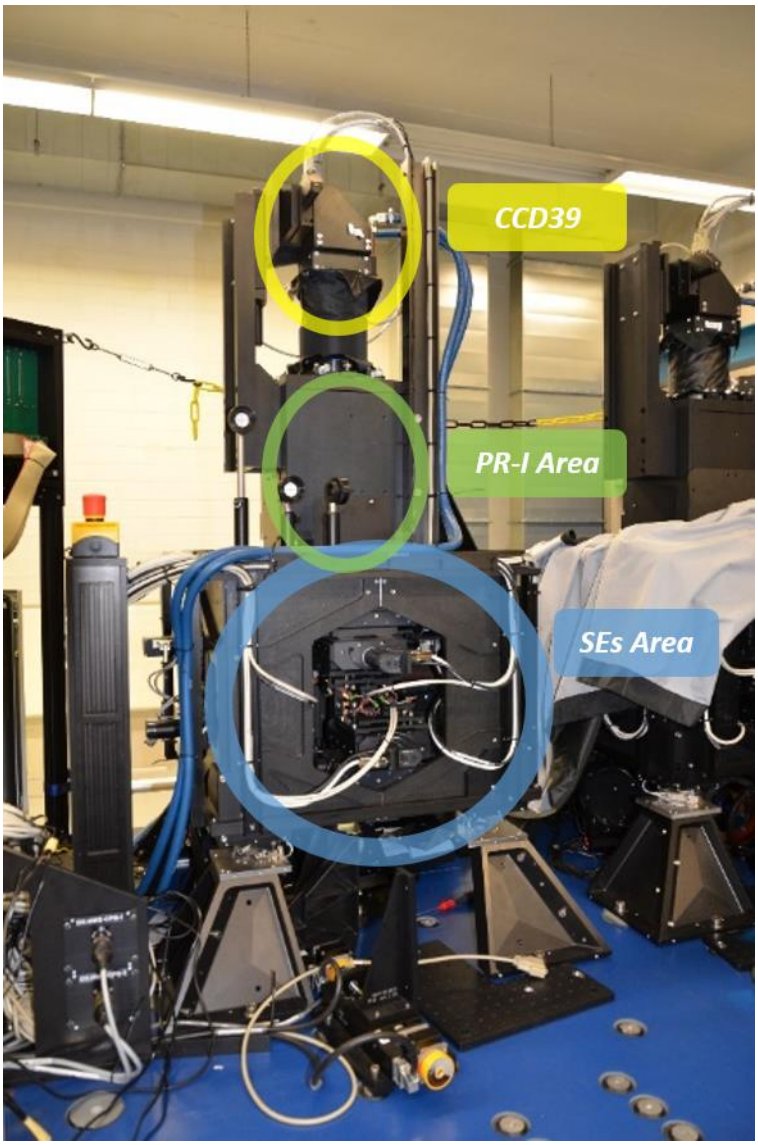

Figure 4-25: the HWS. The PR-I is enclosed in the HWS mechanical structure, to avoid background light

The incoming beam is an F/20, flat and telecentric, and is derotated by a dedicated system (K-mirror) before reaching the HWS. To position the reference stars on the SE with a precision better than 0.1 *arcsec* a Patrol Camera, looking at the same field of the HWS thanks to a beam splitter that can be inserted in the optical train, assists the acquisition.

Similarly to the GWS the light from the reference stars pass through the SEs and a pupil re-imager, constituted of a 7 lenses objective with 112 *mm* aperture and 99 *mm* focal length, resulting in a very fast F/0.88 optics, which re-creates the images of the pupil on a 80 x 80 pixels, 24μm pixelsize, CCD39.
As for the GWS, also for the HWS the problem of the pupils size on the detector arises, and again the problem is solved using the SEs to increase the F/# of the beam hitting the pin of the pyramid. The upper limit to the size of the pupils is driven by the necessity to fit the images of the 4 metapupils in the detector. Since the detector is an 80 x 80 pixels CCD, this translates into a maximum diameter of each metapupil of 38 pixels, leaving a margin of 1 pixel between the metapupils and 1 pixel between the metapupil and the edge of the CCD. This means that the maximum diameter for the pupils produced by each SE is 18 pixels. Since the incoming beam is an F/20, recalling [4-3], an $f/k \approx 8.8$ is required, with f the focal length of the PR-I and k the magnification factor. There are many possible combination of f/k meeting this requirement, however it is preferred to maintain k as low as possible to minimize the physical dimension of the SE, since this imposes a limit on the minimum distance of two reference stars in the sky. On the other hand, a very small k value would require a very small f, with a consequent degradation in the quality of the images produced on the detector.
As a trade-off a $k = 11.25$ has been chosen, which produces an output beam F/225. The mechanical structure of the HWS's SEs is almost identical to the one of the GWS's SEs.
The minimum separation between two reference stars in the sky is then limited by the diameter of the second lens barrel, which is 16 *mm*, plus 1 *mm* of air gap between the barrel and the anti-collision copper stripe. This diameter corresponds to an angular separation of 21 *arcsec* in the sky, so two stars angularly closer than this cannot be used at the same time since the SEs would collide. The SE FoV is 0.88 *mm* in the focal plane, corresponding to 1.1 *arcsec* in the sky. As for the GWS, each SE is mounted on a motorized linear stage, interfaced by a tip-tilt mount for SE fine alignment, to allow SEs positioning.

4.4.4 The Warm Optics

With the name of "warm" optics, so called to distinguish them from the "cold" optics in the cryostat delivering the IR light to the scientific camera, we refer to all the groups of lenses and mirrors, internal to the LINC-NIRVANA bench, the light is passing through before reaching the WFSs.
These optics are grouped in several units with different scopes. They can be summarized as:

- Annular mirror, reflecting the outer 2 – 6 *arcmin* FoV into the GWS. The central 2 *arcmin* FoV passes through a hole in the center of the mirror. This mirror is motorized for tip-tilt and focus adjustment.

- Lenses of the collimator: the collimator optics consists of two-lens group; both must be adjustable in the direction of the optical axis during operation in order to

compensate thermal effects. Manual static alignment is required for centering and tip-tilt adjustment.

- Z configuration mirrors: it is constituted of two mirrors; one of them is the deformable mirror, positioned in a Z configuration, to ensure a compact layout. These mirrors are motorized for tip-tilt adjustment.

- Dichroic mirror: the dichroic mirror splits the light to the WFS (visible light) and to the science channel (IR light). In order to align the optical axis to the FP20 optics a motorized static alignment is possible for tip-tilt.

- K-mirror: the K-mirror is the optical de-rotator for the HWS. It consists of three flat mirrors mounted together in a stiff and stable structure that allows rotation of the assembly around the optical axis of the FP20 camera. This unit lies between the first and second lens group of the FP20 camera and can be adjusted in centering and tip-tilt.

- Lenses of the FP20 camera: the FP20 consists of three lens groups and one filter. Two of the lenses are adjustable in the optical axis direction during operation to compensate thermal effects. Manual static alignment of all components is possible for both centering and tip-tilt.

- Pupil Mask: the pupil mask for the FP20 optics is required for the operation and alignment of the HWS.

Figure 4-26: the light path inside the LINC-NIRVANA bench.

Although located in the warm part of the instrument, the piston mirrors to correct for the OPDs are considered part of the scientific channel and not of the “warm” optics.

5 AIV of the Ground layer Wavefront Sensor

During my Ph.D. I actively contributed to all the phases of Assembly, Integration & Verification of one of the GWSs (GWS SX; in the meantime the GWS DX was at LBT for a Pathfinder Experiment, described in Chapter 6), from the internal alignment of its subsystems to their integration and alignment to the mechanical axis of the bearing, making sure that all the strict tolerances required to ensure the correct operation of the WFS were met.

The large number of opto-mechanical elements (12 star enlargers, each with 3 optical components, moving in a wide annular FoV and sending the light to a common pupil re-imager, which compose the GWS) and consequently the large number of errors potentially introduced, together with the request to obtain a really good pupils super-impositions onto detector, translates into a great number of requirements and tolerances to be met in order to not excessively decrease the performance of the system. The rotation of the entire WFS to compensate for the sky movement, moreover, introduces a further difficulty in ensuring the required pupil superposition stability.

We will examine here what are the main error sources, their effect as blur on the four re-imaged pupils and the related requirement. A blur on the pupil translates into relative

shifts of the sub-apertures in which the pupils are divided, which causes, when superposing the light of several pupils coming from different SEs, a "cross-talk" between adjacent sub-apertures, i.e. in a certain sub-aperture there will be some undesired light coming from the adjacent ones. Of course, this shift should be much smaller than the sub-aperture size in order to minimize the undesired cross talk.
To better understand what could be the performance of an instrument, at the beginning of each project an Error Budget is devised, i.e. an essential tool for evaluating and tracking various factors in a project that may degrade performances. Initially the Error Budget includes only estimations deriving from previous studies of the mechanical and optical design, simulations, experience with previous similar instruments or FEM (Finite Element Method) analysis, but no terms from real data. The Error Budget is then used to evaluate what would be the theoretical performance of the instrument with given requirements and tolerances. Of course, the tighter the tolerances and the more difficult and higher cost will be faced to complete the instrument. For example, it may happen that some well-specified requirements are not met for lack of technology, construction errors or other causes, and this lead to a degradation of performances. Therefore, the Error Budget is a continuously evolving document, where estimations are replaced by real data when available.
In the GWS case, we are interested in how errors in alignment and manufacturing of subsystems infer the performance of the whole GWS.
The sub-apertures considered in the GWS Error Budget presented here have a dimension of 48 μm, and correspond to the maximum sampling of the pupil (24 × 24 sub-apertures). This sampling has been chosen to match an average seeing condition of ~ 0.7 *arcsec*, which normally gives an $r_0 \sim 35$ *cm* in J band.
As said before the alignment and test results presented in this Chapter refer to the GWS SX, with the only exception of the flexures test, described in Section 5.5.4, performed only on GWS DX and here considered representative of the behaviour of GWS SX.

5.1 The GWS Error Budget

- SE diffraction: it is due to the SE optical design, and it is estimated with Zemax computation as a 7 μm blur on the pupil.

- Pyramid chromatism: the pyramids are dispersive elements, and they are working with polychromatic light. The chromatism so introduced is estimated with Zemax computations, resulting in a pupil blur of 6 μm.

- Pyramid vertex angle: the real constraint here is on the repeatability of the pyramid vertex angle of the twelve SEs. The requirement is a ± 17 *arcsec* repeatability, which leads to a blur on the pupil of 5 μm, and a more relaxed ± 58 *arcsec* absolute error.

- Pyramid faces orthogonality: pyramid faces orthogonality requirement asked to the providing company (± 5 *arcmin*) can be translated into a maximum pupil blur of 5 μm. However, the providing company test certificate reports a pyramid face orthogonality better than 50'' for all the delivered pyramids, translating into a pupil blur lower than 1 μm.

- Linear stages wobble: The effect on the detector plane of both pitch and roll of the linear stage, which moves a SE, is a shift of the 4 pupils generated by the pyramid held by that star enlarger. A typical specification is that the maximum shift is of the order of 1/10 of the dimension of the sub-aperture itself, meaning a 25 μrad requirement for the linear stages pitch and roll. The real values measured on the SE positioning stages delivered by the providing company, translate in a SE 10 *arcsec* Peak-to-Valley global tilt, assumed 5 *arcsec* RMS (25 μrad). These values are documented in test reports, provided by the providing company itself. This wobble translates into a pupil blur of about 5 μm.

- Enlarging factor *k*: the real requirement is the repeatability of *k* value, because SEs with different *k* produce pupils of different sizes. Reminding that the chosen value for the GWS SEs is *k* = 12.50, the specification is a repeatability of *k* better than 1/240, which leads to a pupil, blur of 5 μm.

- SE relative tilt: as discussed for the linear stages wobble, the effect of a tilt of a SE with respect to the PR-I optical axis is a shift of the 4 pupils generated by the pyramid. In fact a tilt of a SE by an angle α translates in an exit beam divergence angle:

$$\beta = \alpha \cdot \left(1 + \frac{1}{k}\right) \qquad [5\text{-}1]$$

  And a consequent pupil shift of:

$$\Delta s = \beta \cdot f_l = \alpha \cdot (k + 1) \cdot F \cdot s \qquad [5\text{-}2]$$

  With *s* pupil dimension and *F* the input beam focal ratio. The requirement is a maximum relative SE tilt of 5 *arcsec*, which translates in a pupil blur of 5 μm.

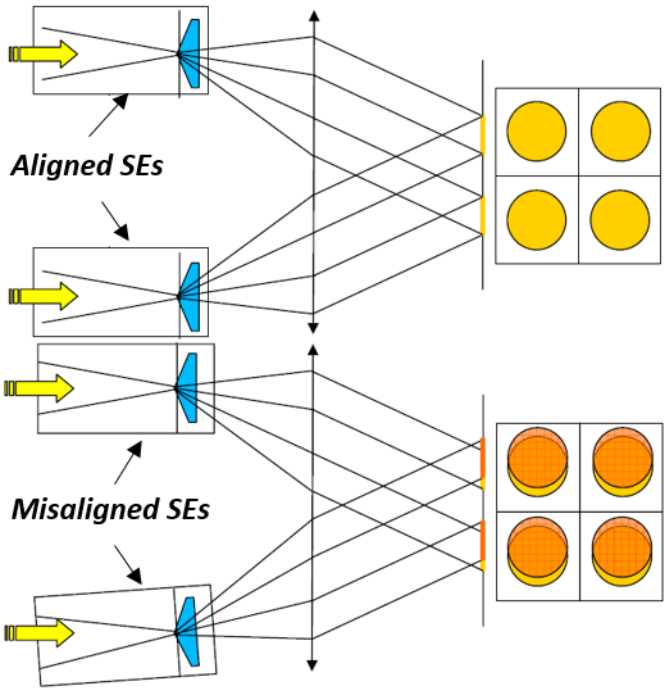

Figure 5-1: Effects on the pupil of a differential tip-tilt between SEs.

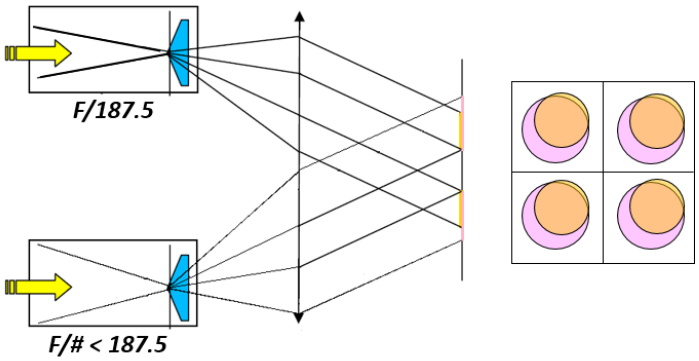

Figure 5-2: Effects on the pupils of two SEs with different magnification factor k. A SE with a smaller k will produce larger pupils.

- Pyramid orientation: a different orientation of one pyramid with respect to the others leads to an incorrect super-position. The tolerance for the pyramids differential orientation is 10 *arcmin*. This leads to a linear shift of the pupils edges that are 1.68 *mm* far from the center of rotation of 1/10 of sub-aperture and a consequent pupil blur of 5 μm.

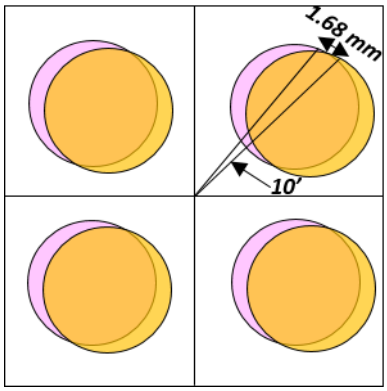

Figure 5-3: Effects of a different pyramids orientation.

- Pupil Re-Imager optical quality: PR-I optical quality in terms of blur onto the pupil image can be directly verified on the PR-I itself once it is aligned, considering it as a stand-alone camera and measuring the RMS spot radius of the spots in its FoV (± 0.44°). Laboratory measurements, obtained feeding the PRI with a wide collimated beam, gave a maximum Root Mean Square (RMS) spot radius in the edges of the FoV lower than 13 μm.

- Thermal effects: LN is required to work in a temperature range from -15°C to +20°C. We can consider negligible the influence of temperature variations in this range on the SE lenses alignment and on the wobble of the linear stages, while the PR-I optical quality degrades for a variation of less than 5°C, resulting in a pupil blur of 7 μm.

- SEs focal plane: the LBT focal plane is spherical, in a way that there is a huge difference in the focal plane position along the optical axis, depending upon the distance from the center of the field. Because the pyramids will be used in non-modulated fashion, must be careful that the "equivalent seeing" on the pin of the pyramid exceed the enlargement of the spot due to the defocus term. Otherwise, the defocus term saturates the pyramid WFS and cause the impossibility to retrieve higher order aberrations. As the GLAO correction leads to a gain in terms of equivalent seeing by a factor two, the above-mentioned condition translates into the one that half of the seeing must exceed the size of the defocused spot, in angular terms. A Δz SE displacement with respect to the LBT F/15 focal plane leads to an angular spot enlargement by:

$$\vartheta'' = \frac{206265'' \cdot \Delta z}{D \cdot F^2} \qquad [5\text{-}3]$$

Using *mm* as unit of measure, we get $\vartheta'' = 0.11\Delta z$. The actual PtV of the curved focal plane in the GWS onboard LINC-NIRVANA is 4.94 *mm*, translating into the condition that the seeing should be worse than 0.55 *arcsec*. Statistics offered

by the Large Binocular Cameras at LBT show that the median image quality is of the order of 1*arcsec*. So the fraction of observing time in which a potential lack of dynamic range could occur coincides with the one of "very good" seeing.
As a solution has been decided to split the SEs into two groups, odd SEs and even Ses. The first group spans the 1 – 2.2 *arcmin* radius area while the second one the 2.2 – 3 *arcmin* radius area, in a way that the two regions have equal areas. For each SEs group has been identified an offset to which align it in a way to both divide their regions into two equivalent areas and to have a similar residual defocus WFE at the edges. The odd SEs are aligned and focused to a radius of 1.71 *arcmin* and their offset is 1.93 *mm* from the 0° FoV focus, while the even SEs are aligned to a radius of 2.63 *arcmin*, with an offset of 4.5 *mm*. The residual maximum defocus for both groups with respect to the LBT focal surface is 1.37 *mm*, so the seeing should be better of 0.15 *arcsec* to become an issue, that is to say a rather unlikely case. Anyhow, the effect of even a huge defocus is negligible in terms of pupil blur on the detector and only results in a defocus signal detected by the WFS, which can be subtracted as a static aberration, during the calibration procedures.

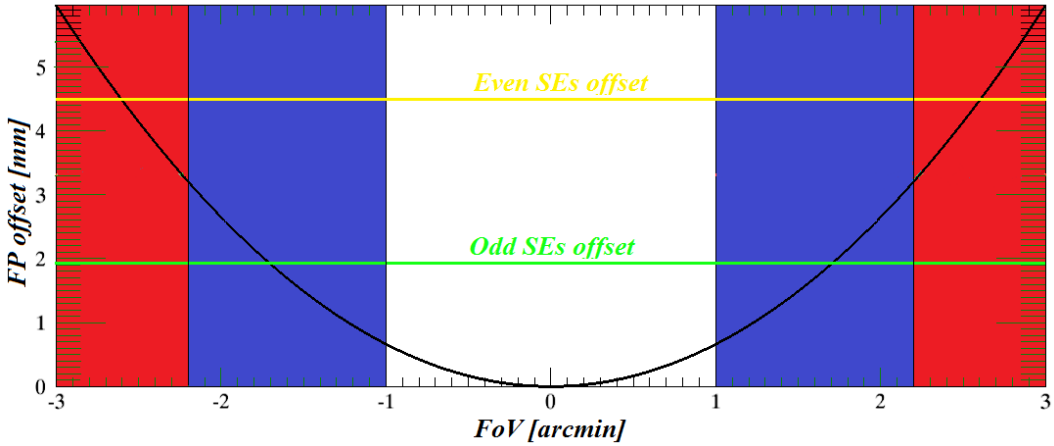

Figure 5-4: Curvature of the LBT focal plane for a 6 arcmin FoV. The coloured areas highlight 2 – 6 arcmin annular FoV that is re-imaged at the GWS entrance focal plane. The blue area is the FoV covered by the odd-SEs, focused on an offset represented by the green line. The red area is the FoV covered by the even-SEs, focused on an offset represented by the yellow line. The two offsets are been chosen in order to minimize the residual defocus WFE on their respective regions.

- Bearing wobble: the bearing wobble is the precession of the rotational axis of the bearing around the mechanical axis. It produces a global tilt of the entire GWS and a consequent pupil shift, according to:

$$\Delta s = \alpha \cdot \frac{f_{PR-I}}{k_{SE}} \qquad [5\text{-}4]$$

Varying with time and so resulting in an additional pupil blur. The measured bearing wobble is lower than 12 *arcsec*, producing a pupil shift of about 1 μm.

- GWS tilt: a tilt of the entire GWS with respect to the optical axis of the incoming F/15 beam results in a displacement of the pupils produced be each SE, according

to [5-3]. This means that a 1 *arcmin* tilt leads to a pupils' translation of about 5 μm. However, this has negligible effect on pupil blur since all the pupils move of the same amount and in the same direction. They can be re-centered in their nominal position just moving the CCD.

- GWS decenter: a rigid translation of the entire GWS with respect to its nominal position on LINC-NIRVANA bench does not cause a significant effect in terms of pupil blur. However, if the rotation axis of the bearing and the optical axis of the incoming F/15 beam are not coincident, a SE initially perfectly centered on its reference star, during the rotation will follow a slightly different trajectory from the one of the reference star, resulting in a tilt signal when analysing the wavefront. Considering a conservative exposure time of 10 minutes at the maximum de-rotation speed of the bearing (8.4 *rad*/*hr*) the maximum separation of the SE from its correct position is $\Delta x_{max} \approx 1.28\Delta x$, where Δx is the separation between the rotation axis and the F/15 optical axis. Considering a re-centering of the SEs every minute, this effect is reduced by a factor of 10 and the maximum not corrected displacement becomes $\Delta x_{max} \approx 0.14\Delta x$. The tolerance identified for Δx is 100 μm, leading to a maximum SE displacement of 14 μm.

Speaking about flexures, the only misalignment induced by them which translates into an actual pupil blur is a differential tilt of the SEs, which cannot be really estimated from the FEM analysis and whose contribution has been quantified at the Max Planck Institute fur Astronomie in Heidelberg, where the GWS was installed on the final LN bench, mounted on a tilt platform allowing the direct measurement of such an effect.

- GWS flexures: this contribution has been measured in Heidelberg during the flexures test, as described in Section 5.5.4, and its contribution to the pupil blur, for an inclination of the LN bench of 60° is 24 μm.

- Bearing flexures: bearing flexures have been analysed with a FEA (Finite Elements Analysis) by the bearing providing company at different inclination angles (0°, 25°, 35° and 60°). The results of the FEA are expressed as the differential movement of one node, positioned in the GWS center of gravity. The typical differential shift of this node during an exposure is 15.5 μm, corresponding to a differential tilt, estimated considering the distance between the node and the closest constraint in which the bearing in fixed to the bench (872 *mm*), of 3.7 *arcsec*. The SE fixed at the maximum distance from the constraint (~1170 *mm*) experiences a tilt of 4.9 *arcsec*, while the SE closest to the constraint (~400 *mm*) experiences a tilt of 1.7 *arcsec*. The maximum differential tilt between SEs is then 3.2 *arcsec*, whose effect on the pupils is a blur of 3.2 μm.

- SE tilt due to support flexures: SE support flexures cause 40 μrad tilt for 90° rotation. Maximum rotation angle during observation is 60°and the SE tilt

becomes approximately 2/3 of 40 *μrad*, translating into a 6 *μm* blur at the level of the pupil.

- SE tilt due to ring flexures: 6 SEs experience no tilt due to ring flexures, while the other 6 have a 60 *μrad* tilt in a common direction. Differential effect is 30 *μrad*. At 60° rotation, the estimated tilt is approximately 20 *μrad*, corresponding to a 4 *μm* blur onto the pupil.

- SE tilt due to stage flexures: the flexures of the coupled linear and tip-tilt stages for different orientations with respect to the gravity vector have been measured by the MPIA team in Heidelberg. The highest differential tilt, retrieved for different orientations of the tip-tilt and the linear stage with respect to the inclination axis, is 24 *arcsec* for a complete 60° range of inclination. This reduces to about 4 *arcsec* of tilt if the maximum differential inclination that the system can experience during one exposure is considered. The effect of such a differential tilt of the SEs, during an exposure, translates into a pupil blur of 4 *μm*.

Summarizing, the sum of all the contributions previously described contributes to decrease the wavefront correction efficiency of the GWS. In fact a blur on the pupil corresponds to a residual error on the wavefront (Wavefront Error, WFE), according to the relation shown in Figure 5-5, which has been computed by an end-to-end simulation (seeing FWHM = 0.7 *arcsec* in R band, turbulence equally divided between ground and high altitude layer).

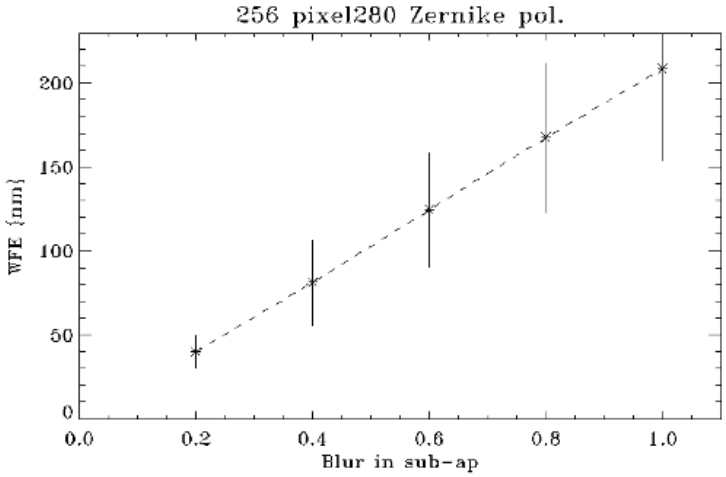

Figure 5-5: Relation between blur in sub-apertures (1 sub-aperture = 48 μm) and WFE.

All the contributions converted in WFE are used to determine the total Strehl Ratio of the GWS, using the Marechal's law:

$$SR(\lambda) = e^{-\left(\frac{2\pi \cdot WFE}{\lambda}\right)^2} \qquad [5\text{-}5]$$

Obviously, to the SR degradation contribute only the terms introducing a blur onto the pupils, while all the other terms, not inferring the resolution of the pupils, introduce low order signals (tip, tilt, and defocus) onto the WFS.

Error Source	**Test ref.**	**Blur [*μm*]**	**WFE [*nm*]**
SE diffraction	C	7	30
Linear stages wobble	B	5	22
Pyramid chromatism	C	6	26
Pyramid vertex angle	A	5	22
Pyramid face orthogonality	A	1	4
SE enlarging factor *k*		5	22
SE relative tilt	A	5	22
Pyramid orientation	A	5	22
PR-I optical quality	B (A) (C)	13	57
PR-I optical quality (thermal)		7	31
GWS global defocus		N/A	N/A
GWS global tilt		N/A	N/A
GWS global de-center		N/A	N/A
Bearing wobble		1	4
GWS flexures	D	24	106
Bearing flexures	D	3.2	14
SE tilt due to support flexures	A (B) D	6	26
SE tilt due to ring flexures	A (B) D	4	17
SE tilt due to stage flexures	A (B) D	2	17
Total WFE		**33**	**144**

Table 5-1: The GWS Error Budget. The total WFE is the square sum of all the contributions. The A, B, C, D letters identify the verification test, or tests, in which the error sources have been measured. These tests are described in detail in Section 5.5.

These signals can be either calibrated and subtracted or simply neglected, making sure, however, that they do not exceed the linearity range of the WFS.
When possible, these error sources have been measured with several tests to verify that their contribution is within the expectances from the Error Budget. The number of

subsystems constituting the GWS and the number of possible blur sources makes basically impossible to test each contribution singularly, so we identified 4 tests in which we measured the combined contribution of several blur sources, verifying that their sum were within the Error Budget. In Table 5-1 the error sources are associated with a letter identifying the test, described in detail in Section 5.5, in which these terms are measured. When into parenthesis, the contribution of that term has been considered, but has negligible value in the test. Items without any letter have been tested in a different way (SE k factor) or simply have no effect on the pupil blur. The goal for the GWS overall performance is to obtain a minimum SR of 0.61 in J band and 0.85 in K band; the final results for the GWS SX are listed in Table 5-11.

5.2 The Star Enlarger internal alignment

As described in Section 4.4.2, the Star Enlarger is an optical system used to enlarge the dimension of the reference star image on the pin of the pyramid, in order to ensure a large linearity range of the WFS, keeping a reasonable pupil image diameter. Each SE consists of 2 lenses (SE1, f = 13 *mm* and SE2, f = 162.5 *mm*) and a refractive pyramid, mounted on three different mounts, all aligned on a common mechanical support. This sub-section describes the internal alignment procedure of the 12 SEs of the second GWS (namely GWS "SX" of LINC-NIRVANA, SX because is the GWS placed on the left part of LINC-NIRVANA bench, looking from the HWSs position).
The tolerances for the SEs internal alignment have been obtained from Zemax Montecarlo simulations, in order to keep the SE performance inside the requirements described in Section 5.1 in terms of SE diffraction, introduced aberrations and enlarging factor k repeatability. The main SE alignment tolerances are reported in

	Tolerance
Distance lens 2 - pyramid	± 21 *mm*
Distance lens 1 – lens 2	± 0.1 *mm*
Relative centering lens 1 – lens 2	± 0.1 *mm*

Table 5-2: SE alignment tolerances.

The SE alignment setup components consists of the following items:

- A laser on a tip-tilt mount
- An interferometer producing highly collimated beam
- A CCD camera (5.2 μm pixel size)
- 2 folding mirrors
- An iris
- A perforated plate with two holes (separation 3.72 *mm*) on a repositionable holder

- 1 repositionable lens with f_1 = 76.2 *mm* (hereafter called L1) on a XYZ stage
- 1 repositionable lens with f_1 = 480 *mm* (hereafter called L2) on a XYZ stage
- 1 repositionable lens with f_1 = 200 *mm* (hereafter called L3) on a XYZ stage
- SE holder on a XYZ-tip-tilt stage

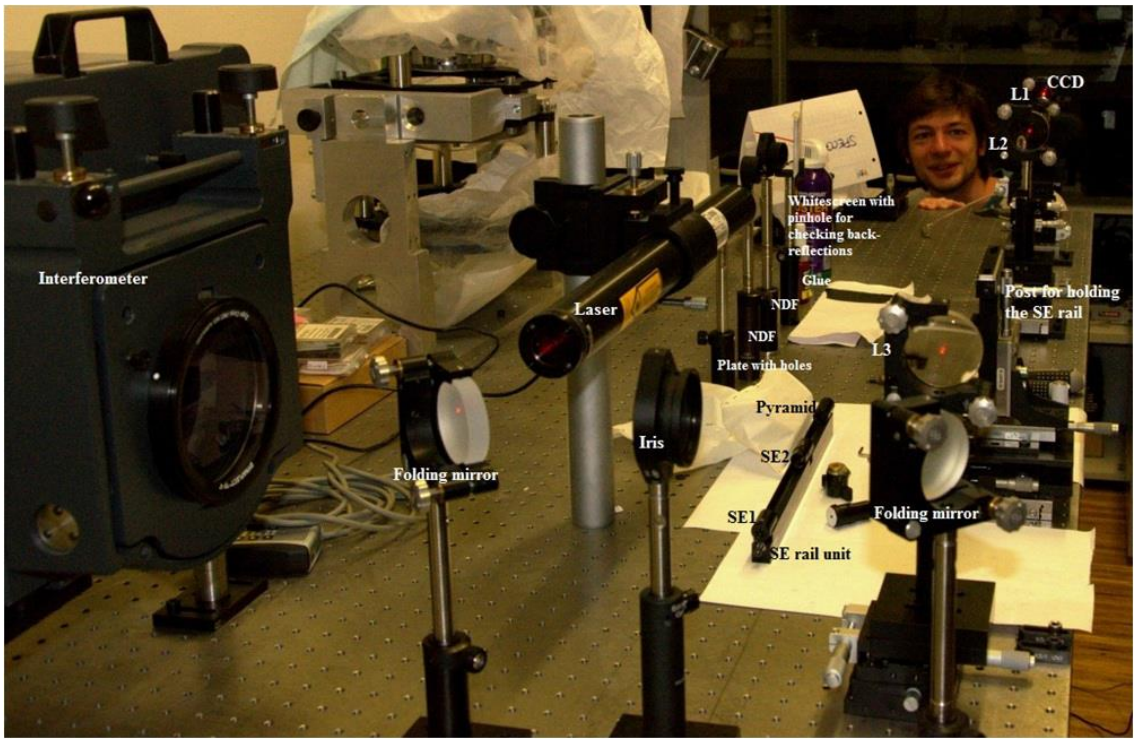

Figure 5-6: SEs alignment setup.

The optical setup for the alignment is devised so that a focused beam is produced at the test CCD by alternatively introducing and removing some setup lenses according to the introduction of SE lenses.
The procedure consists of the following steps:

1. Co-align the laser beam, used for lenses tip-tilt and centering alignment, to the collimated beam, using the laser tip-tilt mount, used for lenses focusing. A 2 inches folding mirror on a repositionable magnetic baseplate was used to select between interferometer beam and the laser beam.

2. L1 is placed in the setup in order to align and focus it, minimizing the spot diameter on the CCD. We define δ_{L1} as the decentering of L1 from the laser beam axis.

3. L1 is removed and the same procedure is repeated with L2. We define δ_{L2} as the decentering of L2 from the laser beam axis. At this point, the centroid of the spots produced by L1 and L2 should be at the same position on the CCD.

4. Mechanical alignment of the main part of the SE (i.e. the rail): fix the rail to the XYZ-tip-tilt SE mount. The rail parallelism to the optical axis is checked by moving a pinhole back and forth on the rail itself. When the rail is parallel to the interferometer (and laser) beam, the spot on the CCD should not move for different positions of the pinhole on the rail (assuming the pinhole is perfectly moved only along the optical axis). The centering of the rail with respect to the reference beams has been checked with the pyramid inside its holder, since this component has a little range of movement in XY direction inside its mount. The rail was considered centered when, rotating the barrel containing the pyramid inside its holder, the brightness of the 4 spots on the CCD was not changing.

5. Alignment of SE2 lens inside its holder: SE2 is glued inside its barrel with a drop of glue on the edge of the lens, to prevent it from moving inside the barrel itself in case of failure of the retaining cap holding the lens. The SE2 lens holder, shown in Figure 4-15, is fixed to the rail two drops of glue, in the proper position, just measured with a ruler. Then the barrel containing SE2 is inserted into its holder and the lens illuminated with the laser beam. SE2 is aligned in tip-tilt and centering looking at the back-reflected light (i.e. the fraction of the light which is reflected back by the entrance and exit surfaces of the lens. When the lens is correctly aligned the two back-reflected beams are coincident, otherwise two different beams propagating backwards are visible), acting on the 6 screws of the holder.

6. Then both L1 and L2 are inserted in the optical path. L2 focal point has to coincide with SE2 focal point, then the entire rail is moved along the optical axis in order to align in focus SE2, minimizing the spot diameter on the test CCD.

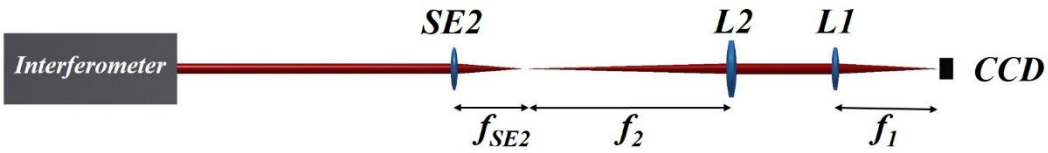

7. L1 is removed and SE1 is inserted in the optical path and aligned. As for SE2, also this lens has been glued inside its barrel. First, we checked the tilt of the lens looking at the back reflected spots (just to check it was not too big). The SE1 mount has focusing and centering movement (shown in Figure 4-14). Acting on both of them, we aligned the lens with respect to SE2. To achieve the best position along the optical axis, we took a certain number of measurements of the spot diameter at different positions of the SE1 along the optical axis, then interpolating them with a quadratic curve. In this configuration comparing the positions of the spot in step 3 and in step 7, one can derive:

$$x = \frac{\delta_{SE1-SE2} \cdot f_2}{f_{SE2}} \qquad [5\text{-}6]$$

We are interested in the $\delta_{SE1\text{-}SE2}$ value, which defines the decentering between the two lenses of the SE. Comparing it with the relative centering tolerance of SE1 and SE2 we obtain that:

$$\delta_{SE1-SE2} < 0.1\ mm \rightarrow x < 0.1 \cdot \frac{480}{162.5} \rightarrow x < 0.29\ mm$$

Which was always kept in specification.

8. L3 is inserted in the optical path so that its focal point coincides with SE1 focal point and aligned.

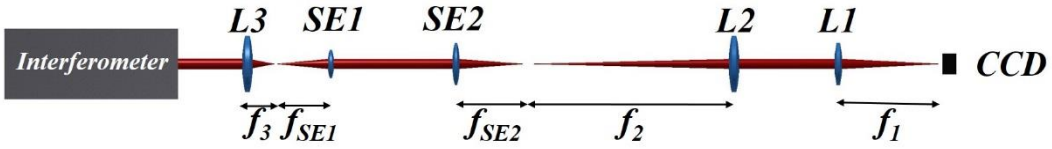

9. L1 is removed again and the perforated plate is positioned in the collimated beam, just before L3, and the distance *d* between the two spots is measured on the camera, to check the magnification factor *k* of the SE, given by:

$$k = \left(\frac{3.72}{d}\right)\left(\frac{f_2}{f_3}\right) \qquad [5\text{-}7]$$

The required value is $k = 12.5$.

10. As last step, the pyramid is placed inside its holder. To reproduce the correct entrance F/# the collimated beam entering L3 must have a diameter of 13 *mm*.

This is easily achieved tuning the iris aperture in front of L3. In this configuration, we checked and tuned the centering of the pyramid (mount shown in Figure 4-16): the four pupils on the detector must have the same intensity.

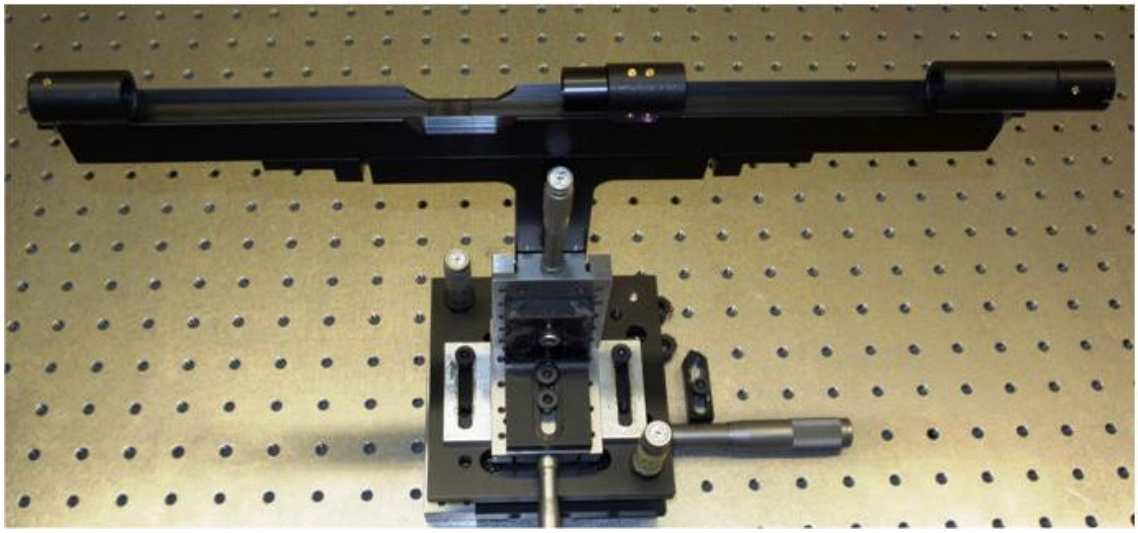

Figure 5-7: SE assembly. Also, XYZ-tip-tilt system is shown.

The results of the alignment are listed in Table 5-5. The real final requirement of this alignment is to obtain a *k* factor of 12.50 with a repeatability better than 1/240 for the 12 SEs.
The *k* factor repeatability obtained is of 1/570, far better than the requirement.

SE#	**x [*mm*]**	**d [pixels]**	**k**
SE01	0.10	137.2	12.50
SE02	0.04	136.6	12.55
SE03	0.03	137.2	12.50

SE04	0.02	137.1	12.50
SE05	0.08	136.8	12.53
SE06	0.05	137.5	12.47
SE07	0.03	137.1	12.51
SE08	0.04	137.2	12.50
SE09	0.05	137.2	12.49
SE10	0.12	137.1	12.51
SE11	0.03	137.1	12.51
SE12	0.13	137.1	12.50

Table 5-3: Main measurements taken during SEs alignment.

5.3 The Pupil Re-Imager internal alignment

As already mentioned in Section 4.4.2, the Pupil Re-Imager is a folded Schmidt camera, composed of a parabolic mirror, a flat folding mirror and a refractive prime focus corrector (or objective), which optically co-add the light coming from the 12 GWS SEs on a common detector.
The goal of the PR-I internal alignment is to obtain a spot produced by the PR-I with a radius RMS less than 13 μm across the whole PR-I FoV (± 0.44°). The possible deterioration on the optical quality due to internal misalignments depends on the combination of defocus, tilt and de-center of the parabolic mirror with respect to the prime focus corrector. We explored several ways to check separately defocus, tip-tilt and de-centering of the parabolic mirror with respect to the prime focus corrector, to define the best achievable combination of tolerances for the three of them in order to be sure we can reach the required optical quality.
To perform the internal alignment the PR-I mechanic is equipped with the following adjusting systems:

- Centering of the parabolic mirror
- Tip-Tilt of the parabolic mirror, which can also move the mirror along the optical axis.
- Tip-Tilt of the folding mirror
- Tip-Tilt of the prime focus corrector as a whole
- Centering of the CCD (motorized)

- Focusing of the CCD (motorized)

We fixed the focus tolerance at 0.5 *mm*, which is achievable with mechanical positioning of the parabolic mirror. The alignment procedure explained in the following should allow us to reach a final alignment better than 0.1 *mm* in de-centering and 0.02° in tip-tilt.
The procedure for the alignment consists in 6 phases; the overall idea is to illuminate the PR-I with a wide collimated beam and to align the parabola to the objective by checking the optical quality over the FoV and the amount of coma on a defocused image of the reference spot on axis.

5.3.1 Phase 1: On axis reference definition on the test camera

This phase has the purpose to align and center a test camera to the objective optical axis materialized by a laser beam and, in particular, to define on the CCD the objective optical axis projection. The optical axis of the objective is materialized using a laser positioned on a breadboard, in front of the objective, with centering and tip-tilt capabilities, and observing at the back-reflected spots. In order to minimize the alignment error, the alignment is performed 14 times and the mean values of centering and tip-tilt positions are considered.

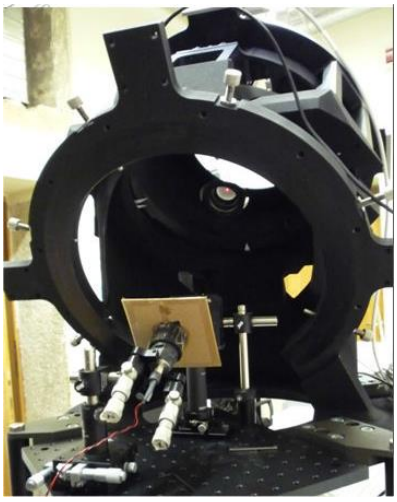

Figure 5-8: Laser source materializing the objective optical axis.

	Tilt x (µm)	***Tilt y (µm)***	***Shift x (mm)***	***Shift y (mm)***
1	109.5	120.5	12.77	4.64
2	110.5	110.0	12.65	4.68
3	109.5	109.5	12.86	4.71
4	110.0	111.0	12.78	4.72
5	110.0	121.5	12.81	4.74

6	114.0	114.0	12.74	4.65
7	108.0	107.5	12.76	4.72
8	105.0	110.0	12.73	4.72
9	112.5	110.0	12.88	4.66
10	110.0	106.5	12.90	4.72
11	104.0	110.0	12.71	4.77
12	116.0	108.5	12.73	4.83
13	112.0	113.5	12.66	4.65
14	109.5	112.0	12.64	4.70
Mean Value	**110.4**	**111.75**	**12.76**	**4.71**
Standard dev.	**2.82**	**4.42**	**0.08**	**0.05**
Max dev.	**12.0**	**15.0**	**0.26**	**0.19**

Table 5-4: Test values of the laser actuator positions. Concerning tip-tilt (1 µm = 5.8 arcsec) and de-centering. "Shift y" actuator values need to be multiplied by cos(56.2°) in order to obtain the true shift in the y-axis.

Considering the standard deviation data (±1σ):
Centering uncertainty: ± 84.7 μm
Tip-tilt uncertainty: ± 5.2 μm = ± 30.4 *arcsec*
Considering the mean values, the corresponding uncertainties are st.dev/√14
Centering uncertainty: ±22.8 μm
Tip-tilt uncertainty: ± 1.4 μm = ± 8.06 *arcsec*
The values obtained for this phase lead to a resulting movement of the spot on the test CCD of ±15 μm

Figure 5-9: Test camera mounted on a repositionable magnetic baseplate, which can be moved with the CCD linear motorized stages in XYZ configuration.

The test camera is centered with the objective optical axis, materialized by the laser, and focused. This CCD is mounted on a magnetic baseplate, repositionable with a precision better than ± 0.55 *mm.* To ensure that the required stability is met this phase required further test.

- Test on re-positionability of the test camera on its magnetic baseplate: the CCD was taken out from the magnetic base and then repositioned 10 times. Each time the position of the laser spot centroid on the CCD was recorded (see Figure 5-10).

The spot centroid moved of 6.2 μm in the camera *x* direction and of 12.1 μm in the camera *y* direction.

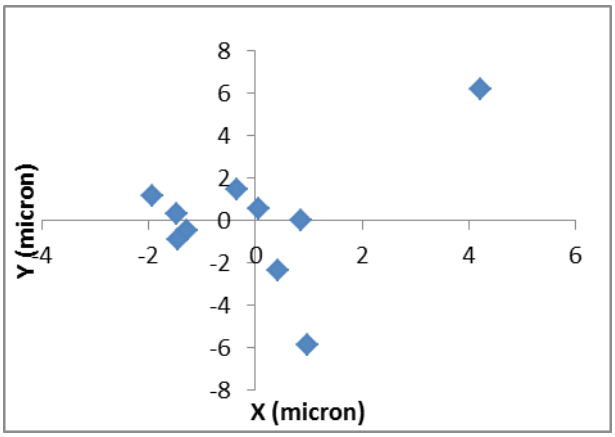

Figure 5-10: Test CCD positioning repeatability.

- Test on the movement of the spot due to motorized stages repositioning: the test camera is mounted on a linear motorized stage system in XYZ configuration. During the test, each of the three stages has been re-initialized and sent to a specific position 10 times and the position of the spot on the CCD has been recorded. Considering all the three contributions in their worst possible combination, the spot centroid is expected to move of 3.3 μm in *x* direction and 4.7 μm in *y* direction (see Figure 5-11)

- Characterization of the angle between the objective optical axis and the z-stage movement axis: this test provides the movement of the spot on the CCD during a small (8.825 *mm*) travel along the direction of movement of the z-stage (resembling the objective optical axis), to characterize the angle between the true movement of the stage and the objective optical axis itself. For a better interpolation, the considered CCD movement range is far larger than what expected to be necessary for the following phases (focusing of the test camera).
  The measured movements of the spot are 52.8 μm in *x* direction and 23.1 μm in *y* direction, well inside the required precision in the camera positioning (0.55 *mm*), even if the range here considered is very wide.

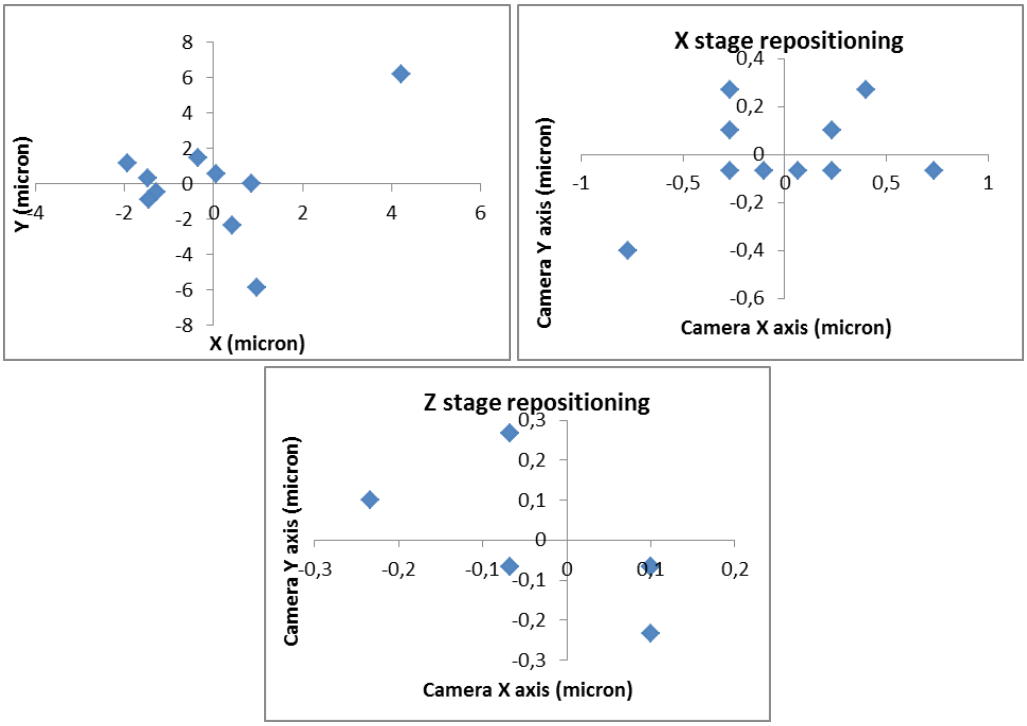

Figure 5-11: Results of the test on the repositionability of the motorized stages in the three axis. The overall maximum displacement has been retrieved as the sum of the three resulting ranges.

The total indetermination on the optical axis definition on the CCD for Phase 1, considering a conservative sum of all the described contributions is ± 94.8 μm, well below the required 0.55 *mm*.

5.3.2 Phase 2: Alignment on axis between the objective and the parabola

In this phase a preliminary, rough, pre-alignment of the parabola to the objective is performed, in order to accomplish, during Phase 3, the alignment of 2 flat mirrors (one of the PR-I and a setup mirror). We call it "rough pre-alignment" since, at this stage, having only one observable, described in the following, it is impossible to distinguish between the decenter and the tilt of the parabola.

- First of all the parabolic mirror is installed on the PR-I main structure and positioned at its nominal focal place with mechanical precision (which should fulfil the tolerance of 0.5 *mm* in focus).

- The CCD is temporarily dismounted and a laser source, mounted on the same side of the test CCD and equipped with centering and tip-tilt adjustment capabilities, shines toward the objective. The parabolic mirror is masked with a black screen so that it cannot reflect the laser light back. The laser is aligned to the objective in a way to materialize the objective optical axis looking at the back-reflected spots (like in Phase 1). This operation has been achieved with a precision better than ± 120 μm in centering and ± 60 *arcsec* in tilt.

- The black screen is removed from the parabola, and the parabola is aligned with respect to the laser. Of course, shining a laser on the center of the parabola, we can only align the parabola surface normal with the incoming laser, since there is always some tilt compensating a certain amount of decenter (and vice versa). This operation has been achieved with a precision of 0.6 *mm* in centering and 0.06° in tilt.

The total indetermination of the alignment of the parabola surface normal with respect to the objective optical axis is the sum of the errors in aligning the parabola (0.6 *mm* and 0.06°) and the propagation of the errors in materializing the objective optical axis with the laser beam (120 *μm* and 60 *arcsec*), giving a total error (in the worst case) of 1.75 *mm* in centering and 0.15° in tilt.

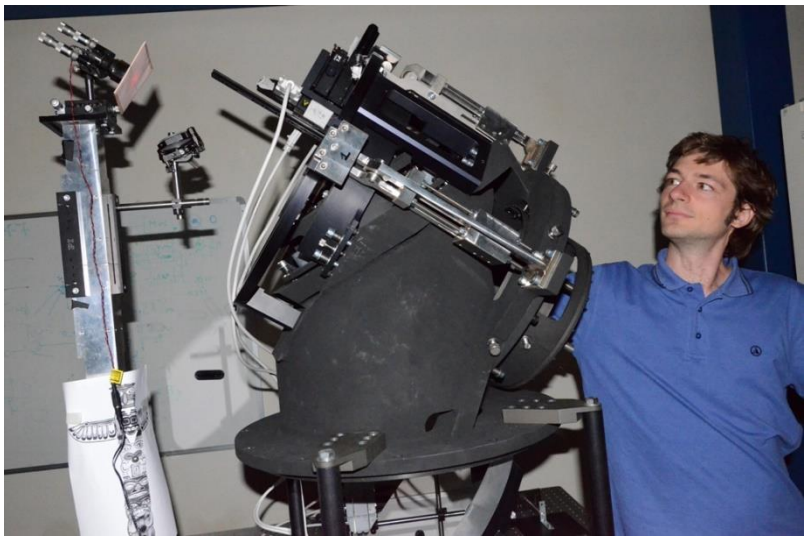

Figure 5-12: Alignment of the laser source to materialize the objective optical axis.

5.3.3 Phase 3: Alignment of the two flat mirrors

This phase has the purpose to feed the PR-I with an extended collimated beam, resembling the on-axis beam coming from the star enlargers. When the beam reaches the parabola, it has to be parallel to the objective optical axis. Once this configuration is reached, there will be only one way to align the parabola minimizing the coma effect and keeping the spot fixed on the recorded position on the CCD (Phase 4 and Phase 5). There are several ways to change the incoming beam inclination: tilting the PR-I flat folding mirror, tilting the setup flat folding mirror, whose custom mount is equipped with micrometric actuators.
The optical setup, shown in Figure 5-13, is composed of:

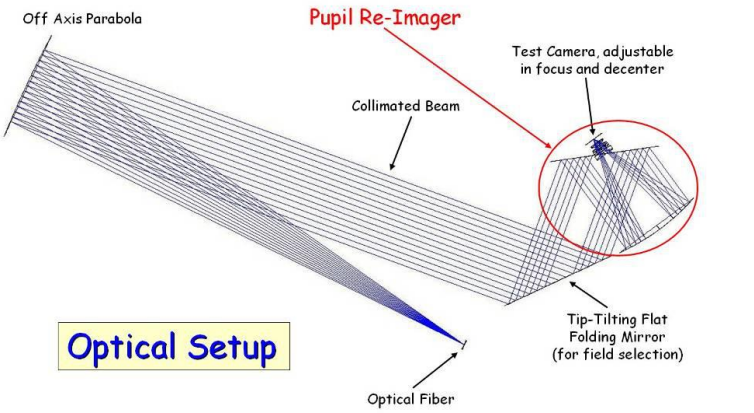

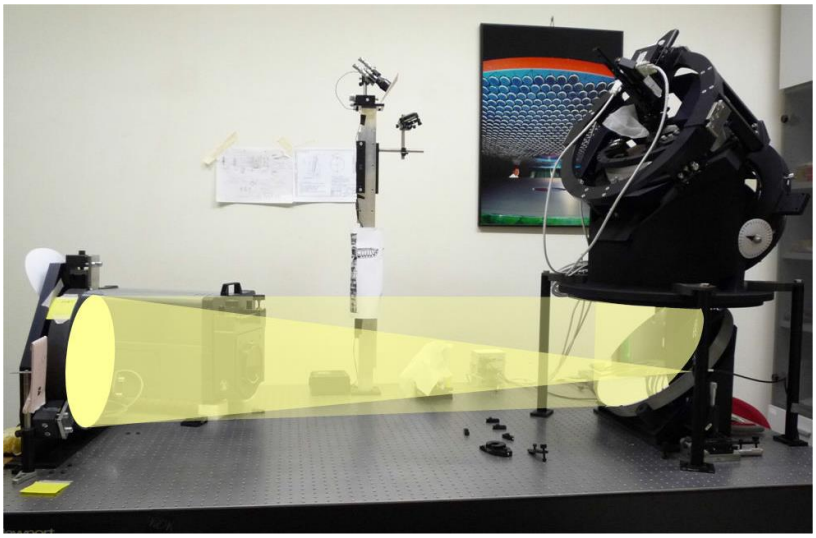

Figure 5-13: The optical setup used to align the PR-I, shown as Zemax layout (top) and in the lab (bottom).

- An optical fiber, 50 μm core, on a XYZ stage and fed with visible light.
- An off-axis parabolic mirror (OAP), mounted on a custom-made tip-tilt mount, to collimate the beam coming from the optical fiber, directing it toward the PR-I.
- An additional setup flat folding mirror, positioned below the PR-I, to send the collimated beam up toward the PR-I itself. This folding mirror has tip-tilt adjustments, in order to tilt the reference created by the fiber over the whole PR-I FoV.
- The test camera (the same used in Phase 1), with a very high spatial sampling (pixel size 1.67 μm) in order to have a high spatial resolution for the evaluation of the images affected by the coma during the alignment procedure.

After the alignment of the OAP the flat folding mirror below the PR-I is tilted in order to superimpose the spot to the reference, recorded on the CCD during Phase 1, within an accuracy of 0.003° (corresponding to a shift of the spot on the CCD of 7 μm)

5.3.4 Phase 4: Alignment of the PR-I

At this point of the procedure the PR-I is fed with a wide collimated beam corresponding to the on-axis beam of the PR-I FoV. The idea is to defocus the test camera in the intra-focal direction of 0.22 *mm* to appreciate coma. The resulting image shows a central dark "hole" due to the central obstruction of the PR-I. To measure the coma, the position of the central obstruction with respect to the whole defocused spot is determined. Using an IDL procedure interpolating the contours of the outer and inner ellipses. Then the decentering between the two ellipses is computed and used to derive the coma measurement.

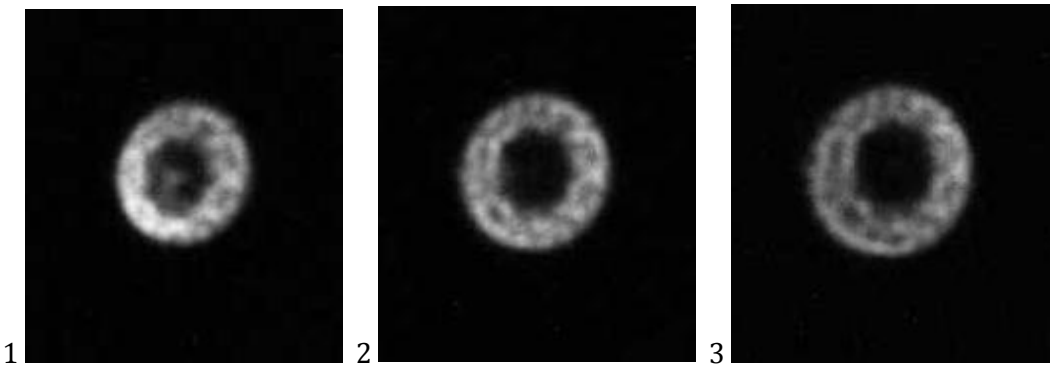

Figure 5-14: Defocused images of the spot (0.22 mm intra-focal direction). Panels 1 and 3 show a de-centering between the inner and the outer ellipses of about 7 µm, while panel 2 shows a de-centering of about 2 µm)

The goal is to iteratively adjust tip-tilt and centering of the parabolic mirror, in order to minimize the de-centering between the two ellipses without changing the position of the focused spot on the CCD. According to the error budget of the PR-I internal alignment, the misalignment accepted in this phase between the parabolic mirror and the objective shall be smaller than 0.17 *mm* in de-centering and 0.014° in tilt, which translates in a de-centering between the ellipses smaller than 5 μm.
The reached value for the de-centering of the two ellipses after the iterative procedure is 3 pixels = 5 μm, corresponding to 6.5 *arcsec* of coma.

5.3.5 Phase 5: Final focus adjustment of the PR-I

The de-center and tilt adjustment of the parabola are not pivoting around its center. Therefore, the alignment procedure described in Phase 4 changes the parabola focal position. This effect is easily detected as a defocus on the CCD or through a mechanical check of the nominal position of the parabola.
A manually operated measurement arm that measures the surface of the real physical objects, tracing the exact coordinates of space, is used to check the distance between the parabolic mirror and the objective. The reference planes are the rear of the parabolic mirror and the flange holding the objective (as shown in Figure 5-15).

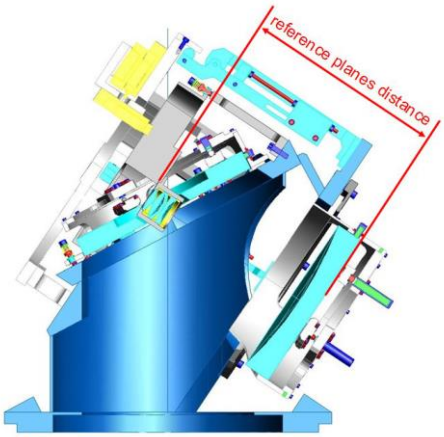

Figure 5-15: The reference planes for the mechanical measurements of the distance between the optics inside the PR-I.

The nominal distance, considering ray tracing analysis and mechanical drawings, is 352.94 *mm*, while the measured one is 353.25 *mm*, giving a discrepancy with respect to the nominal distance of ~ 0.3 *mm*, within the focal positioning requirement of 0.5 *mm*.

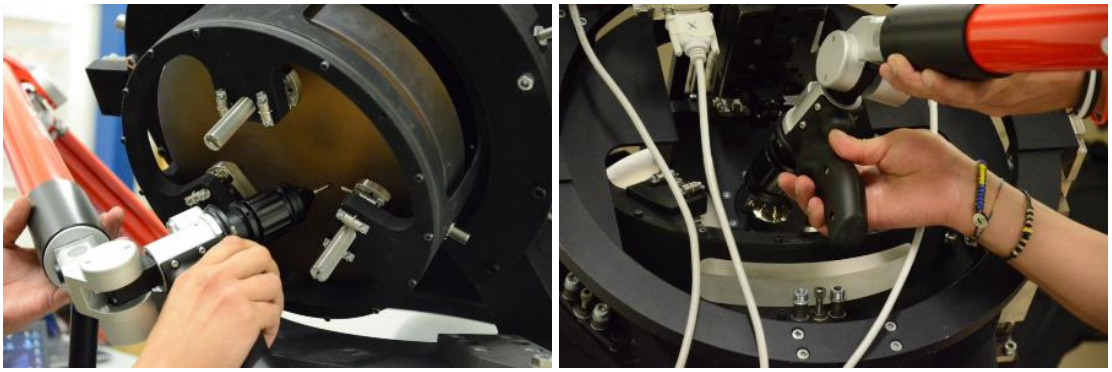

Figure 5-16: Measurement of the distance between the optics inside the PR-I with the measuring arm.

5.3.6 Phase 6: Final PR-I optical quality check

This last phase is just a check to verify that we did not make any error during the alignment procedure.
By tilting the setup flat folding mirror below the PR-I, the off-axis optical quality, until the edges of the PR-I FoV is checked. The flat folding mirror is tilted using three manual actuators positioned on the rear of the mirror, with 120° of relative separation. First, the test camera is precisely positioned on the focal plane, minimizing the spot radius of the image at the center of the FoV.

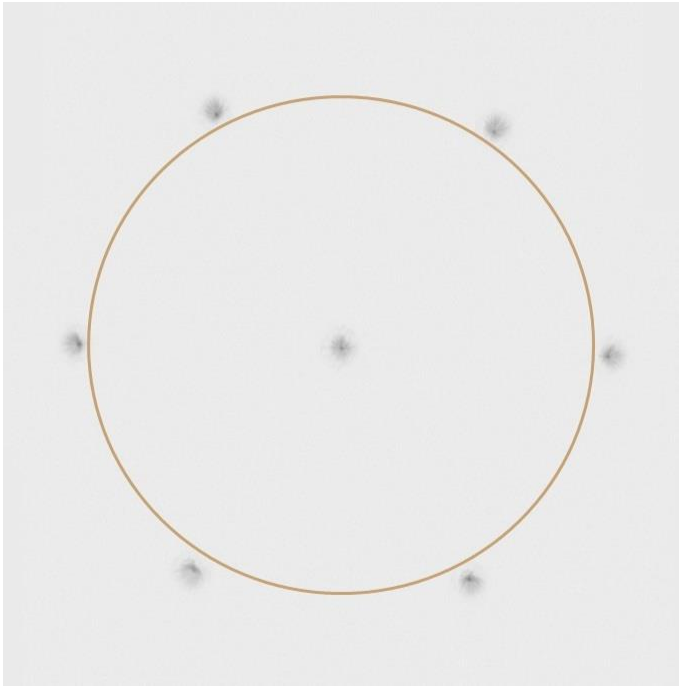

Figure 5-17: Spot out of focus images at the edge of the PR-I FoV (0.88°), used to check the symmetry of the coma. It is clearly visible that the "tails" of the spots on the 0.88° circle are displaced radially, demonstrating the coma symmetry.

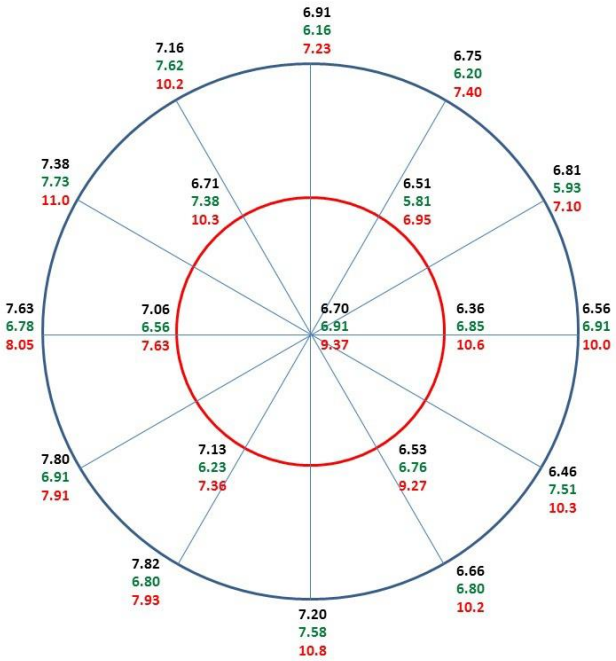

Figure 5-18: Spot radii measurements for different positions along the PR-I FoV. The blue and red circles represent the 0.44° and 0.22° radius FoV, respectively. Black values are the results of a Gaussian fit over the spot, while green and red values are the measured RMS spot radii considering only the pixels values over a threshold of 10% and 5%, respectively, of the peak intensity of the spot. All the values are in μm.

The camera is fixed in position and several measurements of the spot radius across the PR-I FoV are taken, both in focus, to check the optical quality, and slightly out of focus, to qualitatively check if the coma is symmetrical (see Figure 5-17). If symmetrical then the on axis spot would be at the center of the Field of the PR-I. For the spot radius computation both RMS (considering only the pixels with values over a threshold of 5%

and 10% of the peak intensity of the spot at the center of the FoV) and Gaussian fit were evaluated (see Figure 5-18).
All the measured radii are below the required 13 μm over the whole FoV, therefore the alignment satisfies the requirement.

5.4 GWS internal alignment

After the internal alignment of the GWS subsystem, the following step is their integration in the GWS main mechanical structure and in their alignment to the mechanical axis of the bearing, which allows compensating for the rotation of the sky. The GWS internal alignment consists basically in the relative alignment of the 12 SEs, so to avoid a wrong pupil superposition on the detector, the alignment of the PR-I optical axis to the bearing rotation axis, performed with the flat folding mirror at the entrance of the PR-I itself, and the proper positioning of the SEs entrance focal planes (2 different focal planes for SEs odd and even, recalling what discussed in Section 5.1 regarding the SE defocus). All these alignment steps are followed by verification tests, to check if the requirements described in the error budget are met. During these phases a test CCD with a very high spatial sampling (1.67 μm pixel size) has been used in place of the final CCD50, to ensure a better precision in the alignment in order to match the tight requirements presented in Section 5.1.

5.4.1 PR-I flat mirror alignment

The PR-I was then integrated into the main mechanical structure of the GWS, using a crane and a forklift to lift it and position it on the bearing.

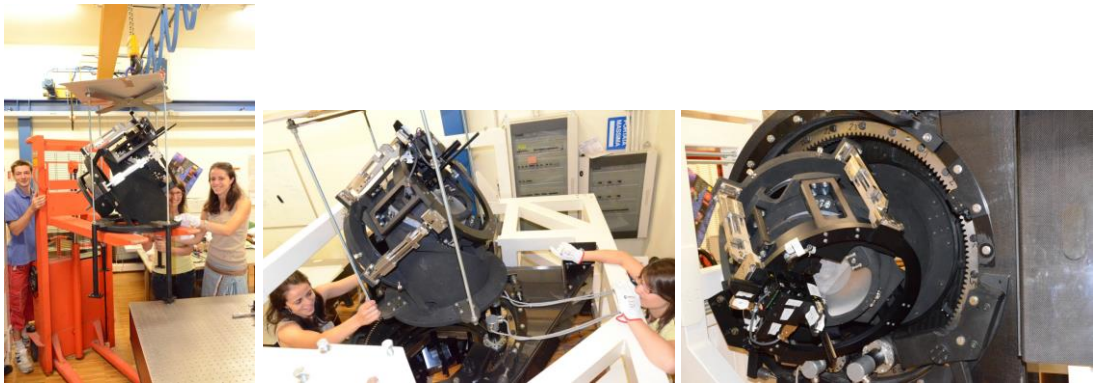

Figure 5-19: Integration of the P-RI into the main mechanical structure of the GWS.

To adjust the tip-tilt position of the PR-I flat mirror, in order to make the GWS rotation axis parallel to the center of the PR-I field of view, defined during the PR-I alignment, a collimated beam, materializing the rotation axis direction, is required. The source we used is an off-axis parabolic mirror, illuminated with an optical fiber and aligned with a

precision that has been verified in Zemax to introduce an aberration on the GWS re-imaged spot negligible with respect to the spot aberrations produced by the PR-I.
The collimated beam produced with the parabolic mirror has been folded with a setup flat mirror toward the GWS entrance. The inclination of such a setup mirror has then been adjusted in order to keep the spot fixed on the test CCD for a complete ± 60° GWS rotation. To align the internal flat mirror of the PR-I, the GWS rotation axis has to be made parallel to the beam defining the center of the field inside the PR-I ± 0.44° FoV. Operatively, the flat mirror inclination has to be adjusted in order to achieve a field (rotating the GWS) in which the optical quality is center-symmetric. The center of the field corresponds to the GWS rotation axis. The results obtained after this alignment are shown in Figure 5-20. The PR-I quality along its FoV is measured as the dimension of the focused spot of the collimated incoming beam, mapping the whole FoV. The measurements have been repeated in three configurations, corresponding to 0°, +60° and −60° rotation angle of the bearing. These results translate into an optical quality, expressed in RMS value, which is lower than the required 13μm in the whole PR-I FoV.

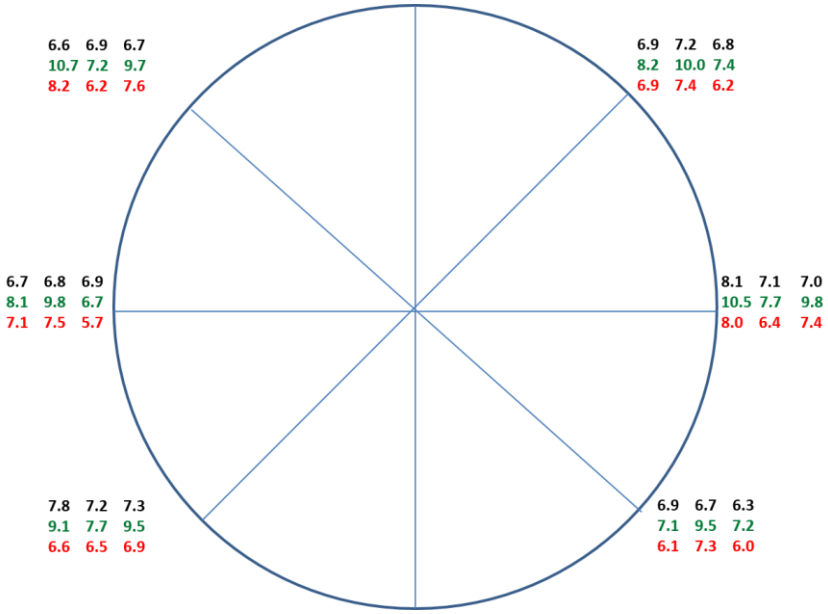

Figure 5-20: Optical quality check after the alignment of the flat mirror of the PR-I. Black values are the results of a Gaussian fit over the spot, while green and red values are the measured RMS spot radii considering only the pixels values over a threshold of 10% and 5%, respectively, of the peak intensity of the spot. The first, second and third column of each block represents the +60, 0 and -60 degrees of rotation of the bearing. All the values are in µm.

5.4.2 SEs to GWS alignment

Once internally aligned the SEs are coupled to their linear stages, interfaced by a stage allowing the SE tip-tilt tuning (visible in Figure 4-22), and then aligned to the optical axis of the GWS, both in tip-tilt and in focus, in order to guarantee the correct superposition of the pupils on the detector and to satisfy the SEs differential tilt requirement. The SE rail is mechanically fixed to a T-arm support and mechanically positioned at the middle of its travel range along the optical axis. Two grub screws allow pushing the SE in the

two directions along the optical axis, in order to adjust the SE focus. When the SE is in the correct position, two blocking screws hold the SE in place. As a safety system, a copper stripe is mounted on the SE (see Figure 5-21), in order to stop immediately the motors in case of collision between two copper stripes, preventing collision between the SEs.

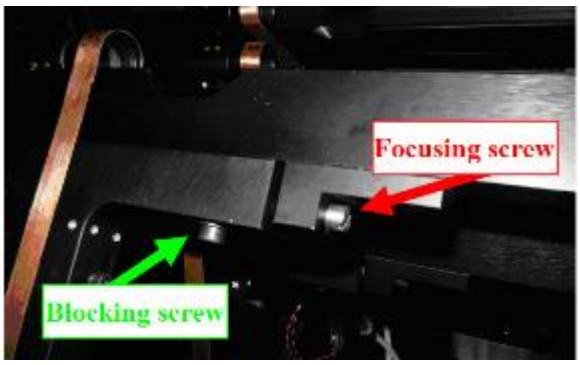

Figure 5-21: Focusing and blocking screws. On the opposite side of the T-arm there is another couple. The two focusing screws act in opposite directions.

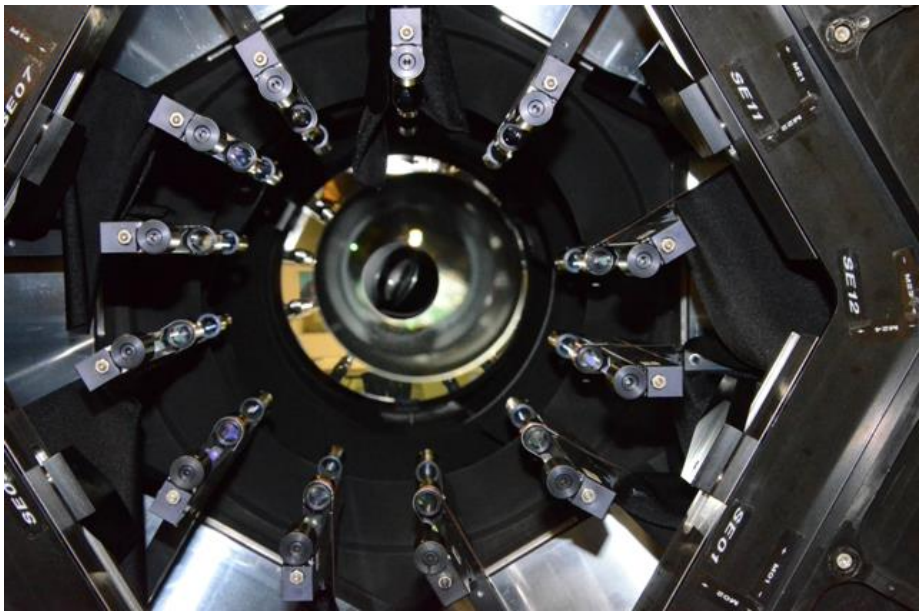

Figure 5-22: The 12 SEs integrated inside the GWS structure.

The alignment of the SEs to the GWS mechanics has been performed using the setup shown in Figure 5-23. The idea is to take advantage of a wide collimated laser beam (d = 100 *mm*, λ = 633 *nm*), coming from a commercial interferometer, as a reference, aligned to the GWS to be parallel to the GWS optical and rotation axis (now coincident). A commercial f = 700 *mm*, 2 inches diameter lens is used to focus part of the wide beam in the SEs focal planes, defined by the mechanics of the GWS itself, and a physical stop positioned at the proper distance from the focusing lens (according to the entrance pupil position at LBT: 14 *m*) defines a F/15 beam. The focused beam (the green one in Figure 5-23), once passed through a SE, produces four images of the pupil stop on the test CCD. The part of the beam that is not focused by the lens (the red one) reaches the GWS optics still collimated. If this collimated beam passes through a SE, it will produce 4 spots on

the test CCD, whose barycenters are defining the positions of the center of the 4 pupils re-imaged when the same SE is reached by a the focused beam. The part of the collimated beam entering the GWS without passing through a SE focuses on the center of the PR-I FoV.

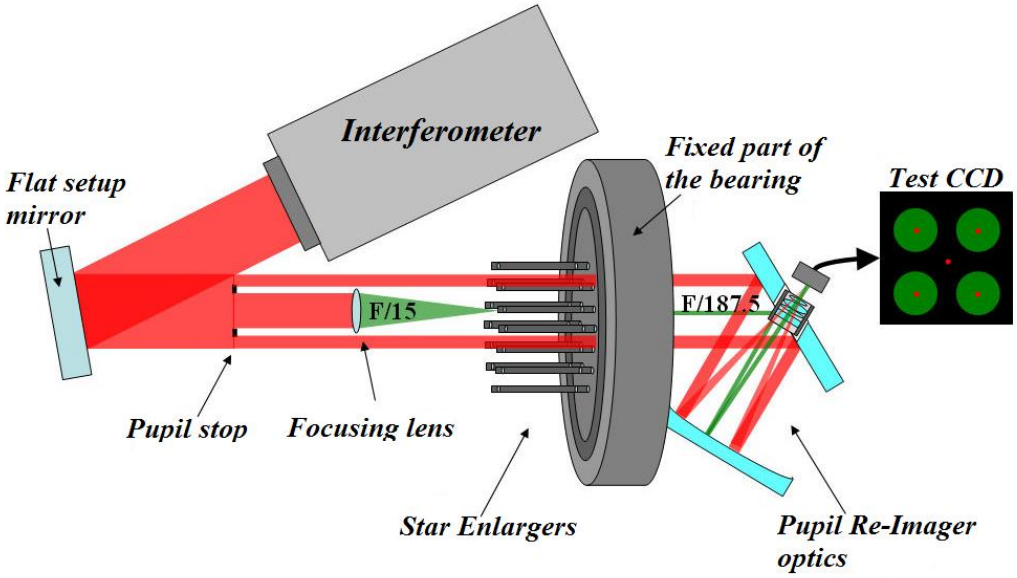

Figure 5-23: SEs to GWS alignment setup.

Materialization of the bearing rotation axis

First of all the wide collimated beam from the interferometer is aligned to the GWS in order to materialize the bearing rotation axis. This is very important for the alignment since a tilt of the collimated beam with respect to the optical axis of the GWS would translate into a general and common tilt of all the SEs. To complete this task, the collimated beam is folded by the flat setup mirror (which make easier to adjust the beam direction) toward the GWS entrance. Here a flat mirror, previously aligned to make its optical axis parallel to the bearing rotation axis with a precision better than 12 *arcsec* (comparable to the wobble of the bearing), reflects the light back into the interferometer. The flat setup mirror is then tilted in order to minimize the number of fringes measured by the interferometer. The lower is the number of fringes measured the lower is the tilt between the interferometer beam and the optical axis of the mirror attached at the GWS entrance (i.e. the GWS optical axis, since they are parallel). The precision of this operation is given by:

$$\frac{Number\ of\ fringes\ \cdot \lambda \cdot 206265''}{Beam\ diameter}$$

We observed 2 fringes, which means a residual tilt between the interferometer beam and the optical axis of the reference mirror at the entrance of the GWS is 2.6''. In this way, we have a collimated beam parallel to the bearing axis with a precision better than 12''.

F/15 simulator lens

While for the tip-tilt alignment of the SEs the collimated beam is sufficient, for the focus alignment a converging beam is required, to simulate the telescope F/15 focal plane at the

entrance of the GWS. A commercial lens (f = 700 mm) is aligned in auto-collimation, placing a reference mirror in the GWS nominal mechanical entrance focal plane, with a 100 μm accuracy.

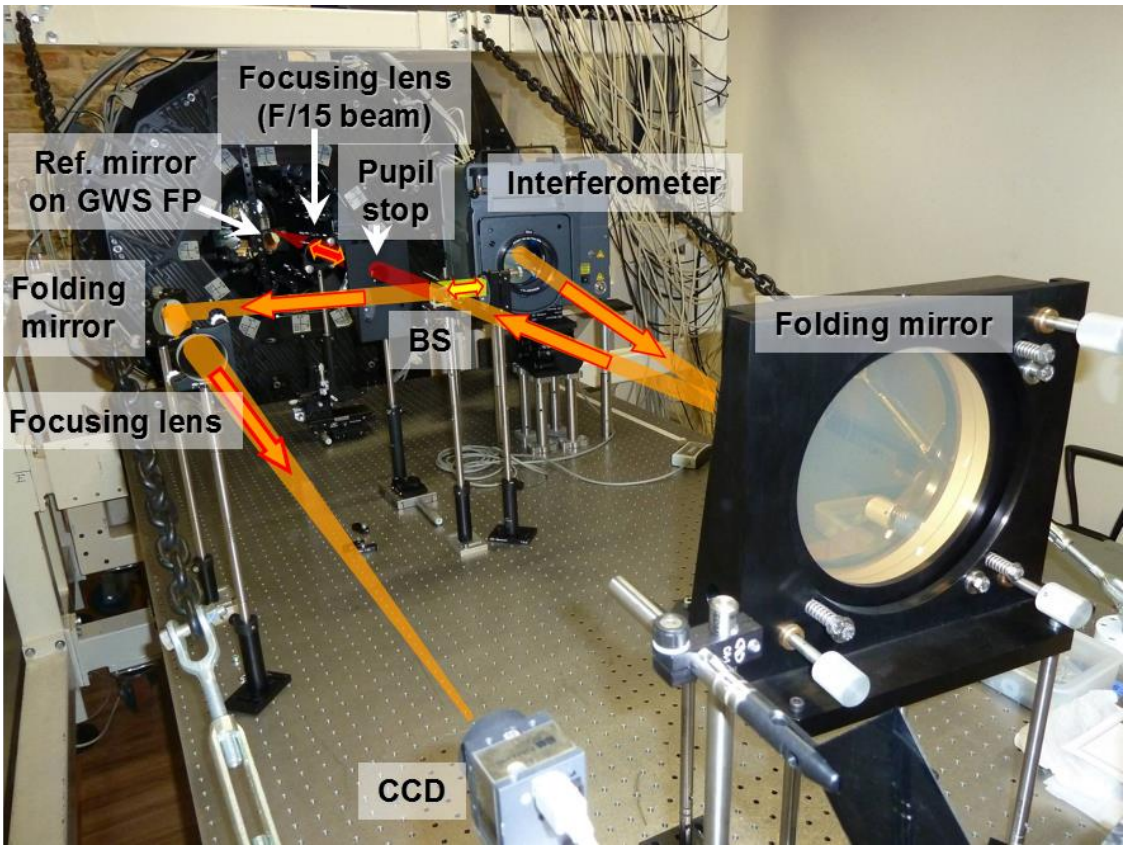

Figure 5-24: setup used for the alignment of the F/15 simulator lens.

The collimated beam coming from the interferometer is divided by a beam splitter into two separate beams: on beam (the yellow in Figure 5-24) is reflected by a flat setup mirror toward a setup lens (f = 500 mm) and focused on a test camera, while the second beam passes through the F/15 focusing lens and is reflected back, by a reference mirror placed in the GWS focal plane, to the beam splitter and focused on the same test camera of the first beam. The setup focusing lens is moved along its optical axis, minimizing the spot size produced by the first beam. The lens focusing the F/15 beam at the entrance of the GWS is moved through focus in order to find the position that minimizes the size of the spot focused onto the detector. At this point the F/15 lens focal point falls on the surface of the reference mirror with a precision of about 50 μm, which, combined with the 100 μm indetermination in the reference mirror mechanical positioning leads, translates into a discrepancy between the focus of our F/15 beam and the nominal mechanical GWS entrance focal plane of maximum $(100^2 + 50^2)^{0.5} = 112$ μm. Such an error would introduce 18 nm defocus signal onto the GWS, still far to exceed the linear regime of the GWS.

SE alignment

Once aligned the lens in the correct position the odd SEs are placed on a 1.71 *arcmin* radius, corresponding to a linear radius of 62.7 *mm*, while the even SEs are placed on a 2.63 *arcmin* radius, equivalent to a 95.7 *mm* linear radius. The SEs alignment to the rest of the GWS is now an iterative procedure consisting of three steps:

- Alignment of the rotation angle of the pyramid: the goal for the precision in the pyramid rotation alignment is 10 *arcmin*, leading to a displacement of the sub-apertures at the outer edges of the pupils of 1/10 of sub-aperture in the direction of the CCD corners. To measure the residual rotation after the alignment, the barycenter positions of the four spots obtained illuminating the SEs with a collimated beam are considered. Because of small defects in the pyramids faces orthogonality, the rotation angle of each pyramid is measured considering 6 different diagonals linking the barycentres of the 4 pupils, shown in, and their mean deviation from the 45° is taken as a rotation measurement. Operatively the alignment is done rotating by hand the pyramid barrel, minimizing the deviation of the diagonal angles from the theoretical 45°.

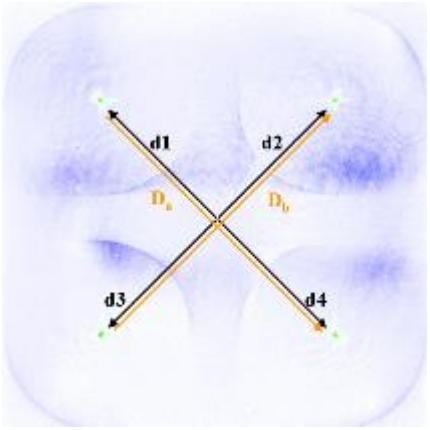

Figure 5-25: The considered diagonals to measure the pyramid rotation with respect to the CCD X and Y directions. d1, d2, d3 and d4 represent the directions between the overall image barycenter and the four spots, while Da and Db are the diagonals of the quadrilateral defined by the four spots. In green, the spots produced by a SE when fed with a collimated beam (which is the case of the pyramid rotation and SEs tip-tilt alignments); in blue the four pupils produced when the SE is fed with the F/15 beam.

- SE tip tilt adjustment: when a collimated beam goes through a SE, four spots appear on the test CCD. The relative distances between the spots depends upon the pyramid vertex angle and faces orthogonality, but the position of the overall barycentre can be used as a measurement of the tilt of the SE with respect to the incoming beam. Before measuring this tilt, the collimated beam, used as reference, has to be adjusted in tip-tilt in order to focus on the center of the field, defined on the camera during the PR-I alignment and corresponding also to the GWS rotation axis projection. The PR-I scale with respect to the test camera is about 2 *arcsec*/pixel. The effect of a tilt of the incoming beam on the four spots is reduced by the SE enlargement of a factor k =12.5. The goal of a tenth of a sub-

aperture shift (4.8 μm) of the pupils is reached with a tilt of the SE lower than 5 *arcsec*, corresponding to a shift of our spot on the Test CCD of 3 pixels. Acting on the adjustment screws of the SE tip-tilt stage we tilted the SEs, moving the four spots on the test CCD until their common barycentre matches the barycentre of the spot produced by the collimated beam not passing through SEs.

Figure 5-26: On the left, all the SEs illuminated by the collimated beam for a first rough tip-tilt alignment. On the right the small spots produced by the 12 SEs on the test CCD before the alignment. After the alignment, all the small spots will be distributed in 4 very small clouds (of few pixels). The central bright spot, whose centroid is our reference for the tip-tilt alignment, is produced by the collimated light not passing through any SE and focused by the PR-I on the center of the CCD.

- SE defocus alignment: to position the SEs in the optical path along the optical axis, the defocus signal retrieved by the wavefront sensor has to be minimized. The F/15 beam passing through one SE is then re-collimated by the pupil re-imager and produces 4 images of the pupil onto the test CCD. The wavefront shape is retrieved comparing the intensities of the four pupils using the quad-cell equations with very small sub-aperture (2 × 2 pixels), and then de-composed into Zernike polynomials. To convert the retrieved Zernike coefficients into metric values, a converting factor has been retrieved using the following procedure: a spatial range along the optical axis, centered on the best focus position, is defined and the defocus coefficient is measured for both the extreme intra-focal and extra-focal positions (which are symmetric with respect to the best focus). The converting factor can be retrieved as:

$$C_{def} = \frac{1}{8 \cdot 2\sqrt{3}} \cdot \frac{1}{F^2} \cdot \frac{\Delta l}{\Delta c}$$

Where F is the incoming beam F/#, Δl is the used range along the optical axis, Δc is the difference between the measured defocus coefficients in the intra and extra-focal positions. The multiplying factor is an approximation that allows converting from RMS to PtV values. The retrieved converting factor for the SEs, illuminated with the light coming from the interferometer ($\lambda = 633\ nm$), is $C_{def} = 0.101nm$. This factor is then multiplied to the retrieved Zernike defocus coefficients in order to obtain the residual defocus WaveFront Error (WFE) in nanometers. The goal for the SEs relative alignment in defocus is to keep them inside the GWS focus depth, leading to a defocus RMS equal to $\lambda/28$, corresponding to a residual WFE

of 20 *nm* for the considered wavelength. Mechanically the focusing of a SE is performed acting on two headless screws, placed on the short side of a L-shaped support fixed to the SE rail, on the opposite side to the one holding the optical elements. These screws push on the mechanical stop of the T-arm, allowing the movement of the entire rail along the optical axis. When the measured defocus coefficient is close to 0, the rail is blocked in position with two blocking screws (see Figure 5-21). Since the SEs must be aligned to two different focal planes, as already discussed in the Error Budget, because of the curvature of the FP15 entrance focal plane, the F/15 lens is moved along the optical axis of 1.93 *mm* and 4.5 *mm* from its starting position for the focus alignment of the odd and even SEs respectively.

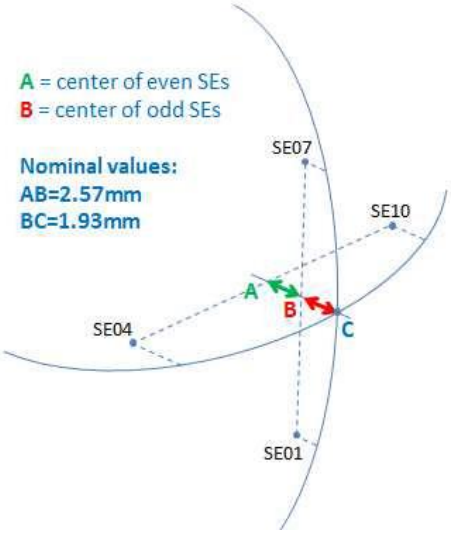

Figure 5-27: Focus position of odd and even SEs with respect to the LBT curved focal plane. SE01 and SE07 are representative of the odd SEs while SE04 and SE10 represent the even SEs.

The results of the SEs alignment for the GWS SX are presented in Table 5-5, all the requirements are fulfilled.
Because of the strict tolerances, this alignment has to be repeated after the shipping to the telescope. This re-alignment is currently on going, on both the GWSs, at the LBT laboratory.

5.5 GWS verification tests

After the GWS internal alignment in static configuration, some verification tests have been performed, in order to double check the alignment results and if some of the items presented in the Error Budget have been underestimated. Since these tests are performed on the completely assembled GWS, they are not sensitive to the single contributors listed in the Error Budget, but rather measure a combination of several contributors, depending on the test. The items affecting a particular test, even if already reported in Table 5-1, will be repeated in the description of the tests. The result of each test is then compared with

the sum in quadrature of its contributor values, from the Error Budget, to verify if it matches the expectations.

SE #	SE tip-tilt [*μm*]	Pyramid rotation [*arcmin*]	SE defocus [*nm* WFE]
SE01	2.7	0.1	4.3
SE02	1.6	-0.2	1.9
SE03	3.3	0.9	-2.3
SE04	2.3	0.6	0.2
SE05	3.1	-1.3	8.9
SE06	1.7	-0.5	-7.4
SE07	0.9	1.8	0.4
SE08	1.7	1.2	2.6
SE09	2.6	-0.7	-5.3
SE10	2.2	-0.9	2.6
SE11	1.8	0.7	1.3
SE12	2.4	-0.1	-7.3
Requirements	**4.8**	**10**	**20**

Table 5-5: SEs alignment results. All the requirements are fulfilled.

5.5.1 Test A: pupil blur due to bearing rotation

The scope of this test is to measure the RMS blur, measured as the RMS differential shift of the spots produced by the 12 SEs illuminated by a collimated beam, during a bearing rotation. Many contributors affect the result of this test:

- Pyramid vertex angle
- Pyramid faces orthogonality
- SEs relative tilt
- Pyramid orientation
- PR-I optical quality (a very small fraction since during this test all the SEs have been placed in a very inner radius in order to feed them all together with the 100

mm beam, so all the SEs experience more or less the same PR-I optical quality. For this reason, this term is neglected.)

- SEs tilt due to support flexures (a fraction. Here considered $1/\sqrt{2}$, since this contributor divides its action between the GWS rotation and its inclination with respect to the ground, analysed in test D).

- SE tilt due to ring flexures (a fraction. Here considered $1/\sqrt{2}$ for the same reason above)

- SE tilt due to linear stages flexures (a fraction. Here considered $1/\sqrt{2}$ for the same reason above)

To perform this test all the SEs have been placed on a very inner radius so to illuminate them all together with the collimated beam and the bearing has been rotated of ± 60° in steps of 30°. For each bearing angle, the position of the spots barycentre for each SE has been measured and plotted in a graph.
Because of the flexures of the mechanical components of the GWS (SE T-arms, tip-tilt stages, linear stages, GWS mechanics, CCD mount), when rotating the bearing we observed that the movement of the spots produced by all the SEs show both a common and differential movements.
The common shift of the pupils is due to the flexures of everything is after the SEs, so mostly the PR-I and the CCD. Since this movement is common to all the SEs, it is not introducing any blur on the pupils and it can in principle be characterized and compensated by moving the CCD in order to keep the pupils fixed. The common mode we measured for a 120° bearing rotation is of 75 μm in one direction and 40 μm in the other direction (see Figure 5-28)

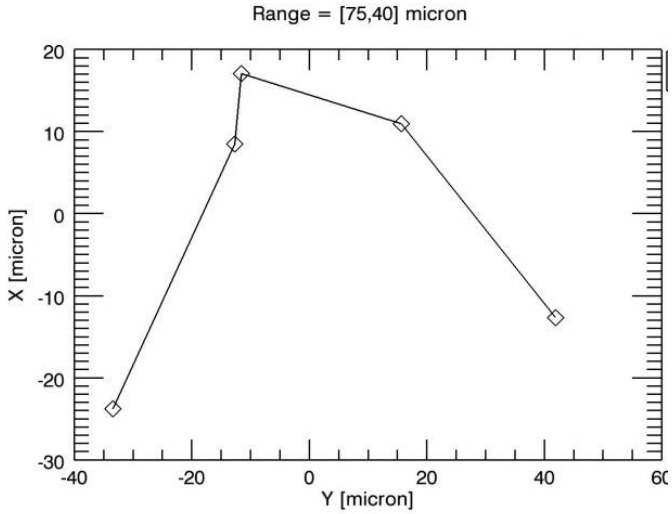

Figure 5-28: Common mode of the pupils produced by all the SEs for a 120° bearing rotation.

On the other hand, the differential movement affects the pupil blur, and, for this reason, it must be characterized and minimized. It is mainly due to the differential flexures of the

SE mechanical structure, tip-tilt stages, linear stages and local deformations of the GWS structure. The common mode was removed and what remains is the differential movement of the SEs (see Figure 5-29). The expected value for this test from the Error Budget is 10.8 μm while our result is 8.0 μm, well below the expectations.

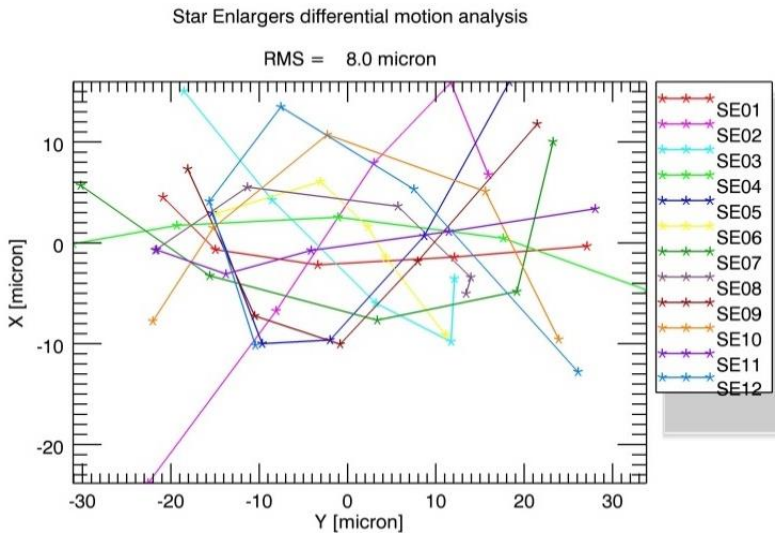

Figure 5-29: Differential movement of the spots baricentres of the 12 SEs for a 120° bearing rotation.

Moreover, despite its capability to perform a 120° rotation, the system is required to rotate for a maximum of 60° inside an observation, so a best 60° range can be selected, to reduce even more the differential movement of the pupils produced by the 12 SEs.
Finally, to further reduce the differential mode in the best 60° of bearing rotation, we computed numerically the theoretical position of the four spots produced by each SE that is minimizing their RMS movement. This numerical operation gives as an output, for each SE, the distance the barycentre of the 4 spots should fall from the pixel materializing the optical axis of the GWS (see Figure 5-30)

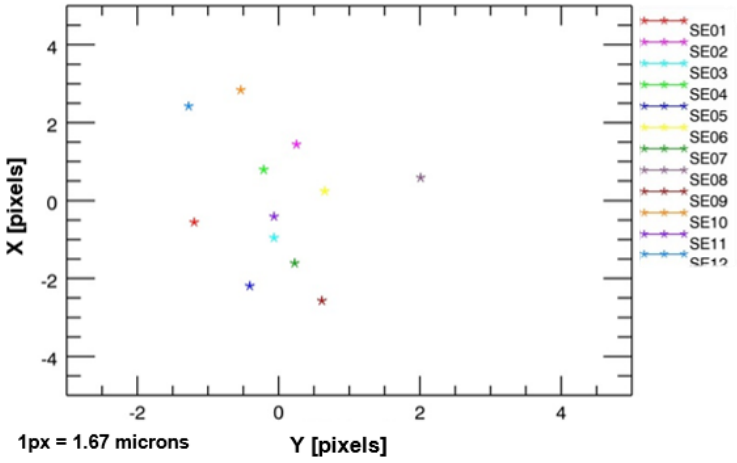

Figure 5-30: Computed SEs alignment position in tip-tilt to minimize the pupil blur in the best 60° bearing rotation. Pixel [0, 0) here represents the pixel materializing the optical axis of the GWS.

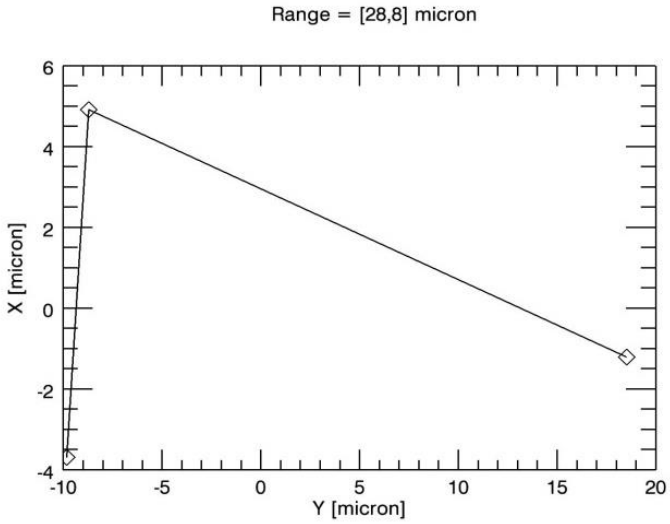

Figure 5-31: Common mode of the pupils produced by all the SEs for the best 60° bearing rotation.

After these optimizations, the measured residual differential movement of the pupils was of 5.8 μm, as shown in Figure 5-32.

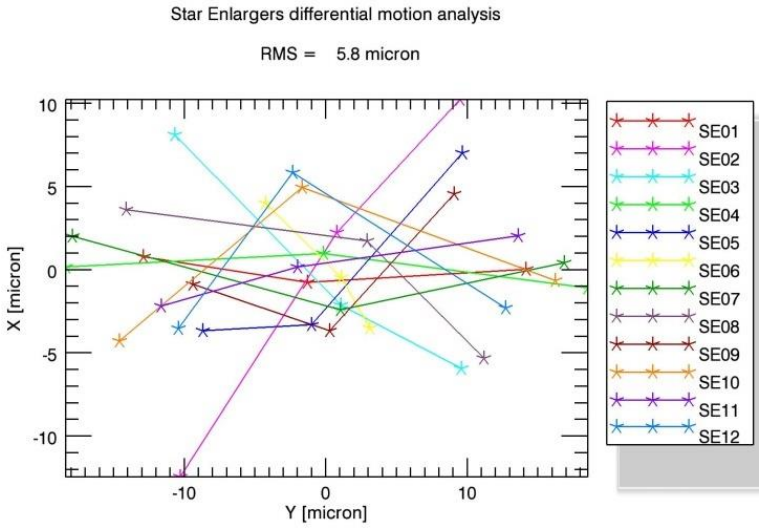

Figure 5-32: Differential movement of the spots baricentres of the 12 SEs after optimization, in the best 60° bearing rotation.

5.5.2 Test B: pupil blur due to SEs linear movement

The linear stages moving the SEs are subject to pitch and roll (movements or oscillation of an object around the axes of movement), and consequently the stage experiences small differential tilts when moving. The tilt of the linear stage is of course reflected on the SE, since they are mechanically coupled, leading to a blur of the pupils. This test is the measurement of the shift of each SE 4 pupil images on the detector. The shift has been measured illuminating the SEs with a collimated beam, and computing the movement of the 4 spots re-imaged on the CCD during the movement of the SE along a pre-defined path. The SEs sampled travels are summarized in and have been considered as representative of the SE behavior on its whole movement range.

Figure 5-33: Definitions of travels considered for test B. x and y lines represent the SEs travel spanned in this test.

The contributors to this test are:

- Pitch and Roll linear stages.
- Optical quality PR-I.
- SEs tilt due to ring flexures (a very small fraction. The SE movement causes a variation of the momentum applied to the linear stage and, consequently, to the ring supporting the linear stage. However, the weight of a SE is negligible compared to the one of the linear stage. For this reason, we will neglect here this term).
- SE tilt due to linear stage flexures (this term is here neglected since this test has been carried out with a fixed gravity vector, so its effect is negligible).
- SEs tilt due to support flexures (negligible for the same reason above).

The resulting RMS shift for each of the travels shown in Figure 5-33 is reported in Table 5-6.
The expected value from the Error Budget, 13.9 μm, is compatible with most of the measured RMS blurs. SE04 and SE09 measured shift blurs resulted to be higher than the expected value, even when the whole y operational range is considered. The range that will be actually spanned by the SEs, however, is even smaller because of the split of the FoV into two annuli: even-labeled SEs will only explore the outer part of the GWS FoV, while odd-labeled SEs will work in the inner part. If these ranges are considered, the

measured wobble is reduced below the expected value of 13.9µm for all the SEs. The requirement is then fulfilled.

SE	*x (µm)*	*y whole range (µm)*	*y operational range (µm)*
SE 01	2.5	5.4	2.9
SE 02	1.7	5.4	5.4
SE 03	4.2	4.2	2.9
SE 04	4.6	33.7	14.2
SE 05	4.2	10.0	9.2
SE 06	1.7	7.1	6.2
SE 07	6.7	11.8	6.2
SE 08	2.5	5.4	3.3
SE 09	2.5	27.5	17.5
SE 10	2.5	35.0	8.4
SE 11	1.7	10.0	4.6
SE 12	3.3	3.3	2.9

Table 5-6: Results of the test on SEs linear stages wobble for GWS SX. Units are microns of RMS displacement of the pupils on the CCD. "Y operational range" is the actual range inside which the SEs explore a 2 to 6 arcmin FoV, while the y whole range exceed this area.

5.5.3 Test C: white light static pupil blur

A pupil blur analysis in static conditions, i.e. without moving the SEs or rotating the bearing, has been performed feeding one of the SEs, SE04, with an F/15 beam in white light. Since in this test there are no moving parts all the flexures terms are here neglected. Moreover, since this test does not give any information about the pupils positions, all the related contributors are also excluded. The terms contributing to the result of this test are then only:

- The SE diffraction.
- The pyramid chromatism.
- The PR-I optical quality (here neglected since for this test only a well-defined small portion of the PR-I is used).

A calibrated USAF resolution test chart (see Figure 5-34) has been used as a reference for the measurement of the Modulation Transfer Function of the system.

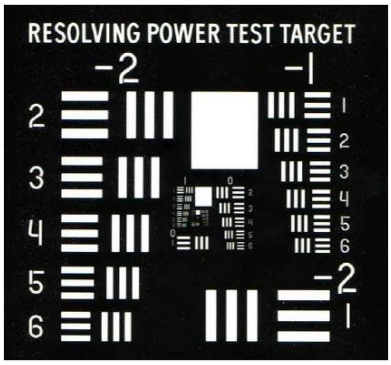

Figure 5-34: USAF 1951 target used for optical quality check of SE04.

This target presents different triplets of lines, with increasing width and separation, which are divided into groups of 6 elements. Table 5-7 summarizes the spatial frequencies of the triplets contained in a complete USAF target, according to the expression:

$$R(lp/mm) = 2 \cdot G + (E - 1)/6$$

Where *R* is the resolution of the considered triplet and *G* and *E* the group and the element numbers, respectively.

Element	**-2**	**-1**	**0**	**1**	**2**	**3**	**4**	**5**	**6**	**7**	**8**
1	0.250	0.500	1.00	2.00	4.00	8.00	16.00	32.0	64.00	128.0	256.0
2	0.280	0.561	1.12	2.24	4.49	8.98	17.95	36.0	71.8	144.0	287.0
3	0.315	0.630	1.26	2.52	5.04	10.10	20.16	40.3	80.6	161.0	323.0
4	0.353	0.707	1.41	2.83	5.66	11.30	22.62	45.3	90.5	181.0	362.0
5	0.397	0.793	1.59	3.17	6.35	12.70	25.39	50.8	102.0	203.0	406.0
6	0.445	0.891	1.78	3.56	7.13	14.30	28.50	57.0	114.0	228.0	456.0

Table 5-7: Number of line pairs/mm in USAF resolving power test target 1951.

Since the lowest group number in our target is 0, the lowest spatial frequency we can take into account is 1 mm spacing between the lines. The target is positioned in the setup pupil stop position and illuminated with the collimated white light produced with a 600 μm core optical fiber. For all the elements composing group 0, the profiles of the re-imaged lines are retrieved and the MTF is measured as the contrast between light and dark regions, according to the following expression:

$$MTF\ (f) = \frac{Peak - Valley}{Peak + Valley}$$

Figure 5-35 shows the obtained MTF for SE04. We define our resolution limit as the spatial frequency at which the MTF reach the 0.5 value, corresponding to a line width of 0.5 *mm*, re-imaged as 0.5 × 21.2 × 1.67 = 17.7 μm onto the test CCD (f_{PRI} /f_{lens}/ k_{SE}/ pixel size).

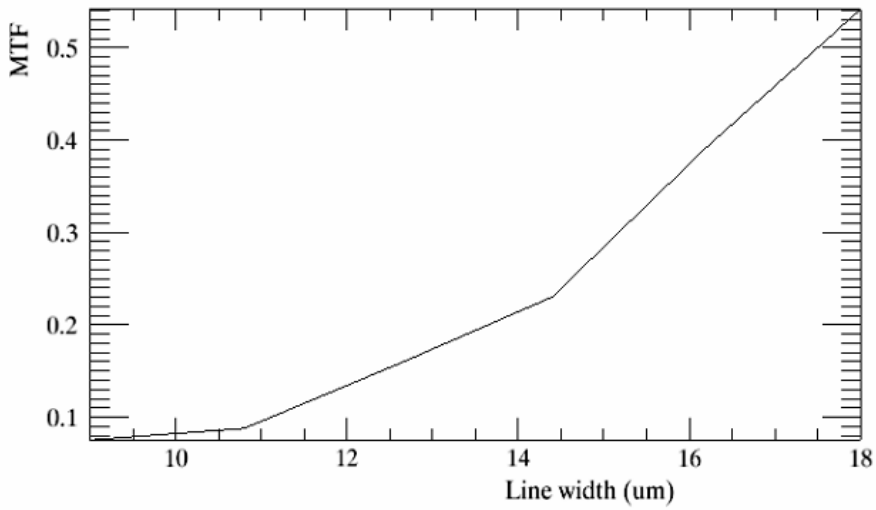

Figure 5-35: Measured MTF of the GWS through SE04.

In Figure 5-36, the convolution of a top-hat repeated pattern, representing the physical lines width re-imaged onto the CCD, with a Gaussian profile 17.7 μm wide (blue line), has been superimposed to the retrieved profiles of the 0.5 *mm* wide lines triplet so as to compare the two shapes and showing good agreement.

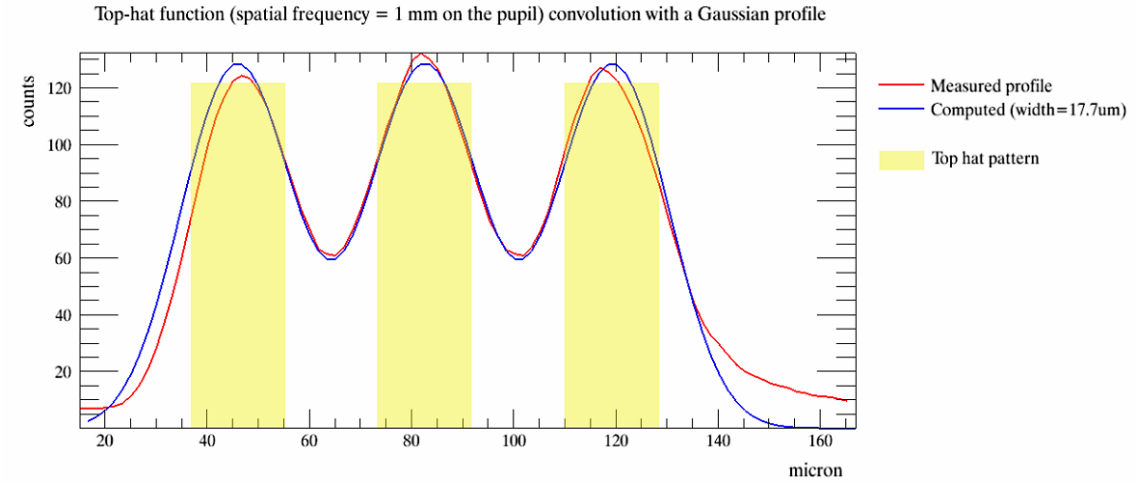

Figure 5-36: Top-hat pattern convolution with a Gaussian profile (Gaussian width = 17.7 µm) for the higher orders (USAF, group #0, element #1). The yellow areas show the top-hat pattern, the red line represents the measured profile, while the blue one is the computed profile with a Gaussian width of 17.7 µm.

To compare the result of this test with the expectations from the Error Budget we have to divide the 17.7 μm by a factor 2, since this value is related to the pupil diameter while the values reported in the Error Budget are related to the radius. The result of this test is then a static blur on the pupil images of 8.9 μm, consistent with the 9.2 μm expectation.

5.5.4 Test D: pupil blur due to GWS flexures

The results reported here refer to the flexures test performed on the GWS DX in Heidelberg, before its shipment to the LBT for a Pathfinder Experiment, and are considered representative of the behaviour of GWS SX, for which this test was not carried out.
The aim of this test is to quantify three main flexures effects:

- SEs shift: it translates into a tip-tilt signal onto the WFS. The common part can be compensated re-centering the SEs during an exposure.

- SEs tilt: it translates into a shift of the pupils on the detector, producing, if relative between different SEs, a pupil blur, to be taken into account in the error budget. The common part can be compensated re-centering the CCD during an exposure.

- SEs defocus: it translates into a defocus signal onto the WFS.

Flexure effects, if repeatable, may be compensated by the available degrees of freedom:

- The pupil displacement, provided it is the same for all the SEs, can be corrected by centering and/or refocusing the CCD camera by means of the motorized linear stages specifically foreseen for this purpose.

- The tilt signal due to a SE lateral shift can be corrected by centering the SE on the respective reference star.

- The defocus signal can be compensated by refocusing the FP15 optics, provided the defocus is the same for all SE.

The contributors affecting the system during this test are:

- GWS flexures.

- Bearing flexures.

- SE tilt due to support flexures (a fraction. Here considered $1/\sqrt{2}$).

- SE tilt due to ring flexures (a fraction. Here considered $1/\sqrt{2}$).

- SE tilt due to stage flexures (a fraction. Here considered $1/\sqrt{2}$).

To carry out this test the GWS DX was mounted on the LN bench, which is in turn mounted on a large tilting stage allowing to change the inclination of the whole bench.

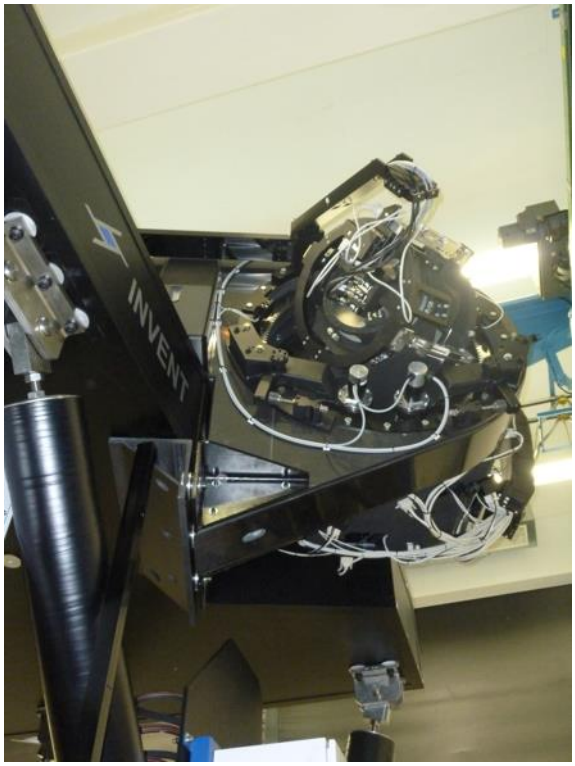

Figure 5-37: GWS DX mounted on the LN bench ready for the flexures test.

An F/15 source was positioned at the entrance focal plane (see Figure 5-38). This source is mounted with mechanical precision and the tilt of the F/15 beam was adjusted by shimming the mount.

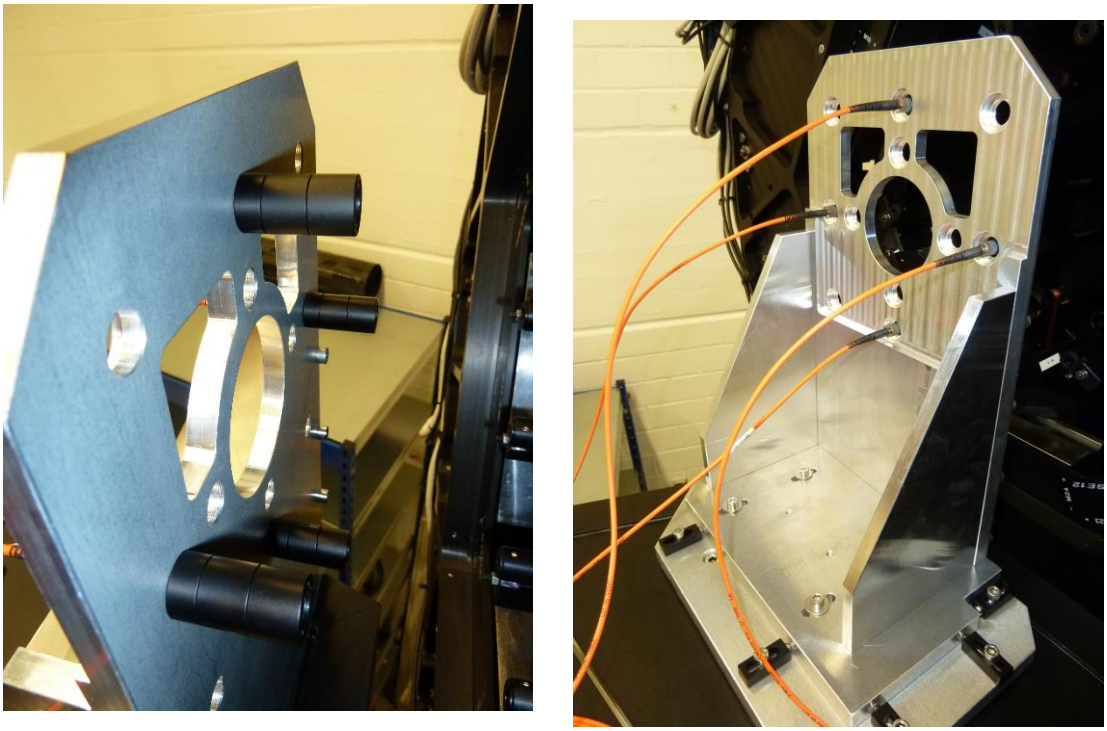

Figure 5-38: F/15 reference sources used during the flexures test.

The F/15 simulator consists of four optical fibers, each re-imaged by a lens at the GWS entrance focal plane. A telecentric aperture stop is placed between the source and the lens, in order to obtain the proper F/#. The fibers have a 200 μm core; this size was chosen in order to have a linear response of the pyramid wavefront sensor under the expected flexures effect (a fiber with a core too small would saturate the signal from the pyramid). The fibers are fed with white light, which can however introduce significant chromatism (i.e. a chromatic focal shift of the F/15 source lens). For this reason, for the defocus measurements a narrow bandpass filter centered at λ = 630 *nm* was inserted in the source in order to cancel chromatic effects.
The images recorded by the CCD50 camera are characterized by four pupil images of approximate diameter 48 pixels. The quantities to be measured are:

- Pupil image lateral shift.
- SE lateral shift or wavefront tilt.
- SE axial shift or wavefront defocus.

The lateral shift of the pupil images is simply computed fitting the edge of the pupil image with a circle, the center of the circle gives a measurement of the pupil position.
The measurement of the SE lateral shift is based on the calculation of the wavefront tilt slope detected by the pyramid WFS. The tilt signal, in arbitrary units, is converted into an equivalent lateral shift of the SE with respect to the F/15 source thanks to a preliminary calibration in which the SE was shifted of known amounts, using its linear stages, and the relative measured tilt signal was recorded (see.
The SE axial shift is measured in terms of wavefront defocus induced by this shift. As for the measurement of the SE lateral shift also in this case the system was calibrated, moving a F/15 source along the optical axis, in front of a SE, of known amounts and recording the corresponding defocus signal measured by the GWS.

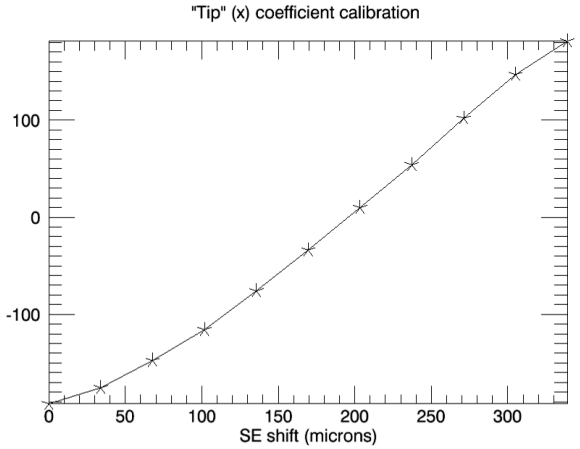

Figure 5-39: Tip-Tilt signal calibration measurement. The Y-axis reports the tilt Zernike coefficient variation.

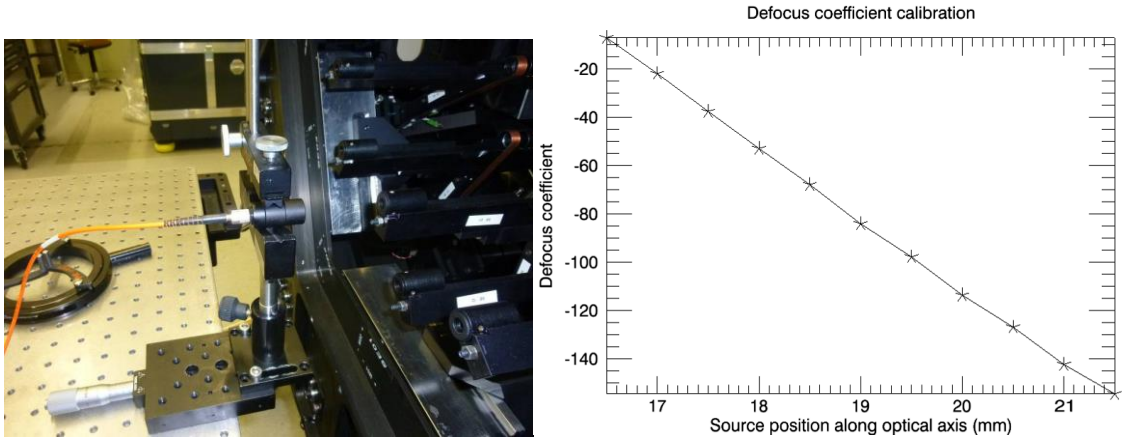

Figure 5-40: On the left, the setup used for the defocus signal calibration. On the right the relationship between a shift of the F/15 source along the optical axis and the defocus signal, expressed in terms of Zernike coefficient, measured by the GWS.

To measure the desired quantities four tests have been performed. All the measurements described in the following have been repeated in a combination of bench tilt angles, bearing rotation angles and SEs radial positioning in the field, to try to disentangle possible flexures sources.

	SEs	**LN bench tilt**	**Bearing rotation**	**SEs radius in FoV**
Test #1	All	0°, 15°, 30°, 45°, 60°	0°	79 *mm* (2.2 *arcmin*)
Test #2	SE02, SE03, SE05, SE06, SE08, SE09, SE11, SE12.	0°, 15°, 30°, 45°, 60°	-60°, -30°, 0°, 30°, 60°	79 *mm* (2.2 *arcmin*)
Test #3	SE02, SE06, SE08, SE12.	0°, 15°, 30°, 45°, 60°	0°	50 *mm* (1.4 *arcmin*) 79 *mm* (2.2 *arcmin*) 108 *mm* (3 *arcmin*)
Test #4	SE04, SE06, SE10, SE12.	0°, 15°, 30°, 45°, 60°	0°	79 *mm* (2.2 *arcmin*) (repeatability test)

Table 5-8: Configurations for the different tests.

Pupil shift

The pupil shift due to flexures has been measured, for each SE source separately, combining the CCD50 movement necessary to keep the pupils inside the chip with the computed shift of the pupils in the images. The first measurement performed at 0° is taken as reference for the pupil image shift of a given SE. In this way, the common mode and each source of relative misalignment are removed.

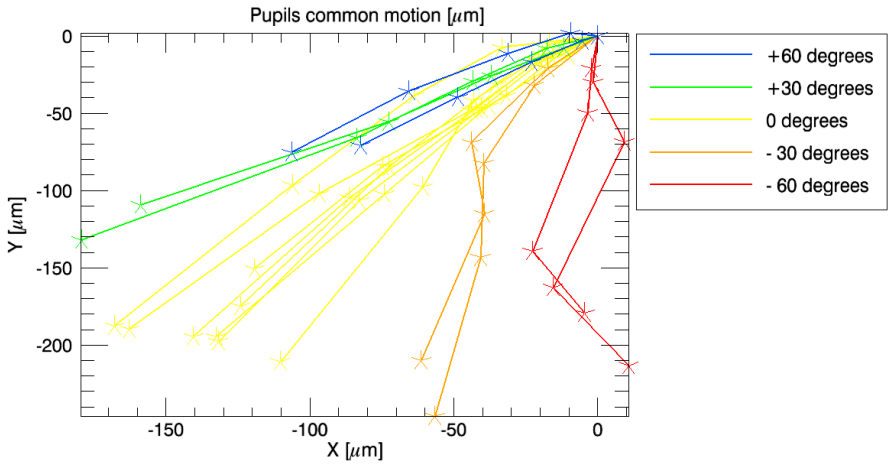

Figure 5-41: Pupils common motion in 16 different bench tilt runs. Different colors represent different bearing rotation angles. Each point of each curve represents a bench tilt.

- Test #1: Figure 5-42 shows the results obtained for the pupils shift due to flexures for each SE. There is no obvious correlations between the measured shift and the SEs position or the considered bench tilting run. The measured RMS shift of the pupils increases with the bench tilt angles (up to ~ 46 μm for a 60° bench inclination), and this effect could partially be due to a CCD50 shift along the optical axis. Such movement could be of the same order of magnitude of the CCD50 lateral shift.

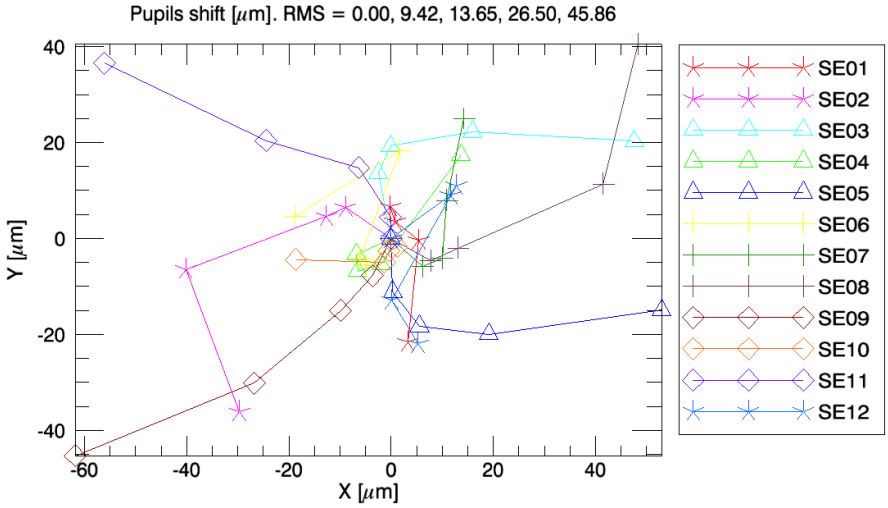

Figure 5-42: Pupils shift measured on the CCD50 for Test#1. Different colors represent different SEs, while different symbols are used to group SEs tested in a common run. Each point of each curve represents a bench tilt. The pupils shift RMS are reported on top of the figure, for the bench tilt listed in Table 5-8.

To try to remove a possible CCD50 axial shift effect from the data, a software routine has been realized. The pupils' barycenters for each SE have iteratively been shifted on the pupil plane in the direction they would have shifted because of a CCD defocus and of an amount proportional to the distance of the source from the center of the GWS FoV. Since, as will be clearer later, the flexures effect seems not to be very repeatable, this procedure has been separately repeated for each run.
The obtained "corrected" pupils shift are reported in Figure 5-43. While a clear evidence of correlation between the measured shift and the SEs position or the considered bench tilting run is still missing, the maximum RMS value decreased from ~ 46 μm to ~ 29 μm for a 60° bench inclination.

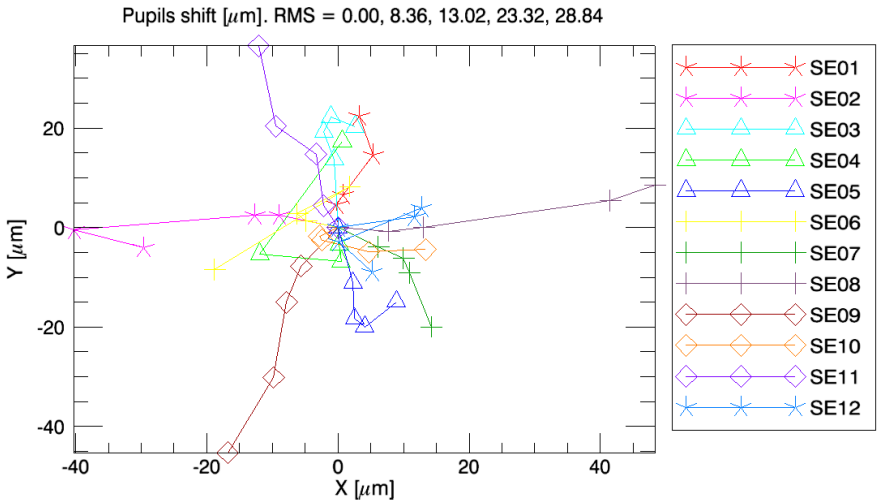

Figure 5-43: Pupils shift measured on the CCD50 and a-posteriori corrected via software optimizing the CCD50 position along the optical axis for Test #1. Different colors represent different SEs, while different symbols are used to group SEs tested in a common run. Each point of each curve represents a bench tilt. The pupils shift RMS are reported on top of the figure, for the bench tilt listed in Table 5-8.

- Test #2: The obtained "corrected" (applying the CCD50 defocus optimization) pupils shift are reported in Figure 5-44. The maximum RMS value for a 60° bench inclination is ~ 23 μm. Any evidence of correlation between the measured shift and the bearing position is missing.

- Test #3: The obtained "corrected" (applying the CCD50 defocus optimization) pupils shift are reported in Figure 5-45. The maximum RMS value for a 60° bench inclination is ~ 30 μm. Also in this case, any evidence of correlation between the measured shift and the SE position is missing.

- Test #4: The obtained "corrected" (applying the CCD50 defocus optimization) pupils shift are reported in Figure 5-46. The maximum RMS value for a 60° bench inclination is ~ 19 μm. Even with all the applied corrections, the measurement repeatability seems to be very low.

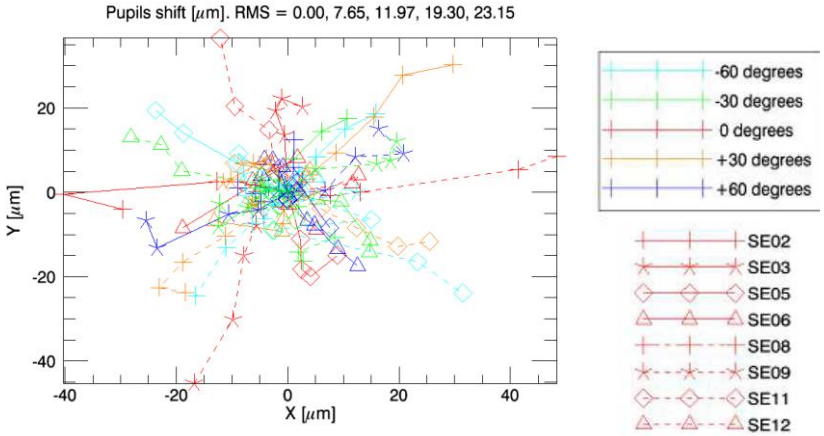

Figure 5-44: Pupils shift measured on the CCD50 and a-posteriori corrected via software optimizing the CCD50 position along the optical axis for Test #2. Different colors represent different bearing rotation angles. Each point of each curve represents a bench tilt. The pupils shift RMS are reported on top of the figure, for the bench tilt listed in Table 5-8.

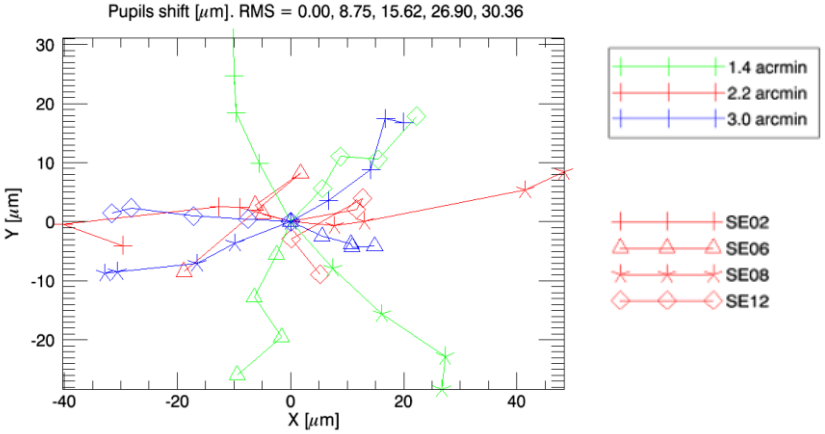

Figure 5-45: Pupils shift measured on the CCD50 and a-posteriori corrected via software optimizing the CCD50 position along the optical axis for Test #3. Different colors represent different SEs radial positions, different symbols represent different SEs. Each point of each curve represents a bench tilt. The pupils shift RMS are reported on top of the figure, for the bench tilt listed in Table 5-8.

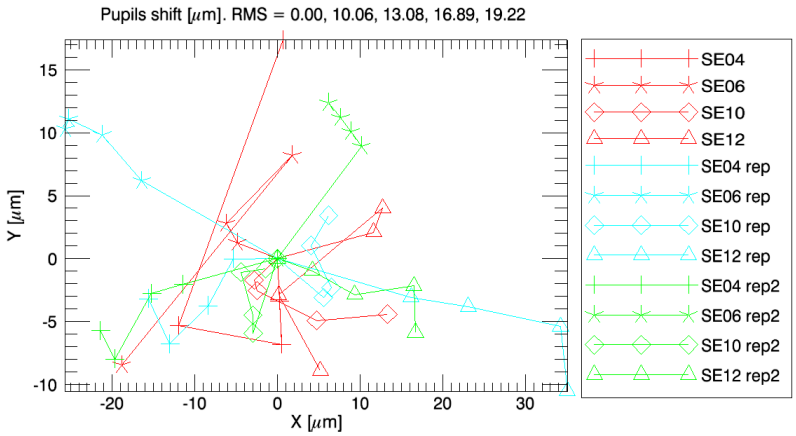

Figure 5-46: Pupils shift measured on the CCD50 and a-posteriori corrected via software optimizing the CCD50 position along the optical axis for Test #4. Different colors represent different runs, different represent different SEs. Each point of each curve represents a bench tilt. The pupils shift RMS are reported on top of the figure, for the bench tilt listed in Table 5-8.

For all the tests described above, the RMS shift of the pupils was basically halved by numerically optimizing the CCD50 position along the optical axis. Table 5-9 are reported all the computed CCD50 axial shifts applied to minimize the RMS shifts shown above.
It is quite clear that the CCD50 axial shift seems to be not repeatable, but rather strongly depending on the bench tilt run. Of course, since this is the result of an optimization it might be possible that, doing this, we are compensating other effects. To check this other two runs have been performed, tilting the bench up to 60° while keeping the bearing rotation fixed.
Figure 5-47 and Figure 5-49 show the measured pupil shifts (red symbols) for run1 and run2, in which two different groups of SEs have been selected. The optimization procedure returned a computed CCD50 axial shift of 131 μm and 154 μm for the two runs, to obtain a minimum expected RMS value of ~ 14 μm and ~ 22 μm, respectively (green symbols). After this first measurements, for each run the CCD50 has been shifted along the optical axis of the computed amount and the pupils' position have been measured again.
Figure 5-48 and Figure 5-50 show the result of this second measurement for the two runs. In both cases a small residual de-focus has been detected (this could due to the lack of a fine-tuning of the computing procedure calibration), but the actual RMS values have decreased from 48.3 μm and 55.5 μm to 14.5 μm and 23.3 μm, in both cases very close to the expectations.

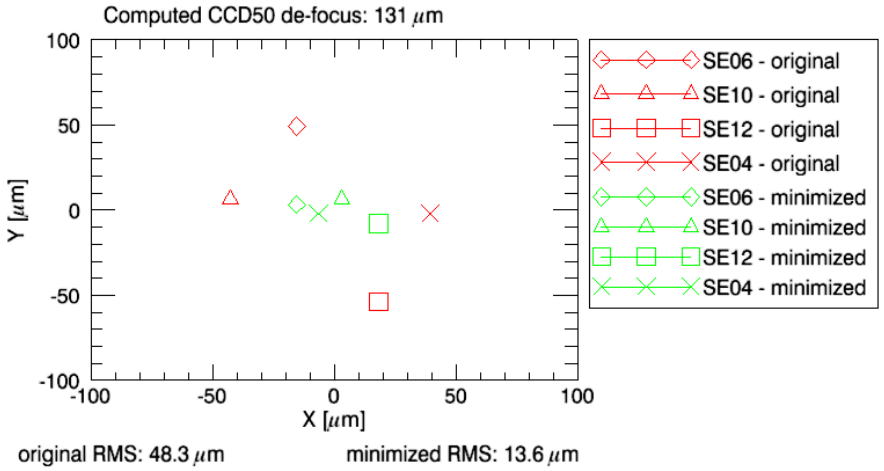

Figure 5-47: Result of run1, in which SE06, SE10, SE12 and SE04 have been considered. Red symbols represent the actual pupil shift, while green symbols represent the expectation of the pupils positions for a 131 μm shift of the CCD50 to compensate for flexures for a 60° bench tilt.

	Bench tilt angle					
Run	**15°**	**30°**	**45°**	**60°**		
1	-6	6	49	130		
2	-6	9	43	127		
3	-20	-20	29	33		
4	-12	-6	17	92		
5	-9	12	69	170		-60°
6	-6	12	69	158		-30°
7	6	29	147	193		0°
8	3	46	92	210		+30°
9	-12	-9	23	81		+60°
10	-32	-43	-43	-6		IN/OUT FoV
11	-20	-29	14	109		
12	12	12	55	147		
13	9	49	144	190		
14	-17	-14	3	63		
15	-23	-35	-20	9		
16	17	55	98	225		

Table 5-9: Computed CCD50 shift [μm] for different runs and bench tilt angles.

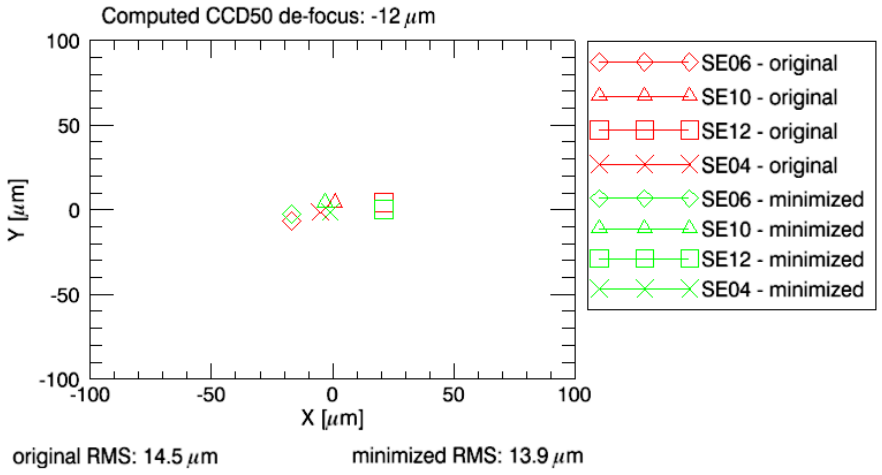

Figure 5-48: Result of run1, after the CCD50 re-adjustment. There is a small residual shift, which could still be better optimized. The measured pupils' positions are very close to the expectations.

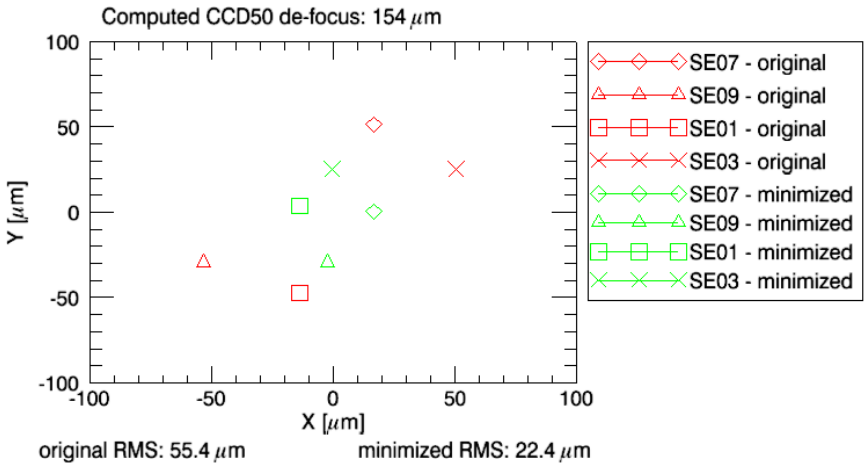

Figure 5-49: Result of run2, in which SE07, SE09, SE01 and SE03 have been considered. Red symbols represent the actual pupil shift, while green symbols represent the expectation of the pupils' positions for a 154 μm shift of the CCD50 to compensate for flexures for a 60° bench tilt.

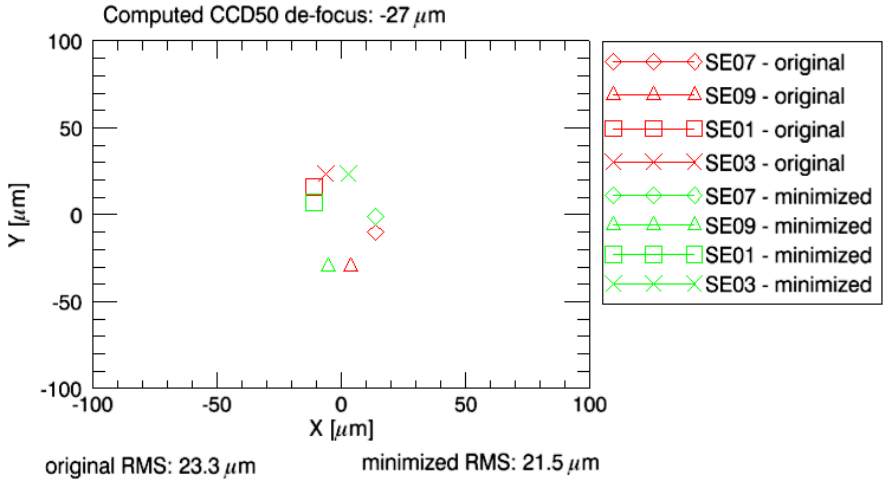

Figure 5-50: Result of run2, after the CCD50 re-adjustment. There is a small residual shift, which could still be better optimized. The measured pupils' positions are very close to the expectations.

To compensate for this effect at the telescope the idea is to implement a software routine correcting the CCD50 position during the exposure.

SEs lateral shift

The Star Enlargers lateral shift due to flexures has been measured, for each SE source couple separately, as the corresponding motor movement necessary to minimize the tip-tilt signature onto the four pupils. The first measurement performed at 0° is taken as reference for the lateral shift of a given SE.
Figure 5-51, Figure 5-52, Figure 5-53 and Figure 5-54 show the shifts, at the entrance focal plane, of the SEs during the tests listed in Table 5-8. The motion of each SE is translated and expressed as a movement in the SE01 reference frame.

- Test #1: All the measured shifts reported in Figure 5-51 are below 300 μm for a complete bench tilt (60°). No particular correlations between the measured shift and the selected SE position have been found.

- Test #2: All the measured shifts reported in Figure 5-52, in which also the GWS rotation angle has been changed, are below 300 μm for a complete bench tilt (60°). No particular correlations between the measured shift and the selected rotation angle have been found.

- Test #3: All the measured shifts reported in Figure 5-53, in which the SE radial position has been changed, are below 300 μm for a complete bench tilt (60°). No particular correlations between the measured shift and the SE position have been found.

- Test #4: All the measured shifts reported in Figure 5-54, concerning the repeatability test, are below 300 μm for a complete bench tilt (60°). However, the repeatability has proved to be not significative.

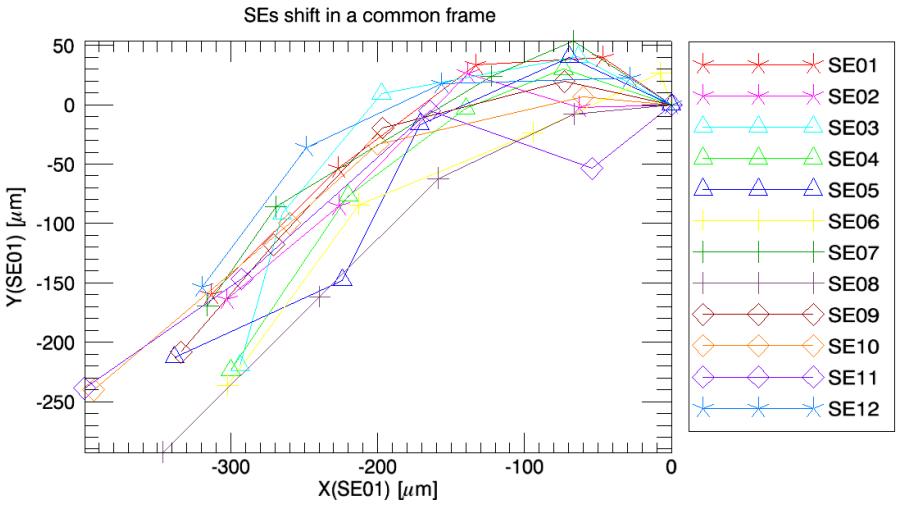

Figure 5-51: SEs shift measured as the motors movements necessary to minimize the tilt signal for Test #1. Different colors represent different SEs, while different symbols are used to group SEs tested in a common run. Each point of each curve represents a bench tilt.

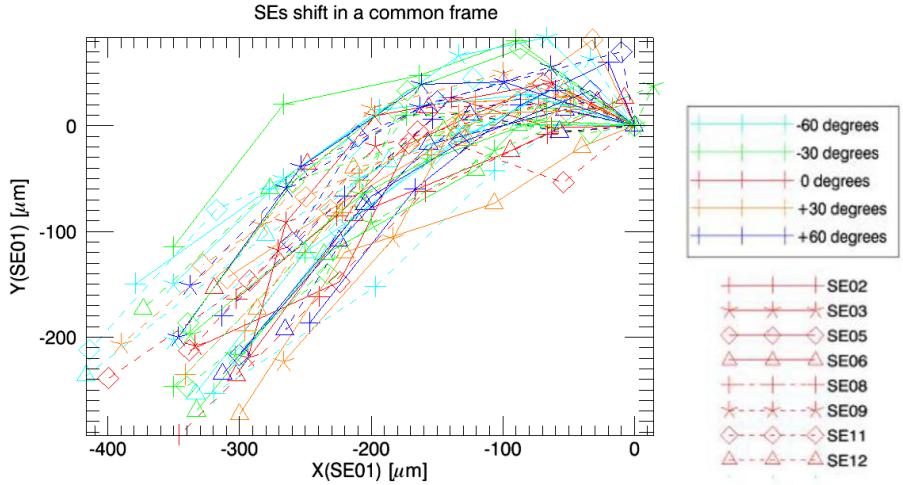

Figure 5-52: SEs shift measured as the motors movements necessary to minimize the tilt signal for Test #2. Different colors represent different bearing rotation angles. Each point of each curve represents a bench tilt.

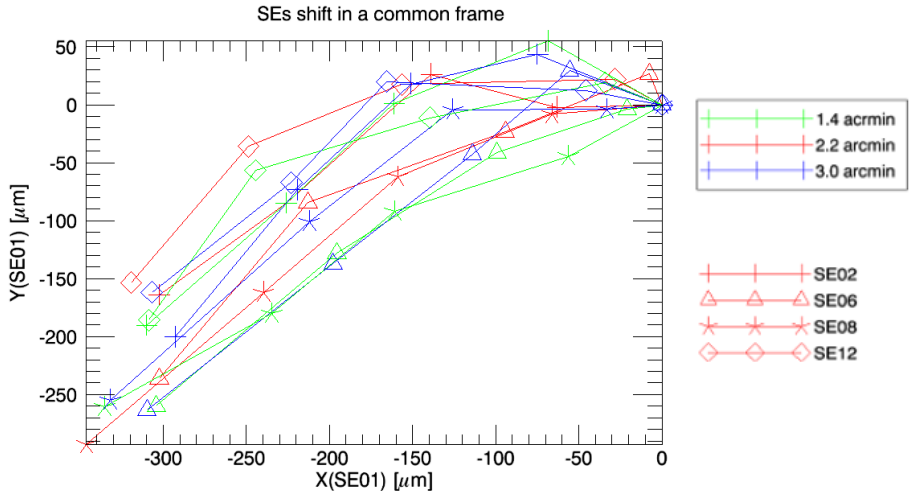

Figure 5-53: SEs shift measured as the motors movements necessary to minimize the tilt signal for Test #3. Different colors represent different radial positions. Each point of each curve represents a bench tilt.

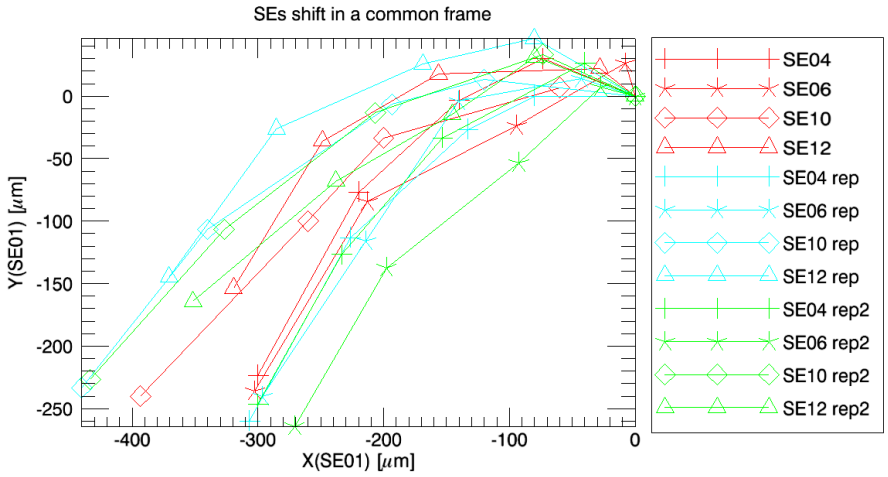

Figure 5-54: SEs shift measured as the motors movements necessary to minimize the tilt signal for Test #4. Different colors represent different runs, while symbols are related to the tested SEs. Each point of each curve represents a bench tilt.

For the compensation of this effect at the telescope, a software routine will re-center in real time the star image on the pyramid pin.

SEs axial shift

The Star Enlargers axial shift due to flexures has been measured, for each SE source couple separately, as the defocus signature into the four re-imaged pupils. The first measurement performed at 0° is taken as reference for the axial shifts of a given SE. In this way, each source relative misalignment is removed. In order to make the Zernike polynomials wavefront fitting as robust as possible, the images were taken after nulling the tip-tit signal. The only specification given for the SEs axial shift was to obtain a differential defocus lower than the one resulting from the curvature of the LBT F15 focal plane. In principle, if the axial shift is similar for all the SEs, this effect can be compensated shifting the annular mirror folding the light at the entrance of the GWS.
Figure 5-55, Figure 5-56, Figure 5-57 and Figure 5-58 show the shifts, along the optical axis, of the SEs during one of the Tests listed in Table 5-8.

- Test #1: all the measured shifts reported in Figure 5-55 for each SE are below 650 μm for a complete bench tilt (60°). No particular correlations between the measured shift and the SE position have been found.

- Test #2: all the measured shifts reported in Figure 5-56 for each SE are below 650 μm for a complete bench tilt (60°). No strong correlation between the measured shift and the bearing rotation position has been found.

- Test #3: all the measured shifts reported in Figure 5-57 for each SE are below 650 μm for a complete bench tilt (60°). No particular correlations between the measured shift and the SE position have been found.

- Test #4: all the measured shifts reported in Figure 5-58 for each SE are below 650 μm for a complete bench tilt (60°). As the previous ones, also this measurement seems not to be repeatable.

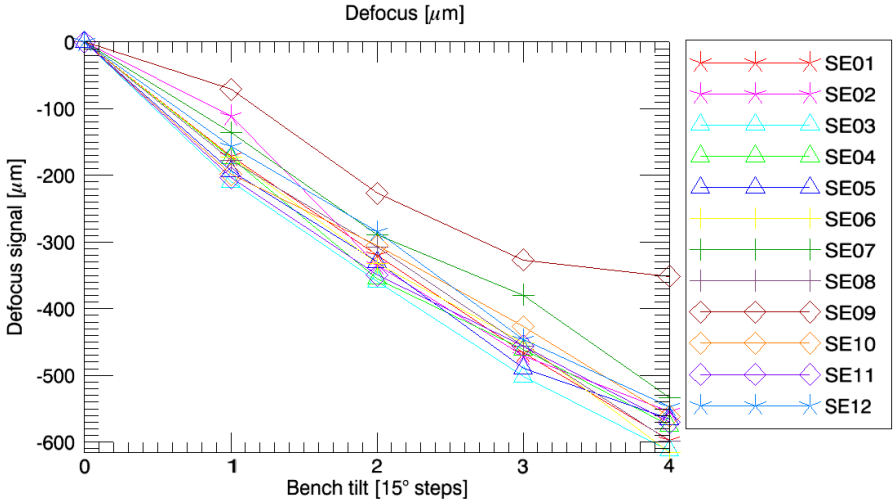

Figure 5-55: SEs axial shift measured as a defocus signature on the pupils for Test #1. Different colors represent different SEs, while different symbols are used to group SEs tested in a common run. Each point of each curve represents a bench tilt.

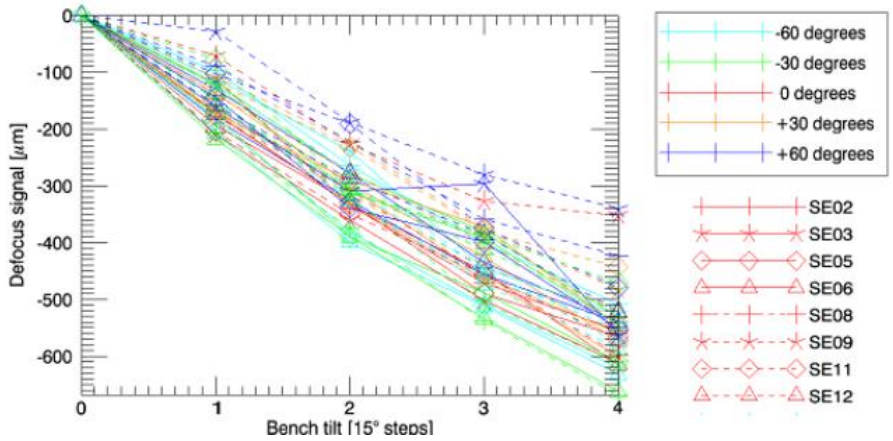

Figure 5-56: SEs axial shift measured as a defocus signature on the pupils for Test #2. Different colors represent different bearing rotation angles. Each point of each curve represents a bench tilt.

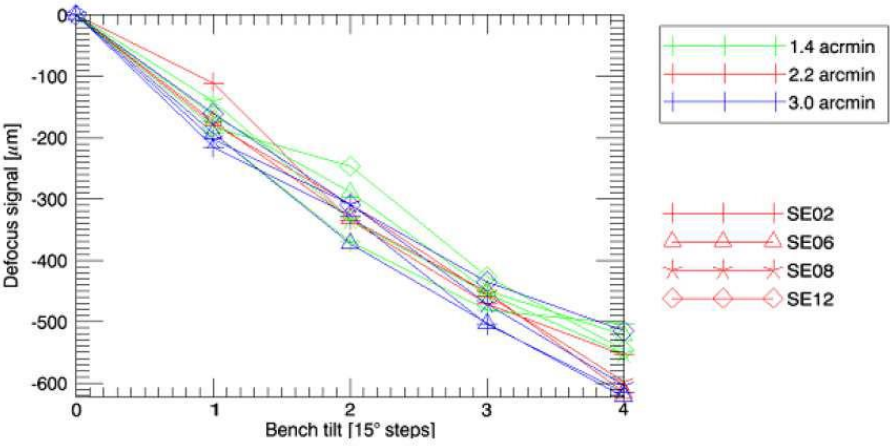

Figure 5-57: SEs axial shift measured as a defocus signature on the pupils for Test #3. Different colors represent different radial positions. Each point of each curve represents a bench tilt.

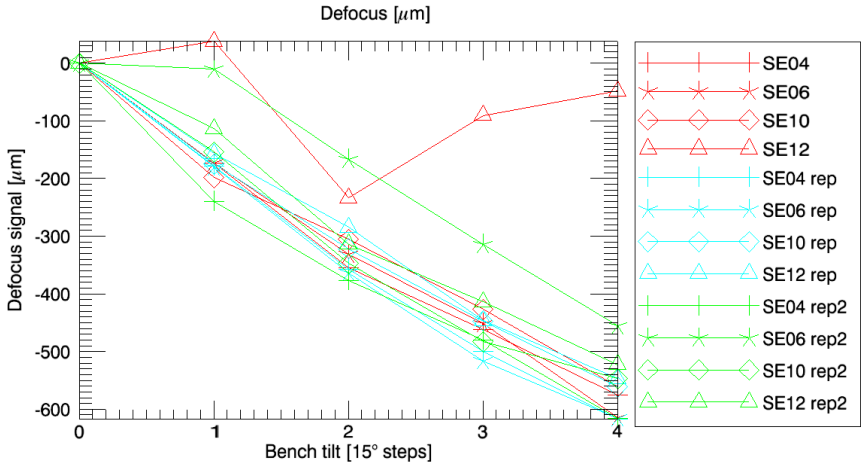

Figure 5-58: SEs axial shift measured as a defocus signature on the pupils for Test #4. Different colors represent different runs, while symbols are related to the tested SEs. Each point of each curve represents a bench tilt.

The result of this test indicates that the differential defocus introduced by the flexures is negligible if compared to the maximum differential defocus experienced by the SEs due to the curvature of the LBT focal plane and therefore this item does not require any software for real time adjustment.

The final result of the flexures test is depicted in Figure 5-59, where the pupils' shift of all the SEs for different bench tilt and bearing angles are represented. Actually this test, more than a verification, was a measurement of the GWS flexures term, which could not be reliably estimated with a FEA.

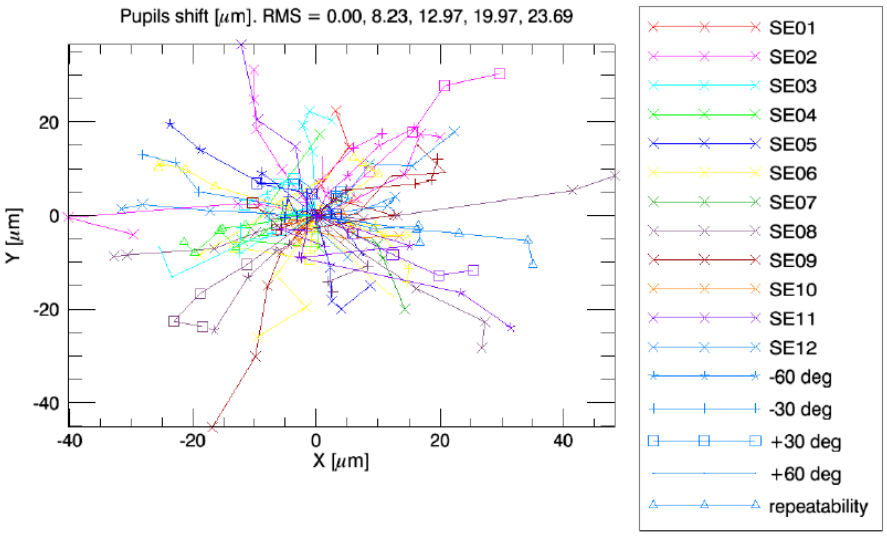

Figure 5-59: Pupils shift measured on the CCD50 and a-posteriori corrected via software optimizing the CCD50 position along the optical axis. Different colors represent different SEs. Different symbols represent different tests. The pupils shift RMS are reported on top of the figure, for the bench tilt listed in Table 5-10.

In Table 5-1 has been considered the conservative value of 24 μm pupil blur retrieved for a bench tilt of 60°, but of course the global performance of the GWS strongly depends from the tilt of the LN bench.
The estimated effect of GWS flexures, for different bench tilt, is reported in Table 5-10.
Due to the scarce repeatability of the flexures effects, look-up tables and software routines are being developed, allowing the re-centering of the SEs and the re-centering and focus adjustment of the CCD during the observation.

Bench tilt	**0°**	**15°**	**30°**	**45°**	**60°**
Pupil blur	0 μm	8 μm	13 μm	20 μm	24 μm

Table 5-10: Estimated pupil blur due to the GWS flexures for different LN bench tilt angles.

5.6 Conclusions

All the tests performed on the GWS demonstrated the validity of the alignment and the compliance of its performances with the expectation from the Error Budget, returning, in some cases, results well below the expectation. This, in principle, allows us to relax the specification for other items, like for example the linear stages pitch and roll (which was not satisfied for all the linear stages, even if I recall they will not span their entire travel range because of the splitted FoV), keeping at the same time the overall performance of the GWS within the expectations.
Considering the values reported in Table 5-1, and using Formula [5-5], the performance of the GWS has been retrieved for different bench tilt angles, in terms of Strehl Ratio in J and K band. The values are reported in Table 5-11 and, even in the worst conditions (bench tilt of 60°), the GWS performance (SR 0.60 in J band and 0.85 in K band) satisfies the requirement. The alignment of the GWS SX was then declared successful and the system was shipped to Heidelberg for installation and alignment to the rest of the instrument.
In the meantime, the GWS DX, after the flexures test here described, was shipped at the LBT for a Pathfinder Experiment.

Bench tilt	**15°**	**30°**	**45°**	**60°**	**Goal**
SR (J)	0.76	0.73	0.65	0.60	0.61
SR (K)	0.92	0.90	0.87	0.85	0.85

Table 5-11: Estimated performance, expressed in terms of Strehl Ratio in J and K bands, of the GWS for different LN bench tilt angles

6 The Pathfinder Experiment

The technical complexity of an instrument like LN often translate into a difficult and long commissioning at the telescope. To mitigate this problem it was decided to sub-divide the commissioning into individual implementation phases. The first phase was the "Demonstration of the Ground layer Wavefront Sensor system", i.e. the Pathfinder Experiment, whose aim was to demonstrate the ability of the GWS to perform an AO correction driving its correcting device. Since the deformable mirror controlled by the GWS is the LBT Adaptive Secondary Mirror ("ASM" hereafter), taking advantage of the natural decoupling between the GWS and the HWS, the GWS was removed from the LN bench and shipped to the LBT. In this way, we were able to verify interfaces and communications between the GWS and the ASM, identifying possible software, mechanical or optical problems early, and thereby keeping the task of solving them out of the critical path. The pathfinder is a test-bed, consisting only of those subsystems needed to operate, stand-alone, the GWS DX of LN, which allowed us also to commission the LN focal station and to gain considerable on-sky experience.
The Pathfinder consists of 3 fundamental components:

- The GWS with the AM and electronics.
- A support structure (called "foot"), which support the GWS and the electronic cabinet, with a small platform where people can stand to perform activities on the GWS.
- The LBT InfraRed Test Camera (IRTC hereafter), to acquire scientific images and characterize the quality of the correction in the central 30'' FoV.

Operatively, the Pathfinder Experiment consisted of 9 runs at the telescope over a period of about 2 years, in which the following main results have been attempted:

- Pathfinder alignment to the telescope.
- Calibration of the interaction matrix.
- Close the loop on a single reference source.
- Close the loop on a single star non-rotating (i.e. on-axis).
- Close the loop on a single bright star, rotating.
- Close the loop on a single faint star, rotating.

Plus two additional extended goals:

- Multiple stars acquisition
- Close the loop on multiple stars

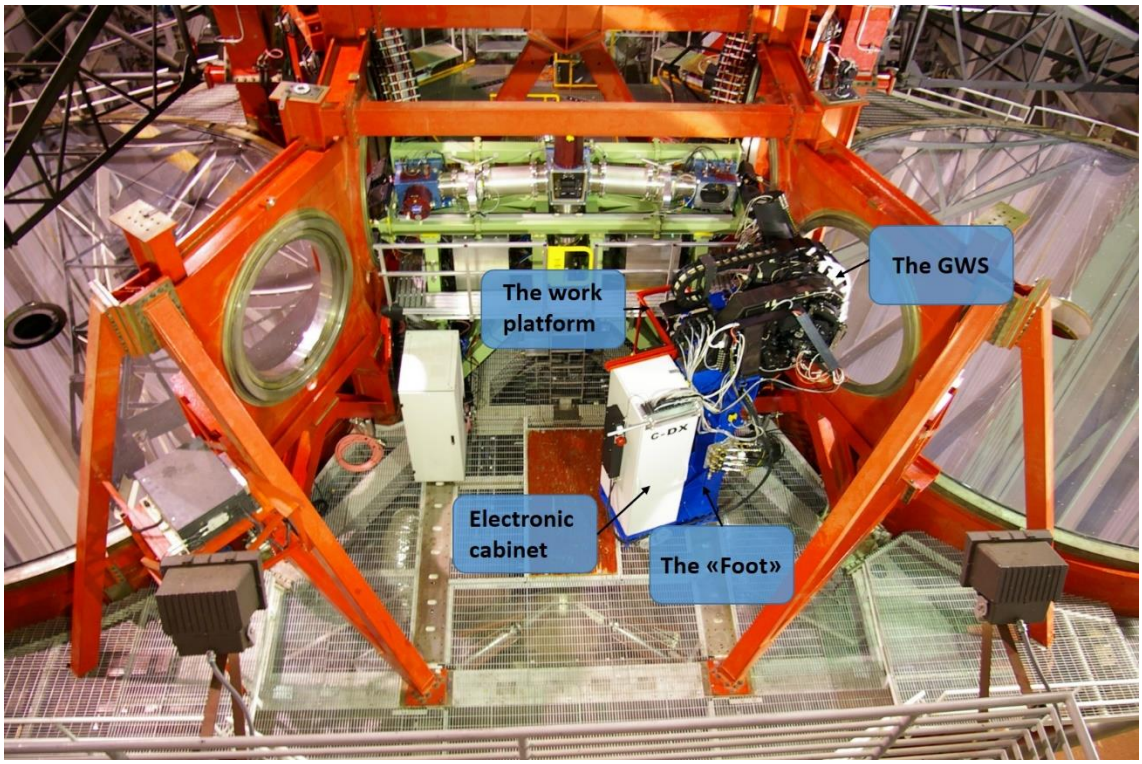

Figure 6-1: The Pathfinder mounted at the telescope and ready for its alignment to the LBT optical axis.

The last two runs are labelled with letter E in Table 6-1, as they were planned to pursue the extended goals ("E" stands for "Extended"). The first 3 Pathfinder runs at the telescope consisted mainly of unpacking, testing and recalibrating the Pathfinder after shipment from Europe, and all the operations preliminary to the alignment of the Pathfinder to the LBT. During T3 the Pathfinder was craned and positioned at the right, rear, bent focus of the LBT, at the same height the GWS will be located when mounted on the LN bench, ready for its alignment to the LBT optical axis.

T1	1 – 15 March 2013	Unpacking, verification of GWS. Assembly of the foot.
T2	3 – 11 April 2013	Star Enlarger mapping and BCU software testing.
T3	24 – 28 April 2013	Craning of Pathfinder from the LBT mountain lab to the telescope.
T4	01 – 08 October 2013	Alignment of Pathfinder mechanical rotation axis to the telescope optical axis.
T5	08 – 19 November 2013	Interaction matrix calibration and loop closed off-sky in the daytime. In nighttime first loop closed on-sky on a single bright star on-axis.
T6	04 – 10 December 2013	Rotating interaction matrices calibration during daytime. In nighttime loop closed on an off-axis bright star.
T7	29 March – 4 April 2014	Rotating interaction matrices calibration during daytime. In nighttime attempt multiple stars acquisition.
E1	29 June – 4 July 2014	Attempt multiple stars acquisition. Integrate IR camera for characterization of the correction.
E2	10 – 15 November 2014	Multiple star acquisition. Attempting to close the loop on multiple stars.

Table 6-1: List of the Pathfinder runs and the main results achieved.

6.1 Pathfinder alignment to the LBT optical axis

Aligning the Pathfinder to the DX telescope of the LBT means to make the optical axis of the telescope coincident with the bearing rotation axis (which also define the GWS optical axis). This created a unique challenge because of the lack of any on-axis surface or fiducials, due to the annular FoV of the GWS.
Conceptually, the idea behind the procedure is:

- To materialize the GWS axis (settled by the AM inclination).
- To materialize the telescope axis (settled by the ASM and the tertiary mirror of LBT (“M3” hereafter) nominal positions.
- To tune the AM and M3 tip-tilt in a way to have the two axis coincident.

To overcome the problem posed by the annular FoV of the GWS, we installed a small laser diode with an adjustable beam-expander (in order to focus the beam at the required distance) to the GWS, so that it can rotate jointly with the GWS bearing. A small folding mirror equipped with a motorized tip-tilt stage is installed on a small bench connected to the bearing in the central area of the GWS FoV and it reflects the light from the laser off the annular mirror to M3 (see Figure 6-6). A translucent screen, shown in Figure 6-5, is located at the telescope prime focus, below the ASM, and a camera with objective looking at it allows tracking the laser spot movement during a complete (120°) rotation of the bearing. Both of them are mounted on the telescope retro-reflector structure. Two different configurations are now used to perform the alignment. On one hand, the laser light is reflected by M3 directly to the translucent screen. When the bearing rotates the laser light traces an arc of a circle on the translucent screen, whose center indicates a point in the space through which the mechanical axis of the bearing passes (see Figure 6-2). On the other hand the laser light is reflected from M3 to the ASM and then to the translucent screen, from the other side (hence the need for a translucent screen). Again, when the bearing rotates, the laser light traces an arc of a circle on the screen, whose center materializes, this time, the optical axis of the telescope (see Figure 6-3). The transition between the two configurations is realized simply changing the tilt of the small mirror connected to the bearing (FM1 in Figure 6-2 and Figure 6-3). By adjusting the tip-tilt of the AM and M3, iterating between these two configurations, the two centers were made coincident and the Pathfinder was aligned to the telescope.

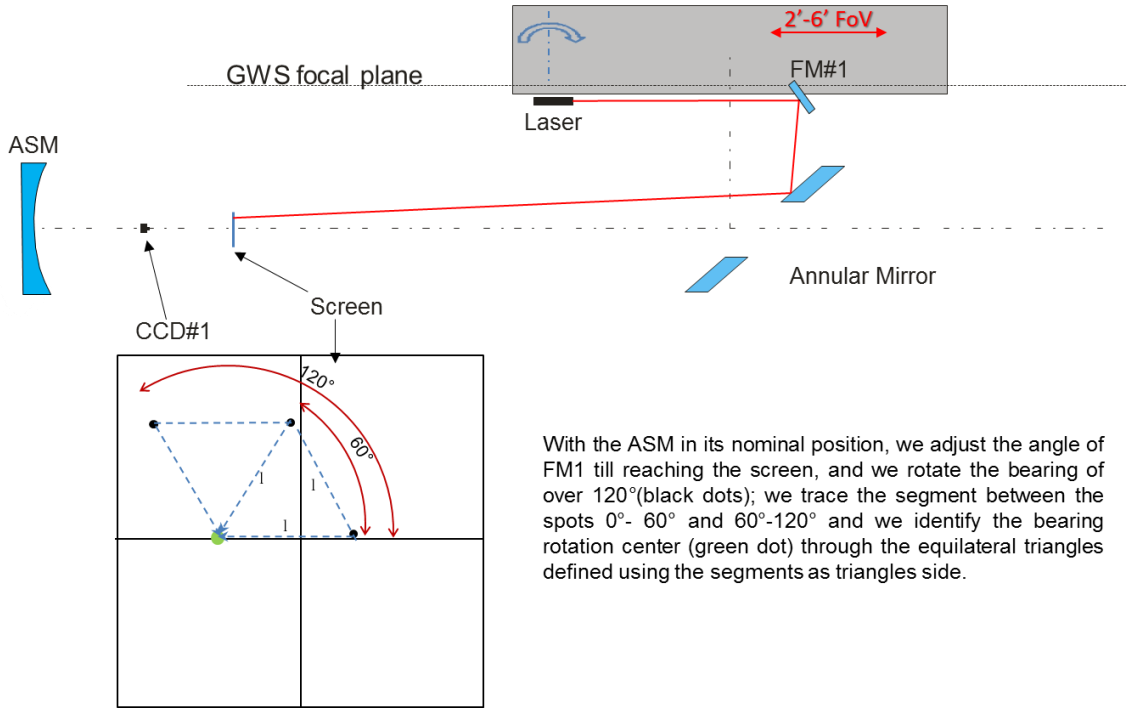

Figure 6-2: A schematic of configuration #1 of the GWS to LBT alignment procedure. M3 is not shown here for sake of simplicity.

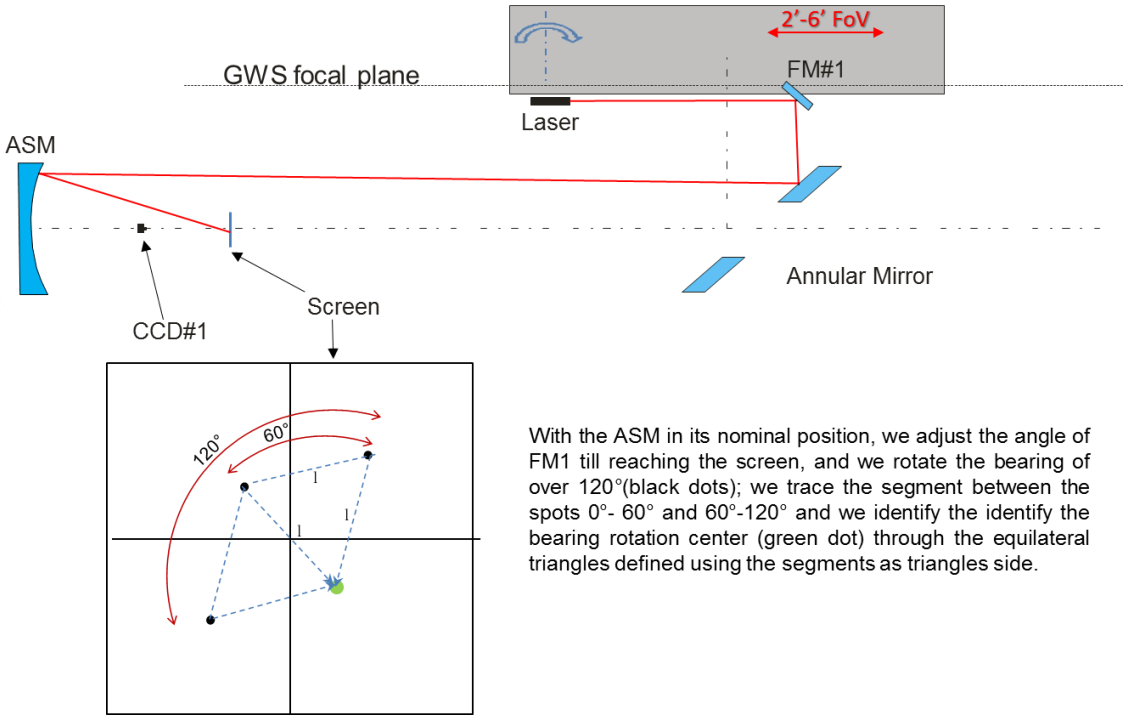

Figure 6-3: A schematic of configuration #2 of the GWS to LBT alignment procedure. M3 is not shown here for sake of simplicity.

Figure 6-4: The Pathfinder at the telescope. The green beam is the beam used in configuration #1 for the materialization of the bearing rotation axis, while the red beam was used in configuration #2 for the materialization of the telescope optical axis.

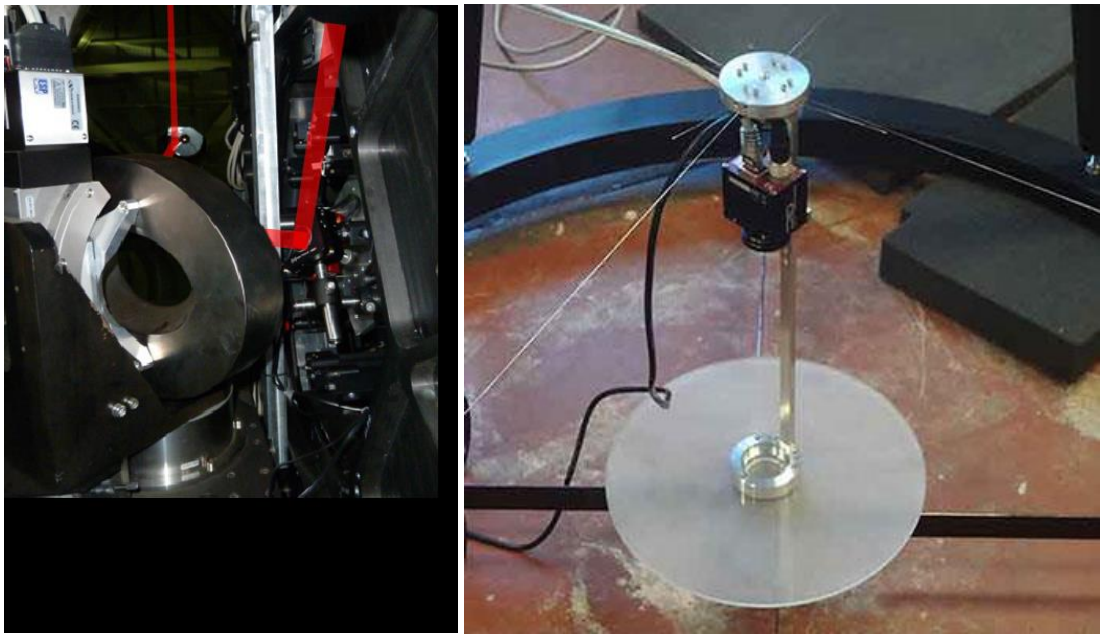

Figure 6-5: On the left the laser shining towards the small setup mirror, which reflects the light off the AM to M3. On the right the translucent screen end the setup camera looking at it, mounted on the telescope retro-reflector mechanics.

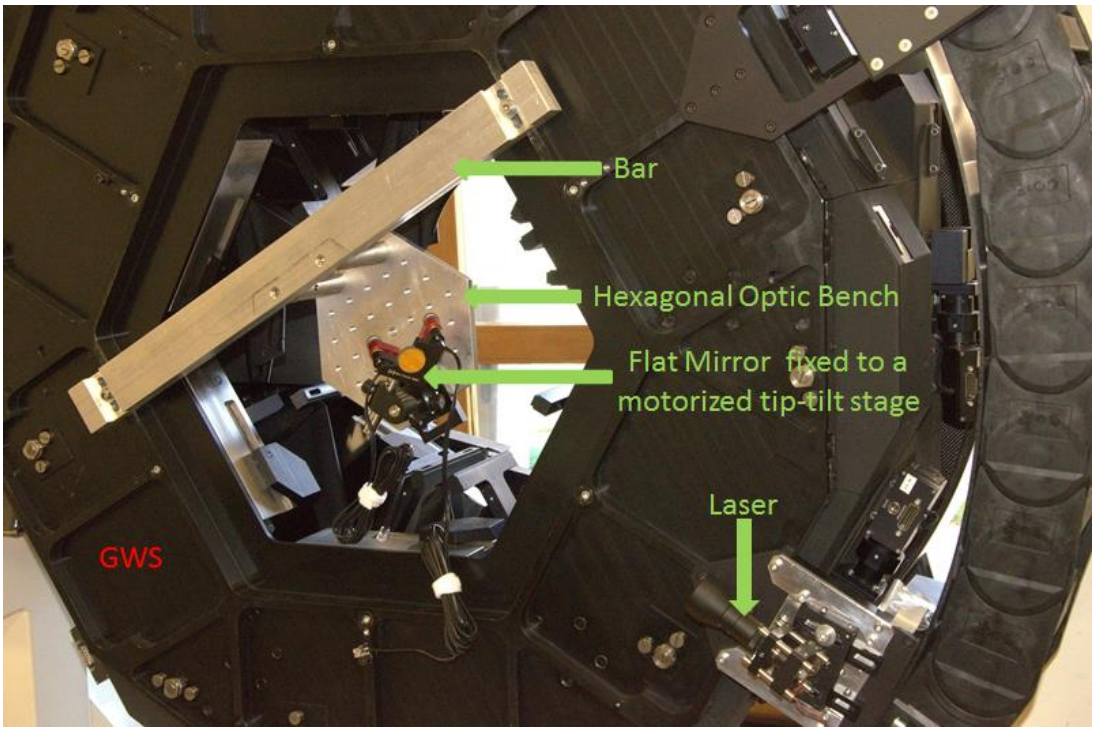

Figure 6-6: The setup mounted on the GWS used for pathfinder alignment.

6.2 Alignment of the IRTC

After the alignment of the Pathfinder to the telescope through AM and M3, whose positions are now frozen, the IRTC has been co-aligned to the GWS, and therefore to the telescope, both in focus, to have parafocality between the two systems, and in centering. The IRTC is a technical camera, developed for the commissioning of the First Light Adaptive Optics (FLAO) system of the LBT in 2008 by INAF – Osservatorio Astronomico di Bologna, Università di Bologna and MPIA in Heidelberg. It is constituted by a detector 320 x 256 pixel, 30 μm pixel size, and a 3 lenses objective in front. Two of these lenses can be moved along the optical axis, by means of 2 linear stages, to change the plate scale of the camera, and consequently the observable FoV. The maximum observable FoV is 30 *arcsec*. The wavelength range is J and H bands, from 0.9 μm to 1.7 μm. Since it observes at IR light, the whole camera is enclosed into a cryostat, to minimize the effect of thermal background radiation. This makes the IRTC quite massive and not easy to position on the Pathfinder. Moreover, the parafocality required between the GWS and the IRTC, demands to position the IRTC pretty close to the GWS entrance focal plane. However, due to its volume, the IRTC cannot be simply positioned in front of the GWS, because it would completely obscure the GWS technical FoV, and it cannot be positioned behind the AM without losing parafocality with the GWS (the IRTC detector is too deeply inside the cryostat). For this reason, a custom-made interface mount was developed to install the IRTC in front of the GWS. It is constituted by a big metal spacer, which allows keeping the whole IRTC above the beam heading toward the AM. This spacer is properly shaped to allow the light reaching the AM. The scientific light is provided to the IRTC by a 2 inches flat mirror, which folds the central part of the FoV (not used by the GWS) toward the IRTC, installed inside the IRTC custom mount.

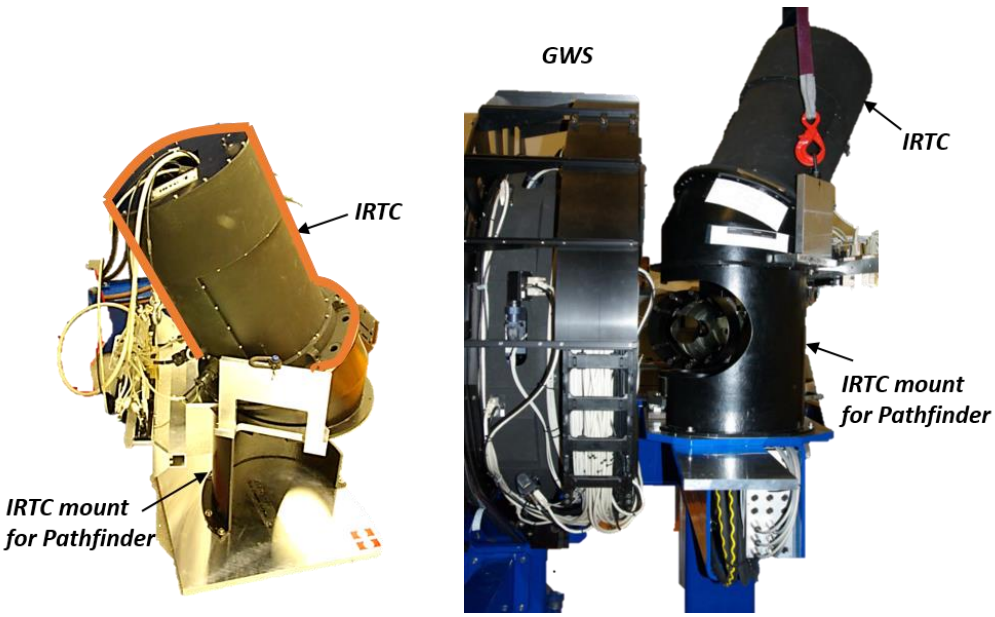

Figure 6-7: On the left, the IRTC installed on its custom-made interface mount. On the right, the complete system mounted in front of the GWS. It is clearly visible the characteristic c-shape of the IRTC mount, which allows the scientific light to reach the AM.

The IRTC folding mirror mount has tip-tilt capabilities, in order to align the IRTC to the GWS, and is equipped with mechanical pins, allowing to remove it during the daytime activities (when on-axis sources are used for Pathfinder calibration) and to precisely reposition it before the nighttime activities.
The idea for the alignment is to materialize the GWS axis, defined now by the AM position, and the GWS F/15 entrance focal plane and then to align the IRTC to the GWS axis and to focus it to the F/15 focal plane.
The procedure we devised and followed is:

- An F/15 light source, called "Magic Lantern" (ML hereafter), equipped with motorized XYZ stages allowing to move the light source across the whole GWS FoV, was placed in front of the AM. The ML motion plane was aligned in tip-tilt and focus to the GWS nominal entrance focal plane using the SEs feedbacks in different positions in the FoV. The ML motion plane is aligned in tip-tilt when the defocus signals retrieved by four SEs located in axis-symmetrical positions in the FoV is below 40 *nm* WFE.

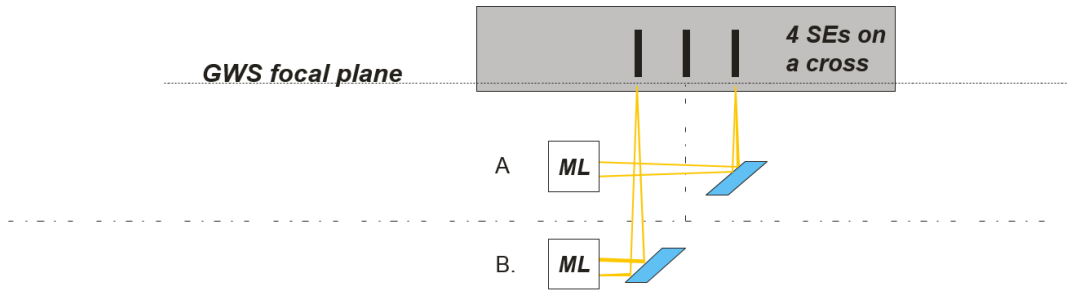

Figure 6-8: Sketch of the procedure used to tune tip-tilt and focus of the ML with respect to the GWS.

- The ML light was reflected by the AM towards SE07, inside the FoV, in order to obtain 4 equally illuminated pupils on CCD50, and the position of the ML was recorded. At this point, the GWS was rotated by 60°. The ML was re-positioned and centered on the same SE and the ML position again recorded. The center of the arc fit to the recorded points materializes the bearing axis. The ML coordinates correspondent to the bearing axis have been computed and recorded. The ML was then positioned to these coordinates; its light was thus passing through the hole in the AM.

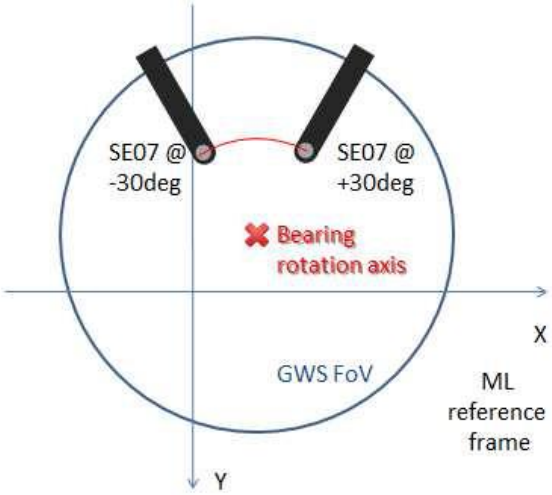

Figure 6-9: Concept for the bearing rotation axis materialization.

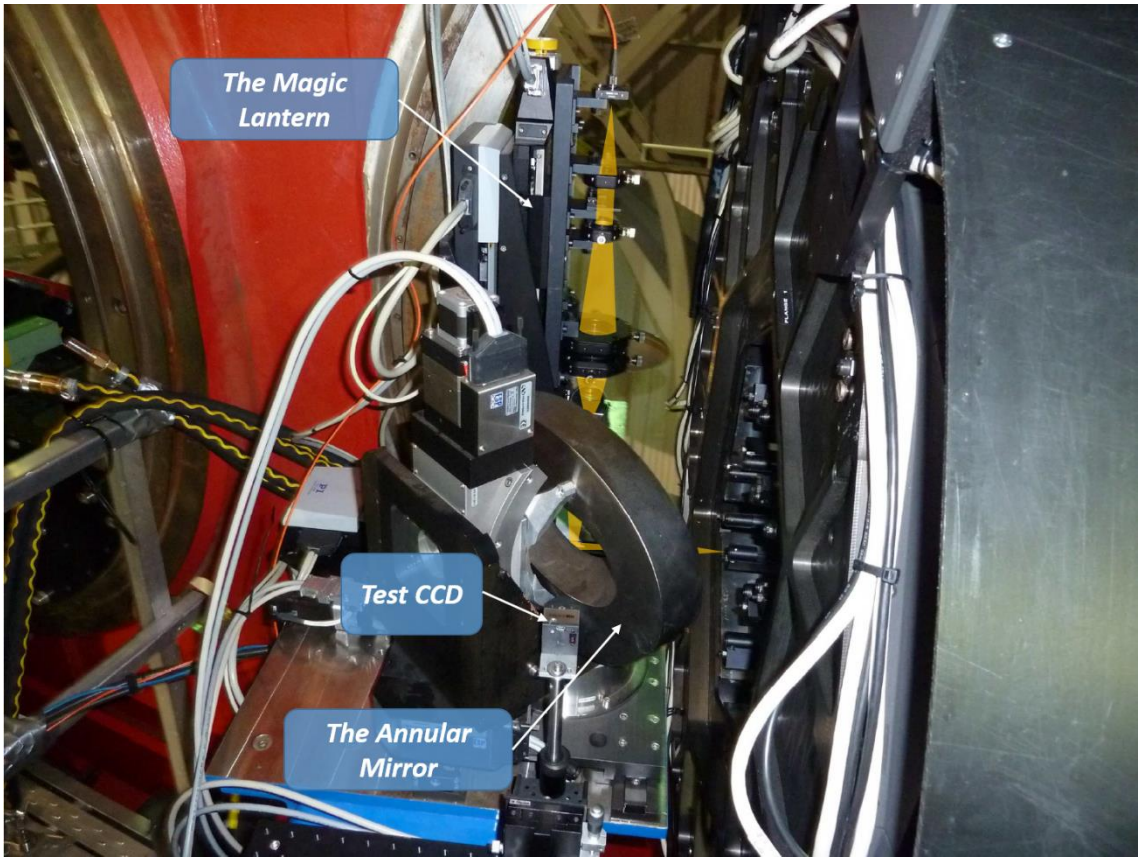

Figure 6-10: The ML in front of the AM during the bearing axis materialization phase.

- A test CCD, visible in Figure 6-10 has been positioned behind the AM and was adjusted in focus in order to be positioned on ML focus. In this way, the Test CCD was co-focal with respect to the GWS focal plane. The test CCD is also centered with respect to the ML spot, so that its center represents the projection of the bearing axis.

- At this point, the ML was removed, since it shared the same position with the IRTC in front of the GWS, and the IRTC was installed. Due to the high weight of the IRTC + mount system, the LBT crane was used for this operation.

- A different light source, constituted by a 50 μm core fiber and a focusing lens placed on a XYZ stage system, called "Agnostic Lantern" (AL hereafter) is located in front of the AM, beyond the IRTC. The F/# of the AL is not important, since it will not be used to feed any SE and its purpose is just to provide a reference for the IRTC alignment. The only point here is that the larger the F/# and the less precise will be the IRTC focus alignment, because of the higher indetermination in the actual AL focal point determination. For the AL has been chosen an F/20.

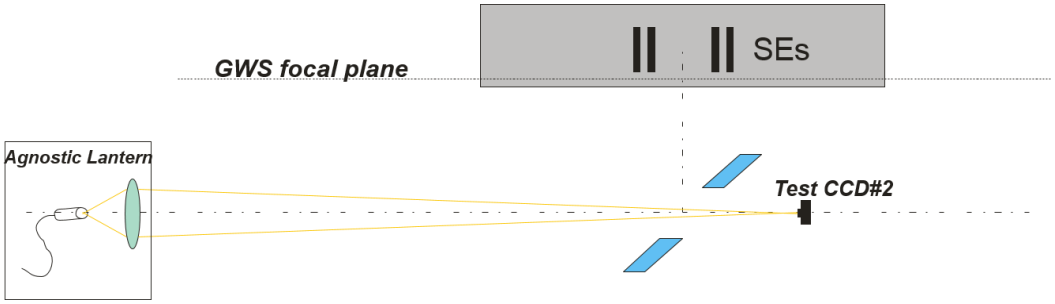

Figure 6-11: Sketch of the setup used for aligning and focusing the AL with the proper reference on Test CCD#2.

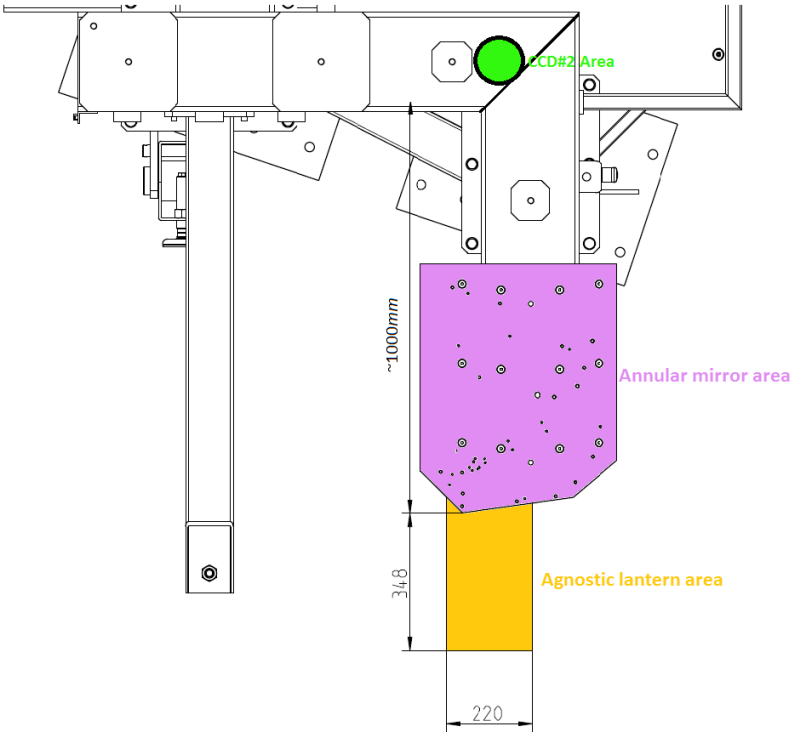

Figure 6-12: The GWS's Foot structure view from the top. The pink area is the board where the AM and the IRTC is installed. Since this board was completely occupied, an additional board (yellow in the picture) has been installed to the Foot, to allow installation of the AL. The big green dot represents the location on the Test CCD#2.

Due to the limited dimension of the area available area in front of the GWS, widely occupied by the IRTC, an additional small bench was connected to the

Pathfinder Foot, in order to install the AL. The AL was positioned and aligned in order to have its focus in the center of the Test CCD.

Figure 6-13: The AL mounted on the additional breadboard. The IRTC is also visible.

- The IRTC mirror was installed and its tip-tilt was tuned until positioning the AL spot on the center of the IRTC detector. Finally, the IRTC was moved in focus, shifting the IRTC internal lens closest to the CCD, until it laid on the AL focus. Parafocality between GWS and IRTC was therefore obtained.

To free the space in front of the GWS entrance, allowing to mount the setup used for GWS calibrations, described in the next Section, the IRTC was removed. Despite the successful alignment, for practical and programmatical reasons, the IRTC was not used anymore during Pathfinder. We decided indeed, starting from T5, to use simpler and more manageable setups for the nighttime activities, obtained by slightly modifying the daytime setups. Since the daytime setups, as it will become clearer soon, have to be mounted and aligned in the same position of the IRTC, a daily re-installation of the IRTC would be required. The weight of the IRTC, which impose craning operation for its movement, and, consequently, the time required for installation/uninstall, plus the fact that correction characterization was not among the Pathfinder primary goals, lead us to this decision.

6.3 Interaction Matrices calibration

During the daytime campaign in T5, our main activity was to calibrate the GWS for adaptive optics correction. This involved measuring the so-called Interaction Matrix, a mapping between known shapes (Karhunen-Loève modal basis) applied to the ASM and the corresponding signal measured by the GWS.

To derive such interaction matrix is obviously required light back from the ASM entering into one SE for the wavefront analysis. To achieve this result during daytime, in order not to waste precious nighttime, we designed a simple double-pass optical configuration. A multimode fiber, whose core diameter is 200 μm in order to create a spot on the pin of the pyramid that is roughly seeing limited (0.67 *arcsec*), was located at the F/15 focal plane. Since, at the beginning, the alignment and the tests were performed with the dome light on, to actually allow us to see the setup and align it, a big screen, called "giant cheerio", was screwed at the GWS entrance to block unwanted light that would contaminate the pupils, preventing the computation of a correct interaction matrix. 12 holes were drilled in the giant cheerio in correspondence of the 12 SEs, to allow scientific light entering into the GWS. As our experience and confidence in the setup increased, we removed this screen and performed the tests switching off all the lights in the dome. The light from the fiber passes through the hole in the annular mirror, through an on-axis beam splitter (BS1), to the M3 and then to the ASM where it is focused at the intermediate Gregorian focal plane and enters a retro-reflector (RR) optics.

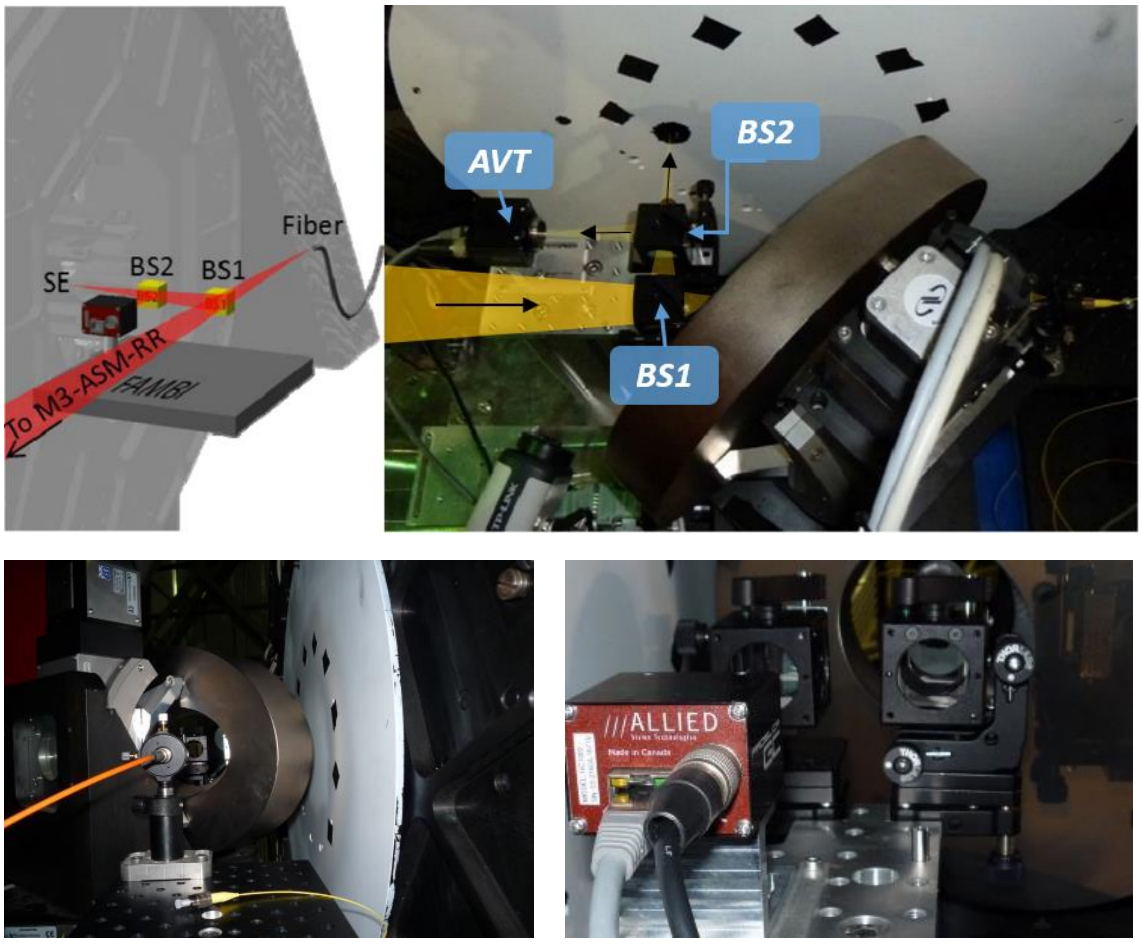

Figure 6-14: The setup used in the daytime for the calibration of the interaction matrix. In the top-left, panel the schematic of the setup. The first beam splitter (BS1) folds part of the on-axis light coming from the ASM towards one SE. The second beam splitter (BS2) folds part of the light toward an ALLIED AVT camera, in order to verify loop closure during the day and the night. In the pictures is visible the giant cheerio installed in front of the GWS to prevent unwanted light entering into the GWS.

The retro-reflector reflects the light back along the same path until reaching the beam splitter, which reflects 50% of the light toward one of the SEs in the GWS. Since the GWS works only with off-axis sources, while we are illuminating the ASM with an on-axis source, it is necessary to pick up the return on-axis beam and to bring it off-axis. This was done by simply positioning BS1 along the optical axis of the beam, in front of the desired SE. By doing this we introduced a defocus into the SE, since we are shortening the light path (see Figure 6-15). To compensate for it we just shifted the ASM along the optical axis, minimizing the defocus signal measured by the GWS. To ease the alignment of the fiber to the retro-reflector, initially we used a very bright green laser light that could be easily seen by eye.

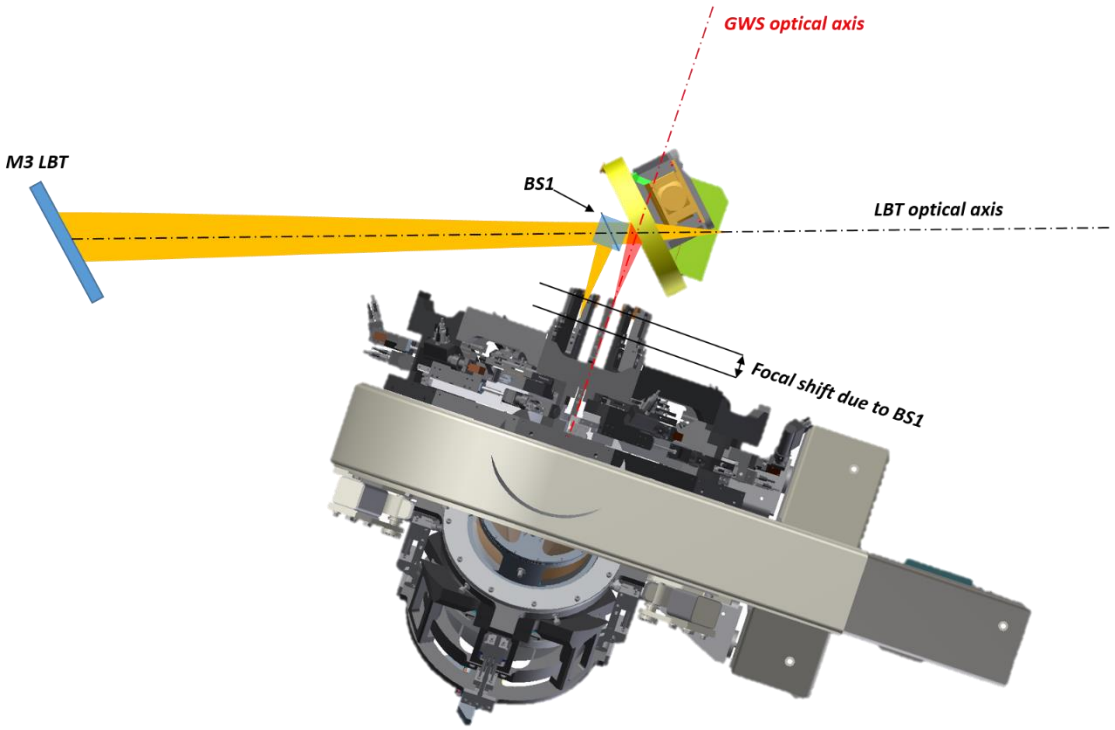

Figure 6-15: Scheme illustrating the focal shift due to the insertion of a BS in the optical path. The reflecting surface of BS1 does not lie on the AM plane, which defines the nominal position of the GWS entrance focal plane, but in front of it. This results in a shortened path for the light, and thus a defocus signal into the SEs. The red beam materializes the theoretical nominal focus position of an on-axis beam entering into the GWS. This effect is compensated shifting the ASM along the optical axis.

To simplify the operations of having light back from the ASM, we decided to slightly steer M3 from the position recorded during T4, as the M3 steering is much more precise and repeatable than the adjustment mechanism of the fiber. After the return beam reflected by the beam splitter was finally visible on the giant cheerio, the alignment was finalized sending the transmitted beam back into the fiber. To ease this operation, the return spot size is minimized by eye, with the help of a piece of paper, by translating the ASM along the optical axis. The returned spot on the giant cheerio was highly comatic, because the fiber beam is hitting the ASM tilted with respect to the ASM optical axis. The gross coma was then removed by tilting and translating the ASM, looking at the defocused spot (similarly to the procedure used for the PR-I alignment, described in Section 5.3.4) and keeping the returned spot in the same position on the giant cheerio.

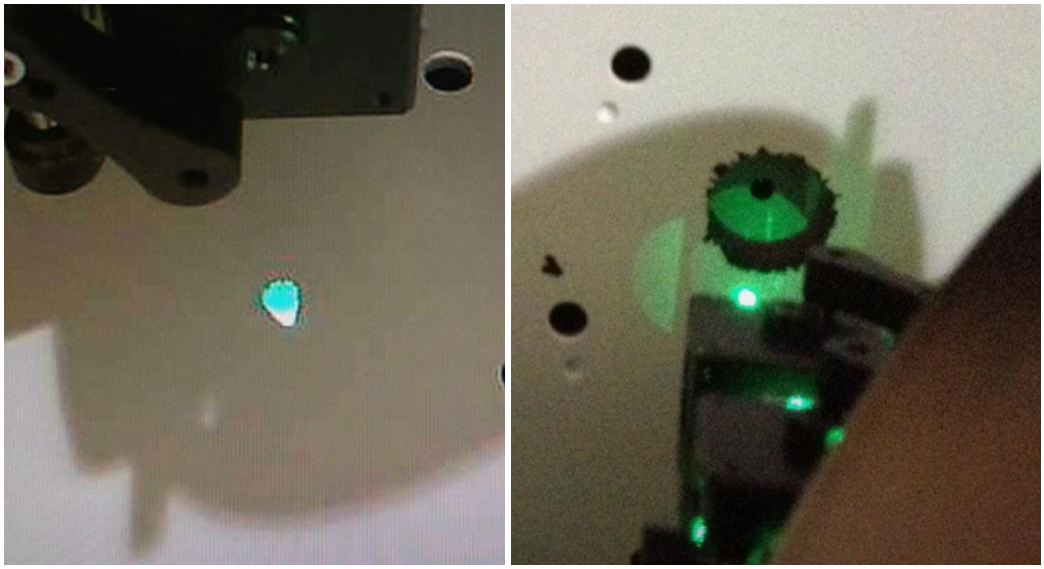

Figure 6-16: On the left the returned spot from the ASM (and RR) before removing coma. On the right, the same spot after coma reduction.

This alignment had to be repeated daily, because temperature variations in the dome and the not perfect repeatability in repositioning the RR (which had to be removed almost every day before nighttime observations) cause small variations in the optimal telescope collimation for the Pathfinder. Since the laser light was too bright and would have completely saturated the CCD50, we switched to a dimmer white light source with a neutral density filter, to further attenuate the light. The bearing was then rotated in order to have the light passing through a hole on the giant cheerio and through one SE. The tip-tilt of the beam splitter is adjusted in order to have the 4 pupil images on the CCD50 in their nominal position (identified during T1 in the same way as explained in Section 5.4) and uniformly illuminated. Residual defocus term on the pupils is minimized by moving the ASM in Z. A second beam splitter just before the SE allowed a small AVT camera to image the spot in a focal plane simultaneously as the pupils were illuminated. This allowed us to verify loop closure during the day and the night (i.e. control if the focused spot size on the AVT camera was reducing and the light stabilizes when performing AO correction with the GWS). BS2 was aligned in order to have the reflected return beam focusing at the center of the AVT and simultaneously the transmitted beam was producing 4 equally illuminated pupil images on the CCD50. The image on the AVT camera showed that the return spot had a significant amount of astigmatism, introduced by the ASM, whose main part was removed by properly shaping the ASM, applying manually the proper Zernike mode and checking at the same time the spot shape on the AVT camera.
We then started sending modes of aberrations to the ASM, using a push and pull scheme. With this method, for each mode, we apply two opposite shapes to the ASM, rapidly enough to freeze the turbulence and vibration. Each shape corresponds to the same mode of aberration, with the same amplitude but with opposite signs. In this way, the GWS returns two corresponding sets of slope vectors. The half of the difference between the two vectors gives the mean value of the slope signals for the given mode, cancelling out those aberrations due to systematic measurement errors in the slope vectors. The result is

finally multiplied by a constant reflecting the scale factor between the signal retrieved by the GWS and the voltages applied to the ASM. This result is used to fill the row corresponding to the mode applied to the ASM in the interaction matrix.
We computed interaction matrices starting with 10 modes and increasing gradually the number of modes until 400. To make the interaction matrix more robust we computed it 12 times and averaged them.
Since an adaptive optics correction loop operates in exactly the opposite way to the interaction matrix (i.e. the WFS retrieve a signal and this is used to compute the shape to apply to the DM for the correction), the interaction matrix was inverted to get the Reconstructor, used to close the loop in daytime and nighttime.
The GWS uses off-axis stars and since the sky rotates, in order to track off-axis stars during night observations, the GWS rotates as well. Since the ASM does not rotate, there is a continuously changing, rotating, relationship between the GWS sub-apertures and the ASM actuators. For this reason an interaction matrix computed at a given bearing rotation angle cannot be used at different angles (a mis-match between subapertures in the pupils and actuators in the ASM would be introduced), thus, to maintain closed-loop with a rapidly rotating FoV, interaction matrices covering the whole bearing rotation range are required. Two possible solutions to address this problem were considered: the first approach is to calibrate interaction matrices every two degrees for the full bearing rotation range (a two degrees rotation leads to a maximum mis-match of half a sub aperture, since the ASM actuators are spaced of 4° at the outer ring).

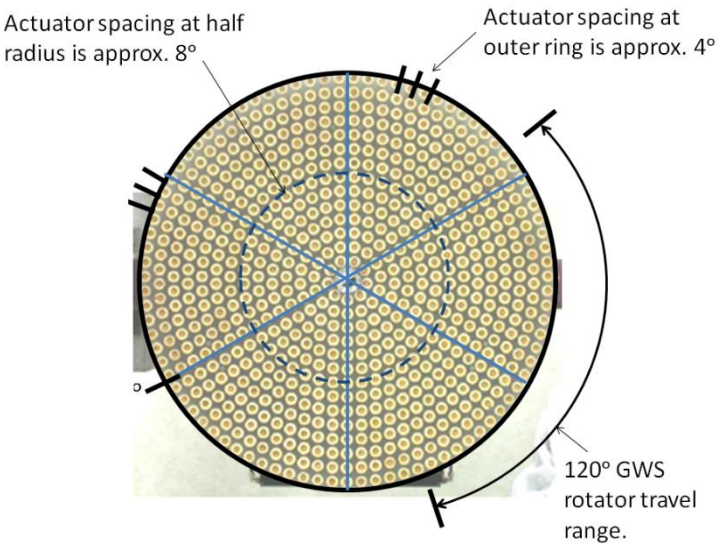

Figure 6-17: ASM actuators disposition. Considering acceptable a maximum mis-match between an actuator and a sub aperture in the pupils of half a sub-aperture, the finest interaction matrices sampling would be every 2°.

A second approach is to calibrate few interaction matrices at different sparse bearing angles in a narrow range, interpolate them and then rotate numerically the resulting interaction matrix to obtain synthetic reconstructors for every degree of rotation. This second approach was tested first, since it is very time efficient, and after intensive tests during T6, it proved to be extremely robust and was used to close the loop with a 100 modes reconstructor up to 60° rotation during daytime activities. Because of flexures the

CCD50 had to be manually re-centered, from time to time, to keep the pupils in their nominal position in the CCD (a script performing this automatically was not ready yet). Operatively, the interaction matrices at different bearing angles used to get the synthetic interaction matrices at all the other bearing angles, are obtained rotating the bearing of few degrees and, since our light source is in a fixed position (not rotating), re-centering the SE on the incoming beam.

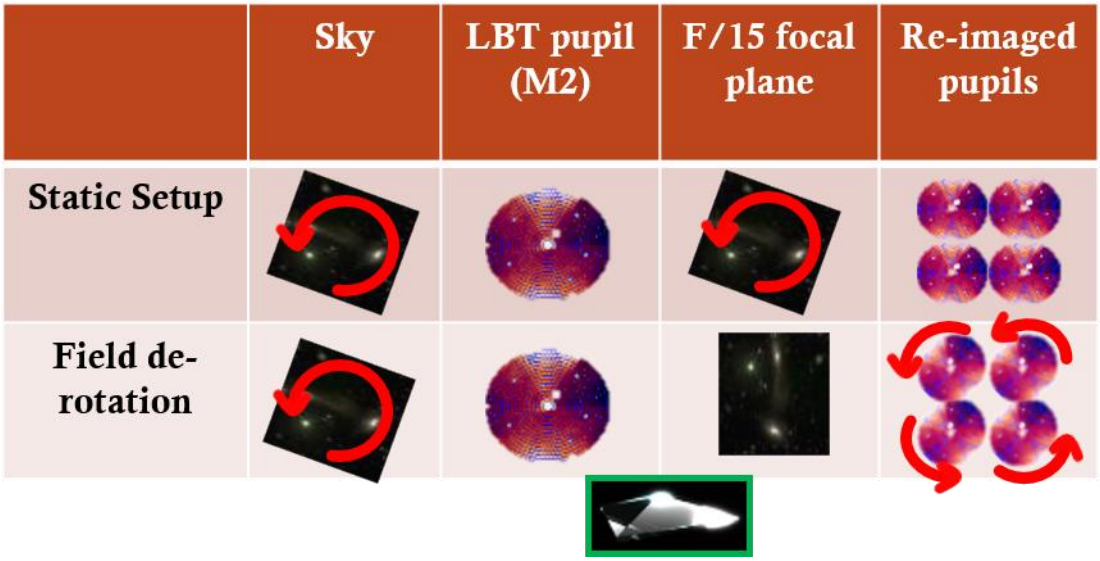

Figure 6-18: When using off-axis stars, sky rotation must be considered. In fact, while the sky rotates (and the GWS as well to keep the stars centered on the respective SEs), the ASM does not. This translates into a variation of the ASM actuators projection into the re-imaged pupils.

During T7 we had also the chance to perform a few calibration tests using the ARGOS (Advanced Rayleigh guided Ground layer adaptive Optics System) on-axis calibration source. This is a single-pass optical test that illuminates the ASM by placing fibers, focusing at the telescope prime focus, in front of the ASM. It consists of two on-axis sources (one bright and one very dim) and three off-axis sources, located in our GWS annular FoV. These sources can be easily deployed on a swing arm with minimal time spent acquiring and aligning the source to the GWS, in contrast with the double pass test, described before, we used for daytime calibrations, which requires the installation of the RR, fiber, beam splitter assembly and few hours for acquisition of the return beam and alignment. Even if the power of the on-axis fiber was low and the fiber too small (6 μm core diameter), causing the saturation of the signal, we were able to close the loop up to 100 modes and for a continuous derotation of 25°, demonstrating the validity of the ARGOS calibration source as an option for GWS calibrations. This synergy with ARGOS for the on-axis calibration source will be important especially for LN, which requires an external reference for calibration of the two GWSs (HWSs, as we will see later, have their own calibration fibers).

During different pathfinder runs, we performed many tests, in many different conditions and with different setups, to verify the efficiency of the computed reconstructors, closing the loop in daytime up to 150 modes while the bearing was derotating and a SE

automatically continuously centered on the incoming source. To perform these kinds of test the reconstruction matrices files were uploaded on the ASM Basic Computational Unit (BCU), together with a disturbance (a sequence of commands simulating a randomly generated turbulence).

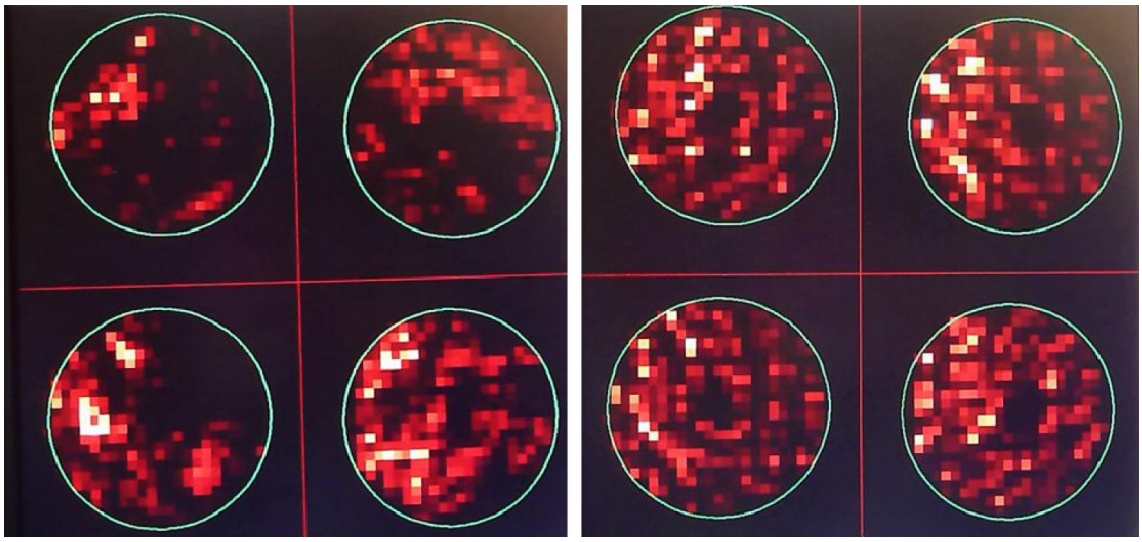

Figure 6-19: Daytime snapshot of 4 pupil images as seen from the GWS. On the left the pupils layout in open-loop with turbulence injected in the ASM (pupils unevenly illuminated, showing clear aberration signatures). On the right, the same pupils when the loop is closed (pupils equally illuminated).

Therefore, basically, the ASM was randomly shaped to simulate a turbulence and, almost at the same time, re-shaped by the GWS commands to compensate for this turbulence. As an example, the result of a test performed using a 100 modes reconstructor, simulated seeing 0.8 *arcsec*, wind speed 15 *m*/*s* is shown in Figure 6-19 and Figure 6-20. This demonstrates, when closing the loop, a gain of a factor 10 in the residual WFE RMS for all the modes corrected, proving the robustness of our reconstructor and, in general, our ability to properly command the ASM.

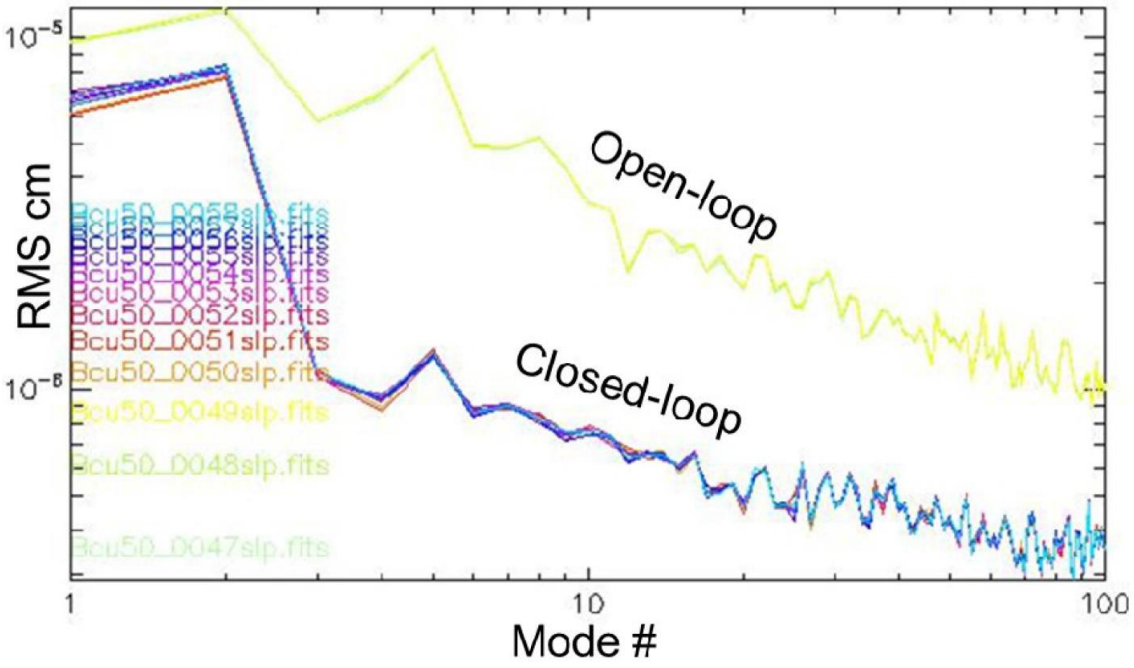

Figure 6-20: Result obtained closing the loop on a simulated turbulence, using a 100 modes recontructor to close the loop. The frames are taken at a frequency of 884 Hz, close to the maximum frequency of 1 KHz the GWS will drive the ASM in LN. It shows the WFE RMS computed by the GWS for each mode. In yellow is plotted the open loop curve, while all the other colors represent different sets of closed loop, which essentially all overlap. A gain of about a factor 10 is visible for all the modes except for the very low orders. This is due to the partial saturation of the signal for these modes. In fact, the actual tip-tilt RMS in open loop is about a factor 10 times larger than the measured, and here reported, value.

6.4 First light and nighttime activities

As said before, initially our plan for the nighttime activities was to use the IRTC to acquire scientific images and test the quality of the GLAO correction performed by Pathfinder. However, during our T5 daytime tests, we realized that it would have been much simpler and time saving to slightly modify our daytime setup, at least for the first nighttime tests. In fact, to arrange the T5 setup, depicted in Figure 6-14, for nighttime operation was just sufficient to remove the RR. The goal for T5 nighttime campaign was, since we were operating at an unconventional location on an uncommissioned focal station, just to acquire a bright on-axis star and to try to close the loop on it. Using on-axis stars of course facilitated the acquisition and does not require any de-rotation software (which was in a preliminary state at the time). On the other hand, we could not use the AM, which does not intercept the central 2 *arcmin* FoV, using instead the BS1 of the daytime setup to fold the starlight towards the same SE used for calibrations. BS2 was folding part of the light toward the AVT camera, which was used, other than for closing-loop verification, also to assist the star acquisition. In fact, a SE has a very narrow FoV (about 1 *arcsec*), so blind acquisition with the bare SE would be challenging. The AVT camera allows a slightly larger FoV, which, even if not huge (just 5 *arcsec*), surely facilitates this operation. Since we had 2 BSs in our setup and it was our first nighttime observation run, we clearly decided to start with a very bright, easily observable star. We chose for the Pathfinder

first light a 0th magnitude star, Capella. After a short spiraling search, moving the whole telescope on a spiral path in steps of few *arcsec*, we were rewarded with Pathfinder first light, which was a quite poor and out of focus image of Capella. Anyhow, this enough for the achievement of the first on-sky Pathfinder goal, the mere acquisition of a bright, on-axis, star, useful to understand the offset between the telescope optical axis and our SE position (the center of the AVT camera is fairly co-aligned with the pin of the pyramid in the SE).

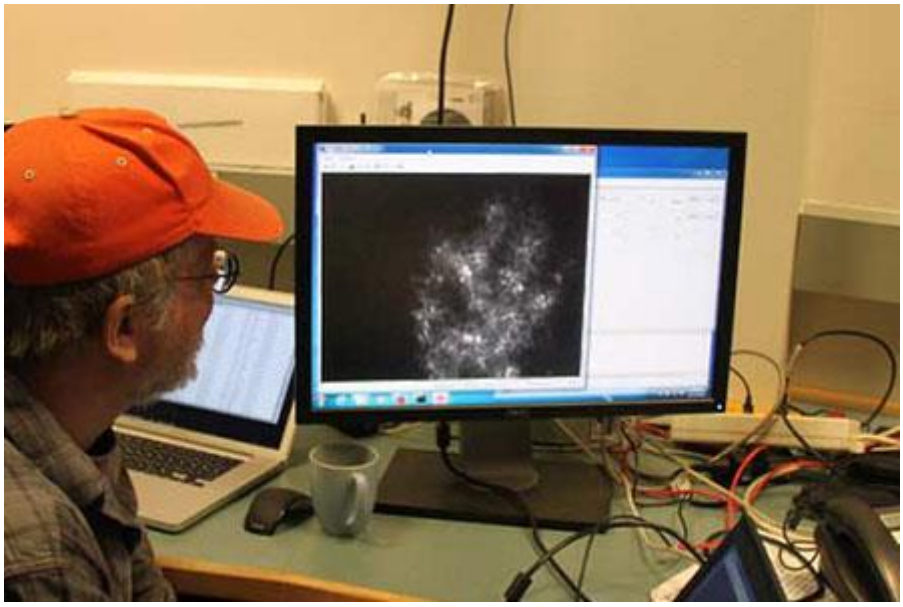

Figure 6-21: Pathfinder first light on the AVT camera. The image was very aberrated and out of focus, but enough to reach the first Pathfinder nighttime goal, the mere acquisition of an on-axis star.

We then approached the next and more important goal, closing the loop on an on-axis star. Capella proved to be too bright for this purpose, its light was saturating the CCD. We then pointed the telescope at ε Aurigae, a 3th magnitude (V band) star in the Auriga constellation. After 35 minutes from Pathfinder first light, we were able to close the loop, initially using a 10 modes reconstructor, and, shortly after, using a 50 modes one. In Figure 6-22 two images of ε Aurigae, in open-loop and closed-loop. These images are taken in visible band, as imposed by the wavelength range of the AVT camera, where AO correction performs worse than in IR light, and with a seeing of 2.3 *arcsec*. Considering that the SE FoV is 1.3 *arcsec*, and thus part of the starlight does not even enter into the SE, it is not hard to understand that the system was working in really challenging conditions. Despite these considerations, the advantage and the image quality improvement is clear when the loop is closed. Due to the tough conditions in which these images were acquired, the characterization of the correction was not performed, since it would not be representative at all of the GWS performance in LN. This characterization was postponed to later runs, when an IR camera will be available and the seeing will not exceed the SE FoV.

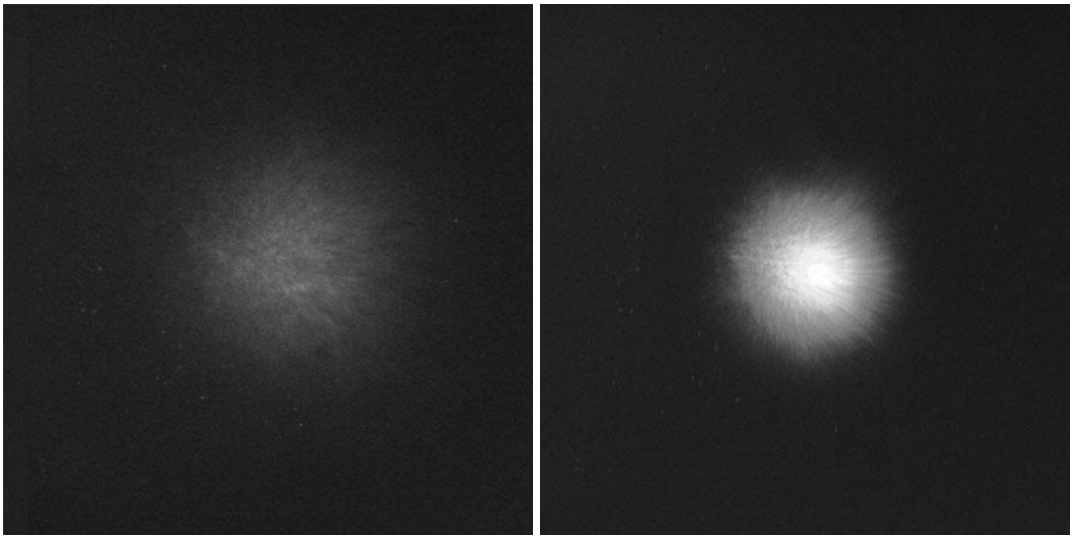

Figure 6-22: First Pathfinder closed-loop on an on-axis star, ε Aurigae, 3th magnitude in V band. Images are taken with a visible broadband AVT camera. The seeing was 2.3'', exceeding the SE FoV, but the improvement in the image quality is still clear. On the left the star in open-loop, on the right the star in closed-loop, using a 50-modes reconstructor.

Before even trying the correction characterization, however, others Pathfinder more important goals must be addressed. The first one is the acquisition and loop-closure on an off-axis star, to test the GWS under conditions more similar to those it is required to work.

It is clear that the setup used during T5 cannot be used for this purpose, since BS1 is folding the light of on-axis stars. The nighttime setup for T6 was then modified as following:

- BS1 was removed at the end of daytime activities (it can be repositioned with good accuracy the next morning thanks to a magnetic baseplate). The reflection of off-axis stars light is addressed to the AM.

- BS2 and the AVT camera were mounted on a custom-made aluminum arm, fixed to the bearing in order to follow the sky rotation. The arm is devised to keep the BS in front of the SE04 aperture. In the same way as T5, the tip-tilt of the BS is adjusted so to have a focused spot at the center of the AVT camera simultaneously with 4 equally illuminated pupils on the CCD50. An identical arm was mounted in front of SE06, so to allow acquisition of more than one star (or acquisition of the same star with two different SEs).

- A Canon 5D MkII Digital Single Lens Reflex Camera (DSLR hereafter) was positioned behind the AM, in place of the on-axis fiber used for daytime calibrations (repositionable with a magnetic baseplate). This allowed us to better understand the sky orientation of the pathfinder focal plane, by iteratively moving stars from on-axis position (defined by the DSLR) to off-axis positions (defined by the SEs positions). Its FoV is about 1 *arcmin*.

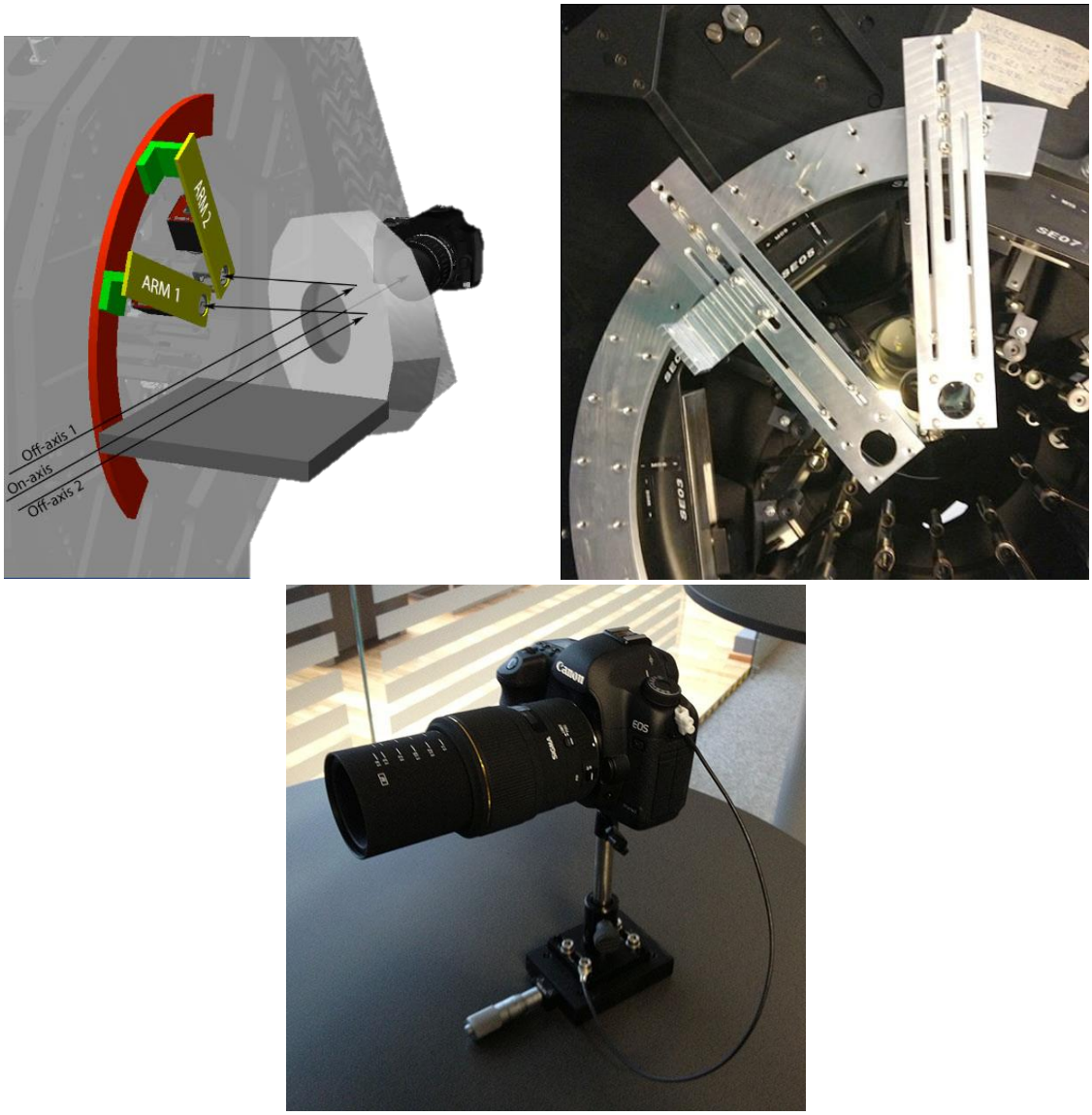

Figure 6-23: Setup used during T6 nighttime campaign. The reflection of the off-axis stars toward the GWS is from the AM. The on-axis star is acquired by a DSLR, working in visible light, placed behind the AM. Two small metal arms allocate a beam splitter and an AVT camera each, to assist star acquisition.

Obviously, for the achievement of this goal, it is required a derotation software able to keep the star fixed into the SE and a software automatically uploading on the ASM BCU new reconstructors, without stopping the correction, as the bearing rotates. To make things easier, we started the T6 nighttime campaign acquiring only one star (α Andromeda, 2nd magnitude). Initially we positioned the star at the center of the DSRL on-axis camera, and then we computed the telescope offset to position the same star on SE04 (through the AM) as Elevation = + 153 *arcsec* and Azimuth = - 9 *arcsec*. We had light on the AVT camera, even if not perfectly on its center (and thus the SE was not yet illuminated), demonstrating that our computations were accurate. We optimized the telescope position to have the star at the center of the AVT camera and, consequently, focused on the pin of the pyramid, obtaining the new and more precise offset of Elevation = + 153 *arcsec* and Azimuth = -10.5 *arcsec*. To test the derotation service and the script uploading new reconstructors as the bearing angle changes we decided to switch to a star

rotating faster, Capella, used in T5 for the first light. We verified that the derotation service was perfectly working, keeping the star perfectly centered on the AVT camera (as a double-check we also stopped the derotation and we saw the star drifting away), and we uploaded new reconstructors every 1 degree of bearing rotation. Since the star was really bright and saturating the pupils only 10 modes reconstructors could be applied.
In the following night we also managed to move a star (γ Andromeda, 2nd magnitude) from on-axis to two different SEs (SE04 and SE06), offsetting the telescope, making another step in our understanding the orientation between the sky and the Pathfinder focal plane.
Due to bad luck with the weather (almost 1.5 nights out of 2 were lost because of clouds and humidity) we were not able to achieve the multiple stars acquisition, but we made some decisive steps in this direction, as we improved our understanding of the sky orientation at the entrance of the GWS.
During T7, we continued pursuing the multiple stars acquisition, using a slightly modified setup. While the DSRL remained untouched, behind the AM, the arms in front of SE04 and SE06 were replaced by small circular screens (called "cheerios" for their characteristic shape), with a small hole in the center, directly interfaced to the SE mechanics. Their purpose is the same of the AVT cameras on the arms, i.e. assist the star acquisition, but they ensure much more freedom in choosing the stars asterism. In fact, the arms in front of the SEs were in a fixed radial position (they were screwed to the bearing), and, consequently, defining the relative position of our targets, while these screens move together with the SEs, hugely increasing the number of possible targets.

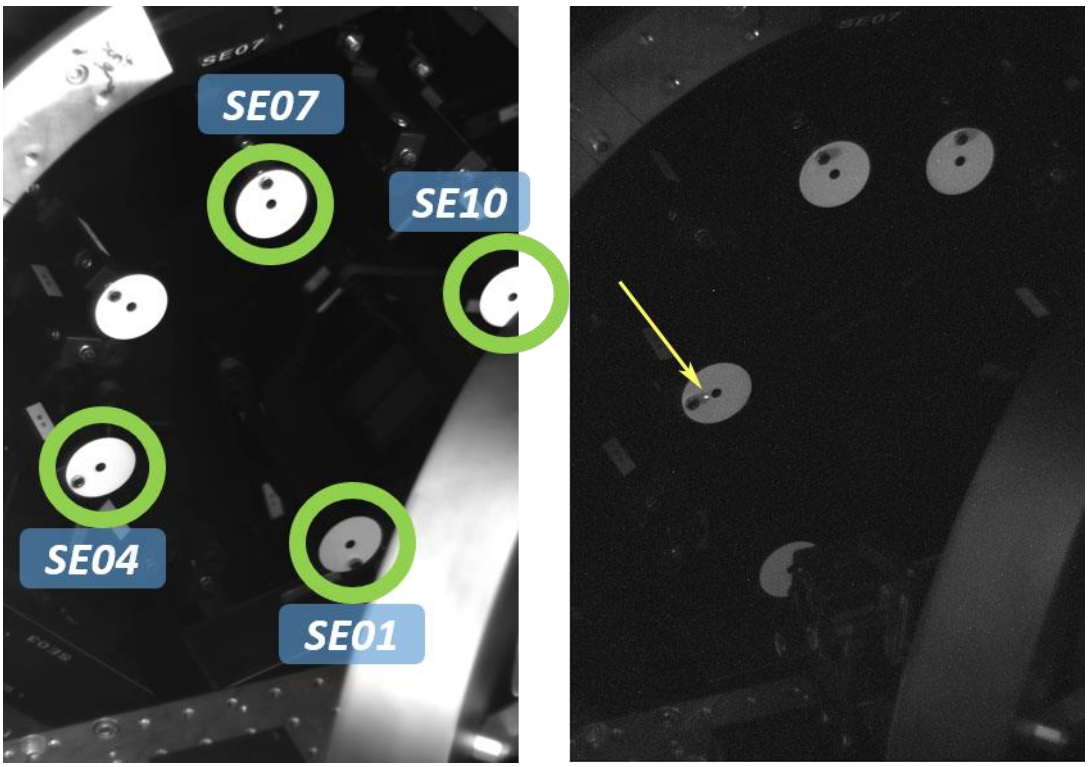

Figure 6-24: The "cheerios" installed on several SEs, used to assist stars acquisition. The SEs actually used during the night are encircled in green color. On the right, highlighted by a yellow arrow, one star focusing on the cheerio, as seen from the surveillance camera.

Moreover, due to their limited size, we could easily install them on more than 2 SEs, while this operation would not be trivial with the arms used during T6, due to their physical size.
An external surveillance camera with objective, looking at the GWS entrance, allowed the observer to eventually see the focused star on the cheerio and acquire it moving the SE (or the telescope, if needed).
It is clear that with this setup we were still required to use bright stars, with the limit magnitude set by the sensitivity of our eyes (experimentally this was about V ~ 5 mag). Blind acquisitions will be possible only when the geometry of our focal plane will be completely characterized. In T7 run our main achievement was to successfully offset a star (γ Hercules, V ~ 3.75 mag) from on-axis to 4 different SEs (SE01, SE04, SE07 and SE10), unambiguously defining the mapping of the Pathfinder focal plane for any bearing rotation angle and parallactic angle. The plate scale of Pathfinder was measured, to be compared with the theoretical one of 0.613 $\mu m/arcsec$, simply moving the star between two SEs whose relative distance was well known. The ratio between the SEs relative distance and the tilt applied to the telescope to shift the star from one SE to the other returned exactly the expected plate scale.
All the prerequisites to perform multiple acquisition and AO correction using multiple stars are now satisfied. Thus, from E1, we decided to replace the DSRL with an IR compact camera, in order to characterize the GLAO correction (IRTC was not re-installed since at this point we were pretty used to the setup configuration of the previous 3 runs, and pretty confidents of its proper functioning).
E1, however, did not start under the best conditions, as the ASM was malfunctioning, and this prevented us to even try AO correction. All our effort was then in pursuing the multiple stars acquisition. Unluckily, a heavy monsoon shower hit the telescope, so hard that some water was leaking from the ceiling. Part of this water affected the control electronic of M3, which became unresponsive to any command. Due to the impossibility to steer M3 towards the Pathfinder, E1 finished before starting.

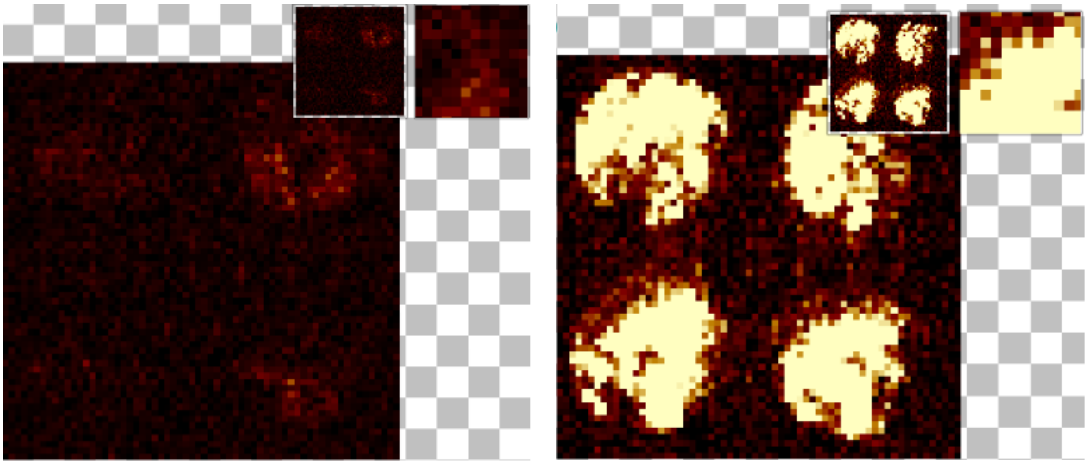

Figure 6-25: Pupils produced on the CCD50 by the faint star (left), and by the two stars together (right).

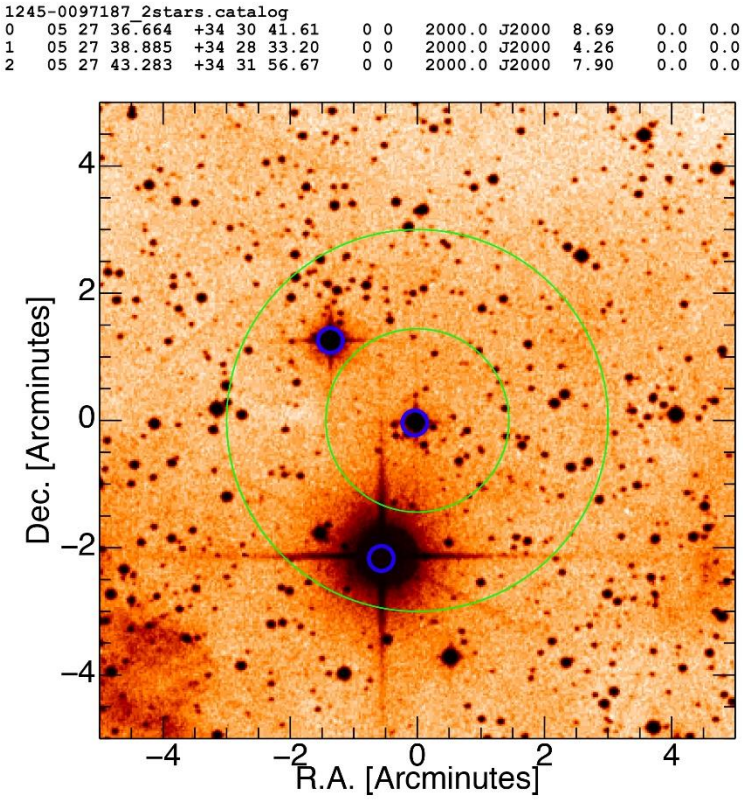

Figure 6-26: Asterism used for multiple star acquisition. While the DSRL was observing at the central star (V ~ 9.6 mag), two SEs acquired simultaneously the two stars encircled in blue. The brightest star is φ Aurigae.

E2 has finally seen come true the long coveted goal of multiple star acquisition. We in fact acquired two stars, one V ~ 5 mag and another of V ~ 8.1 mag, onto two SEs at the same time.

Again, weather and mechanical issues (the bearing was stuck and it was not possible to fix it on the fly) prevented us to achieve the last extended goal of Pathfinder. Anyhow, since we were able to close the loop on a rotating single star, nothing made us doubt that we could do the same with more than one star.

6.5 Pathfinder focal plane orientation

Four mirror reflections, different bearing rotation angles and foci made understanding the Pathfinder focal plane orientation a complex task, which required us several pathfinder runs to define it unambiguously. Here are summarized the calculation to transform star positions into millimeters in the Pathfinder focal plane.

Let us start defining a coordinate system for Pathfinder focal plane. The traditional definition is to place north up and east to the left, with distances measured in *arcseconds* or millimeters in the focal plane. Pathfinder, with its multiple reflections and two sensors (GWS and the on-axis DSLR), poses an additional challenge, in that sky coordinates have to be correctly transformed into the instrument focal plane and the two sensor systems

have to have a mutually consistent frame. We adopt the following standards for defining Pathfinder coordinates:

- The Sky coordinate system is the one of an observer looking out of the slit riding a telescope. We translate star offsets in right ascension and declination from the center of the target into a separation in *arcseconds* and a position angle. This is followed by a transformation into the horizon coordinates, a process depending on the parallactic angle of the target, which in turn depends on the (RA, dec) and the sidereal time. We refer to the resulting separation and position angles of the reference stars as being in the **Slit** coordinate system.

- For the on-axis instrument (DSLR or IR camera), locations are measured in a Cartesian coordinate system with the Y-axis pointing up (toward the secondary mirror) and X increasing to the right, from the viewpoint behind the on-axis instrument looking at the tertiary mirror. We refer to this as the **DSLR** coordinate system.

- For the telescope-fixed GWS focal plane, locations are measured in a Cartesian coordinate system with the Y-axis pointing up (toward the secondary mirror) and X increasing to the right, from the viewpoint behind the annular mirror looking at the GWS entrance. We refer to this as the **Plastic Screen (PS)** coordinate system. Note that this system is in the focal plane of the GWS, but it is fixed to the telescope and does not rotate with the GWS bearing

- There is a final coordinate system, called **GWS**, which is fixed to the front plate of the GWS and which rotates with the sensor. It is otherwise identical to the Plastic Screen system in terms of units, handedness, etc. The GWS and PS systems overlap when the bearing angle is 0°.

Whenever a coordinate system reflects off a mirror, a "flip" takes place, resulting in a change in handedness or chirality of the coordinates. For example, a simple X-Y Cartesian system will have X-axis flipped after reflection off a 45° mirror. Coordinate modification also occurs when an optical beam passes through a focus. For example, a convex lens produces an inverted image (but with the same handedness). Note that at LBT, there are two such foci, since the telescope operates in a Gregorian configuration. The situation for Pathfinder is further complicated by the fact that we operate at an offset focus, about 18.5° displaced from the midline of the telescope. Reflection off the tertiary therefore produces a field rotation, and the annular mirror introduces a final handedness flip. Because of all this coordinate complexity, we analysed, using the Zemax optical design program, how a constellation of star would appear at the entrance of the GWS and later confirmed the transformations on sky during T7.
Transforming the location of a reference star with respect to the target field center from RA and Dec (Sky coordinates) to position angle and separation in Slit coordinates is a quite simple task, as they represent the same view at the sky looking out the slit. This

transformation requires only a rotation of the original separation vector by the parallactic angle. Assuming that R_i and D_i represent RA and dec of a given star, after motion correction, then we get that its offset from the center of the field is simply:

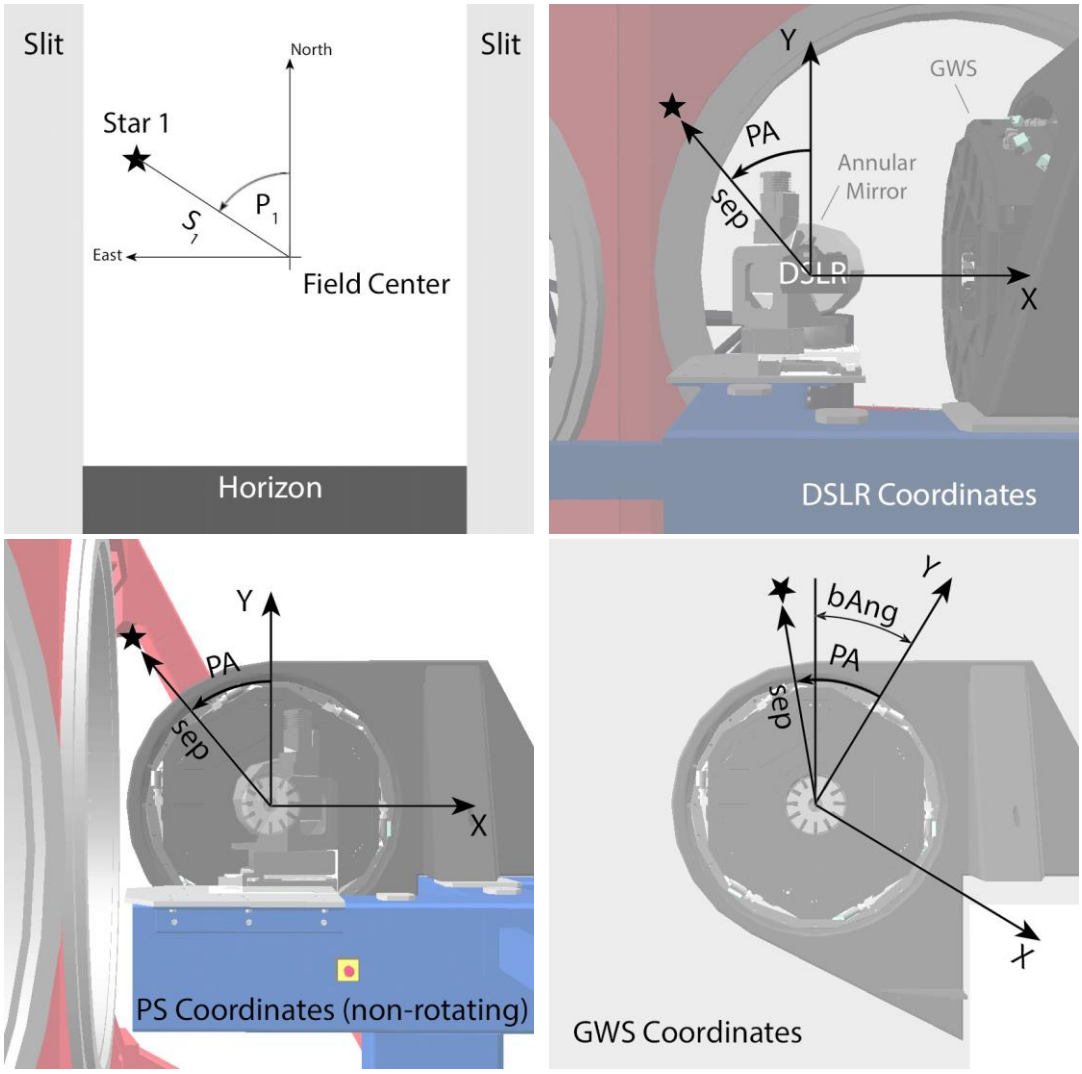

Figure 6-27: Coordinates systems as defined in the text. PA and sep are the position angle and the angular separation of a given object, bAng is the bearing angle.

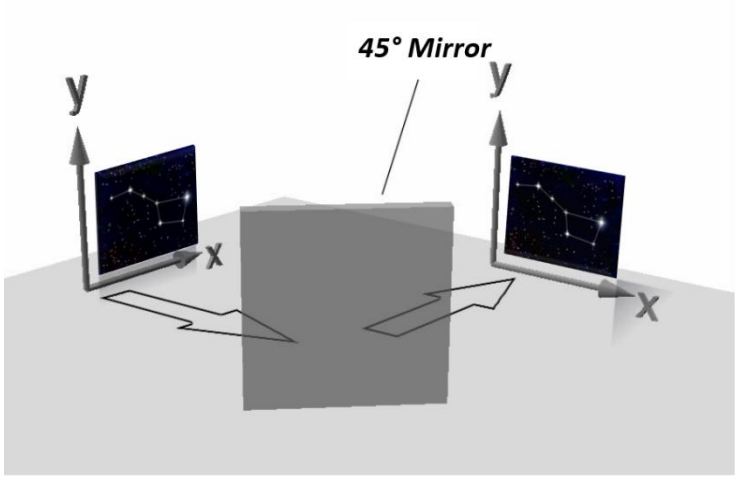

Figure 6-28: After reflection from a mirror, a coordinate system is flipped.

$$dR_i = R_i - R_0$$
$$dD_i = D_i - D_0$$

The separation *S* is given by the spherical law of cosines:

$$S_i = arccos[sinD_0 \cdot sinD_1 + cosD_0 \cdot cosD_i \cdot cos(|R_0 - R_i|)]$$

And the position angle is:

$$P_i = arctan\left[\frac{sin(dR_i)}{cosD_0 \cdot tanD_i - sinD_0 \cdot cos(dR_i)}\right]$$

The output of the last formula is still in Sky coordinates. To have it in slit coordinates it is necessary to subtract the parallactic angle of the field:

$$P_{islit} = P_i - Parallactic\ Angle$$

To transform from slit coordinates to DSLR or GWS coordinates we must take into account the previously mentioned flips and rotations due to mirror reflections and foci.
In short, to transform from the slit view and the DSLR view we have to flip the field North-South, and then rotate it 71.5° counter-clockwise (computed via Zemax and then verified during T7). The same transformation applies for a viewpoint looking at the face of the GWS from behind the AM (the flip in handedness due to the AM reflection is

canceled by the change in viewpoint, so that the two coordinates systems are identical). The position angle in DSLR (or plastic screen) coordinates is given by:

$$P_{iDSLR} = 180° - P_{iSlit} + 71.5°$$

The final transformation to GWS coordinates is easy, involving a simple offset to the position angle by the current bearing angle:

$$P_{iGWS} = P_{iDSLR} + Bearing\ Angle$$

Extracting the GWS focal plane location in millimeters is then a simple matter of converting the separation (still in arcseconds) to millimeters and then project it along the axes:

$$S_i\ [mm] = S_i[''] \cdot 0.613\ mm/''$$

$$x_{iGWS} = -S_i\ [mm] \cdot sinP_{iGWS}$$

$$y_{iGWS} = S_i\ [mm] \cdot cosP_{iGWS}$$

Where 0.613 is the plate scale of the system and x_{iGWS} and y_{iGWS} are the x, y coordinates of an *i* star, in millimeters, in the GWS coordinate system.

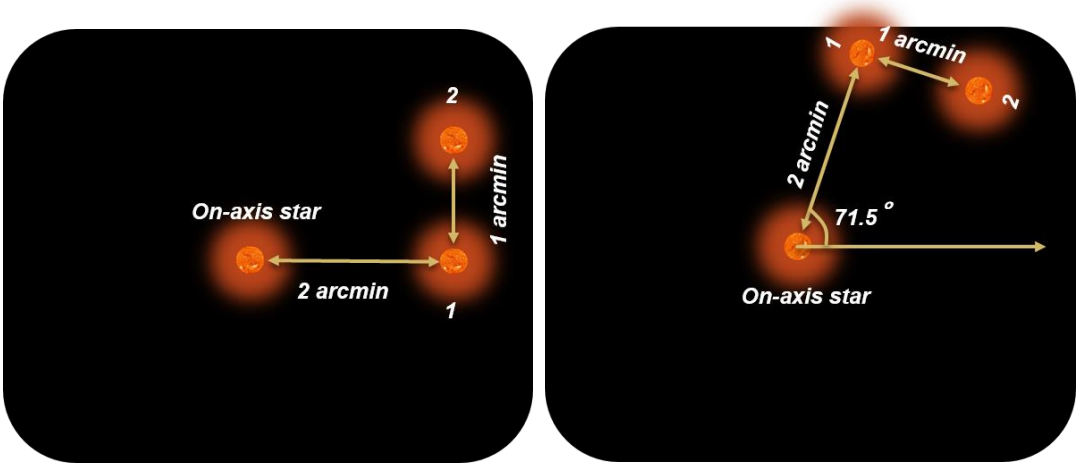

Figure 6-29: On the left a simple asterism as viewed out of the slit. On the right, the same asterism after passing through the telescope, as seen from the DSLR, resulting from a flip of the Y-axis followed by a 71.5° counter-clockwise rotation.

6.6 Conclusions

LN is a very ambitious project ambitious project, which will effectively upgrade the LBT to the first Extremely Large Telescopes. To achieve this result, LN implements some novel concepts (layer oriented MCAO using NGSs), only tested on sky once with a demonstrator (MAD), using 4 pyramid WFSs, employing, all together, up to 20 NGSs.

To reduce the risks related to the complexity of LN and to accelerate the commissioning of the instrument, the LN team launched a Pathfinder Experiment, testing one of the GWSs in its final environments, as a stand-alone system. The main goals of Pathfinder, in a nutshell, were to test the communication between the GWS and the LBT ASM and to understand the mapping of the stars from the sky on to the pyramids.
In summary, the Pathfinder Experiment can be considered a success. Despite the bad luck with weather and telescope failures (about 2 half-night out of 14 were usable), and despite all the issues encountered, mainly related to the fact of Pathfinder being an experiment, we were able to accomplish all the baseline goals.
In particular, during the daytime, we proved that it is possible to successfully use synthetically rotated reconstructor and upload them automatically as the bearing rotates, closing the loop up to 60° bearing rotation (i.e. the whole scientific range). We also performed valuable tests using the ARGOS calibration source, which proved to be potentially very useful for the calibration of the GWSs.
In the nighttime campaign we closed the loop on many, on-axis and off-axis, single stars, we sorted out the geometry of the Pathfinder focal plane, succeeding in acquiring one star with different SEs (1'' FoV each) and also multiple stars simultaneously. We also tracked rapidly rotating stars, demonstrating the validity of the derotator service.
Concluding, other than the successful results, Pathfinder offered us the possibility to gain valuable on sky experience and to better understand which problems and challenges we should expect and we will face during the commissioning of the whole LN, proving to be a good test-bed for the future.

Figure 6-30: Satisfaction of the team after Pathfinder first light.

7 MCAO module integration on the LN bench

Similarly to the GWS DX used in Pathfinder, the HWSs were tested to verify their performances and their ability to drive the relative DM. Since the DMs driven by the HWSs are located on the LN bench, these activities took place in Heidelberg, at Max Planck Institute fur Astronomie (MPIA) premises. In this framework I spent about 8 months of my Ph.D. in Heidelberg, performing the activities described in the following.

7.1 Warm Optics alignment

The HWSs are feeded by the FP20 optics, it is then clear that the pre-condition to align the HWS is to align first the fore-optics. As already mentioned in Section 4.4.4, the LN optics is basically divided in two main parts: first, the warm optics consisting of the collimator optics, including the DM and fold mirror in the Z-configuration, the K-mirror and the FP20 optics; second, the cold optics, which is a sort of Cassegrain telescope inside a cryostat.
The optical interface between warm and cold optics is the infrared pupil, located at the entrance of the cryostat, formed by each of the two arms. I call here “infrared pupil” the pupil produced by the light transmitted by the dichroic, located just after the piston mirror, while its counterpart, produced by the light reflected by the dichroic, is here called “visible pupil”. These pupils needs to be homotetic in order to avoid field dependant OPD, and the OPD must be 0 at these positions (and after). In addition, the piston mirror has a rigid design, no angle adjustment is possible, since this mirror is the actuator for the piston control loop (so it can only rigidly translate along its optical axis). For these reasons the alignment of the warm optics starts at the pupil, and only after the other optics, in front and behind the pupil, are aligned.

Figure 7-1: The large reference mirror below the bench

The goal of the alignment of the warm optics is to deliver to the HWS a wavefront of the highest possible quality, so to minimize the static aberration and keep the wavefront sensor far from its saturation regime.

To assist the alignment, a large reference mirror is located at the infrared pupil position (the cryostat is not installed) and aligned to the optics in the cryostat (procedure not described in this thesis).
This mirror is the reference for the direction of both collimator optics and for wavefront error of the individual collimators.
A pupil mask is placed in a dedicated holder, which can be placed above the large reference mirror, in order to define the position of the infrared pupils.
This mask has a central target for alignment and was previously aligned to the cryostat optics. Aligning the warm optics to the reference mirror, for direction, and to the pupil mask, for position, we make sure that warm and cold optics are co-aligned.

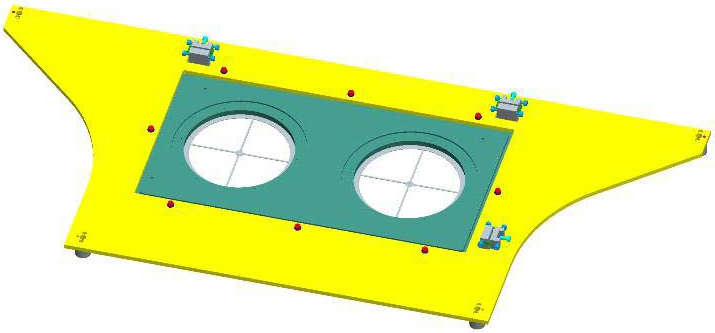

Figure 7-2: The pupil mask on its holder.

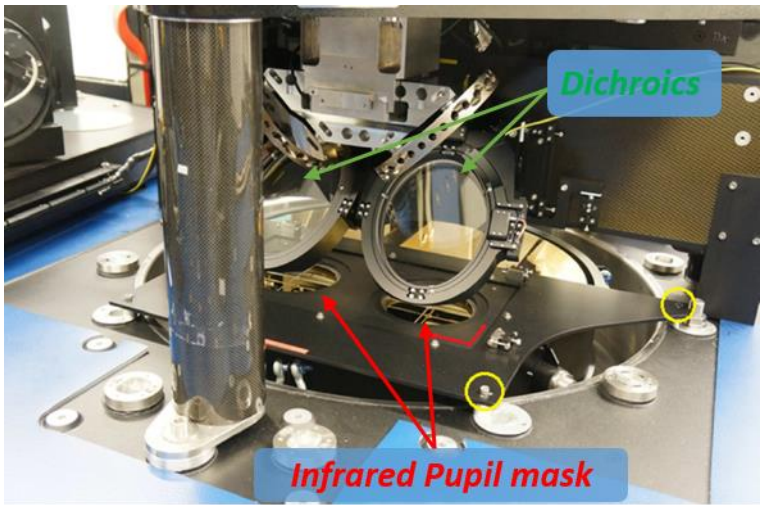

Figure 7-3: the pupil mask and its holder on the LN bench, just above the large reference mirror. Yellow circles show the mechanical pins allowing to precisely re-position the pupil mask, in case it has to be removed.

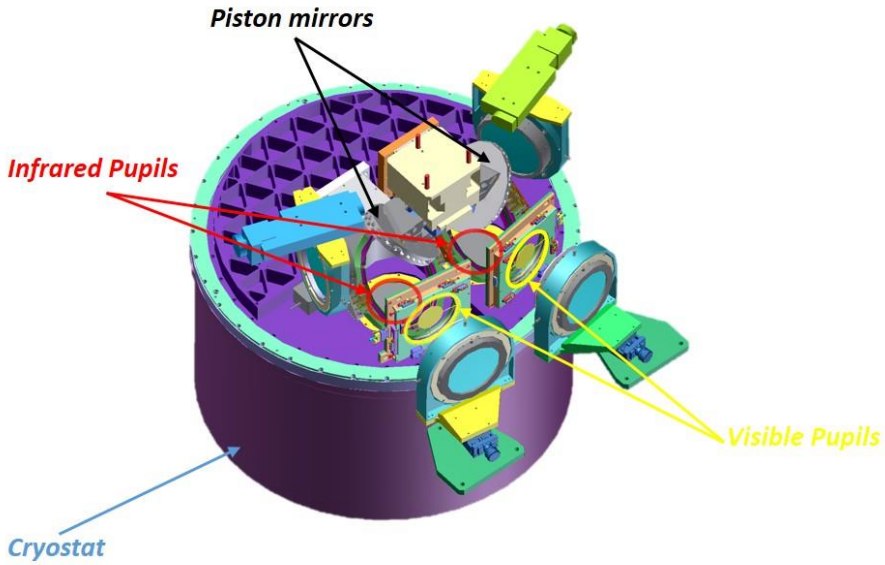

Figure 7-4: sketch of the piston mirror area and positions of the Infrared and Visible pupils.

7.1.1 Alignment of the collimator optics

This alignment can be divided into several minor steps. First, a laser source (we used a FISBA Twyman-Green interferometer), is shined directly to the piston mirror and aligned to the large reference mirror by minimizing the number of fringes measured by the interferometer. Now the laser beam is aligned to the reference mirror, and so to the cold optics, but in this position the beam would be blocked by the DM structure, when installed (see Figure 7-5). The FISBA must be rigidly translated to a position simulating the on-axis beam of the telescope entering the LN bench. To do this, a reference flat mirror is mounted in front of the FISBA beam and aligned perpendicular to the FISBA (one fringe of tilt). The DM and fold mirror in Z configuration, internally pre-aligned, are installed with mechanical precision on the LN bench. The FISBA is then translated to its nominal position, accordingly to the CAD drawing, adjusting its tilt in order to maintain only one fringe (as the number of fringes is directly related to the differential tilt between the outward and return beams). The flat reference mirror is removed, so now the light can go through the flat mirror, the DM, the piston mirror, the large reference mirror and come back into the interferometer along the same path. Any misalignment is adjusted by slightly changing the tilt of the flat mirror, looking at the number of fringes in the interferometer.

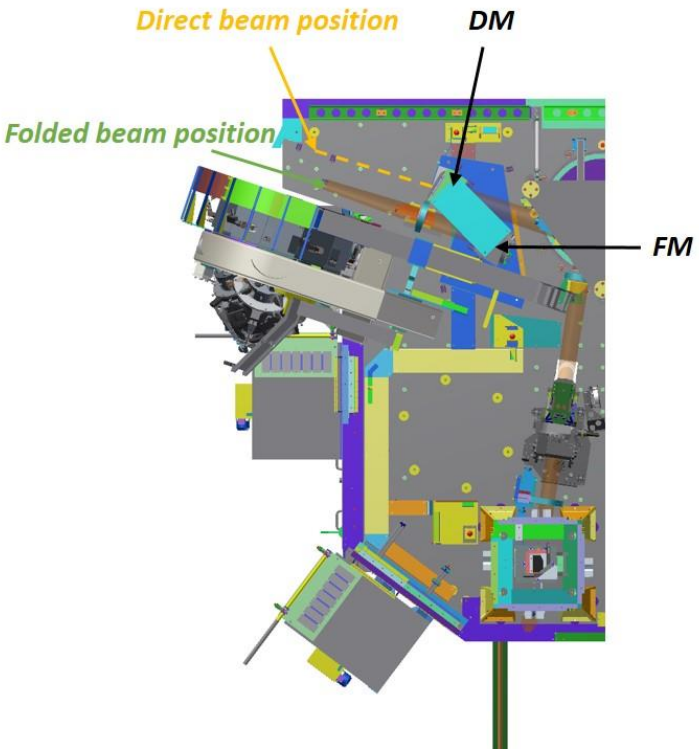

Figure 7-5: Initial position of the FISBA beam (direct beam), and its nominal and final position (folded beam).

The collimator axis is now defined and is now possible to proceed integrating the collimator powered optics. For a first coarse alignment, the back-reflection from the lenses is used, while for the fine tuning of the alignment we installed to the FISBA a spherical objective, so that the lenses are feeded with a F/15 beam.

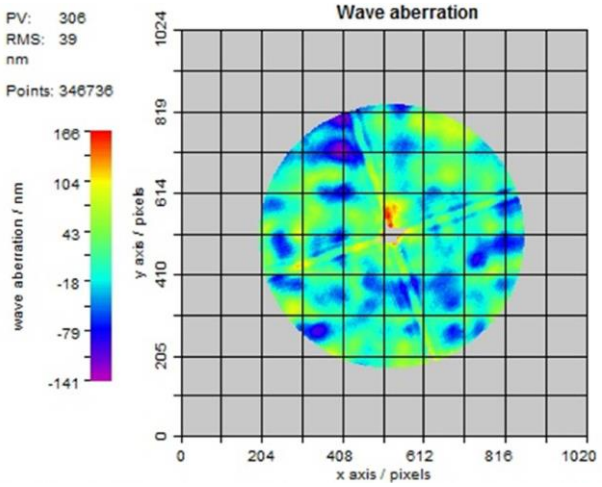

Figure 7-6: Wavefront measurement for the collimator powered optics. The cross pattern visible in the wavefront is the crosshair in the pupil mask, whose center materializes the on-axis beam.

In this way, the beam is collimated by the powered optics and reflected back by the large reference mirror. The wavefront is analysed by the interferometer and minimizing the RMS wavefront error we fine tuned the collimator optics. The result of the alignment is a residual error of 39 *nm* RMS, about 1/15 of the used wavelength.

7.1.2 Alignment of the FP20 optics

Similarly to the collimator optics, the alignment of the FP20 optics is in two steps. First, the optical axis is aligned through the flat mirror components, and second the powered optics are installed and aligned. Since the sensor is in a fixed position on the bench and its mechanical axis cannot be aligned, the FP20 optics are aligned to the HWS mechanical axis. To perform this operation the collimator lenses were removed (they can be accurately re-positioned using very precise mechanical pins) and we used the collimated 10*mm* beam from the FISBA as a reference. Two targets were installed, with mechanical precision, in the HWS, to define the vertical mechanical axis of the HWS. To maximize our sensitivity performing this alignment, the two targets were positioned at the maximum possible distance; therefore, the first target was at the entrance of the HWS, just after the 45° mirror folding the beam up toward the HWS, while the second target was just before the CCD camera. Tilting the 45° mirror using the tip-tilt piezoactuators of its mount, the incoming beam is centered with respect to the two targets and the beam is aligned to the bore sight of the HWS.

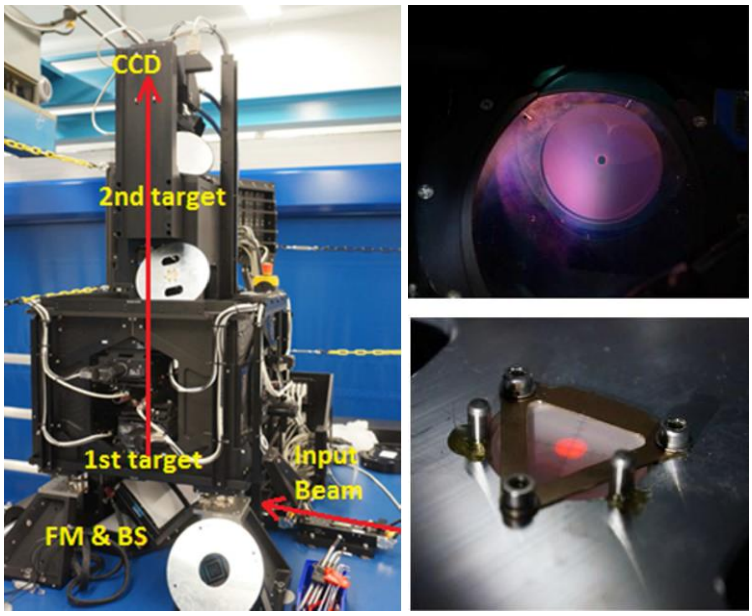

Figure 7-7: on the left, side view of the HWS and approximate position of the 2 targets used for the alignment of the beam to the mechanical axis of the HWS. On the right, an image of the 2 targets and the beam aligned to both.

We then installed the K-mirror on the bench. The K-mirror is a widely adopted solution for field derotation in alt-azimuth mounting telescopes, and is the HWS counterpart of the GWS bearing. This device corrects a rotation angle θ by rotating $\theta/2$ arount its axis. The K-mirror consists of three flat mirrors assembled on a single stiff and stable frame mounted on a bearing, whose rotation axis has to be aligned to the FP20 optical axis. To assist the alignment of the K-mirror we used a specific custom tool, showed in Figure 7-9. This consists of a reference mirror for tilt measurement (using the FISBA in double pass), a position sensor, which measures lateral displacement of the beam, and a beam splitter, which splits the light, sending 50% to the mirror and 50% to the position sensor. In this configuration both parameters can be measured simultaneously, simplifying the

alignment of the K-mirror, as tilt and decenter are not independent in the adjustment procedure of the K-mirror.

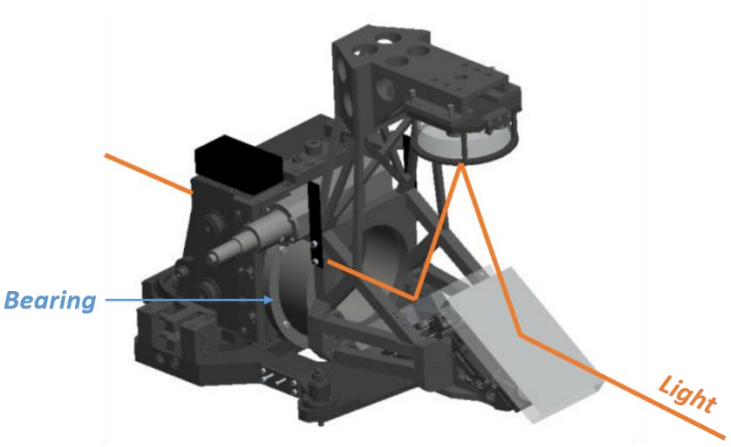

Figure 7-8: the K-mirror in the vertical (0°) position.

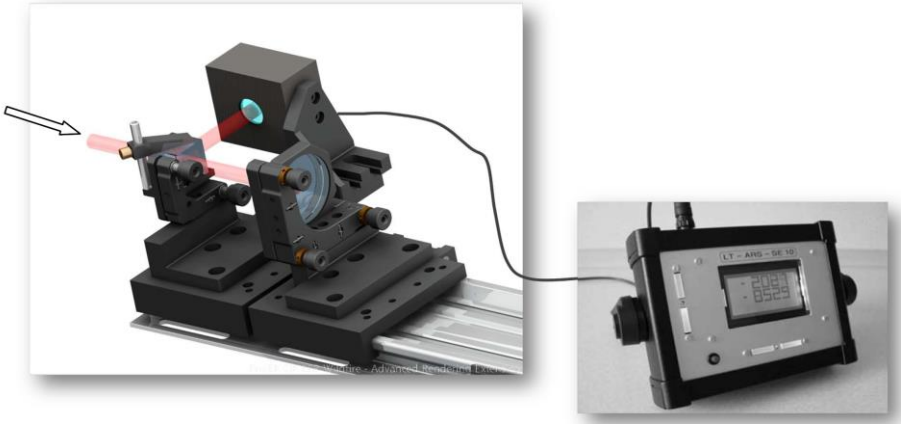

Figure 7-9: alignment tool for the K-mirror. To retrieve the tilt of the beam the light reflected back from the mirror is analysed by the FISBA, to retrieve the lateral shift a position sensor measures the movement of the beam folded by the beam splitter.

This tool was mounted behind the K-mirror position and aligned to the optical axis, materialized by the 10 *mm* diameter beam delivered by the FISBA, before the installation of the K-mirror on the bench. In this way the K-mirror is placed and aligned, until de-center and tilt are identical to the values measured before insertion of the K-mirror. Screw mechanisms allow to adjust pitch, yaw and de-centering of the whole K-mirror. The goal of the alignment is to obtain a spot as stable as possible during a full rotation of the K-mirror, and anyhow a de-center of the chief ray below 100 μm and a tilt of 40 *arcsec*. Fulfilling the de-center requirement we ensure that the image of a star will always be well within the SE FoV (1.1 *mm* in the focal plane), while a tilt of the beam by 40 *arcsec* would lead to a shift of the pupils of 1/10 of subaperture.
The result of the K-mirror alignment is a lateral shift of the beam of about 100 μm for a 90° rotation and a tilt of 15 *arcsec*, satisfying both the requirements.
Finally the powered optics of the FP20, consisting of 3 lenses, were integrated in the path. For a first coarse alignment, the back reflected light, starting from the last lens, was used. With the FP20 lenses roughly in their nominal position, the collimator lenses were re-installed and the spherical objective is mounted back on the FISBA. A spherical mirror,

with its center of curvature coinciding with the focal point of the FP20 optics, reflects the light back into the interferometer. The fine tuning of the FP20 lenses is done by minimizing the wavefront error of the returned beam.

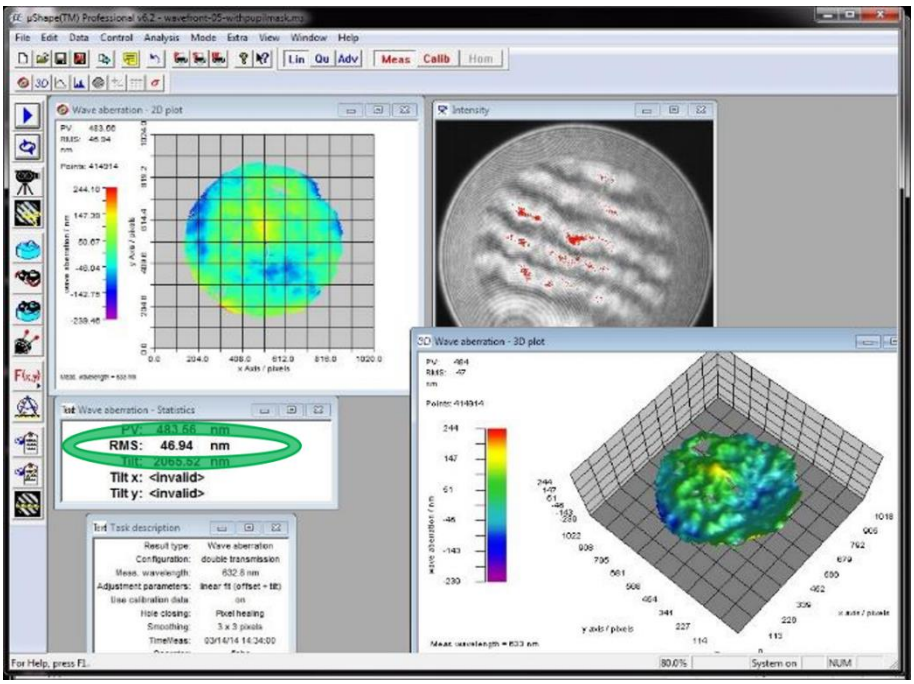

Figure 7-10: Final wavefront measurement after FP20 alignment.

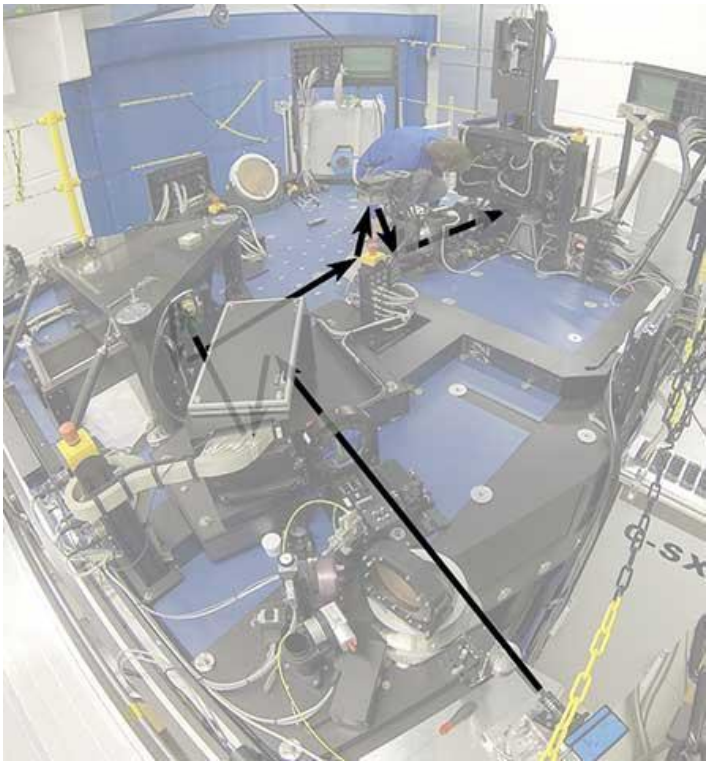

Figure 7-11: Light from the telescope enters at lower right and passes through the collimating lenses before bouncing off a flat mirror. The second reflection takes place at the surface of a 349 actuator deformable mirror before continuing on to the midline of the instrument. Reflections off the piston mirror and a visible-infrared dichroic send the radiation to the FP20 lens system at upper right. The K-mirror precedes a final mirror, which sends the light upward into the wavefront sensor.

The wavefront delivered to the HWS from the warm optics has a residual WFE of less than 50 *nm* (at a wavelength of 633 *nm*) whose main part comes from the DM. It is then clear that this number can be further minimized shaping the DM in an appropriate way, even if the result is already extremely good, thinking at the number of optics the light is passing through.

7.2 HWS Alignment

With all the fore-optics aligned, we could finally start the HWS alignment. It basically consists in centering the HWS's CCD to the on axis reference beam, conjugate it to the proper height and co-align the 8 SEs in tip-tilt and focus to avoid incorrect overlap of the pupils on the detector.
Since the HWS works with up to 8 stars, distributed on a 2 *arcmin* FoV, while the FISBA beam simulates only an on-axis star, the alignment of the HWS cannot be fully accomplished just using the FISBA beam, but it relies on the previous alignment of a fiber plate (which is part of the calibration unit of the instrument) containing 23 fibers, 1 on-axis and 22 off-axis evenly distributed over a 2 *arcmin* FoV.
In turn, the alignment of the fiber plate cannot be performed before a preliminary partial alignment of the HWS to the on-axis reference beam, leading to a multi-steps alignment procedure, described hereafter.

7.2.1 Alignment of the lateral position of the CCD39

A mask with a small central hole is inserted in the light path, at the visible pupil plane. No SEs are inserted in the path, so the light enters the HWS passing directly through its pupil re-imager and is imaged on the CCD. The CCD is moved on its plane till the centroid of the spot produced by the on-axis beam falls at the center of the CCD. However, because of the non-perfect perpendicular mounting of the CCD stages, a motion along the optical axis shifts the spot also in X and Y direction. The lateral position is then re-adjusted after the CCD is focused to the pupil plane.

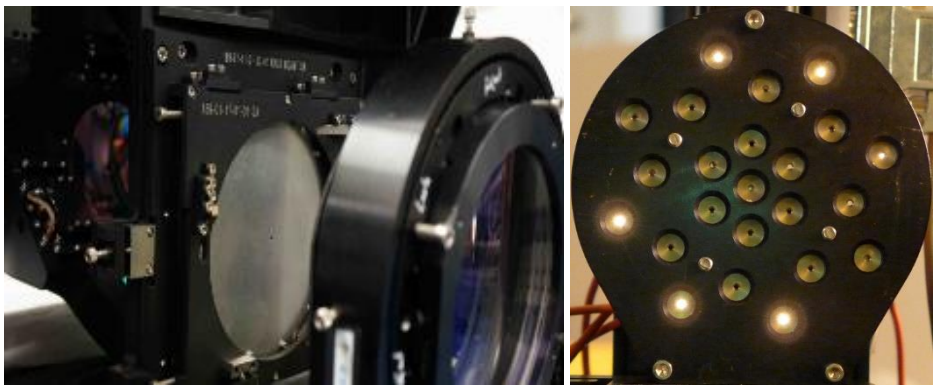

Figure 7-12: on the left the mask with a 2 mm central hole positioned in the visible pupil plane, used for the CCD39 centering and conjugation to the pupil plane and for the SEs tip-tilt alignment. On the right, the fiber plate containing 23 fibers (1 on-axis) distributed in a 2 arcmin FoV, used during the HWS alignment.

7.2.2 CCD conjugation to the pupil plane

The CCD is initially conjugated to the pupil plane rather than to its correct conjugation height, to ease and speed up the alignment of the SEs of the HWS. In fact, when the CCD is conjugated to the pupil the images of the pupil produced by each SE are perfectly superimposed on the detector, if all the SEs are perfectly co-aligned. Misalignment between SEs leads to a relative displacement of the pupil images on the CCD, which can be easily evaluated when the CCD is conjugated to the pupil, since all the pupils should have the same barycenter position. On the other hand, when the CCD is conjugated to a different height, the pupil images superposition on the detector is only partial, resembling the superposition of the reference stars footprints occurring in the atmosphere at the conjugation height. Therefore, even when the SEs are perfectly aligned, the barycenters of the pupil images produced by each SE on the detector fall on different pixels, making harder to understand when a satisfactory alignment is achieved. The CCD conjugation to the pupil plane is done using more than one fiber (we used 4) of the fiber plate, whose light passes through the PR-I of the HWS and is focused on the CCD. The CCD is optically conjugated to the pupil plane when the spots produced by each fiber perfectly overlap with the ones produced by the other fibers. The fact that the fiber plate is not yet aligned to the reference beam has a negligible effect in this phase, provided that the light from the fibers used at this stage passes through the PR-I. Once the CCD is properly focused to the pupil plane, its lateral position is adjusted as described before.

7.2.3 Preliminary alignment of the SEs tip-tilt

The 8 SEs of the HWS are then pre-aligned in tip-tilt, a step necessary for the tip-tilt alignment of the fiber plate. At this point the only reference source is the on axis beam of the FISBA, so first of all we checked that all the SEs could reach the reference beam, which is at the edge of their travel ranges, and verified that the pyramid rotation angle of each SE was aligned with the CCD rows/columns to 0.1 pixel. Each SE is then finely centered on FISBA PSF. This operation is performed removing the mask in the pupil plane so that the SE is receiving the whole beam and produces on the CCD 4 images of the pupil. The SE is correctly centered on the reference beam when the 4 pupils are equally illuminated. For the SE tip-tilt alignment the holed mask is introduced in the path, in order to have 4 small spots on the CCD instead of 4 big pupil images, to facilitate the completion of this task (it is easier and more accurate computing a centroid on a small spot rather than on a big one).

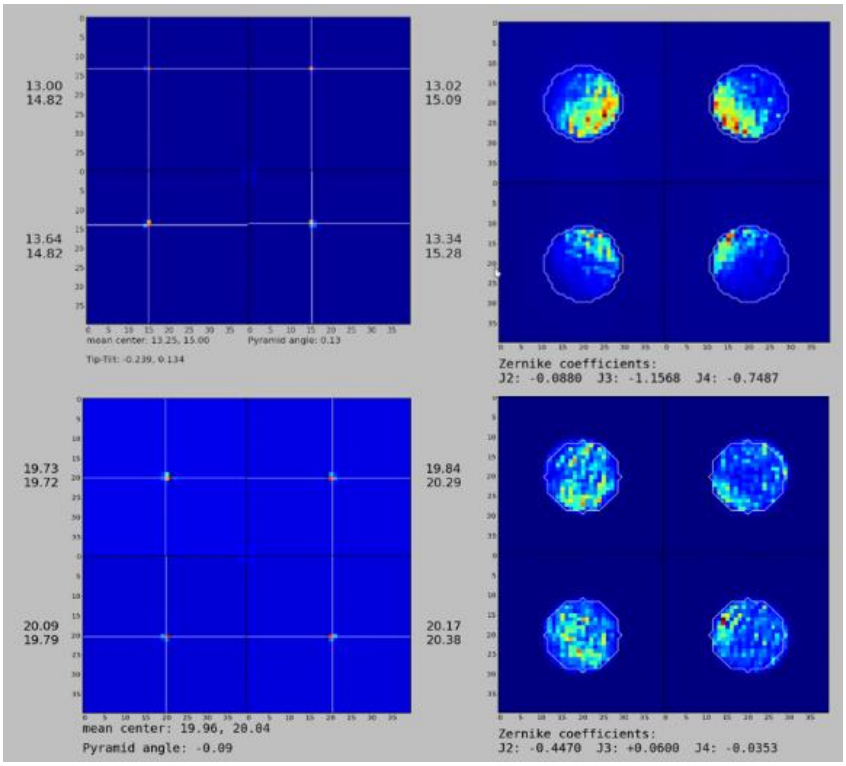

Figure 7-13: in the top panels the signatures on a mis-aligned SEs. On the left the four small spots produced by a SE used for the tip tilt alignment. On the right the four pupils produced by a SE used for its focus alignment (a clear intrs-focus signal is visible in the top-right panel). In the bottom panel the signatures of an aligned SE (centroids of the 4 spots on the right pixel within the requirements and pupils evenly illuminated).

The goal of the alignment is to obtain, for each SE, that the centroid of the 4 spots produced by all the SE falls on the same CCD pixels, namely pixel (20, 20) of each CCD quadrant, with a maximum discrepancy of 0.1 pixels (1/10 of a subaperture, as for the GWS, as 1 pixel corresponds to 1 subaperture). When this result is achieved, all the SEs are well co-aligned in tip-tilt and can be used as a reference for the tip-tilt alignment of the fiber plate.

7.2.4 Fiber plate alignment

As stated before the fiber plate is constituted of 23 fibers, displaced on a 2 *arcmin* FoV, inserted in a curved aluminum plate to simulate the curved FoV (FP15), delivered from the LBT, entering the LN bench. Its alignment to the reference beam is crucial to refine the alignment of the HWS SEs. The initial step is to align the central fiber to the telescope focal plane as defined by the FISBA beam. A flat mirror in the calibration unit, with the possibility to rotate, is positioned so to reflect the light from the central fiber of the fiber plate into the main beam beam of the telescope, toward the HWS. A SE is positioned on axis, intercepting the light of the FISBA beam and producing 4 equally illuminated pupil images on the detector. The FISBA is then switched off and the fiber plate is moved, thanks to its motorized stages, initially on its XY plane until the PSF produced by the central fiber is perfectly centered on the on-axis SE, and then in Z axis to minimize the focus term measured by the WFS. The central fiber of the fiber plate is now aligned to

the FISBA beam. Four different SEs are then centered, one at the time, on the on axis fiber and aligned in focus adjusting the focus mechanism of the SEs, minimizing the defocus term measured by the HWS.

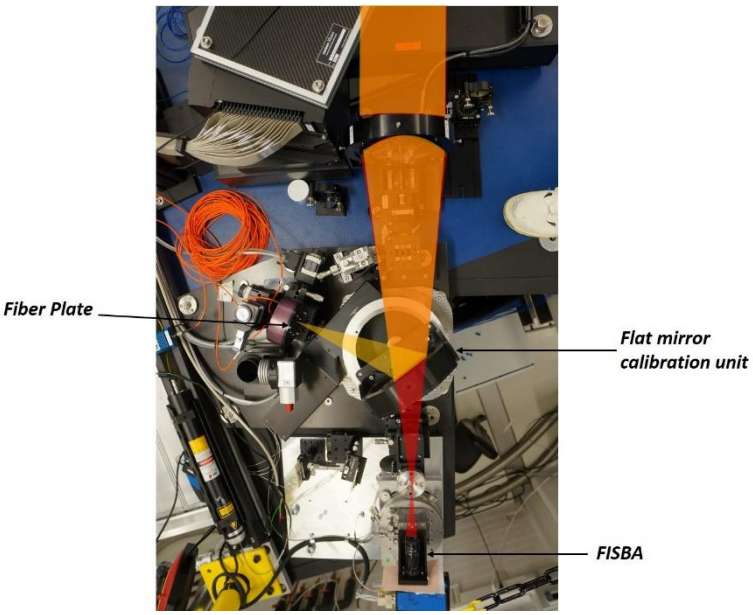

Figure 7-14: Reference light sources area. The fiber plate on-axis beam (yellow) is co-aligned to the reference FISBA beam (red) translating the fiber plate and rotating the flat mirror of the calibration unit.

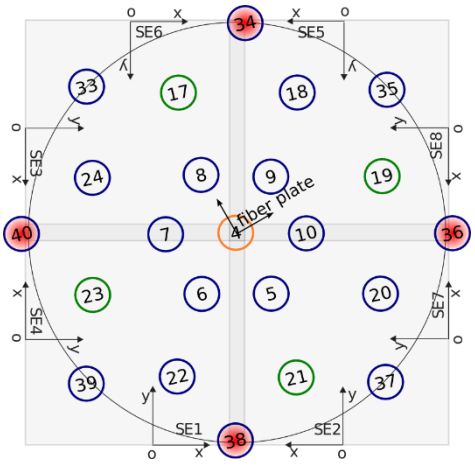

Figure 7-15: coarse positions of the fibers on the fiber plate. The circle represents the 2 arcmin FoV, the different squares represent the areas spaned by different SEs. The central fiber is reachable by all the SEs. The tip tilt alignment of the fiber plate was done on the green positions (fibers #17, #19, #21 and #23). The fibers in red were not reachable by any SE since the outermost fiber ring of the fiber plate has a diameter that proved to be slightly larger than the diameter corresponding to the 2 arcmin FoV.

The same 4 SEs are used for the tip-tilt alignment of the fiber plate, achieved with an iterative procedure centering the aligned SEs on the on axis and off axis fibers.
Since the curved focal plane delivered from the LBT is flattened at the HWS entrance by the FP20 optics, the fiber plate tip tilt alignment is performed by simply minimizing the focus gradient along each tilt axis by tilting the fiber plate.

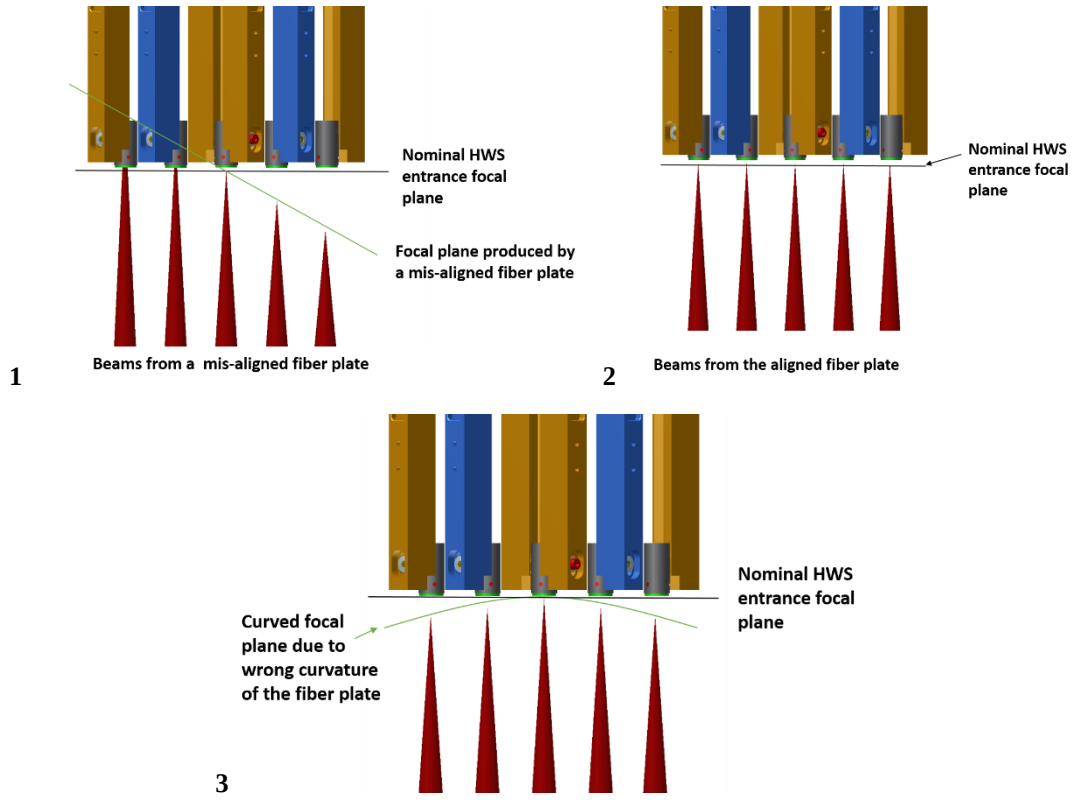

Figure 7-16: In panel 1 is depicted a focal plane delivered by a tilted fiber plate (the effect is here greatly magnified). In panel 2 the focal plane when the fiber plate is perfectly aligned. In panel 3 a representation of the initial result of the alignment (again the effect here is greatly magnified). The fiber plate is well aligned in tip tilt but the delivered focal plane shows a residual curvature, probably due to a wrong curvature of the fiber plate.

When the defocus signals measured by the 4 SEs on various fibers in different FoV (#17, #19, #21 and #23 in Figure 7-15) positions are the same, the fiber plate is aligned and the absolute focus is adjusted by moving it along Z direction to minimize the defocus signal. What we measured at the beginning was a symmetric defocus gradient across the FoV, indicating that the fiber plate was correctly aligned in tip-tilt but the HWS entrance focal plane was not flat as it was supposed to be. This problem could derive from: a wrong curvature of the fiber plate, some effects introduced by the FP20 optics or an inclination of the linear stages moving the SEs. To investigate this problem we moved the fiber plate on a plane perpendicular to the optical axis of known amounts (8.25 *mm*). The fact that the fiber plate is curved, to mimic the curvature of FoV delivered by the LBT (FP15), and we are moving it on a plane translates into an axial shift of the sources, depending on their position in the fiber plate and on the lateral shift applied to it.

Knowing these parameters and the curvature radius of the FP15 we derived the expected defocus signals for different shifts of the fiber plate The measured values are then compared with the expected ones.
The expected focal shifts resulting from these lateral displacements of the fiber plate are:

- - 0.19 *mm* in FP15 coordinates (0.25 *mm* in FP20) for a shift of -8.25 *mm*, giving a defocus signal on the HWS, in arbitrary units, of - 0.17.
- + 0.25 *mm* in FP15 coordinates (0.33 *mm* in FP20) for a shift of +8.25 *mm*, giving a defocus signal on the HWS, in arbitrary units, of + 0.23.

Measured results:

- -0.1 arbitrary units
- +0.1 arbitrary units

Due to vibrations, the precision in measuring the defocus signal with our setup was ~ 0.05 arbitrary units. This test is basically insensitive to the fiber plate curvature, while it measures a possible defocus signals introduced by the FP20 lenses and inclinations of the SEs linear stages. Since the result of the test is almost consistent with our expectations, and anyhow below the relative focus alignment tolerance for the SEs of 0.15 arbitrary units, we concluded that FP20 lenses and SEs linear stages are working as expected, unless the very unlucky and unlikely case they are compensating each other. The different focus signals measured moving a SE on and off-axis was then considered mainly as the result of a wrong curvature of the fiber plate, that was redesigned, reworked and tested. The new fiber plate reduced the residual curvature at the HWS entrance focal plane, and, even if this parameter is not totally eliminated, it is now within the requirements.

7.2.5 SEs fine alignment

Once the fiber plate is aligned we had a large number of fibers available to refine the SEs tip-tilt and focus alignment. Since the linear stages moving the SEs are affected by pitch, roll and yaw, to minimize their effects on the pupil images, the idea is to move each SEs to the middle of its travel range and then to center it to the closest fiber for tip-tilt and focus alignment.
The tip-tilt alignment concept is the same described in the paragraph of the SE preliminary alignment.

SE	***Defocus [nm WFE]***	***Tip-Tilt (mean center)***
SE01	7	20.09, 19.99
SE02	20	20.03, 19.98
SE03	4	20.03, 19.97
SE04	4	19.97, 20.02
SE05	10	20.00, 20.00
SE06	2	20.05, 20.03
SE07	20	20.01, 20.06
SE08	3	20.00, 20.01
GOAL	**20**	**(20.00, 20.00) ± 0.1**

Table 7-1: Results of the HWS SEs fine alignment.

The SE focus alignment is performed shifting the whole SE along the optical axis to minimize the defocus signal measured by the HWS. The goal is to have, for all the SEs, a residual wavefront error due to the defocus term of less than 20 *nm*, corresponding to 0.15, arbitrary units, in our measurement system. The results of the alignment are presented in Table 7-1, showing the requirements have been succesfully met for all the SEs.

7.2.6 CCD conjugation to the deformable mirror

To conclude the alignment of the HWS, the CCD39 was conjugated to the correct altitude. A holed mask is located as close as possible to the optical surface of the deformable mirror, which is optically conjugated to the required altitude of 7.1 *km*. One SE is centered on the on-axis fiber and another SE is centered on an off-axis fiber, the CCD is then moved along the optical axis until the spots produced by the 2 SEs overlap on the detector.

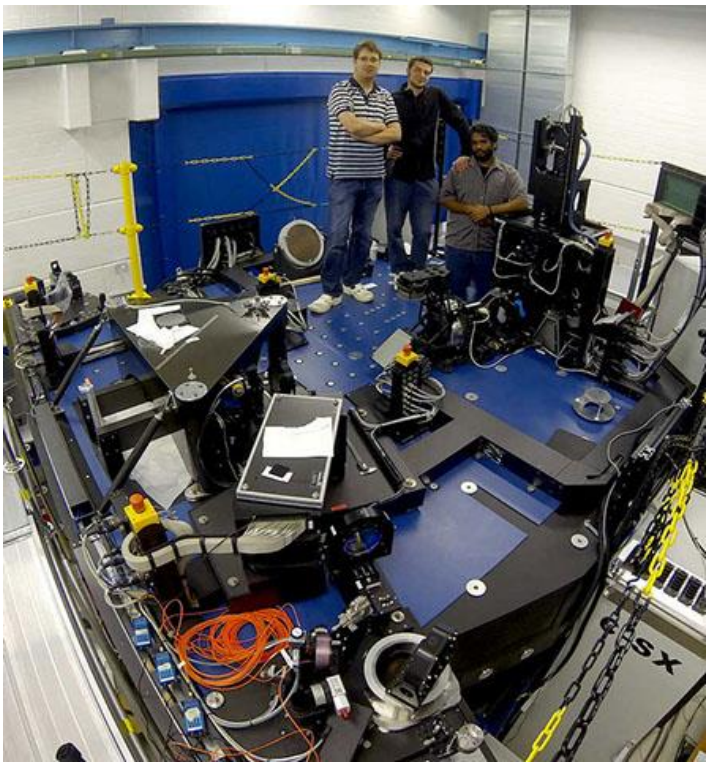

Figure 7-17: satisfaction after the alignment of the first HWS.

7.3 Mapping of the HWS Star Enlargers

The HWS is now aligned and ready to be tested in the lab, trying to close an adaptive optics loop injecting some artificial turbulence in the beam and correcting for it with the DM. In the lab the acquisition of the sources of the fiber plate was done by manually moving the SEs in the FoV, using an engeeneristic interface to command the linear stages of the SEs, until we could see some light passing through the SE. Of corse this in not

possible when observing on sky; the acquisition of guide stars must be automatic and in one shot.

To do this it is necessary to have a good knowledge of the relative orientation of the HWS entrance focal plane and of the movement axes of each SE. Now, F_{HWS} is the focal plane coordinate system of the HWS, fixed with respect to the reference star selection unit of the HWS, i.e. the mechanical structure that holds all SEs stages. The origin of the Cartesian coordinate system is the nominal centre of the focal plane, the orientation is as seen from the rear end (CCD) of the HWS looking into the direction of the focal plane. The coordinates in the focal plane are given in μm. F_{SEi} represents the coordinate system of SE i. The base vectors (see Figure 7-18) point in the direction of travel, the units in this coordinate system are in steps of the encoder of the motor moving the SE. The scope of the mapping is to estabilish a correct transformation between these two coordinates systems. In this way, once the position of a star in the focal plane is known, the positioning software of the SEs perfectly knows the command to apply to a given SE in order to acquire that star.

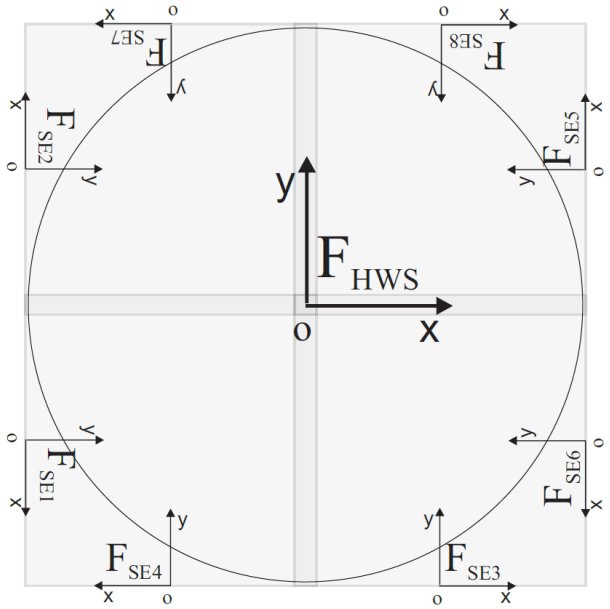

Figure 7-18: Coordinate system definition for the HWS. The circle represents the theorical 2 arcmin FoV, each square represents the area spanned by a SE.

The FoV of a SE is about 1.1 *arcsec* corresponding to about 0.88 *mm* in the focal plane. The precision in the acquisition of a reference star with a SE shall then be better then this. After a coarse positioning of the SEs, the position of each SE will be optimized by minimizing the tip/tilt signature retrieved by the HWS with an automatic script.

The parameters to be determine to build the transformation matrix between the two coordinate systems are the skew angles between the x-y axes of F_{HWS} and F_{SEi} and the distance between their origins.

The idea was to use different fiber positions of the fiber plate, one on axis and 8 off-axis. The focused spot produced by the on axis fiber was of course defining the origin of the MHWS focal plane coordinate system. Each SE shall be moved on 3 different stars simulated by the fibers of the fiber plate, the one on axis and 2 off axis, and for each position the linear stage coordinate shall be noted down. Knowing the relative

displacement of the fibers in the fiber plate, it is possible to retrive for each SE the orientation of their X and Y stages with respect to the X and Y axes of the MHWS focal plane. To start, since the linear stages were positioned with a good mechanical accuracy in the HWS structure, I considered all the SEs to have their movement axes perfectly parallel (or perpendicular, depending from the axis) to the ones of F_{HWS}. All the SEs were moved to the central fiber, defining the origin of F_{HWS}, so to define the distance between the origins of the coordinates systems. SE07 could not really reach the central fiber, only some light was visible at the edge of the pupil images, meaning that the image of the fiber was at the edge of the SE07 FoV. Then I exploited the full travel range of each SE, both in x and y, to define the true areas spanned by the SEs (the one shown in Figure 7-18 are just an ideal representation).

	X		**Y**	
	Steps	***μm***	***Steps***	***μm***
SE01	-3009000; +3195000	51493.2	0; +6160000	51128
SE02	-3026000; +3235000	51966.3	0; +5991000	49725.3
SE03	-3042000; +3215000	51933.1	0; +6119000	50787.7
SE04	-3062000; +3203000	51999.5	0; +6120000	50796
SE05	-3056000; +3191000	51850.1	0; +6111000	50721.3
SE06	-2954000; +3192000	51011.8	0; +6187000	51352.1
SE07	-3037000; +3188000	51667.5	0; +6253000	51899.9
SE08	-3053000; +3172000	51667.5	0; +6167000	51186.1

Table 7-2: SEs total travel range.

Each SE was then homed (positioned in the origin of its coordinate system) and then sent to two specific positions, different for different SEs, in the F_{HWS}, in correspondence of, according to our calculations (knowing the relative positions of the fibers on the fiber plate), the image of a fiber of the fiber plate. The source is considered perfectly acquired when the pupil images produced by the SE are equally illuminated. Using a skew angle of 0° for all the SEs both in x and y axes we were able to acquire, even if not perfectly, the two fibers reachable by a given SE. To have an estimate of the precision in the

acquisition, for each SE we fine tuned its position so to get 4 equally illuminated pupils on the CCD and we recorded the number of encoder steps we have moved it from its original position. Converting this number in linear coordinates of the F_{HWS} we obtained the distance at which the SE arrived from a perfect acquisition. These discrepancies are reported in Table 7-3.

	SE01		***SE02***		***SE03***		***SE04***		***SE05***		***SE06***		***SE07***		***SE08***	
Fiber	***Δx***	***Δy***	***Δx***	***Δy***	***Δx***	***Δy***	***Δx***	***Δy***	***Δx***	***Δy***	***Δx***	***Δy***	***Δx***	***Δy***	***Δx***	***Δy***
#17	-	-	-	-	170	20	-	-	-	-	170	30	-	-	-	-
#18	-	-	-	-	-	-	-	-	70	20	-	-	-	-	Collision detected	
#19	-	-	-	-	-	-	-	-	50	20	-	-	-	-	0	0
#20	-	-	Collision detected		-	-	-	-	-	-	-	-	250	140	-	-
#21	-	-	130	60	-	-	-	-	-	-	-	-	320	150	-	-
#22	120	50	-	-	-	-	Collision detected		-	-	-	-	-	-	-	-
#23	200	20	-	-	-	-	50	50	-	-	-	-	-	-	-	-
#24	-	-	-	-	180	0	-	-	-	-	Collision detected		-	-	-	-

Table 7-3: Measured discrepancies, in µm, between the position reached by the SE and the exact position of the fiber image at the F_{HWS}.

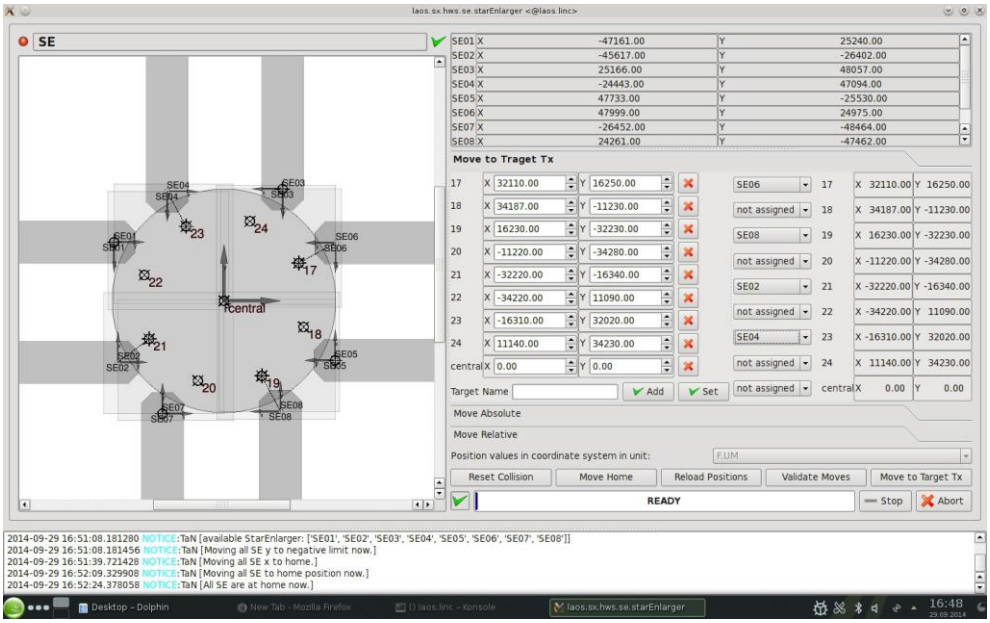

Figure 7-19: Position of the fibers used fot the verification of the mapping. Each SE can reach only the 2 fibers inside its spanned area (represented by the square). Some combinations are not possible because of detected collisions between SEs. The grey silhouettes represent faithfully the SEs. The software predict a collision when, executing the user command, a silhouette would touch another one.

Note that for some SEs (SE02, SE04, SE06 and SE08) was not possible to acquire two different sources, since the software was detecting a collision with the neighbour SE when trying to reach that position, not allowing then to move the SE there.
In all the possible combinations, and for all the SEs, pupil images were immedialty visible on the CCD, validating the mapping of the SEs. Moreover, for all the SEs but SE07, the discrepancy between the position of the SE and the exact position of the source image at the F_{HWS} coordinate system is less than 200 μm, less than 1/4 of the SE FoV and more than sufficient for the scope of the mapping. The worse performance of SE07 is due to the fact that was not possible to correctly define the distance between its origin coordinate system and the F_{HWS} origin, as it could not perfectly reach the central fiber. The measured discrepancies are anyhow well below the SE FoV.

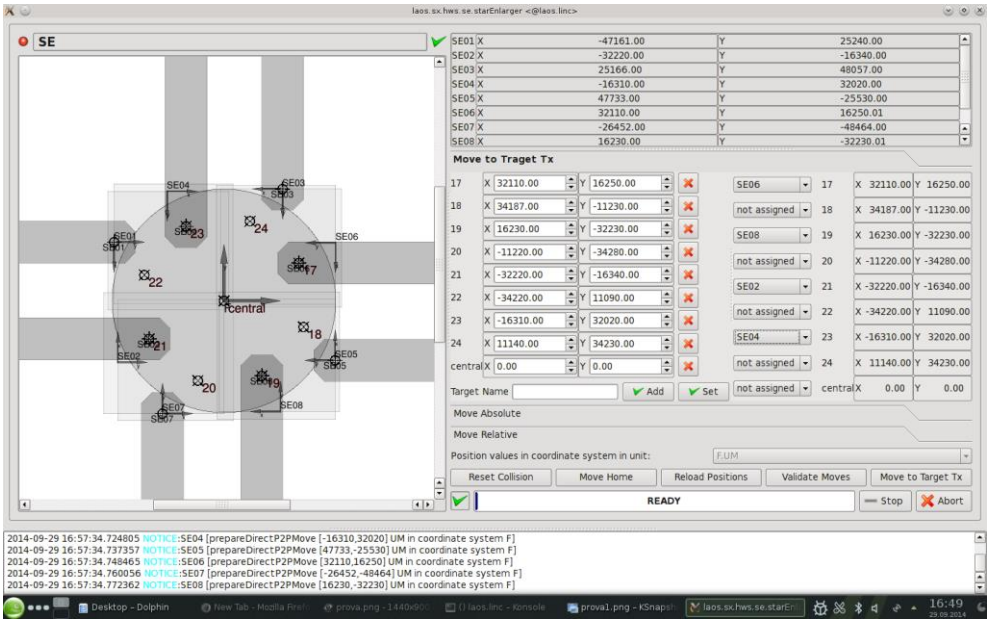

Figure 7-20: The SEs move to one of the fiber's position.

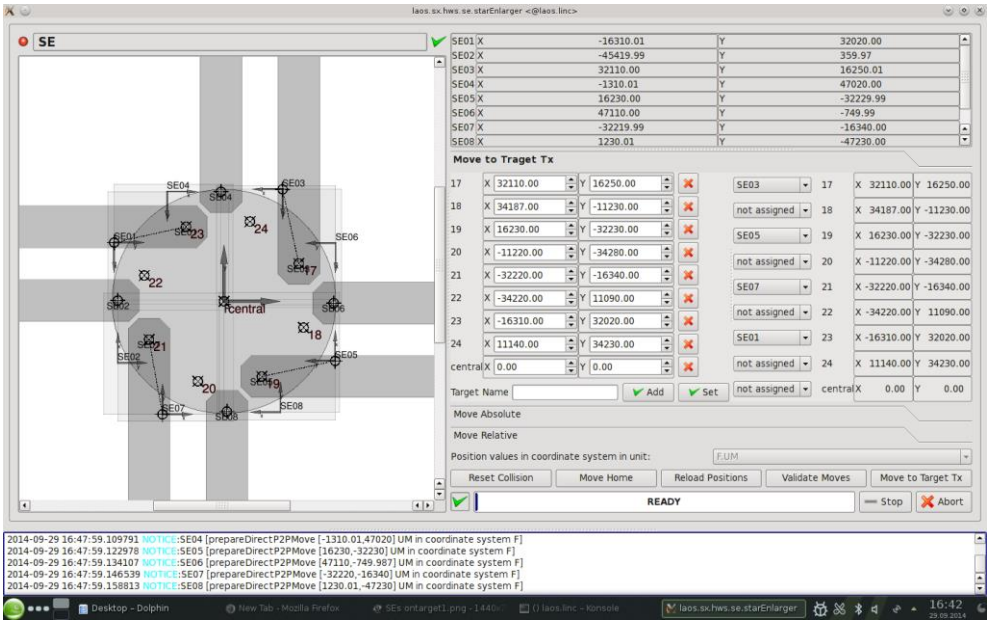

Figure 7-21: The other 4 SEs acquiring the same fibers. The second fiber in each quadrant is not reachable by both the SEs because of detected collisions.

7.4 AO correction with the HWS

Finally we verified the performances of the HWS and its ability to drive the XINETICS DM. An interaction matrix has been measured, using the same scheme to the one used for Pathfinder, but with much less actuators (349 of XINETICS DM vs 672 of the ASM), to calibrate the response of the HWS. We used 8 fibers of the fiber plate and 8 SEs to completely fill the metapupil and we measured the residual WFE before and after correction. To simplify operations, we tested the system at a single fixed rotation angle of the K-mirror, to avoid computing rotating interaction matrices, as done during Pathfinder. The results are shown in Figure 7-22.
In summary the plot shows the residual WFE in *nm* for 4 different cases:

- 0 – 1000 frames: open loop, DM flat and no disturbance injected.
- 1000 – 2000 frames: closed loop and no disturbance injected.
- 2000 – 5000 frames: open loop with disturbance.
- 5000 – 10000 frames: closed loop with disturbance.

As for the Pathfinder the turbulence was injected in the DM, and we corrected the first 150 modes of aberration. The WFE drops from about 400 *nm* RMS to about 150 *nm*, leading to a Strehl Ratio of about 0.2 in visible light (at 600 *nm*), using Formula [5-5].

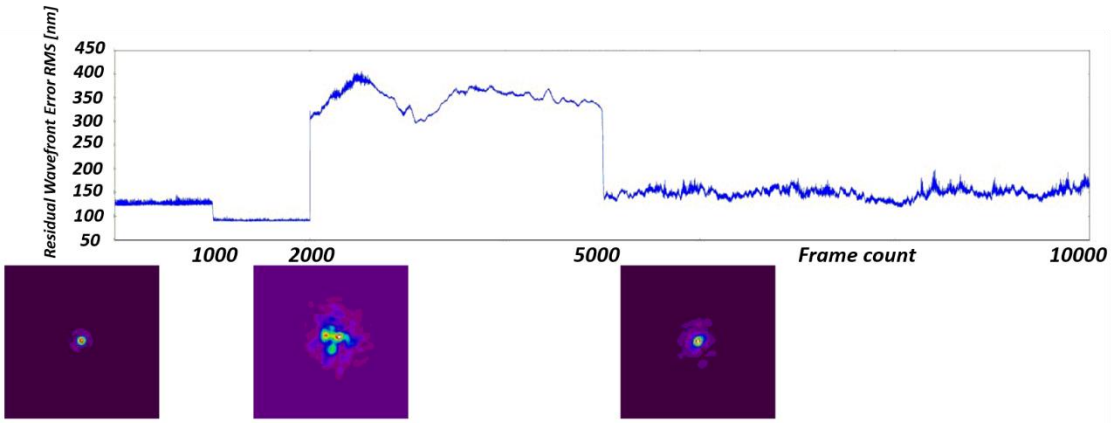

Figure 7-22: Residual wavefront error in the 4 different cases. The WFE drops from 400 nm to about 150 nm when correcting the first 150 modes of aberration with the DM. The three small panels on the bottom are real IR images taken with the scientific camera at 1.3 μm. The first on the left is with the flat DM and no disturbance, the second in open loop with disturbance and the third is closed loop with disturbance.

7.5 GWS alignment to LN bench

The last subsystem to be integrated and aligned in order to complete a full MCAO arm is the GWS. Since the sensor was already internally aligned, as described in Chapter 5, the goal is to co-align the rotation axis of the GWS to the optical axis of LN and to properly focus the GWS through the AM. Differently from the HWS, the GWS does not have a calibration source integrated in the LN bench, so for these operations we had to use an external source. The Magic Lantern (the same used during Pathfinder) is placed in front of the annular mirror.

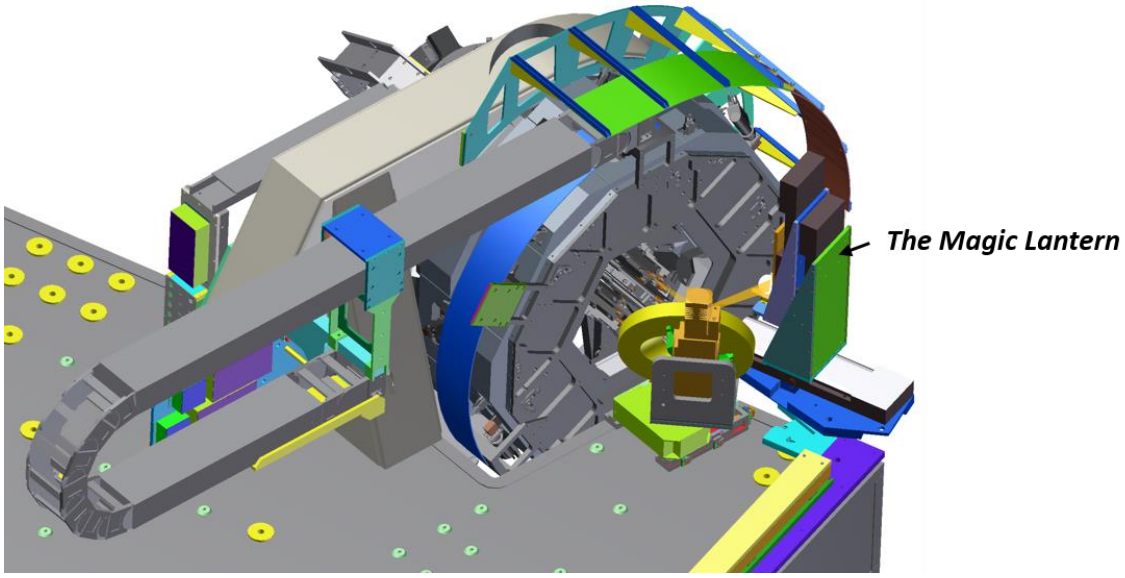

Figure 7-23: Setup used for the alignment of the GWS to the rest of the instrument. The Magic Lantern is calibrated shining its light through the hole in the AM and using the feedback of the HWS SEs.

The ML has to be moved in 3D such that its F/15 beam is positioned along the curved focal plane. Its stages move in a plane which may not be exactly perpendicular to the optical axis of the instrument. Therefore, the position and orientation of the ML with respect to the instrument has to be calibrated before the alignment of the GWS can start.

To calibrate the ML, we initially shined its light through the AM hole, spanning the HWS FoV and acquiring its light with different HWS SEs at well known positions. The feedback signal (tilt and defocus) from the HWS was used to adjust the ML position on different HWS SEs. The set of stage coordinates that represent the in-focus position was then used to fit a spherical model, which is used to extend the 2 *arcmin* FoV just computed to the 2 – 6 *arcmin* FoV of the GWS. The AM mount features 1 tilt stage, 1 rotation stage and a translation stage (along the optical axis), the response from the GWS is used to adjust the AM position. Any residual misalignment that cannot be compensated with the AM has to be adjusted by shimming the whole GWS.

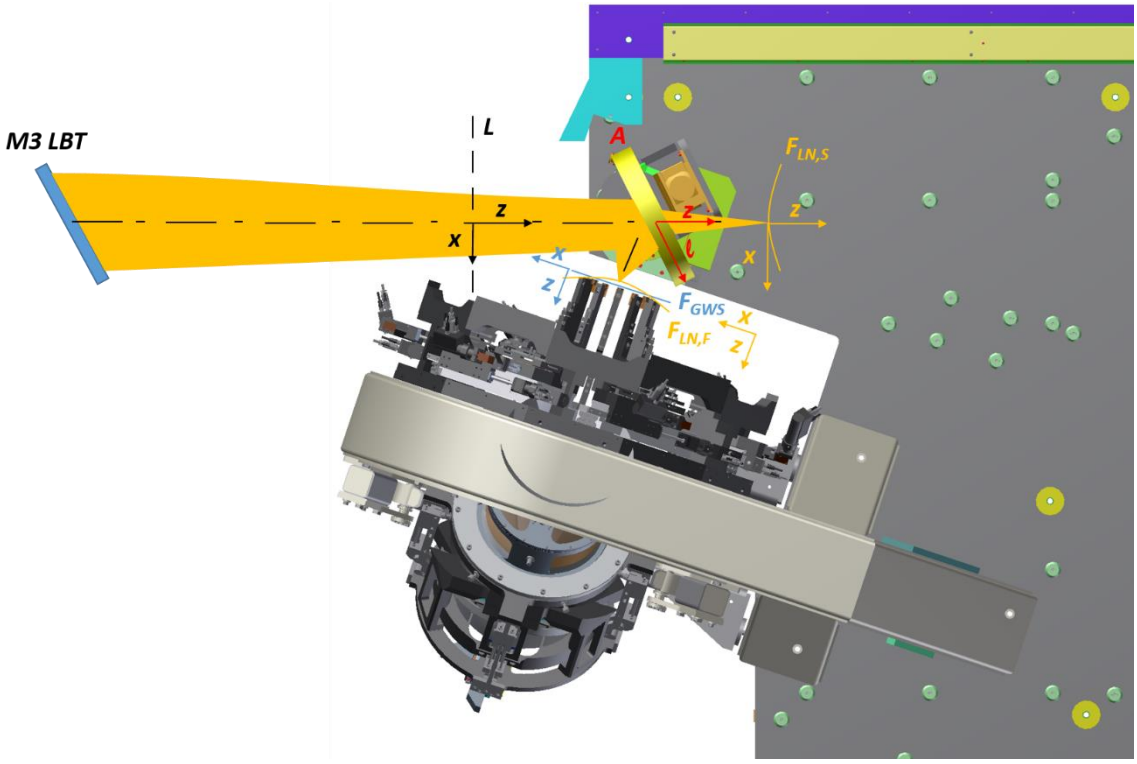

Figure 7-24: Sketch of the relevant reference planes for the GWS alignment to the rest of LN.The y axis, not shown here, is always directed toward the reader.

- **$F_{LN,S}$:** the straight LN internal F/15 focal plane to which the full instrument arm is aligned to. The straight telescope focal plane has to coincide with **$F_{LN,S}$**

- **$F_{LN,F}$:** the folded LN internal F/15 focal plane is defined by **$F_{LN,S}$** and the position and orientation of the AM

- **F_{GWS}** : the GWS internal focal plane, defined by the common nominal focus of the SEs and the rotation axis of the GWS bearing.

- **A**: Annular Mirror surface with the origin in the pivot point of the AM, directions y and l in the surface of the mirror, z in direction of straight light propagation.

- **L**: plane parallel to the tangential plane passing through the vertex of $\mathbf{F_{LN,S}}$ but in front of the AM. The Magic Lantern is positioned along this plane.

The goals of the alignment are:

- Minimize the tilt of $\mathbf{F_{LN,F}}$ with respect to $\mathbf{F_{GWS}}$

- Minimize the difference of the focus position of $\mathbf{F_{LN,F}}$ and $\mathbf{F_{GWS}}$ over the entire 2 – 6 *arcmin* FoV

- Minimize the decentering effect, i.e. reduce separation of the centers of $\mathbf{F_{LN,F}}$ and $\mathbf{F_{GWS}}$ in x and y directions.

After having made the ML parallel to the nominal optical axis of the LN arm (z-axis of **L** reference frame co-aligned with z-axis of $\mathbf{F_{LN,S}}$ reference frame), looking at the positions of the pupils produced on the HWS, we tested the possibility to align the AM tip-tilt using the position of the pupils on the CCD50 of the GWS as a reference. In fact, as already pointed out in Section 5.1, the position of the pupils on the CCD is sensitive to the tilt of the beam entering into the SEs. To do this we performed the following steps:

- The Magic Lantern is positioned at [0, 68] *mm* in the $\mathbf{F_{LN,F}}$ x-y coordinate system

- SE07 is positioned at [0, 68] *mm* in the $\mathbf{F_{GWS}}$ x-y coordinate system.

- The AM tip-tilt has been adjusted in order to center the pupils on the CCD50 with 1 pixel precision, equal to 24 μm.

A shift of the pupils on the CCD50 of 1 pixel corresponds to a tilt of the AM of :

$$Tilt = \frac{1}{2} \cdot \frac{k}{f_{PR-I}} \cdot Pupil\ shift\ on\ CCD \cdot 206265''$$

Where $f_{PR\text{-}I}$ is the equivalent focal lenght of the GWS Pupil Re-Imager and k is the star enlerger enlarging factor. Since, in our system, $f_{PR\text{-}I}$ = 223.9 *mm* and k = 12.5, the AM is aligned with respect to the GWS optical axis with a precision better than 138 *arcsec*. Using a centroid routine to measure the pupils positions with sub-pixel accuracy the precision could be easily improved of one order of magnitude.
The AM was homed several times and moved back to the same position to check its positioning repeatability, which resulted to be extremely good.
For the AM focus alignment we used the defocus signal measured by the GWS. As for the AM tip-tilt alignment, SE07 was moved at position [0, 68] *mm* in the $\mathbf{F_{GWS}}$ x-y coordinate system and the Magic Lantern was centered on SE07, so to obtain 4 equally illuminated pupils. To reduce the defocus term measured through SE07 the AM was shifted along the LN optical axis, with SE07 tracking the beam at the same time. This happens because focus compensation with the AM introduces a lateral shift of $\mathbf{F_{LN,F}}$. The

same was done using three other SEs positioned on a cross pattern on a circle of 68 *mm* in radius. Their positions are listed in Table 7-4.

	SEs starting position	**SEs focused position**	**Delta**
SE01	[0, -68] mm	[-6.1, -66.5] mm	[-6.1, 1.5] mm
SE03	[-68, 0] mm	[-75, 1.9] mm	[-7, 1.9] mm
SE07	[0, 68] mm	[-6.1, 70] mm	[-6.1, 2] mm
SE09	[68, 0] mm	[61, 1.5] mm	[-6, 1.5] mm

Table 7-4: positions of the SEs in the F_{GWS} x-y coordinates system before focusing the AM (SEs starting position) and after focusing the AM (SEs focused position). On average, to get focused pupils from the SEs we had to shift them by 6 mm in X axis and 2 mm in Y axis in the F_{GWS} coordinates system.

The result is that, to compensate the offset in focus between $\mathbf{F_{GWS}}$ and $\mathbf{F_{LN,F}}$ we introduced a lateral shift of $\mathbf{F_{LN,F}}$ wrt $\mathbf{F_{GWS}}$ of about 6 *mm* in the X axis and 2 *mm* in the Y axis.

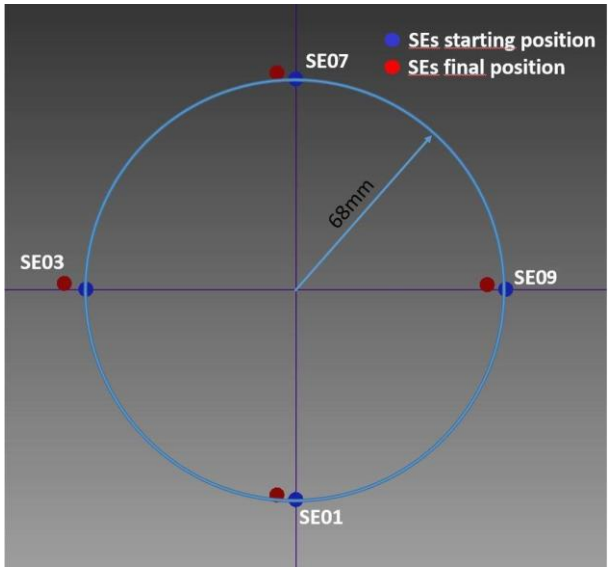

Figure 7-25: position of the SEs used for tip-tilt and focusing alignment of the AM, as seen from in front of the GWS entrance. The SEs were initially positioned on a cross pattern (blue circles) on a circle 68mm in radius, centered on the nominal center of the GWS focal plane. The pupils we got in these positions were highly defocused, so we moved the AM in focus, tracking the beam at the same time with the SEs. The red circles represent the positions of the SEs where we had, at a visual inspection, pupils with no defocus signal. The final positions of the SEs are shifted, on average, of 6mm in X axis and 2mm in Y axis wrt the starting position

To double-check this result in a different way, the Magic Lantern was positioned at [0, 68] *mm* in the $\mathbf{F_{LN,F}}$ focal plane and SE07 was centered onto the ML spot, corresponding to position [-6.17, 69.866] *mm* in the $\mathbf{F_{GWS}}$ focal plane, with the bearing at 0°. The bearing was then rotated of ±60° in steps of 15°, and at the same time the ML was displaced simulating a rotating FoV. For each position of the bearing, the discrepancy between the ML spot position in the $\mathbf{F_{LN,F}}$ focal plane and the SE position translated in the $\mathbf{F_{GWS}}$ focal plane has been recorded (see Table 7-5).

Offset X [*mm*]	Offset Y [*mm*]	Bearing rotation angle
-6.93	1.82	-60°
-6.29	2.57	-45°
-6.16	2.398	-30°
-6.093	2.178	-15°
-6.17	1.866	0°
-6.155	1.795	+15°
-6.21	1.588	+30°
-6.34	1.48	+45°
-6.50	1.36	+60°

Table 7-5: offsets in mm between ML spot position in $F_{LN,F}$ focal plane and SE07 position in F_{GWS} focal plane at different bearing rotation angles.

Considering the range [-30°, +30°] of bearing rotation, which is the bearing operative range when at the telescope, the mean offset between the centers of **F_{GWS}** and **$F_{LN,F}$** is [-6.2, 1.96] *mm*, confirming what measured during the AM focus alignment. The 2 *mm* offset in Y axis can be compensated by incresing the shims under the GWS, while the 6 *mm* offset in X direction cannot be really compensated since the only way to reduce it would be moving the AM along the optical axis, consequently introducing an offset in focus, or a very invasive remachining of the SEs.

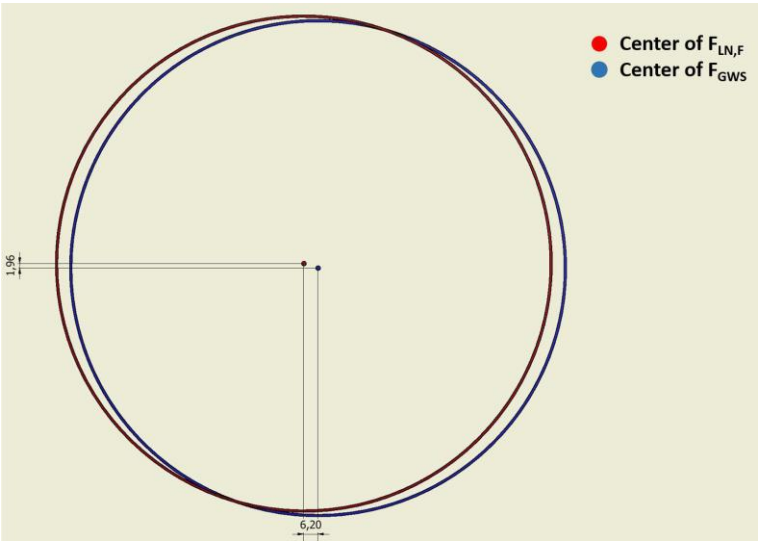

Figure 7-26: decenter between the $F_{LN,F}$ and the F_{GWS}

During investigations to understand the cause of this large offset between **F_{GWS}** and **$F_{LN,F}$** focal planes, it was found that the GWS is 5.4 *mm* closer to the center of the LN reference sphere (representing the on-axis focus position of **$F_{LN,S}$**) than what expected from the drawings. The reason of this discrepancy was found to be due to an incorrect positioning of the FISBA beam, which, due to an error in the CAD model, was shifted 4.3 *mm* toward the **F_{GWS}** from its correct nominal position.

The alignment of the collimator optics has been performed again with the correct reference beam while the GWS was not re-aligned, since this alignment was basically to demonstrate the validity of the GWS to bench alignment procedure and the GWS must be anyhow dismounted from the bench for the shipment to the LBT and re-aligned at the telescope.

8 Conclusions

Aligning an instrument with such a complexity, number of subsystem and degrees of freedom presents unique challanges. Numerous issues have been considered in advance in the alignment procedure and in the sequence of events, enabling a procedure that proved to be robust and lead to the succesful alignment of the MCAO module in the lab, allowing at the same time to detect some issues and problems, readily resolved in the lab but whose detection on the mountain would take a much longer time and effort. To cope with its complexity, LN is subdivided into different integration and alignment levels.
Each subsystem is firstly integrated and aligned separately, and when their performances are tested and verified to be compliant with the estabilished requirement, they proceed to the next higher level, which can be their integration to other subsystem (as for example the SEs inside the GWS structure) or to the LN bench.
Following this philosophy, the GWSs were integrated and aligned in Padova, at INAF – Osservatorio Astronomico di Padova premises. The GWS itself is a really complex instrument; the presence of 12 SEs, each one constituted of three optical elements, moving in a wide annular 2 – 6 *arcmin* FoV and sending light to a common Pupil Re-Imager, and the necessity to obtain and keep a very good super-imposition of the pupil images on the CCD, led to an overall alignment procedure in which more than one hundred degrees of freedom have to be contemporary adjusted. The rotation of the entire GWS to compensate for the sky rotation introduces further difficulties both in the alignment and in ensuring the required pupil super-imposition stability. We devised an Error Budget of all the possible error sources affecting the GWS, succeeding to match the tolerances we set in order to deliver a WFS with the required performances, both in static and rotating configurations. The whole alignment procedure and its result are presented in this Thesis.
The LN consortium confirmed the GWS readiness for its integration on the LN bench, the sensor was then shipped to Heidelberg at MPIA premises, where the rest of the instrument was located.
The same concept applies to the HWS, integrated and aligned at INAF Bologna and successively integrated on the LN bench. Differently from the GWS, the HWS is not feeded by the direct F/15 beam from the telescope, but from a F/20 beam.
To deliver to the HWS a high quality F/20 beam, an optical train (warm optics) consisting of 5 lenses, 7 mirrors (1 deformable), 1 dichroic and 1 filter was properly aligned before starting the alignment of the HWS to the LN bench.
With a multi-steps procedure, the HWS was aligned, through its SEs, to the on-axis beam used as reference for the alignment of the warm optics. Using the feedback of the HWS SEs, we aligned the calibration unit of the instrument, constituted of an on-axis reference fiber, a fiber plate with 23 fibers evenly distributed in a 2 *arcmin* equivalent FoV and an integrating sphere (not used for the alignment of the MCAO arm, and then not described in this Thesis, but needed for the flat fielding of the scientific CCD).
The HWS was successfully tested, closing an adaptive optics loop in the lab, injecting turbulence in the deformable mirror and correcting the first 150 modes of aberration.

The first MCAO arm was completed mounting the GWS on the bench and aligning it, through the AM, to the rest of the instrument.
To mitigate the risks of commissioning a so large and complex instrument, the first scientific instrument of its kind, as the only precursor implementing the same concept was just a demonstrator (MAD@VLT), the LN team decided to split the commissioning in different phases. The first phase is to test the performances of one GWS on sky during a so called Pathfinder Experiment, whose main aims were to test the GWS's communication and control of the ASM of the LBT, to test the GWS calibration strategies, the acquisition of reference stars so to understand the orientation between the GWS focal plane and the sky and to attempt closing the loop on sky. In an exciting, but also very unlucky, in term of weather and telescope failures (only 2 half-nights out of 14 could be used), campaign composed of 9 runs at the telescope for a total of about 70 days, we were able to overcome all the issues and problem arisen, successfully completing all the main goals estabilished for Pathfinder.
Also in light of these results, the instrument successfully passed the Preliminary Acceptance Europe review and was finally shipped, divided in several boxes and containers, to the LBT, where the instrument will be re-integrated and re-aligned and finally commissioned. These operations, planned for 2016 (already on-going at the time of submission of this Thesis), preliminary to the instrument installation on the telescope, despite the complexity of the instrument and the long time required for the alignment in the lab (just the alignment of the MCAO arms took almost one year), are expected to require roughly 130 days of work, divided in several runs, taking advantage of the experience acquired in the lab and of the pins located on LN bench to accurately reposition various lenses and mirrors of the instrument, removed before the shipment for safety reasons. Thanks to the valuable experience acquired with the alignment in the lab and the Pathfinder Experiment, we are confident to match the schedule, so to enable the early science with LN by the beginning of 2017.

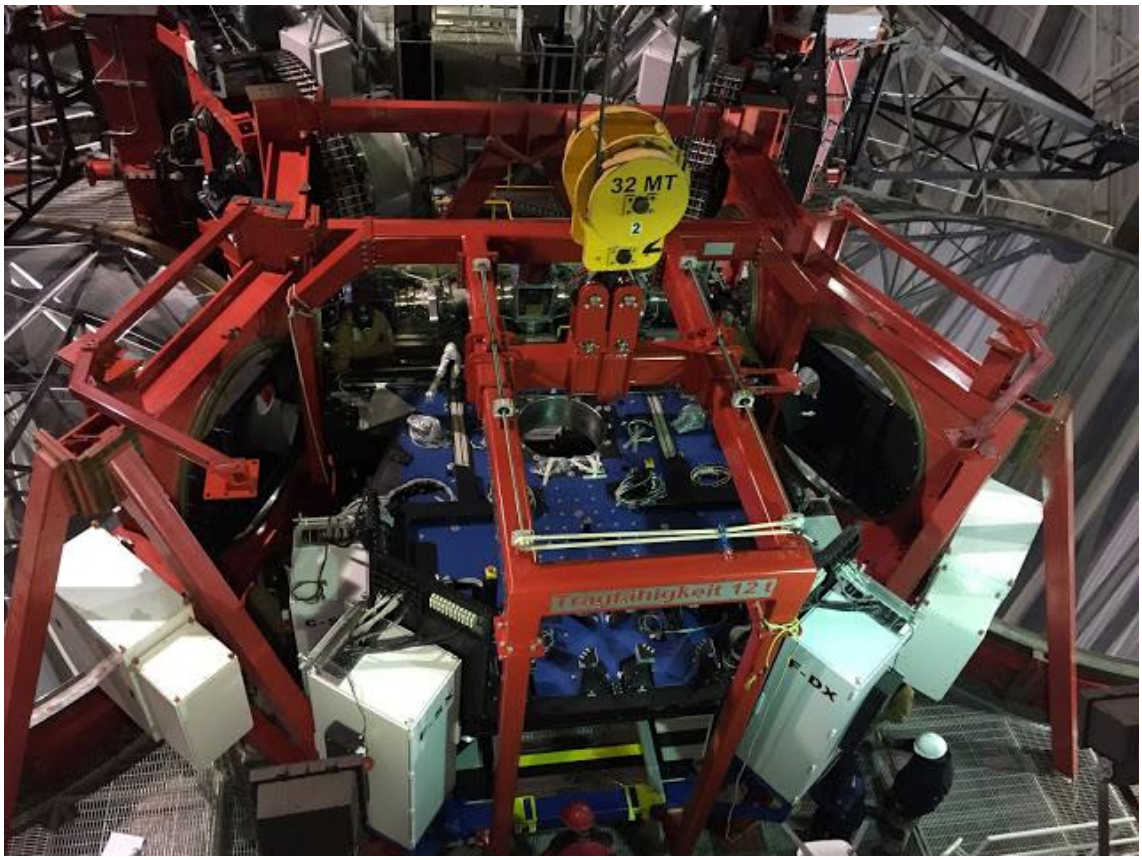

Figure 8-1: LINC-NIRVANA finally at the telescope, ready to be re-assembled and re-aligned.

9 Bibliography

D. R. Andersen, J. Stoesz, S. Morris, M. Lloyd-Hart, D. Crampton, T. Butterley, B. Ellerbroek, L. Jolissaint, N. M. Milton, R. Myers, K. Szeto, A. Tokovinin, J.-P. Veran & R. Wilson. *Performance Modeling of a Wide-Field Ground-Layer Adaptive Optics System.* PASP, 118, 1574–1590, 2006.

J. R. P. Angel, J. M. Hill, P. A. Strittmatter, P. Salinari & G. Weigelt. *Interferometry with the Large Binocular Telescope.* Proc. SPIE, 3350, 881–889, 1998.

C. Arcidiacono, E. Diolaiti, R. Ragazzoni, J. Farinato, & E. Vernet-Viard. *Sky coverage for layer-oriented MCAO: a detailed analytical and numerical study.* Proc. SPIE, 5490, 563–573, 2004.

C. Arcidiacono. *MAD Layer Oriented Technical Nights Report*. 2007.

C. Arcidiacono, M. Lombini, R. Ragazzoni, J. Farinato, E. Diolaiti, A. Baruffolo, P. Bagnara, G. Gentile, L. Schreiber, E. Marchetti, J. Kolb, S. Tordo, R. Donaldson, C. Soenke, S. Oberti, E. Fedrigo, E. Vernet & N. Hubin. *Layer Oriented Wavefront sensor for MAD on Sky operations*. Proc. SPIE, 7015, 2008.

H. W. Babcock. *The Possibility of Compensating Astronomical Seeing.* PASP, 65, 229, 1953.

J. M. Beckers. *Detailed compensation of atmospheric seeing using multi-conjugate adaptive optics.* Proc. SPIE, 1114, 215–0, 1989.

J. M. Beckers. *Adaptive optics for astronomy - Principles, performance, and applications.* ARA&A, 31, 13–62, 1993.

H. Bouy, J. Kolb, E. Marchetti, E. L. Martín, N. Huélamo and D. Barrado y Navascués. *Multi-conjugate adaptive optics images of the Trapezium cluster*. A&A, 477, 681-690, 2008.

J. B. Costa, R. Ragazzoni, A. Ghedina, M. Carbillet, C. V´erinaud, M. Feldt, S. Esposito, E. Puga, & J. Farinato. *Is there need of any modulation in the pyramid wavefront sensor?* Proc. SPIE, 4839, 288–298, 2003.

E. Diolaiti, R. Ragazzoni & M. Tordi. *Closed loop performance of a layer-oriented multi-conjugate adaptive optics system.* A&A, 372, 710, 2001.

S. Esposito & A. Riccardi. *Pyramid Wavefront Sensor behavior in partial correction Adaptive Optic systems.* Astron. Astrophys, 369, L9, 2001.

J. Farinato, R. Ragazzoni, E. Diolaiti, E. Vernet-Viard, A. Baruffolo, C. Arcidiacono, A. Ghedina, M. Cecconi, P. Rossettini, R. Tomelleri, G. Crimi, & M. Ghigo. *Layer oriented adaptive optics: from drawings to metal*. SPIE Proc. 4839, 588-599, 2003.

R. Foy & A. Labeyrie. *Feasibility of adaptive telescope with laser probe*. A&A, 152, L29–L31, 1985.

D. L. Fried. *Optical Resolution Through a Randomly Inhomogeneous Medium for Very Long and Very Short Exposures.* JOSA, 56, 1372, 1966.

D.L. Fried. *Atmospheric turbolence optical effects: understanding the adaptive optics implications.* In NATO ASIC proc., 1-25, 1995.

T. Fusco, M. Nicolle, G. Rousset, V. Michau, A. Blanc, J.-L. Beuzit & J.-M. Conan. *Wavefront sensing issues in MCAO.* Comptes Rendus Physique, 6, 1049–1058, 2005.

W. Gaessler, R. Ragazzoni, T. M. Herbst, D. R. Andersen, C. Arcidiacono, H. Baumeister, U. Beckmann, J. Behrend, T. Bertram, P. Bizenberger, H. Bohnhardt, F. Briegel, E. Diolaiti, T. M. Driebe, A. Eckhardt, S. E. Egner, J. Farinato, M. Heininger, M. Kurster, W. Laun, S. Ligori, V. Naranjo, E. Nussbaum, H.-W. Rix, R.-R. Rohloff, P. Salinari, R. Soci, C. Storz, C. Straubmeier, E. Vernet-Viard, G. P. Weigelt, R. Weiss & W. Xu. *LINC-NIRVANA: how to get a 23-m wavefront nearly flat*. Proc. SPIE, 5490, 527–534, 2004.

E. Gendron, F. Vidal, M. Brangier, T. Morris, Z. Hubert, A. Basden, G. Rousset, R. Myers, F. Chemla, A. Longmore, T. Butterley, N. Dipper, C. Dunlop, D. Geng, D. Gratadour, D. Henry, P. Laporte, N. Looker, D. Perret, A. Sevin, G. Talbot & E. Younger. *MOAO first on-sky demonstration with CANARY* . A&A, 529, L2, 2011.

F. Hammer, V. Hill & V. Cayatte. *Giraffe sur le VLT: un instrument dédié à la physique stellaire et extragalactique.* Journal des Astronomee Francais 60, p. 19, 1999.

F. Hammer, F. Sayède, E. Gendron, T. Fusco, D. Burgarella, V. Cayatte & J. Conan. *Scientific drivers for ESO future VLT/VLTI Instrumentaion.* Proc. of the ESO Workshop, Garching, Germany, p. 139, 2002.

J.W. Hardy. *Adaptive optics for astronomical telescopes*. Oxford University Press, 1990.

T. Herbst, R. Ragazzoni, D. Andersen, H. Boehnhardt, P. Bizenberger, A. Eckart, W. Gaessler, H.-W. Rix, R.-R. Rohloff, P. Salinari, R. Soci, C. Straubmeier & W. Xu. *LINC-NIRVANA: a Fizeau beam combiner for the large binocular telescope*. Proc. SPIE, 4838, 456–465, 2003.

T. M. Herbst & P. M. Hinz. *Interferometry on the Large Binocular Telescope*. Proc. SPIE, 5491, 383, 2004.

T. Herbst, R. Ragazzoni, D. Andersen, H. Boehnhardt, P. Bizenberger, A. Eckart, W. Gaessler, H.-W. Rix, R.-R. Rohloff, P. Salinari, R. Soci, C. Straubmeier & W. Xu. *LINC-NIRVANA: a Fizeau beam combiner for the large binocular telescope*. Proc. SPIE, 4838, 456–465, 2003.

T. M. Herbst, R. Ragazzoni, A. Eckart & G. Weigelt. *LINC-NIRVANA: achieving 10 mas imagery on the Large Binocular Telescope.* In Proc. SPIE, volume 7014, 2008.

T. M. Herbst, R. Ragazzoni, A. Eckart & D. Weigelt. *Imaging beyond the fringe: an update on the LINC-NIRVANA Fizeau interferometer for the LBT*. In Proc. SPIE, volume 7734, 773407, 2010.

J. M. Hill & P. Salinari. *Large Binocular Telescope project*. Proc. SPIE, 4837, 140–153, 2003.

N. Hubin, R. Arsenault, R. Conzelmann, B. Delabre, M. Le Louarn, S. Stroebele & R. Stuik. *Ground Layer Adaptive Optics*. Comptes Rendus Physique, 6, 1099–1109, 2005.

A. Kolmogorov. *The Local Structure of Turbulence in Incompressible Viscous Fluid for Very Large Reynolds' Numbers.* Akademiia Nauk SSSR Doklady, 30, 301–305, 1941.

LINC-NIRVANA team. *LINC-NIRVANA Final Design Review*. 2005.

L. Marafatto, M. Bergomi, A. Brunelli, M. Dima, J. Farinato, G. Farisato, L. Lessio, D. Magrin, R. Ragazzoni, V. Viotto, T. Bertram, P. Bizenberger, M. Brangier, F. Briegel, A. Conrad, F. De Bonis, T. Herbst, R. Hofferbert, F. Kittmann, M. Kürster, L. Mohr & R.R. Rohloff. *Aligning a more than 100 degrees of freedom wavefront sensor*. Proc. SPIE, 2012.

E. Marchetti, N. N. Hubin, E. Fedrigo, J. Brynnel, B. Delabre, R. Donaldson, F. Franza, R. Conan, M. Le Louarn, C. Cavadore, A. Balestra, D. Baade, J.-L. Lizon, R. Gilmozzi, G. J. Monnet, R. Ragazzoni, C. Arcidiacono, A. Baruffolo, E. Diolaiti, J. Farinato, E. Vernet-Viard, D. J. Butler, S. Hippler & A. Amorin. *MAD the ESO multi-conjugate adaptive optics demonstrator.* In Proc. SPIE, volume 4839, 317–328, 2003.

E. Marchetti, R. Brast, B. Delabre, R. Donaldson, E. Fedrigo, C. Frank, N. Hubin, J. Kolb, J.-L. Lizon, M. Marchesi, S. Oberti, R. Reiss, J. Santos, C. Soenke, S. Tordo, A. Baruffolo, P. Bagnara, & The CAMCAO Consortium. *On-sky Testing of the Multi-Conjugate Adaptive Optics Demonstrator*. The Messenger, 129, 8–13, 2007.

E. Marchetti, R. Brast, B. Delabre, R. Donaldson, E. Fedrigo, C. Frank, N. Hubin, J. Kolb, J.L. Lizon, M. Marchesi, S. Oberti, R. Reiss, C. Soenke, S. Tordo, A. Baruffolo, P. Bagnara, A. Amorim & J. Lima. *MAD on sky results in star oriented mode.* Proc. SPIE 7015, 2008.

T. Morris, Z. Hubert, R. Myers, E. Gendron, A. Longmore, G. Rousset, G. Talbot, T. Fusco, N. Dipper, F. Vidal, D. Henry, D. Gratadour, T. Butterley, F. Chemla, D. Guzman, P. Laporte, E. Younger, A. Kellerer, M. Harrison, M. Marteaud, D. Geng, A. Basden, A. Guesalaga, C. Dunlop, S. Todd, C. Robert, K. Dee, C. Dickson, N. Vedrenne, A. Greenaway, B. Stobie Heather Dalgarno & Jure Skvarc. *CANARY: The NGS/LGS MOAO demonstrator for EAGLE*. EDP Sciences, 2010.

R. J. Noll. *Zernike polynomials and atmospheric turbulence*. JOSA, 66, 207–211, 1976.

R. Ragazzoni. *Pupil plane wavefront sensing with an oscillating prism*. JModOpt, 43, 289–293, 1996.

R. Ragazzoni. *No Laser Guide Stars for adaptive optics in giant telescopes?* A&A, 136, 205–209, 1999a.

R. Ragazzoni, E. Marchetti & F. Rigaut. *Modal tomography for adaptive optics.* A&A, 342, L53–L56, 1999b.

R. Ragazzoni, J. Farinato & E. Marchetti. *Adaptive optics for 100-m-class telescopes: new challenges require new solutions.* Proc. SPIE, 4007, 1076–1087, 2000a.

R. Ragazzoni, E. Marchetti & G. Valente. *Adaptive-optics corrections available for the whole sky.* Nature, 403, 54–56, 2000b.

Ragazzoni R. *Adaptive optics for giant telescopes: NGS vs. LGS*. ESO Conf. Workshop Proc., 57, 175, 2000c.

R. Ragazzoni, E. Diolaiti, J. Farinato, E. Fedrigo, E. Marchetti, M. Tordi & D. Kirkman. *Multiple field of view layer-oriented adaptive optics. Nearly whole sky coverage on 8 m class telescopes and beyond*. A&A, 396, 731–744, 2002.

R. Ragazzoni, T. M. Herbst, W. Gaessler, D. Andersen, C. Arcidiacono, A. Baruffolo, H. Baumeister, P. Bizenberger, E. Diolaiti, S. Esposito, J. Farinato, H. W. Rix, R.-R. Rohloff, A. Riccardi, P. Salinari, R. Soci, E. Vernet-Viard & W. Xu. *A visible MCAO channel for NIRVANA at the LBT.* Proc. SPIE, 4839, 536–543, 2003.

R. Ragazzoni, E. Diolaiti, E. Vernet, J. Farinato, E. Marchetti & C. Arcidiacono. *Arbitrarily Small Pupils in Layer-Oriented Multi-Conjugate Adaptive Optics*. PASP, 117, 860–869, 2005.

R. Ragazzoni, Y. Almomany, C. Arcidiacono, R. Falomo, J. Farinato, M.Gullieuszik, A. Moretti, E. Diolaiti, M. Lombini, G. Piotto, R. Turolla, E. Marchetti & R. Donaldson. *Layer oriented: science with MAD and beyond*. Proc. SPIE, 7015, 2008.

F. Rigaut. *Ground Conjugate Wide Field Adaptive Optics for the ELTs*. ESO Astrophysics Symposia, 58, 11, 2002.

F. Roddier. *The effects of atmospheric turbulence in optical astronomy*. Prog. Optics, 19, 281–376, 1981.

R. V. Shack & B. C. Platt. *Production and use of a lenticular Hartmann screen*. JOSA, 61, 656, 1971.

V. L. Tatarski. *Wave propagation in a turbulent medium*. Dover Publications, 1961.